Adsorption and desorption kinetics of dry sorbents for CO_2 capture

J Williams

orcid.org/ 0000-0002-7575-7935

Dissertation accepted in fulfilment of the requirements for the degree *Master of Engineering in Chemical Engineering* at the North-West University

Supervisor: Prof RC Everson

Co-supervisor: Dr GN Okolo

Graduation: June 2025

DECLARATION

I, Juan Williams, hereby declare that the dissertation entitled: "***Adsorption and desorption kinetics of dry sorbents for CO_2 capture***", submitted in the fulfilment of the requirements for the degree of Masters in Chemical Engineering, is my own work except where acknowledged in text, it has been language edited as required and has not been submitted to any other tertiary institution in whole or in part.

I understand that the copies handed in for examination are the property of the North-West University.

Signed at Potchefstroom on the 15th day of June 2024

J Williams (Student)

25919784

University number

ACKNOWLEDGEMENTS

The author of this dissertation expresses his appreciation and gratefully acknowledges the following persons:

- My supervisor and co-supervisor, Professor Raymond Everson and Doctor Gregory Okolo thank you for your guidance, suggestions, and criticisms, without which this dissertation would not have reached finalisation.
- I want to thank Professor John Bunt for facilitating the agreement from the National Research Foundation (NRF) [Coal Research Chair Grant no. 86880], who financially supported this work. The opinions, findings, and conclusions or recommendations expressed in any publication generated by the NRF-supported research are that of the author(s) alone, and the NRF accepts no liability whatsoever in this regard.
- Professor Hein Neomagus, thank you for stepping in as a temporary supervisor when needed and providing invaluable insights into experimental design and methodology.
- Dr Frikkie Conradie, for contributing knowledge and critical thinking concerning the CO_2 analysing equipment and data collection.
- Professor Dimitri Bessarabov from DST HySA infrastructure Centre of Competence at NWU, thank you for your financial support and interest in the carbon capture research.
- Dr. Paola Ammendola and Dr. Federica Raganati from Istituto di Scienze e Tecnologie per l'Energia e la Mobilita Sostenibili (STEMS)-CNR in Naples, Italy, for your expertise shared with the processing of the experimental work and setup and the modelling thereof as part of a collaborative international university partner.
- Mr. Frikkie van der Merwe, for his wisdom and motivating words when I needed them.
- Dr Gerrit Grobler for the help with the Matlab code used to fit the kinetic models to the experimental data.
- Dr Gerald Marewo, for his tireless work towards the solutions of the partial differential equations required to predict the breakthrough behaviour of the kinetics experiments.
- Mr. Marcus Keulder, thank you for sharing your expert knowledge of the experimental setup and small talk during the long experimental hours.
- Mr. Maritz Maass, thank you for being a good friend and helping keep me motivated when I needed it most.
- Mr. Johan Griessel, thank you for the long conversations during this dissertation, listening to all the problems I encountered and then providing me with words of encouragement to keep working through them.

- My mother, Gerda Williams, and my brother, Ethan Williams, thank you for providing me with a place to come home whenever I required a break and needed to 'recharge' and keeping my spirits up and checking in on me regularly.
- My wife, Marianca Williams, thank you for your continuous support and love during my long hours of working on this dissertation and the years of studying leading up to this moment.

ABSTRACT

This study focused on commercially available activated carbons' adsorption and desorption kinetics using a laboratory-scale fixed-bed reactor. The three activated carbons are CQ650, derived from coconut shells and activated with a combination of steam and KOH impregnation; CQ30P, derived from coal, also using a combination of steam and KOH impregnation. The third is CQ006, derived from coal and activated using steam and an acid wash. Ten continuous adsorption and desorption cycles were performed at 30 to 70 ℃ with 10 ℃ increments and two CO_2 concentrations of 5 and 15 vol.%. The characterisation data of the samples show that CQ006 has the highest fixed carbon content while CQ650 has the highest BET surface area of 517.1±4.5 m^2/g and the highest Dubinin–Radushkevich micropore surface area at 735.0±27 m^2/g. A scanning electron microscopy analysis revealed that the activated carbon samples have well-developed pore structures over the entire surface.

All the investigated sorbents performed well under cyclic operation with no significant difference in adsorption capacity between cycle 1 and cycle 10. The most significant difference is the completion time, with CQ650 taking 8600 seconds at 60 ℃ and 15 vol.% CO_2 feed concentration, while the quickest sorbent, CQ006, took 5900 seconds under the same conditions. CQ650 have the highest adsorption quantity overall at 5 and 15 vol.% CO_2 feed concentration with 0.96 mmol/g and 1.67 mmol/g, respectively. CQ30P and CQ006 have near-identical adsorption capacities of 0.85 mmol/g and 0.83 mmol/g at 5 vol.% CO_2 feed and 1.03 mmol/g for both at 15 vol.% CO_2 feed concentration.

The increased temperatures decreased the sorbents' saturation times and adsorption capacities, while the feed concentration also significantly affected the CO_2 quantity adsorbed and the saturation times of the experiments. CQ006 has the best cyclic desorption efficiency, with the lowest efficiency achieved at 93.2%; CQ650 is second with the lowest cyclic efficiency at 90.1%, and CQ30P at 86.7%. The same trend is seen when looking at the overall desorption efficiency across the 5 temperatures (30, 40, 50, 60 and 70 ℃), where CQ006 averages at 98.3% and 99.1% for the 5 and 15 vol.% CO_2 feed concentrations, 96.5% and 95.1% for CQ650 and 93.4% and 92% for CQ30P at 5 and 15 vol.% CO_2 feed concentrations, respectively.

Three kinetic models were tested, with Avrami being the most suitable with a quality of fit of (99.1%), followed by the pseudo-first-order (94.7%) and the pseudo-second-order kinetic model (87.6%). The desorption activation energy is higher than the adsorption activation energy for all conditions, indicating that desorption (reverse adsorption reaction) requires more energy to remove the molecules from the surface of the sorbent than the energy released by binding to the

surface of the sorbent. The thermodynamic results indicate that the adsorption mechanism is physical adsorption with a change in enthalpy of (–10 to –20 kJ/mol). The negative change in enthalpy indicates that the reaction is exothermic, aligning with other reports from the open literature. The entropy in all conditions is also negative (–0.00198 kJ/mol to –0.00660 kJ/mol), implying that the molecules are slightly more orderly when adsorbed. A negative change in the Gibbs free energy (–18.37 kJ/mol to –22.57 kJ/mol) implies that the reactions occur spontaneously.

The breakthrough analysis using the Avrami equation for adsorption and a modified Avrami equation for desorption provided satisfactory results. The Avrami is well suited to predict adsorption breakthrough behaviour, with the lowest QOF% achieved being 96.4%. In contrast, the modified Avrami equation does not adequately predict the desorption breakthrough behaviour of the sorbents, with the QOF% ranging from 63.2% to 87.9%.

Keywords: Carbon capture, CO_2, adsorption, desorption, kinetics, activated carbon, thermodynamics

TABLE OF CONTENTS

LIST OF TABLES

LIST OF FIGURES

LIST OF ABBREVIATIONS AND SYMBOLS

Symbol	Description	Unit
A	Pre exponential factor	–
A_C	Ash yield percentage	%
Å	Angstrom	10^{-10} *m*
C	Concentration	mol
C'	Concentration	$mol.cm^{-3}$
$C_{A_{max}}$	Maximum actual concentration of the CO_2 gas	%
$C_{A_{min}}$	Minimum actual concentration of the CO_2 gas	%
C_e^a	Adsorption equilibrium adsorbate concentration	*mol*
C_e^d	Desorption equilibrium adsorbate concentration	*mol*
C_i^a	Adsorption CO_2 concentration at a specific time	*mol*
C_i^d	Desorption CO_2 concentration at a specific time	*mol*
C_x	CO_2 concentration measured with the CO_2 analyser	%
$C_{Z_{max}}$	Maximum CO_2 concentration measured with the CO_2 analyser	%
$C_{Z_{min}}$	Minimum CO_2 concentration measured with the CO_2 analyser	%
C_0	CO_2 feed concentration	*mol*
C^θ	Standard state of adsorption gas	*mol/L*
c_F	Fractional order Avrami order constant	–
D	Diffusivity	$cm^2.s^{-1}$
D_s	Surface diffusion coefficient	
d	Particle diameter	*m*
E_a	Adsorption activation energy	*kJ/mol*
E_d	Desorption activation energy	*kJ/mol*
F_{CO_2}	Molar flow rate of CO_2	*mol/s*
G^o	Gibbs free energy	*kJ/mol*
H^o	Enthalpy	*kJ/mol*
K_d	Distribution coefficient	*L/kg*
K_F	Freundlich isotherm model constant	$mmol/g.kPa^{1/n}$
K_L	Langmuir equilibrium adsorption constant	*1/kPa*
K^θ	Standard equilibrium constant	–
k_1	Pseudo-first order rate constant	s^{-1}
k_1'	Pseudo-first order desorption rate constant	s^{-1}
k_2	Pseudo-second order rate constant	$g/mmol.s$

k_2'	Pseudo-second order desorption rate constant	$g/mmol.s$
k_A	Avrami kinetic constant	s^{-1}
k_A'	Avrami desorption kinetic constant	s^{-1}
k_F	Fractional order Avrami constant	–
M	Moisture content percentage	%
m	Desorption order	–
m_F	Fractional order constant	–
m_1	Mass of empty tray	g
m_2	Mass of tray and sample before drying	g
m_3	Mass of tray and sample after drying	g
N	Number of data points	–
n	Avrami stretching parameters	–
n_A'	Avrami desorption stretching parameter	–
P	Pressure	kPa
P_{CO_2}	Pressure of CO_2	kPa
$P_{CO_{2,0}}$	Saturation pressure of CO_2	kPa
q	Solid phase CO_2 concetration	mol
q_{BET}	Maximum multilayer adsorption capacity	mmol/g
q_{CO_2}	CO_2 equilibrium adsorption quantity	mmol/g
q_e^a	Adsorption quantity at equilibrium	mmol/g
q_e^d	Desorption quantity at equilibrium	mmol/g
q_i	Quantity of gas i adsorbed	mmol
q_s	Maximum monolayer adsorption capacity	mmol/g
q_t^a	Adsorption capacity at a specific time	mmol/g
q_t^d	Desorption capacity at a specific time	mmol/g
q^θ	Standard state of solid	mol/m^2
R	Universal gas constant	kJ/mol.K
r	Average diameter of adsorbent particle	cm
S^o	Entropy	kJ/mol
T	Absolute temperature	K
t	Time	s
V	Volatile matter percentage	%
v_i	Volumetric flow rate of the adsorbed gas	mL/min
vol.%	Volume percentage	%
wt.%	Weight percentage	%

x	Modelled data point	–
x_{exp}	Experimental data point	–
y	Avrami desorption proportion	–

Greek Letters

α	Initial adsorption rate constant	–
β	Desorption rate constant	–
Θ	Surface coverage	–
ρ_p	Particle density	kg/m^3
ω_{H_2O}	Moisture content	%

Abbreviations

AC	Activated carbon/s
ARE	Average relative error
BET	Brunauer-Emmet-Teller
CFB	Circulating Fluidised Bed
CFBR	Circulating Fluidised Bed Reactor
CO	Carbon Monoxide
2-D	Two dimensional
DEA	Diethanolamine
D-R	Dubinin-Radushkevich
ESS	Error sum squared
HDM	Homogeneous diffusion model
H-K	Horvath-Kawazoe
IUPAC	International Union of Pure and Applied Chemistry
MEA	Mean absolute error
MOF	Metal-organic frameworks
PFO	Pseudo-first order
PSO	Pseudo-second order
RMSE	Root mean squared error
SCM	Shrinking core model
SEM	Scanning electron microscopy
SRT	Statistical rate theory
WGSR	Water-gas shift reaction

Chapter 1

CHAPTER 1: INTRODUCTION

1.1 Background and motivation

Global warming is one of society's most prominent global problems, affecting people and the environment. The effects of global warming presently, such as the shrinking ice sheets and fauna and flora geographical ranges shifting, are irreversible on the time scale of people alive today, and these effects will continue to worsen for decades to come (NASA, 2022). The noticeable effects of global warming include shrinking glaciers, ice on rivers and lakes breaking up earlier, plant and animal ranges shifting, and trees flowering sooner (NASA, 2022).

The most felt impact of global warming is the extreme weather events that occur more regularly (Bolan *et al.*, 2024). Weather events such as droughts are more severe, frequent, and longer-lasting, and wildfires are more frequent, not only due to the increased heat but also the irregularity in the rainfall of a region (Kabir *et al.*, 2023; Bolan *et al.*, 2024). The worst extreme weather events are flooding, where the increased atmospheric temperatures increase the atmosphere's moisture content, leading to a higher frequency of tropical cyclones and more powerful hurricanes (Hou *et al.*, 2023; Bolan *et al.*, 2024). As such, to comply with national and international emission control restrictions, the capturing, storage and conversion of valuable chemicals utilising carbon dioxide that originated from coal-fired plants must be examined.

The South African Centre for Carbon Capture and Storage (SACCCS) roadmap for carbon capture started in 2004 with an assessment of the potential for CCS in South Africa, followed by a CO_2 geological storage atlas development in 2010. The third step in 2017 involves a test injection of CO_2, followed by a demonstration plant (100 000t CO_2/year). From 2025 onwards, the aim is to implement commercial CCS deployment to store 1 000 000t CO_2/year (Beck et al., 2013). As South Africa is responsible for approximately 500 million metric tonnes of CO_2, establishing the country's first pilot carbon capture, utilisation, and storage is critical to reducing the country's carbon footprint(Sinazo Mkoko, 2024). A characterisation and feasibility study on the site reveals a potential storage capacity of 34 gigatonnes of CO_2, paving the way for Phase 2, which focuses on design and construction (Sinazo Mkoko, 2024).

To achieve carbon capture regulations, it is necessary to effectively capture carbon dioxide from the flue gases of coal-fired power plants (containing ≈ 15 volume % CO_2) to obtain pure carbon dioxide to enable effective transport and storage in deep-seated aquifers and for converting carbon dioxide to beneficial chemicals, such as methanol, methane and liquid fuels (Allen *et al.*, 2019). Thus, suitable industrial capturing processes must be developed to ensure the adequate capture and production of pure carbon dioxide. There are three main approaches to carbon

capture: pre-combustion, oxyfuel combustion and post-combustion carbon capture. Pre-combustion requires the fuel to be prepared by extracting CO_2 from a fossil fuel, usually during gasification, before the combustion process, while the oxyfuel approach requires the fuel to combust in an oxygen-rich environment, creating a flue gas consisting of CO_2 and water. On the other hand, the post-combustion does not alter the combustion process and, thus, can be easily retrofitted into existing infrastructure (Leung et al., 2014).

Post-combustion CO_2 capture can be further divided into subsections: cryogenic distillation, membrane separation and adsorption. Cryogenic distillation is very expensive in terms of energy usage, and membrane separation's efficiency is limited by low flue gas pressure (Leung et al., 2014). The capture of CO_2 by adsorption systems can also be divided into wet, dry and semi-dry processes, with the wet process being the least desirable as it uses a large amount of water. Dry and semi-dry processes are more favourable than wet processes due to the high energy demands for solvent regeneration, limited selectivity among acid gasses, expensive materials, substantial absorption of heat, and potential environmental harm (Khan *et al.*, 2023). Dry and semi-dry processes using circulating fluidised beds (CFB) with sorbents (such as activated carbons, zeolites and potassium carbonate) consisting of adsorption and regeneration processes are one of the most cost-effective and easiest to retrofit into existing infrastructure and processes (Kakaras et al., 2012).

However, the modelling (of the process with equipment design) and the characterisation of the sorbents used need to be improved for accurate techno-economic analysis to justify the process for industrial application. Industrial sorbents are available, and there is a need to evaluate these sorbents in greater detail for the development of circulating fluidised bed technology, especially the integrated design of the riser and regenerator (Bhatta et al., 2015). The characterisation of the sorbents would involve physical and chemical properties, sorption capacities, adsorption and desorption kinetics, and the thermodynamic properties of the adsorption and desorption processes.

Evaluating the sorbents' adsorption and desorption kinetics rates is required in combination with the process hydrodynamics for the final process modelling. The kinetics can be experimentally assessed in microreactors, and the data obtained can then be fitted to the various kinetic rate equations to determine the model that best describes the adsorption and regeneration processes.

1.2 Research problem, research purpose and objectives

1.2.1 Research problem

The design of a dry sorbent circulating fluidised bed requires a comprehensive computational fluid dynamics model. Such a model requires accurate adsorption and desorption kinetic rate data and the physico–chemical properties of the adsorbents that can be utilised in such a carbon capture process. This research aims to provide critical kinetic adsorption and desorption rate data required to design a practical, working circulating fluidised bed process used for CO_2 capture.

1.2.2 Research purpose

This investigation aims to quantify CO_2 adsorption and desorption properties, adsorption and desorption rates and kinetics, and thermodynamic properties of dry activated carbon (AC) sorbents for CO_2 capture from simulated flue gas that is suitable for advanced process modelling for the designing of an industrial-scale carbon capture circulating fluidised bed. Also, the investigation aims to identify the optimal conditions for the dry activated carbon sorbents to be used for the carbon capture process. With accurate adsorption and desorption kinetic rate data, future studies can compare the data from pure CO_2 capture to data that involve a mixture of gasses that more closely resembles a typical flue gas to see how other gas components affect the adsorption and desorption behaviour of sorbents.

1.2.3 Research objectives

- Conduct a literature survey on the parameters and properties required for modelling industrial/pilot processes for high-purity carbon dioxide capture in circulating fluidised beds involving adsorption and regeneration.
- Develop and execute an experimental procedure on a laboratory-scale microreactors for dry sorbents' adsorption and desorption kinetic studies.
- Determine dry-activated carbon sorbents' chemical, physical, and thermodynamic properties and their adsorption and desorption kinetics.
- Identify the sorbents' properties that impacted the carbon capture process.
- Evaluate adsorption and desorption kinetic models that best fits the experimental results for both adsorption and desorption.
- Evaluate a breakthrough curve model for adsorption and desorption.

1.3 Layout of dissertation

This investigation includes conducting adsorption and desorption experiments on activated carbons to determine their adsorption capacity, kinetics and adsorption and desorption rates using a fixed-bed reactor setup.

Chapter 1 (Background and motivation)

This chapter is concerned with the introduction, motivation and the aims and objectives of this research work.

Chapter 2 (Literature review)

To achieve the research aims and objectives set out and discussed in Chapter 1, a literature sreview was conducted on carbon capture, carbon capture processes, adsorbents suitable for carbon capture and adsorption and desorption kinetic models for modelling experimental data.

Chapter 3 (Materials and methods)

This chapter introduces the materials used for experimentation and explains in detail how the experiments were carried out. All calculation procedures followed for adsorption capacity calculations, kinetics, and thermodynamics were explained in detail.

Chapter 4 (Adsorption characterisation)

The characterisations of the three activated carbon samples include proximate analysis, ultimate analysis, surface area analysis, pore size analysis, pore volume analysis and scanning electron microscopy analysis. The characterisation results were presented, discussed and compared with similar data from activated carbon samples found in the open literature.

Chapter 5 (Experimental results and discussion: adsorption and desorption)

This section presents and discusses the results of the fixed-bed adsorption and desorption experiments. These results include the cyclic operation of adsorption and desorption, the effect of feed concentration on sorbent performance, the effect of temperature on sorbent performance, and the effect of temperature on the quantity of CO_2 adsorbed and desorbed. All these results were compared to results of similar activated carbons found in the literature.

Chapter 6 (Results and discussion: kinetic modelling)

Kinetic modelling consists of finding the most accurate adsorption and desorption models from three well-known kinetic models and using the best-fitting model to model all experimental results. Once the kinetic results were obtained, the activation energy and a thermodynamic analysis were conducted on the adsorption and desorption experimental results from the fixed-bed reactor. These results were then compared to those reported in the literature using similar activated carbons.

Breakthrough modelling was done using the Avrami kinetic equation for adsorption and a modified Avrami kinetic equation for desorption. This was done to check if simple kinetic models can be used to generate a relatively accurate predictive model for adsorption and desorption breakthrough behaviour.

Chapter 7 (Conclusions and recommendations)

The main conclusions drawn from the characterisations, experimental results, and modelling results are presented in this chapter, along with further research recommendations that are not covered within the scope of this dissertation.

Chapter 2

CHAPTER 2: LITERATURE REVIEW

In this chapter, a literature review of research conducted on carbon capture technologies and processes, the sorbents suitable for CO_2 capture and regeneration, and the properties of the sorbents that make them viable was undertaken. Furthermore, the literature review also covered kinetic models applicable to adsorption/desorption processes. The survey in this chapter was considered appropriate to provide the necessary background for executing this research work.

2.1 Emissions in South Africa

The earth is surrounded by an atmosphere that contains greenhouse gasses that allow the earth to be habitable and sustain life. The greenhouse gasses include carbon dioxide, methane and nitrous oxides. These gasses form a heat-trapping blanket that prevents the planet from radiating heat back into space, thus keeping the earth warm (Stannard, 2018). Without the natural greenhouse effect, the average surface temperature would be around −21℃ (Anderson et al., 2016; Sloss, 2017). The problem with carbon dioxide as a greenhouse gas is that its content in the atmosphere significantly increases, causing more heat to be trapped and warming the earth further.

Like numerous developing nations globally, South Africa faces challenges in supplying electricity to its expanding population while mitigating detrimental environmental impacts (Sloss, 2017). Consequently, emissions within South Africa surged by 41% between 1990 and 2017. The power sector is the primary contributor to CO_2 emissions, accounting for approximately 47% of the nation's overall emissions. With 18 coal-fired power stations, South Africa is the 14th largest CO_2 producer globally, generating 400 million tonnes (Mcsweeney and Timperley, 2018).

Given that South Africa ranks as the 7th largest coal producer worldwide, the country heavily depends on coal-fired power stations due to the affordability of coal as a fuel source, which is crucial for meeting the escalating electricity demand (Mcsweeney and Timperley, 2018). Despite this reliance amidst global advocacy for sustainable energy sources, South Africa has established mitigation objectives to diminish its dependency on coal within the power sector. The South African Integrated Resources Plan for Electricity proposes to stop the construction of new coal power stations after 2030, advocating instead for increased investment in renewable energy and emissions reduction measures for existing facilities (Mcsweeney and Timperley, 2018).

Figure 2-1 shows that the rate of increase in CO_2 emission is quite significant as it has a positive slope, indicating that it will increase in the future. Therefore, the general idea of carbon capture worldwide is to reduce the slope of the graph of every country's CO_2 emissions; ideally, the slope should become negative, meaning that year-on-year emission is reduced.

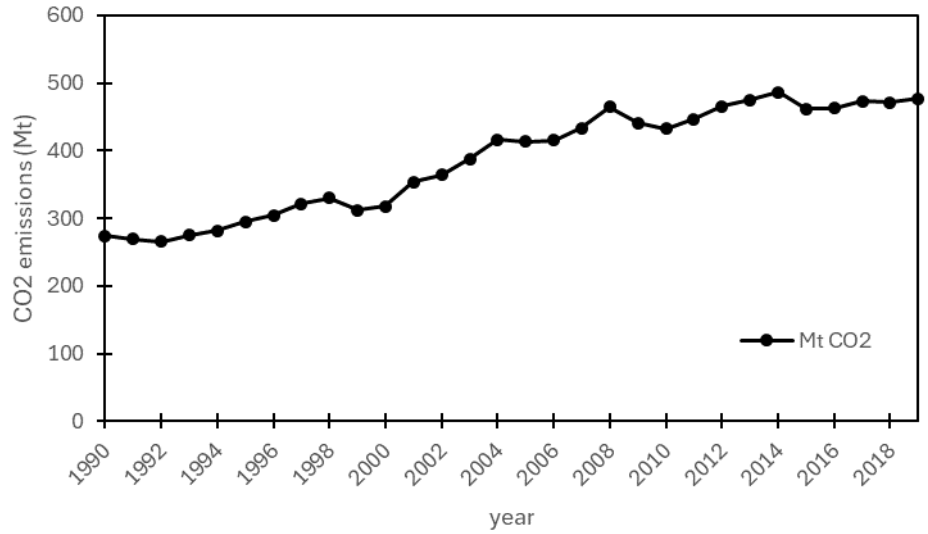

Figure 2-1: General trend of CO2 increase in the energy sector in South Africa (Ge *et al.*, 2020).

2.2 Carbon capture processes and technologies

CO_2 capture and storage technologies from flue gases are considered cost-effective means for capturing, utilising, and sequestration from large stationary sources, thus lessening global warming (Ammendola et al., 2017).

2.2.1 Carbon capture technologies

Three leading technologies today can be implemented to remove CO_2 from industrial processes. They are pre-combustion capture, post-combustion capture and oxyfuel combustion.

2.2.1.1 Pre-combustion capture

Pre-combustion capture is the removal or capturing of CO_2 before the combustion process. In this decarbonisation route, the traditional fuels react with the air, which contains O_2 and with or without steam to produce syngas, which is a mixture of carbon monoxide (CO) and hydrogen (H_2) (Osman *et al.*, 2021). Equations 2-1 and 2-2 describe the primary reaction for producing syngas from partial oxidation and steam reforming reactions, respectively (Osman *et al.*, 2021).

$$C_nH_m + \frac{n}{2}O_2 \rightarrow nCO + \left(\frac{m}{2}\right)H_2 \quad \Delta H_{CH_4} = -36\ kJ.mol^{-1} \qquad 2\text{-}1$$

$$C_nH_m + nH_2O \rightarrow nCO + \left(\frac{n+m}{2}\right)H_2 \quad \Delta H_{CH_4} = 206\ kJ.mol^{-1} \qquad 2\text{-}2$$

Partial oxidation is usually done with oxygen that is separated from the air, and in the case where both steam and oxygen are used, the process is referred to as auto-thermal reforming since the exothermal partial oxidation reactions balance the endothermic reforming reactions (Jansen *et al.*, 2015).

Following syngas production, a water-gas shift reaction (WGSR) converts CO to CO_2 and H_2 by adding steam according to equation 2-3 (Jansen *et al.*, 2015).

$$CO + H_2O \rightarrow CO_2 + H_2 \quad \Delta H = -41\ kJ.mol^{-1} \qquad 2\text{-}3$$

CO_2 is separated at ambient temperature using conventional washing steps by chemical and physical adsorption. Then, the hydrogen-rich gas is used as a low-carbon fuel source in a Bryton and Rankine combined cycle plant for power generation (Jansen *et al.*, 2015). The drawback of utilising this technology is the solvent and efficiency losses of up to 16% points, with the syngas production accounting for 6% points, WGSR for 3% points, the H_2/CO_2 separation section (5% points) and the CO_2 drying and compression section (2% points) (Smith *et al.*, 2013). In theory, the pre-combustion capture route could offer a cheaper cost than post-combustion and oxyfuel combustion technologies; however, retrofitting current facilities adds significantly to capital cost and complexity, limiting their commercial viability (Osman *et al.*, 2021).

2.2.1.2 Post-combustion capture

Post-combustion capture treats the exhaust or flue gases resulting from a combustion process by removing the CO_2, thereby cleaning the flue gas before it gets released into the atmosphere (de Coninck and Benson, 2014; Abu-Zahra et al., 2016). Post-combustion capture processes are preferred for use in existing power plants as these plants can be retrofitted since the power generation process has not been changed. However, for post-combustion capture to be economically feasible, a CO_2 purity of > 95.5% is required, and to achieve such high purity from a flue gas stream containing < 15% CO_2, a large amount of energy is needed (Leung et al., 2014).

The post-combustion capture technology has been proven at small-scale pilot plants, with CO_2 recovered at rates up to 800 t/day, but with the main challenge being the large parasitic load (low CO_2 level in the flue gas), the energy penalty is high (Wall, 2007). For example, the U.S. National Energy Technology Laboratory (NETL) estimated that post-combustion CO_2 capture would increase the cost of electricity production by 32% and 65% for gas and coal-fired plants, respectively (Kanniche *et al.*, 2010). In addition, at the low CO_2 concentrations and atmospheric

pressures that coal-fired power plant flue gases are exhausted, the thermodynamic driving force for CO_2 capture is low (Figueroa *et al.*, 2008). Figure 2-2 shows a simplified schematic of a post-combustion capture process.

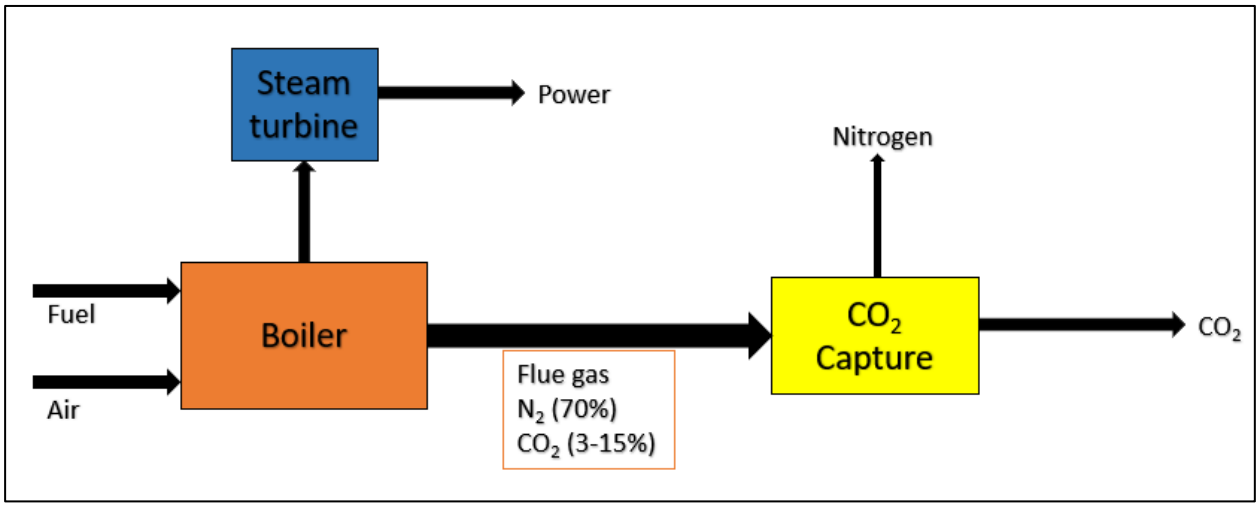

Figure 2-2: Schematic of a post-combustion CO_2 capturing process (Figueroa *et al.*, 2008)**.**

2.2.1.3 Oxyfuel combustion

Oxyfuel combustion carries out the combustion process by removing nitrogen from the oxidiser, which is why combustion occurs in nearly pure oxygen (Wang, 2018). Generally, the oxyfuel combustion technology recycles flue gas to lower the flame temperature (although it is exceptionally high), making it an efficient energy-saving combustion technology. However, combustion in an oxygen-rich environment produces a flue gas with water vapour and a high CO_2 concentration (Stanger *et al.*, 2015). This high CO2 concentration in the flue gas makes it ideal for carbon capture processes.

Oxyfuel combustion generally consists of the following key units, as in Figure 2-3 (Stanger *et al.*, 2015) :

- Air separation unit – oxygen production
- Boiler or gas turbine – combustion of fuel & heat generation
- Flue gas processing unit – flue gas cleaning or gas quality control system
- CO_2 processing unit – final purification of the CO2 for transport & storage.

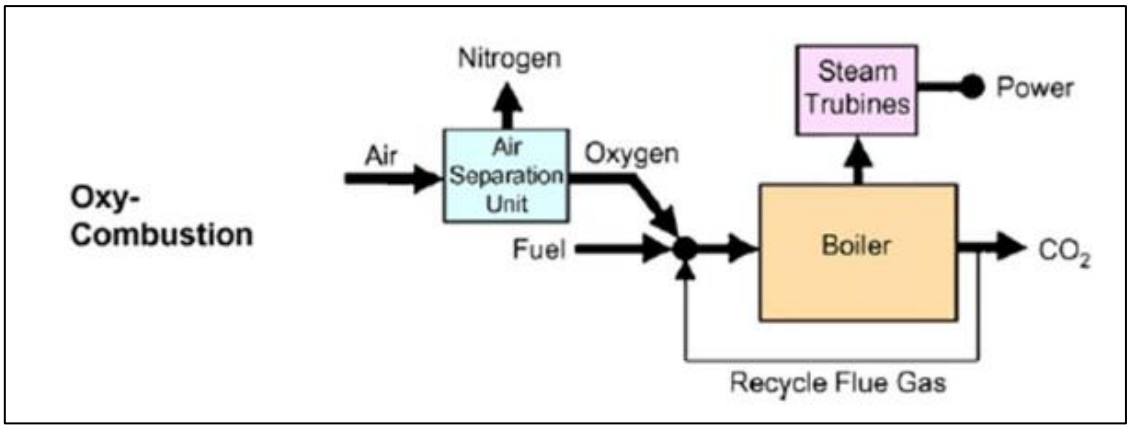

Figure 2-3: Example of oxyfuel combustion CO_2 capture (Figueroa *et al.*, 2008)**.**

Although this oxyfuel combustion technology is promising and has energy-saving potential, two main disadvantages generally prevent implementation on an industrial scale in South Africa. First, as nearly pure oxygen is used for the combustion, the flame temperature is high, requiring extensive modifications to the existing powerplants to cope with the heat generation (Yoro and Sekoai, 2016). Secondly, the on-site oxygen production on a large enough scale is very energy-intensive and comes at a high cost as cryogenic methods and high pressures are required for oxygen production and storage (Yoro and Sekoai, 2016).

2.2.2 Circulation fluidised bed reactor

A circulating fluidised bed reactor (CFBR) is a process designed for gas separation, purification and regeneration. The carbonation reactor and the regeneration reactor are the main sections of a CFBR that require the most attention during the design phase. The riser section (carbonation rector) in Figure 2-4 is where the flue gas is passed through a bed of sorbents to be 'cleaned' through physical adsorption. The sorbents containing the adsorbent are then circulated to the regenerator zone, where desorption/regeneration can occur through temperature swings or pressure swings. The CFB aims to extract relatively pure CO_2 from the regenerator section to be refined for further use.

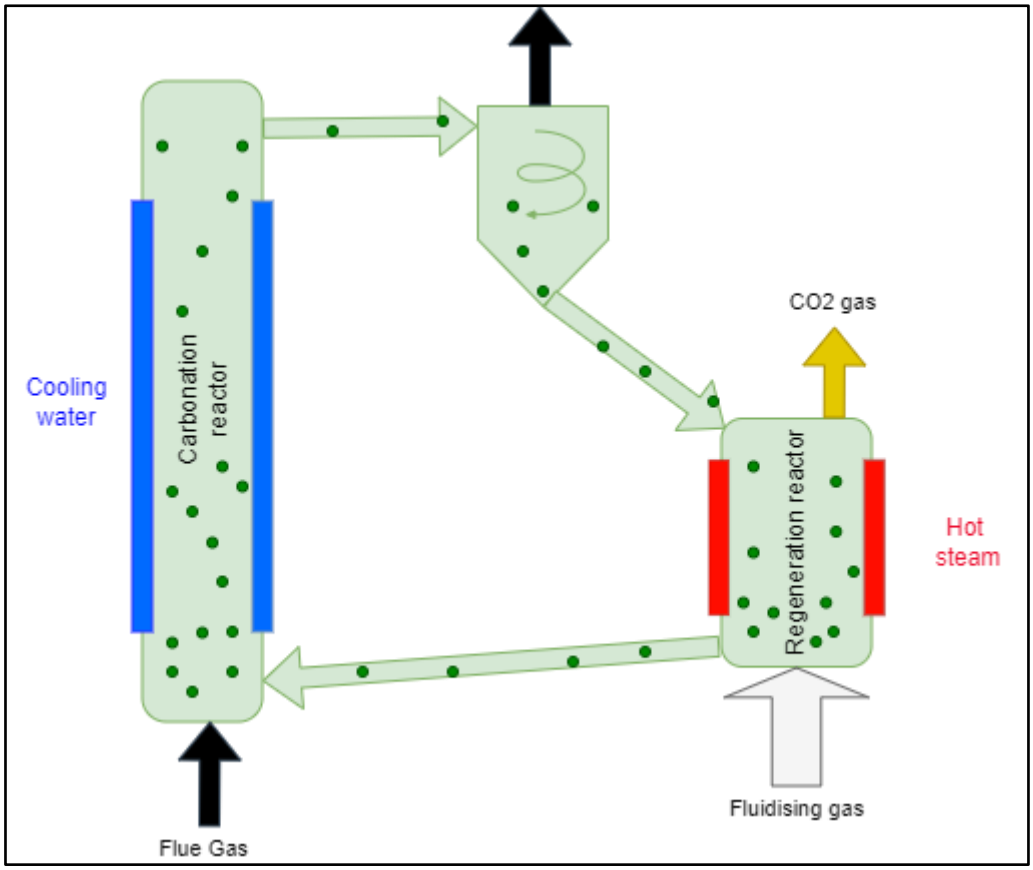

Figure 2-4: Schematic of a simplified CFB reactor for CO_2 capture (Choi *et al.*, 2021)**.**

There are various options and variants in CFB geometry; for example, the cross-section may be circular, rectangular, or square, as in special cases (Grace and Lim, 2013). Most CFB combustors are rectangular in cross-section; however, most of the experimental work on CFB combustors is on cylindrical columns (Grace and Lim, 2013). The typical particle size for fluidised beds with solid sorbents are particles with a diameter of 10 – 300 μm, however with particles on the lower end of the size scale, agglomeration of the particle bed can occur that causes channels to form within the bed and ruin the efficiency of the process (He *et al.*, 2020).

Once a reactor configuration, particle properties, and operating gas have been decided, the operating variables that control the hydrodynamics and reactor characteristics are (Grace and Lim, 2013) :

- Operating temperature and pressure;
- Superficial gas velocity (equal to the volumetric gas flow at the midpoint of the riser divided by the total cross-sectional area); and
- Net circulation flux of solid particles.

The next challenge to building a large-scale CFB is scaling from the smaller experimental reactors to the actual size. Scaling up is challenging because the hydrodynamics of small fluidised beds significantly differ from those of large fluidised beds (Knowlton, 2013). Contributing to the difficulty is that different particle sizes scale up differently, and unfortunately, scale-up can not be reduced to a set of mathematical equations that can tell the engineer precisely what is required (Knowlton et al., 2005). To overcome this scale-up problem, the scale-up is done step-wise, meaning that it is easier to scale up from a commercial size to a larger commercial size than it is to scale up from a bench size to a commercial size. Factors such as the wall effect of the fluidised bed are present in a bench-size setup but not in larger commercial-size setups, affecting the hydrodynamics, yield, and selectivity (Knowlton, 2013). Meanwhile, scaling up from a commercial size that does not have wall effects to a larger commercial size that still does not have wall effects does not change the hydrodynamics and yield as much (Knowlton, 2013).

2.2.3 Fixed-bed reactor

Everyday adsorption operations are performed in fixed-bed reactors; however, this technology does not appear suitable to match the requirements of the adsorbent materials, that is, to fully exploit the potential of fine-manufactured adsorbent materials. For these fine materials to be used in fixed-bed operations, a pelletisation step is needed to overcome the excessively high-pressure drops related to fine particle beds (Ammendola et al., 2017). The shaping process, however, could negatively affect the adsorption process such that the palletisation could lead to additional intraparticle diffusion resistance, thereby reducing the global adsorption kinetics. In addition, the shaping process can drastically decrease the specific surface area and block some pores, reducing the adsorption capacity (Ammendola et al., 2017).

Pressure drop is an essential parameter when using fixed-bed reactors as it is directly related to the energy consumption of gas-sorbent contacting (Yu and Brilman, 2017). The handling of a large amount of gas so that CO_2 can be captured is inevitable since the CO_2 amount in gasses is low in terms of the composition of the gas; therefore, a low bed height, in the order of several centimetres is the key to realise a low-pressure drop (Yu and Brilman, 2017).

2.3 Sorbents suitable for carbon capture

In this chapter, sorbents that are suitable for CO_2 adsorption and regeneration and their properties required are introduced.

2.3.1 Introduction to sorbents

Choosing a sorbent is challenging as a wide variety is available, each with its unique properties. The sorbents are selected according to the required process performance, process design and the location of the capture technique along the gas path (Bhatta et al., 2015). Sorbents are derived from various materials, such as natural carbon-rich substances (activated carbons) or artificially enhanced carbons and metals, to increase desired properties.

2.3.1.1 Properties important for CO_2 capture

Generally, the most important properties a sorbent should possess are high adsorption capacity and selectivity for the intended adsorbate gas (CO_2 in this case), the cost of the adsorbent (this includes the cost of adsorbent to purchase and the energy consumption required for adsorption and desorption) (Gao *et al.*, 2022). In addition, the sorbent should also have long-term stability, including thermal and chemical stability. A summary of properties required for CO_2 capture is shown in Figure 2-5. Fine particles exhibit significant potential as they can be customised to meet specific needs or perform particular functions through adjustments to their physical and chemical characteristics (Ammendola et al., 2017). For instance, by incorporating functional groups with a strong affinity for CO_2 molecules into the pore structure of the sorbent, the adsorption capacities can be readily modified (Ammendola et al., 2017).

Stability is the ability of the sorbent to retain its adsorption capabilities, while there are changing factors that can be detrimental to the adsorption capacity and kinetics. (Mesfer *et al.*, 2020). Thermal stability is the ability of the sorbent to keep its operational characteristics and resist the effect of heat without being severely impacted under various temperature ranges (Król-Morkisz and Pielichowska, 2019). Having high thermal stability is necessary for processes that work at high temperatures. Sorbents like zeolites have decreasing adsorption capacity with increasing temperature (Mesfer *et al.*, 2020). Chemical stability refers to the sorbent's tolerance to impurities, like water vapour, which can harm a sorbent's adsorption capacity and kinetics.

Moisture is one of the biggest inhibitors of a sorbent's ability to adsorb. When moisture is present in the adsorbate, the water molecules start to occupy the micropores of the sorbent, thereby inhibiting and competing with the adsorbate molecules on the active sites (Chulliyil *et al.*, 2024). This effect of moisture inhibits various sorbents, especially activated carbons, zeolites and metal-organic frameworks.

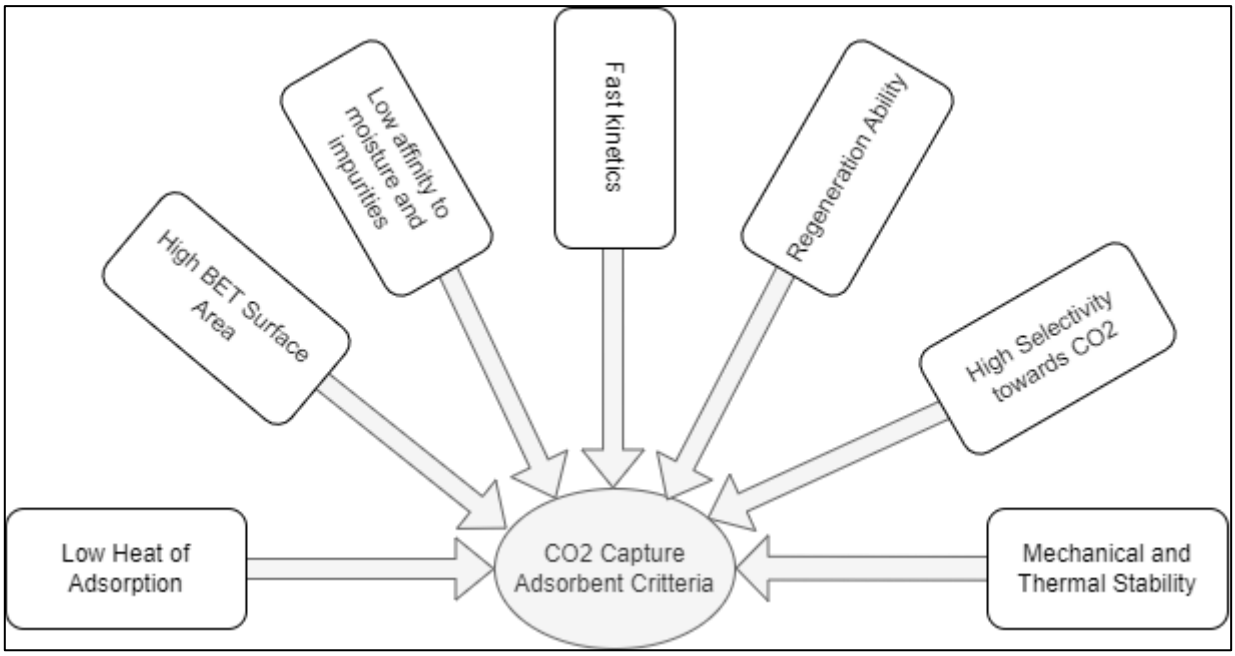

Figure 2-5: Sorbent properties for ideal CO_2 capture (Gao *et al.*, 2022).

2.3.2 Various types of sorbents

Activated carbons are the most straightforward, cheapest and widely available sorbents for adsorption/desorption applications. New materials are continually being developed to suit specific applications and conditions, such as metal-organic frameworks (MOF). The materials developed to perform better than activated carbons are more expensive, significantly increasing both the capital expenses and maintenance costs thus making them less viable in some specific applications (Samanta *et al.*, 2012). Various carbon materials for CO_2 adsorption are illustrated in Figure 2-6.

2.3.2.1 Activated carbons

Activated carbon is a form of carbon processed with a large pore volume, resulting in a high surface area ideal for adsorption applications. Carbon must go through either thermal or chemical activation or a combination of both to become activated carbon. More details on the carbon activation process can be found in Section 2.4.

Activated carbons are made from naturally occurring carbon sources, such as hardwoods, coconut shells, fruit stones, coal and synthetic macromolecular systems (Glenna *et al.*, 2023). Hundreds of activated carbons are available commercially with varying properties; however, only a select few have the required properties to make them viable choices for adsorption/desorption systems (Marsh and Rodríguez-Reinoso, 2006a). Moreover, various activated carbons can be

produced from the same base material, resulting in differences in pore sizes and carbon content (Marsh and Rodríguez-Reinoso, 2006a). The adsorption mechanism of activated carbons relies on van der Waals electrostatic forces, which are stronger in activated carbons compared to some other adsorbents (Lu *et al.*, 2018).

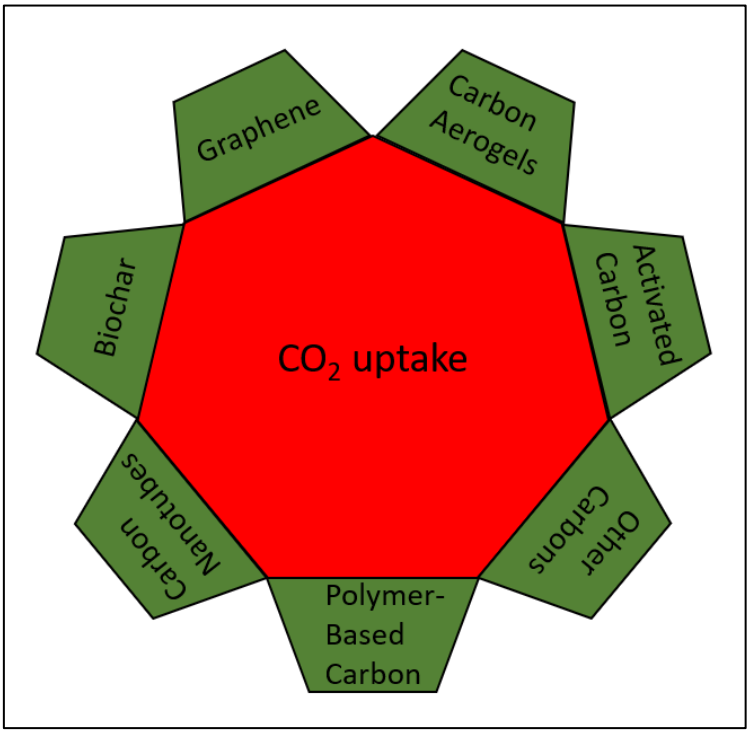

Figure 2-6: Carbon materials for CO_2 adsorption (Kamran and Park, 2021; Gao *et al.*, 2022)**.**

2.3.2.2 Zeolites

Zeolites are crystalline aluminosilicates that exhibit adsorption due to interactions involving localised electrostatic and polarised molecules (Nakao et al., 2019). Furthermore, Zeolites have 3-dimensional uniform pores of several angstroms (Å) levels close to the molecular diameter of the gas. These pores are composed of four- to fourteen-membered oxygen rings that show the molecular sieve effect (Nakao *et al.*, 2019). The size of these oxygen rings governs the diffusion of molecules into the pores, making it essential that the molecule size is smaller than the zeolite pore size when employing zeolites for gas separation purposes.

2.3.2.3 Metal-organic frameworks

Metal-organic frameworks (MOF), also known as porous coordination polymers, are engineered materials constructed from metal ions and inorganic ligands (Nakao *et al.*, 2019). MOFs can outperform traditional porous solids such as zeolites and activated carbons, but they face a significant obstacle in the implementation into large-scale applications due to their sensitivity to

water. Moisture decreases the performance of the MOFs and can even cause the framework to collapse (Nakao *et al.*, 2019).

2.4 Carbon activation

It is well known that the ability of sorbents to capture CO_2 is dependent on the high specific surface area, porous structure and surface composition. However, these properties can be improved and modified further to increase the ability of the sorbent to capture CO_2. This altering of the properties is known as activation, and various methods are used to activate the sorbents. By activating a sorbent, it is found that the porosity, surface area and pore volume can be significantly improved compared to unactivated carbons (Bamdad et al., 2018; Singh et al., 2021).

2.4.1 Physical activation

Oxidising agents such as carbon dioxide, steam, and oxygen are employed at elevated temperatures in the physical activation process. These gas molecules penetrate the interior of carbon materials, vaporising carbon atoms through reactions with active sites and surface carbon-containing groups, thereby creating a distinct pore structure (Sevilla and Mokaya, 2014; Gao *et al.*, 2022). The surface chemistry can be altered by using different activation gases (Álvarez-Gutiérrez *et al.*, 2016). The following section delves into two types of physical activation methods.

2.4.1.1 CO_2 activation

When exposed to CO2, the carbon matrix undergoes partial gasification into CO, creating high porosity and surface area (Prauchner et al., 2016). Activating a range of biomass molecules in CO_2 also substantially increases specific surface area, rising from 38 – 92 m^2/g to 400 – 1000 m^2/g (Zhang *et al.*, 2004). The activation temperature and duration are the two key variables significantly impacting the adsorption capacity. In an analysis of activated carbon (AC) activated at 740 ℃ and 760 ℃, it was found that the micropore volume percentage reduced from 87.7% to 71.6%, indicating the transformation of micropores to mesopores and macropores at higher temperatures (Mazlan *et al.*, 2016).

In addition to higher temperatures, longer residence times also result in increased surface areas. For instance, extending the activation period from 60 minutes to 240 minutes at 900 ℃ in a CO_2 atmosphere increased the surface area of activated carbon derived from coconut shells, rising from 1425 m^2/g to 1888 m^2/g (Yang *et al.*, 2010). However, prolonged activation was observed to cause a severe reaction between CO_2 and the carbon surface, resulting in pore enlargement and subsequent collapse in some cases. Additionally, higher levels of ash residue produced during intensified activation blocked pores and hindered CO_2 adsorption (Rouzitalab *et al.*, 2018; Gao *et*

al., 2022). These conflicting findings underscore the variability in optimal activation conditions among different activated carbons.

2.4.1.2 Steam (H_2O) activation

The primary stages of steam activation include chemisorption, oxidation, gasification, and the water-gas shift reaction (Lussier et al., 1998; Gao et al., 2022). Following steam activation, mesopores and macropores dominate due to the carbon matrix's rapid oxidation, effective penetration into the internal structure of carbon, and transformation of micropores. This differs from CO_2 activation, which typically results in the formation of uniform micropores through a slower process (Halder et al., 2016; Singh et al., 2019; Gao et al., 2022). For instance, steam activation of coconut shells at 900 ℃ increased the surface area from 1425 to 2288 m^2/g, whereas CO_2 activation increased it from 1425 to 1888 m^2/g (Yang *et al.*, 2010).

Certain biomass precurses react differently to steam and CO_2 activation; when Jatropha hull was activated in both CO_2 and steam, opposite results were obtained in the sense that CO_2 activation had a higher surface area (1207 m^2/g) than that of steam activation (748 m^2/g) (Xin-hui *et al.*, 2011). The variability in activation indicates a strong relationship between the applicability of the activation method and the type of precursor.

2.4.2 Chemical activation

Chemical activation is more efficient and energy-saving than physical activation and is widely used for biomass precursor treatment. Chemical activation is, however, corrosive and requires further washing to remove excess residue, but it requires less energy than physical activation due to the lower temperatures involved (Hao *et al.*, 2013; Song *et al.*, 2015). Several activating agents are used in industry, and three of the most commonly used are discussed below.

2.4.2.1 Alkalis

The activation mechanism for KOH and NaOH involves a similar primary reaction where the carbon matrix reacts with the alkalis to produce metals, metal carbonates, and hydrogen (Gong *et al.*, 2015; Pezoti *et al.*, 2016). Alkalis are widely applied in biomass precursors' chemical activation to generate pores of various shapes and sizes, modifying the porosity and increasing the CO_2 adsorption capacity (Pezoti *et al.*, 2016; Mathangi *et al.*, 2018; Ma *et al.*, 2020; Gao *et al.*, 2022).

Above 700 ℃, metal carbonates undergo decomposition or react with carbon to produce metal oxides, CO, and CO_2 (Gao *et al.*, 2022). Increasing the temperature to 800 ℃ allows carbon to

further reduce metal oxides to metals and CO (Gao *et al.*, 2022). The utilisation of carbon during alkali activation contributes to the formation of pores, which is particularly beneficial for generating micropores that enhance CO_2 adsorption (Gao *et al.*, 2022).

The other factor that has a significant effect on the surface area is the mass ratio of the activating agents and carbons; among three feed ratios of KOH and hydrothermally treated carbon (1:1, 3:1 and 5:1), the highest micropore contents (97.9%) and the largest specific surface area (2879 m^2/g) were obtained for 3:1 ratio (Sun *et al.*, 2016; Gao *et al.*, 2022). In contrast, the sample with a 5:1 ratio showed a lower micropore content of 57.8%, attributed to the intense reaction with the carbon matrix, whereas the sample with a 1:1 ratio displayed a less developed pore structure, likely due to the lower quantity of KOH used (Gao *et al.*, 2022).

2.4.2.2 Acids

Acid treatment results in a greater micropore volume than alkali activation, primarily because of the increased solubility of volatile organic matter in biomass precursors (Mallesh *et al.*, 2020). The resulting microporous structures benefit CO_2 adsorption, with the commonly used acids being H_3PO_4, H_2SO_4 and HNO_3 (Román *et al.*, 2008; Sevilla *et al.*, 2012).

H_3PO_4 is an effective activation agent that can modify the pyrolytic pathways of biopolymers, enhance the porosity and couple to the carbon surface P-containing functional groups (Hulicova-Jurcakova et al., 2009; Liu et al., 2010; Martínez de Yuso et al., 2014). The activation mechanism of H_3PO_4 is proposed as follows: P_2O_5 derived from the dehydration of H_3PO_4 reacts with carbon to release P and CO_2; meanwhile, the decomposition of polyphosphoric acid generated O, P and steam in gaseous states (Olivares-Marín *et al.*, 2006; Gao *et al.*, 2022). Furthermore, during the activation process, bond cleavage and phosphate cross-linking reaction (condensation and crystallisation) were promoted, generating gaseous products like CH_4, CO_2 and CO (Jagtoyen and Derbyshire, 1998; Gao *et al.*, 2022).

2.5 Sorbent characterisation

Characterisations help determine what properties of a sorbent help or hinder the capacity or rate of adsorption and desorption; therefore, understanding individual characteristics of sorbents can improve the process design and effectiveness.

2.5.1 Proximate and ultimate analysis

A proximate analysis presents a sample's properties in four categories: volatile matter, moisture content, ash content and fixed carbon, whereas the ultimate analysis is a more comprehensive

analysis of the sample as it breaks the sample down into its elemental compositions of carbon, hydrogen, nitrogen, sulphur and oxygen (CHNSO) contents. The proximate analysis further quantifies the ratio of combustible to non-combustible constituents in the sample and gives insight into the quality of the carbonaceous material (Mayoral *et al.*, 2001).

2.5.2 Surface structural properties

A few methods exist for the analysis and characterisation of the porosity of a porous sorbent. The most widely used method is gas adsorption for dry sorbent porosity and surface area properties (Cazorla-Amorós et al.,1996). The most common gasses used for adsorption characterisation are CO_2, N_2, Ar, He and CH_4; however, the gas used depends highly on the pore range to be analysed (Thommes and Cychosz, 2014; Medina-Rodriguez and Alvarado, 2021). There are generally three ranges in which pores are distributed, especially in activated charcoals: micropores ($r < 20$ Å), mesopores ($20 < r < 500$ Å) and macropores ($r > 500$ Å) (Zdravkov *et al.*, 2007).

One of the techniques to measure the surface area of a porous sorbent using N_2 is the Brunauer-Emmet-Teller (BET) isotherm method for surface area determination. The BET surface area serves as a characterisation parameter for porous materials' surface areas and is determined by gas adsorption experiments at a constant temperature (Keller and Staudt, 2005). The maximum adsorption capacity of the monolayer load can be determined from Equation **2-4**

$$\frac{P}{(P_0 - P)q_{BET}} = \frac{C-1}{Cq_{CO_2}}\left(\frac{P_{CO_2}}{P_{CO_{2,0}}}\right) + \frac{1}{Cq_{CO_2}} \qquad 2\text{-}4$$

Where C and q_{BET} are determined with non-linear regression, restricted to the region $0 < \frac{P}{P_0} < 0.3$ (Brunauer et al.,1938a).

2.5.3 Scanning electron microscopy

Scanning electron microscopy (SEM) is a physical characterisation method commonly used to capture the image of the microstructure and morphology of materials. In SEM, an electron beam with low energy is radiated to the surface of the material and scans the surface of the sample, where different interactions occur as the beam enters the material, and that leads to the emission of photons and electrons from or near the sample surface (Omidi *et al.*, 2017). The electrons emitted from the sample are known as secondary electrons (SE), which are detected by the SE detector on the SEM fitted with a positively biased grid to attract more SEs to the grid (Kruk and Jaroniec, 2001).

2.6 Adsorption

Adsorption is a promising technology for capturing CO_2 from flue gases after combustion (Ammendola et al., 2017). Unlike absorption, where CO_2 is separated using a liquid sorbent, adsorption relies on the interaction of CO2 with a solid sorbent (Nakao *et al.*, 2019). This method avoids the drawbacks associated with using aqueous amine solutions and the high energy consumption of cryogenic methods for CO2 capture (Ammendola *et al.*, 2017). The effectiveness of adsorption hinges largely on the specific properties of the adsorbent material, which are detailed in Section 2.3.1.1.

Depending on surface properties, four primary adsorption mechanisms can be employed: quantum sieving, kinetic trapping, physical adsorption, and chemical adsorption (Abd et al., 2021). Quantum sieving is influenced by the de Broglie wavelength and diffusion rates of gas molecules, allowing all gas molecules to pass through adsorption pores, while specific species capture depends on the surface characteristics of the adsorbate and adsorbent molecules (Gao *et al.*, 2022). In the instance where the surface nature is mainly dominated by polarizability, dipole moment and magnetic selectivity, it is referred to as the dynamic impact mechanism (Mallesh *et al.*, 2020; Gao *et al.*, 2022).

Physical (pore-filling) adsorption and chemical (hydrogen bonding) adsorption are distinguished depending on the interaction between the CO_2 molecules and the adsorbent. With physical adsorption, the CO_2 molecules are adsorbed onto the carbon sample via the van der Waals force that is related to the temperature and pressure (Wang *et al.*, 2017). Furthermore, CO_2 adsorption is enhanced when the adsorbent has a pore diameter close to that of the CO_2 molecule diameter (Seredych et al., 2014). For example, a CO_2 molecule has a diameter of 0.33 nm, which is smaller than that of N_2 at 0.36 nm; it is also found that with an increase in the total pore volume, CO_2 adsorption increases (Gao *et al.*, 2022). Therefore, the increase in CO_2 adsorption at smaller pore volumes indicates that the adsorption of CO_2 by ultramicropores is governed by physical adsorption.

Chemical adsorption (hydrogen bonding) involves the interaction where a hydrogen atom forms a covalent bond with acceptors like nitrogen or oxygen atoms, typically found in surface functional groups of carbon such as -OH, -COOH, and $-NH_2$ (Gao *et al.*, 2022). These hydrogen bonds commonly occur between hydrogen atoms and nitrogen or oxygen atoms on the carbon surface. For instance, oxygen atoms in CO_2 possess a negative charge due to differing electronegativities, facilitating weak hydrogen bonds with C-H bonds on the carbon surface (Kim and Kim, 2008; Gao *et al.*, 2022).

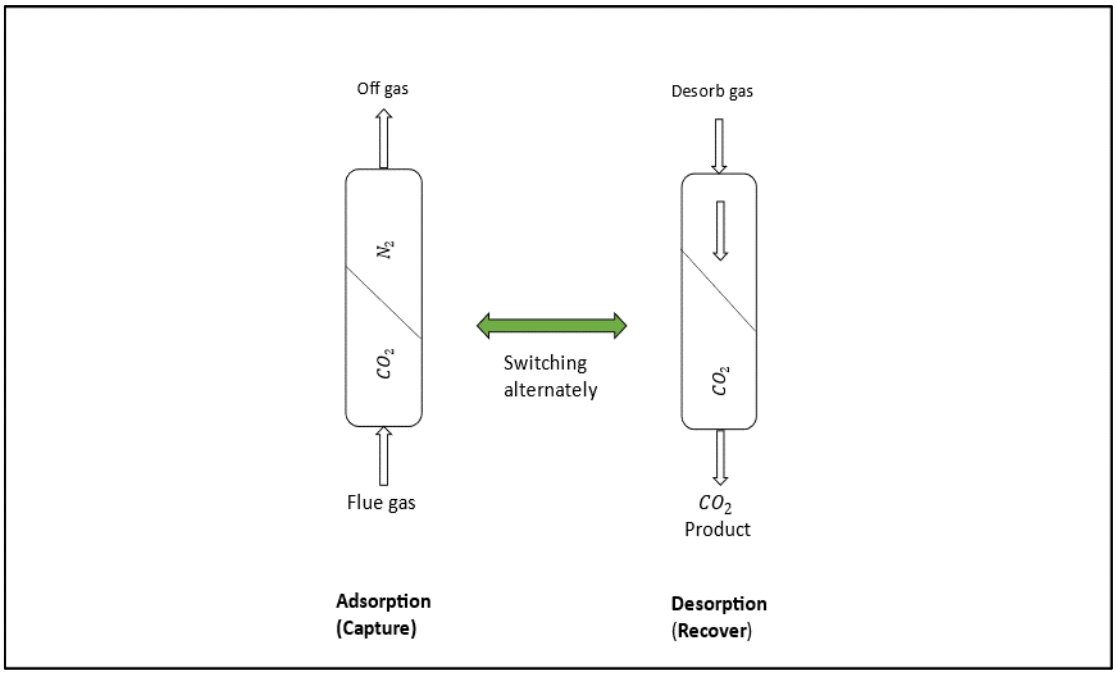

Figure 2-7: Principle of the adsorption separation method (Nakao *et al.*, 2019)**.**

Among the various CO_2 separation technologies, adsorption onto porous solid materials is considered a promising technique due to the general high efficiencies, low power consumption and operating costs, and because it can be used in a vast range of temperatures and pressures (Wjihi *et al.*, 2021).

2.7 Desorption/regeneration

Many studies of carbon capture and storage technologies focus mainly on desorption investigations (Lou *et al.*, 2021). Desorption is essentially the reverse process of adsorption, where the adsorbed molecule separates from the surface of the adsorbent. Desorption is also regarded as a uniform, statistically independent event where the rate is proportional to the surface coverage, and for recombinative desorption of dissociatively adsorbed molecules, the rate is proportional to the surface coverage squared (Günther *et al.*, 2014). Therefore, Equation 2-5 is the desorption rate law and is given as:

$$\frac{d\Theta}{dt} = -k_{des}\Theta^{m} \qquad 2\text{-}5$$

Where Θ is the surface coverage, and m is the desorption order that is more often than not a fractional number rather than a natural number as expected, this model is equivalent to a mean-field treatment of the desorption, going back to Lagmuir, but is widely used for analysing modern surface kinetics (Günther *et al.*, 2014).

Temperature-programmed desorption is the standard method for determining desorption kinetics, and it has been shown that multiple adsorption states and interactions between the particles affect the kinetics (Günther *et al.*, 2014). Substantial deviations may occur if the adsorbed particles form two-dimensional (2D) islands (the peaks of the adsorption rate over temperature), as with most adsorbates. Then, depending on the mobility of the adsorbate layer (which determines whether it is in 2D equilibrium during desorption or not), the consequences will be different (Günther *et al.*, 2014). When mobility is restricted, one expects only the particles at the islands' perimeter to desorb, which should lead to a value of m = ½. However, coverage-dependent lateral interactions in uniform adsorption layers can explain fractional desorption orders (Günther *et al.*, 2014). Conversely, islands do not need to lead to m = ½ if the islands are in equilibrium with a dilute 2D phase, while observations of zero-order desorption have been explained in this way (Günther *et al.*, 2014).

2.8 Adsorption kinetics

Adsorption kinetics models describe the path of the reaction and predict the time to reach equilibrium. The study of the adsorption kinetics shows the efficiency of the adsorbent to adsorb the adsorbate that can involve more than one step, including film diffusion, surface diffusion, intraparticle diffusion and adsorption at the surface of the pores or a combination of the steps (Chegeni *et al.*, 2022). Generally, the kinetics models are used to calculate the adsorption rate, which depends on the physical and chemical properties of the adsorbent, as they affect the adsorption mechanism (Chegeni *et al.*, 2022).

There is a wide range of kinetic models that are available in literature. A typical approach is to fit experimental data to several established models and select the best-fitting model. This approach is used due to the complexity of predicting the kinetic parameters. The simplest kinetic models that describe kinetics on solid sorbents are Pseudo-first order (PFO) and Pseudo-second order (PSO) (Patil *et al.*, 2024). The PFO model represents the reversible reaction between the adsorbent and the adsorbate, whereas the second-order model assumes that the interaction between the adsorbent and adsorbate is caused by the strong binding of the gas to the surface of the adsorbent (Ammendola et al., 2017).

The Avrami kinetic rate adsorption model was initially intended to model phase transitions and crystal growth of materials. (Czerw, Baran and Zarębska, 2017) have successfully applied the Avrami kinetic rate model to CO_2 adsorption modelling onto an amine-functionalized adsorbent. This model introduces a stretching parameter n ($0 < b < 1$) with a value of 1 or close to one, indicating a narrow relaxation time; the value increases as the value of n deviates from 1 (Czerw, Baran and Zarębska, 2017).

The temperature at which the adsorption occurs significantly affects the kinetics of the reaction and the amount of adsorbate that the sorbent can adsorb; thus, by examining the effects of temperature, it is possible to optimise the quantities adsorbed and energy usage of the reaction (Chegeni *et al.*, 2022). Table 2-1 presents some models frequently used for adsorption.

Table 2-1: Kinetic models for adsorption

Model	Model equation	Model parameters	Reference
Pseudo-first-order	$\frac{q_t^a}{q_e^a} = [1 - \exp(-k_1 t)]$	$k_1 = Pseudo - first - order\ rate\ constant\ [s^{-1}]$ $k_2 = Pseudo - second - order\ rate\ constant\ [g/mmol.s]$ $k_A = Avrami\ kinetic\ constant\ [s^{-1}]$ $k_F = Fractional\ Avrami\ order\ kinetic\ constant$ $c_F = Fractional\ order$ $m_F = Fractional\ order$ $\beta = Desorption\ rate\ constant$ $\alpha = Initial\ adsorption\ rate\ constant$ $n = Avrami\ stretching\ parameter$ $q_t^a = Adsorption\ capacity\ at\ time\ t\ [mmol/g]$ $q_e^a = Equilibrium\ adsorption\ capacity\ [mmol/g]$ $A = Pre\ exponential\ factor$ $R = Universal\ gas\ constant$ [kJ/mol.K] T = Temperature [K]	Ammendola et al., 2017
Pseudo-second-order	$q_t^a = \frac{{q_e^a}^2 k_2 t}{1 + q_e^a k_2 t}$		
Fractional-order Avrami	$q_t^a = q_e^a - \frac{1}{\left[(n-1)\frac{k_F}{m_F} t^{m_F} + \frac{1}{{q_e^a}^{c_F - 1}}\right]^{\left(\frac{1}{c_F - 1}\right)}}$		Wei and Zhao, 2021
Elovich	$q_t^a = \frac{1}{\beta} ln(1 + \beta\alpha t)$		Heydari-Gorji and Sayari, 2011
Avrami	$\frac{q_t^a}{q_e^a} = 1 - exp[-((k_A t)^n)]$		Wei and Zhao, 2021
Power law	$\frac{d\alpha}{dt} = A.exp\left(-\frac{E}{RT}\right) * \left[\left({}^2/_3\right) \alpha^{-{}^1/_2}\right]$		Wei and Zhao, 2021

2.9 Desorption kinetics

As the inverse of adsorption, desorption is also a vital study content, and compared to CO_2 adsorption kinetics, the kinetics of CO_2 desorption have not been given enough attention (Wei et al., 2017). Whether different CO_2 concentrations can influence CO_2 desorption is essential to the desorption process; thus, the fact that the extent of conversion of CO_2 desorption is independent of the CO_2 concentration is consistent with expectations (Wei et al., 2017). This means that CO_2 desorption is a stand-alone process independent of adsorption conditions. Furthermore, CO_2 desorption is only affected by the desorption temperature and pressure irrespective of the CO_2 concentration, the extent of conversion of CO_2 desorption is always the same at the same temperature (Wei et al., 2017).

Different kinetic models can be used to analyse adsorption and desorption kinetics. Suppose it can be assumed that the desorption of CO2 can be represented as the decomposition of carbonate/bicarbonate, and the kinetic models can simulate the adsorption process. In that case, most of the decomposition process can be represented by the same kinetic models (Liu and Yu, 2018). Some of the simple kinetic models, like the pseudo-first-order and the pseudo-second-order models, have been used extensively to model adsorption kinetics. For the modelling of desorption kinetics, models like the ion exchange models and the simple kinetic models are the popular models used to describe the kinetics of desorption (Wehrung et al., 2023). The ion exchange models include the homogeneous diffusion model (HDM) based on Fick's law and the shrinking core model (SCM) based on modified Levenspiel's theory (Azizian and Bashiri, 2008).

Furthermore, the kinetics are modelled by using the same fraction as for adsorption kinetics (q_t/q_e); the profile of the curve that results is the same, and that also implies that the adsorption kinetic models can be used to model desorption kinetics. Therefore, the desorption kinetics are generally modelled with simple kinetic models such as the pseudo-first-order, pseudo-second-order and Avrami, which are used in laboratory-scale experiments (Liu and Yu, 2018). The desorption kinetic models are presented in Table 2-2

Table 2-2: Kinetic models for desorption

Model	Model equation	Model Parameters	Reference
Pseudo-first-order	$\frac{q_t^d}{q_e^d} = [1 - \exp(-k_1' t)]$	$k_1' = Pseudo - first - order\ desorption\ rate\ constant\ [s^{-1}]$ $k_2' = Pseudo - second - order\ desorption\ rate\ constant\ [g/mmol.s]$ $k_A' = Avrami\ kinetic\ constant\ [s^{-1}]$ $n_A' = Desorption\ Avrami\ stretching\ parameter$ $q_t^d = Desorption\ capacity\ at\ time\ t\ [mmol/g]$ $q_e^d = Equilibrium\ desorption\ capacity\ [mmol/g]$ $q = Solid\ phase\ concentration\ of\ CO_2\ [mol]$ $C = Concentration\ [mol.cm^{-3}]$ $D = Diffusivity\ [cm^2.s^{-1}]$ $r = Average\ raduis\ of\ adorbent\ particle\ [cm]$ $X = Active\ site\ concentration\ [mol.cm^{-3}]$ $D_s = Surface\ diffusion\ coefficient$ $y = \text{Desorption partion}$	Al-Marri et al., 2017
Pseudo-second-order	$q_t^d = \frac{{q_e^d}^2 k_2' t}{1 + q_e^d k_2' t}$		Gunawan et al., 2018
Shrinking core model	$\frac{6D}{r^2 X}\int_0^t C\,dt = 1 - 3\left(1 - \frac{X_t}{X}\right)^{2/3} + 2\left(1 - \frac{X_t}{X}\right)$		Seki and Suzuki, 1999
Homogeneous diffusion model	$\frac{\partial q}{\partial t} = \frac{D_s}{r^2}\frac{\partial}{\partial r}\left[r^2 \frac{\partial q}{\partial r}\right]$		Qi et al., 1994
Avrami	$y = 1 - \exp\left(-(k_A' t)^{n_A'}\right)$		Raganati et al., 2019

2.10 Activation energy

The activation energy for adsorption (E_a) is the difference between a gas-phase molecule's energy and molecules' energy in the activated or transition state (Panczyk & Rudzinski, 2004). Contrary to adsorption, in desorption, it is assumed that the desorbing molecule must pass through an activated state before desorbing. The activation energy for desorption (E_d) is the difference in energy between the adsorbed molecules and those in the activated state for desorption. Furthermore, it is assumed that the adsorbed molecules are in equilibrium with the molecules in the activated sites (Panczyk and Rudzinski, 2004).

The activation energy is an essential parameter of the adsorption process as it indicates the minimum energy requirement that the adsorbate molecules must overcome; therefore, adsorption equilibrium can either be achieved quickly or slowly depending on the activation energy required (Ammendola et al., 2017). The Arrhenius equation (Equation 2-6) can be used to estimate the activation energy once the kinetic constant is known.

$$k_f = Aexp\left(-\frac{E_a}{RT}\right) \quad \text{2-6}$$

Where A is the pre-exponential factor. By plotting ln k_f against 1/T, E_a and A can be obtained from the slope ($-E_a/R$) and the intercept of the linear plot (Ammendola et al., 2017).

2.11 Isotherm models

Isotherms models describe the behaviour of adsorbents under conditions specified by the user. In addition, the models indicate the equilibrium data to describe the interaction of pollutants and adsorbate materials (Al-Ghouti & Da'ana, 2020).

2.11.1 Langmuir model

Among the variety of isotherm models, the Langmuir isotherm model is the simplest theoretical model that describes monolayer adsorption onto the homogeneous surface (Ammendola et al., 2017). Specifically, the basic assumption on which the model is based are as follows (Ammendola et al., 2017):

- The molecules are adsorbed at a fixed number of defined localised sites.
- Adsorption is monolayer.
- Each site can hold one adsorbate molecule, and the adsorbed molecules will not move to another adsorption site.

- The adsorption energy of every adsorption site is the same; namely, the surface adsorbent is homogeneous.
- There is no interaction between molecules adsorbed and neighbouring sites.
- The adsorption system is in dynamic equilibrium, and the adsorption rate equals the desorption rate.

The mathematical expression of the Langmuir equation is as follows:

$$q_e^a = \frac{q_s K_L P_{CO_2}}{1 + K_L P_{CO_2}} \quad \text{2-7}$$

Where q_s (mmol.g^{-1}) is the maximum monolayer adsorption capacity of the adsorbent,

The specific equilibrium amount for a specific temperature and CO_2 partial pressure can be determined by integrating the breakthrough curves according to the following mass balance equation:

$$q_e^a = \frac{1}{m}\int_0^{t_s} \left(F_{CO_{2,in}} - F_{CO_{2,out}}\right) dt \quad \text{2-8}$$

Where q_e^a (mmol.g^{-1}) stands for the specific CO_2 adsorption capacity of the adsorbent, m is the mass of adsorbent in the bed, $F_{CO_{2,in}}$ and $F_{CO_{2,out}}$ refer to the molar flow rate of the CO_2 at the inlet and the outlet of the bed, respectively. T_s refers to the time required to reach saturation.

2.11.2 BET adsorption isotherm model

The Brunauer-Emmet-Teller (BET) model extended the Langmuir monolayer isotherm model to a multilayer adsorption isotherm model as given by Equation 2-9.

$$q_{CO_2} = \frac{q_{BET} C \left(\frac{P_{CO_2}}{P_{CO_2,0}}\right)}{\left(1 - \left(\frac{P_{CO_2}}{P_{CO_2,0}}\right)\right)\left[1 + (C-1)\left(\frac{P_{CO_2}}{P_{CO_2,0}}\right)\right]} \quad \text{2-9}$$

Since the BET model is an extension of the Langmuir model, the same assumptions are used to derive the Langmuir model (Li et al., 2012; Ammendola et al., 2017):

- The molecules are adsorbed at a fixed number of defined localised sites.
- Adsorption is monolayer.
- Each site can hold one adsorbate molecule, and the adsorbed molecules will not move to another adsorption site.

- The adsorption energy of every adsorption site is the same; namely, the surface adsorbent is homogeneous.
- There is no interaction between molecules adsorbed and neighbouring sites.

These are also used in the derivation of the BET model with the following assumptions added et al., 1938b; Okolo, 2017):

- The multilayer adsorption where each adsorbate molecule in the initial layer serves as an adsorption site for an adsorbate molecule into the consecutive layer.
- The attractive forces between the adsorbate molecules are negligible.
- The heat of adsorption in the second layer is different from the heat of adsorption in the first layer and equal to the heat of condensation (liquefaction) of the adsorbate.

2.12 Thermodynamic Properties

Thermodynamic data only provide information about the final state of a system. Many studies have focused on the effect of operating parameters on the CO_2 adsorption process, but fewer studies have focused on a thorough modelling analysis of the thermodynamic data. The thermodynamic data can go beyond the phenomenological experimental results (Wjihi *et al.*, 2021).

A reliable theoretical model can significantly help to understand the adsorption mechanisms by determining model parameters to which a physical meaning is associated. Simultaneously, determining fundamental thermodynamic properties can further improve comprehension of the network of the occurring phenomena (Wjihi *et al.*, 2021). This represents a powerful tool for designing and optimising an adsorption intervention, which is mandatory to make the carbon capture step sustainable.

As reported in the literature, the thermodynamic laws combined with experimental data obtained from the isotherm models can be used to determine the thermodynamic parameters (Hauchhum and Mahanta, 2014a; Adelodun et al., 2017; Ammendola et al., 2017; Sing and Kumar, 2017).

2.12.1 Gibbs free energy

The Gibbs free energy change (ΔG) is a critical factor for determining the spontaneity of the process. A process is defined as spontaneous if it can occur favourably and spontaneously at a given temperature. If the Gibbs free energy change is less than zero ($\Delta G < 0$), the process is referred to as spontaneous, and if ($\Delta G > 0$), it will be non-spontaneous and non-feasible (Ammendola et al., 2017; Wjihi et al., 2021). The pore structure of the coal applies an unbalanced

force on the surface carbon atoms, and the carbon atoms on the surface are attracted by the vertically pointing force on the coal body (Du *et al.*, 2021). Due to the force, the carbon atoms tend to migrate towards the interior of the coal, thus providing the carbon atoms with extra energy, free surface energy (Du *et al.*, 2021).

The Gibbs free energy is generally calculated using the Vant Hoff equation in Equation 2-10. The Vant Hoff equation uses the Freundlich or Langmuir isotherm model constant to determine the Gibbs free energy, enthalpy and entropy of the reaction. However, the Vant Hoff equation can also be used with a standard equilibrium constant instead of the isotherm constants in Equation 2-11, where K^{θ} is the standard equilibrium constant (Chen et al., 2021).

$$\Delta G^{o} = -RTln\left(K_{L/F}\right) \quad 2\text{-}10$$

$$\Delta G^{\theta} = -RTln\left(K^{\theta}\right) \quad 2\text{-}11$$

The standard equilibrium constant, in this case, can be represented by $K_d = \frac{\mathrm{q}_e^a}{C_e}$ where K_d (L/kg^{-1}) is the distribution coefficient, q_e^a (mmol/g) the adsorption capacity at equilibrium and C_e (mol) is the equilibrium adsorbate concentration (Chen et al., 2021). However, the experimental equilibrium constant must be transformed into the standard equilibrium constant, which is dimensionless.

The transformation occurs through Equation 2-12, where C^{θ} (mol/L) and q^{θ} (mol/m^2) are the standard states of adsorption of gas and solid, respectively (Chen et al., 2021).

$$K_d^{\theta} = K_d \times \left(\frac{C^{\theta}}{q^{\theta}}\right) \quad 2\text{-}12$$

2.12.2 Enthalpy

Enthalpy generally indicates whether the adsorption process is endothermic (+ΔH^o) or exothermic (-ΔH^o) (Ammendola et al., 2017). Exothermic processes release energy into the surroundings because the energy absorbed to break the bond is lower than the energy released from the bond breaking. In contrast, endothermic processes absorb energy from their surroundings as the energy released from the bond breaking is less than the energy required to break the bond (Ammendola et al., 2017).

The magnitude of absolute physical adsorption is generally less than 20 kJ.mol^{-1}, while for chemisorption, it is between 80 – 200 kJ.mol^{-1} (Ammendola et al., 2017). The well-known van't

Hoff equation can be used to calculate the enthalpy from the slope of the plot ln K^{θ} against 1/T (Chen et al., 2021).

2.12.3 Entropy

The magnitude and sign of the entropy indicate if the interaction between the solid/gas interface during the adsorption process becomes more ($\Delta S^{o} > 0$) or less random ($\Delta S^{o} < 0$). The entropy is also calculated from the van't Hoff equation using the intercept between the plot of ln K^{θ} against 1/T (Chen et al., 2021).

2.13 Breakthrough modelling

Breakthrough curves can be considered the last of the essential characterisations of activated carbon, where equilibrium isotherms provide data on the capacity of the carbon and the kinetics give information on the rate of adsorption (Marsh and Rodríguez-Reinoso, 2006b). A breakthrough curve is a plot of the duration of the test against the concentration of the adsorbate in the effluent stream of a mixture of gasses. Initially, a mixture of gas enters into a bed of carbon where the adsorbate is adsorbed, and the residual gas passes out of the bed; this continues as long as the carbon in the bed still has available capacity to adsorb the adsorbate (Marsh and Rodríguez-Reinoso, 2006b). At saturation, the adsorbate is detected in the effluent gas and its concentration increases until no further adsorption takes place and the composition of the effluent gas is equal to the concentration of the initial entry gas mixture (Marsh and Rodríguez-Reinoso, 2006b).

Fixed-bed column mathematical models are used to predict the transient behaviour of concentration profiles for defined changes in the initial parameters, and the complete mathematical model that is capable of describing the dynamic behaviour of adsorption systems is established based on relatively complex partial differential equations that are constructed from the conservation of mass, momentum, and energy (Shafeeyan et al., 2014).

Predicting the breakthrough behaviour of CO_2 adsorption through a fixed bed column packed with activated carbons, the following model is proposed with assumptions based on mass balance concepts combined with the Avrami kinetic model (Shafeeyan *et al.*, 2015).

- The gas behaves as an ideal gas
- Axially dispersed plug flow model is adopted
- Radial gradient of the concentration is negligible
- The fixed bed operates isothermally

- The feed contains low CO_2 concentrations, thus the pressure drop through the column is negligible
- Linear velocity remains constant along the bed
- The effect of nitrogen adsorption is negligible
- External mass transfer is negligible
- The Avrami kinetic rate model describes the rate of adsorption

Chapter 3

CHAPTER 3: MATERIALS AND METHODS

This chapter explains the materials used in the experiments, experimental setup and calculation procedures for the proximate analysis, data processing, thermodynamics and kinetic model validation in detail.

3.1 Sorbents

3.1.1 Activated carbon

Three activated carbon samples (CQ650, CQ006 and CQ30P) were obtained from ChemQuest (Germiston, South Africa). Table 3-1 compares the samples' materials of origin and activation methods.

Table 3-1: Origin and activation methods for the sorbents

	CQ650	CQ006	CQ30P
Material of origin			
Coal		X	X
Coconut	X		
Activation method			
Steam	X	X	X
Acid washed		X	
KOH impregnation	X		X
Extra high activity		X	

These activated carbons display different pore sizes and characteristics depending on the origin material. For instance, activated carbons derived from wood are characterised by abundant macropores, which are beneficial for adsorbing larger molecules. In contrast, activated carbons derived from coconut shells are naturally hard, abrasion-resistant, and predominantly microporous, making them well-suited for adsorbing smaller molecules such as CO_2 and recovering precious metals. Coal-based sorbents contain micropores, mesopores and macropores, meaning they are tri-dispersed, making them suitable for the adsorption of a range of molecules from small to large molecules.

Physical activation is a combination of carbonisation and activation. Carbonisation is a devolatilization or charring process in an inert atmosphere at a temperature range of 250 – 650 ℃. The activation, in turn, is controlled oxidation in the presence of steam or other oxidising agents

at a temperature range of 750 – 1200 ℃ for long periods with precise control, which ensures a well-developed internal pore structure, uniform activation and abrasion resistance.

Chemical activation partially replaces the oxidizing process of physical activation by using lower temperatures in the presence of substances like phosphoric acid or zinc chloride. This method results in an activated carbon material characterized by a well-defined structure of macropores and mesopores.

3.2 Sample characterisation

The characterisation of the activated carbons is essential to make an informed assumption on the sorbents' adsorption and desorption kinetics based on the sorbent's physical properties.

3.2.1 Proximate analysis

Proximate analysis is used to quantitatively describe the material in terms of moisture, volatile matter, fixed carbon content and ash yields. A standard experimental procedure was followed to calculate the moisture content, volatile matter, ash yields and fixed carbon content. These are discussed in Sections 3.2.1.1 – 3.2.1.3. Fixed carbon content was determined by the difference between 100 and the sum of the percentages of volatile matter content, ash yield and moisture content.

3.2.1.1 Moisture content

A weighed sample of $(1 \pm 0.1g)$ is dried in an oven for 3 hr, and the moisture content is calculated from the sample mass before and after the drying period, as shown in Equation 3-1 following the ISO11722 standard of 2013.

$$M = \frac{m_2 - m_3}{m_2 - m_1} \times 100 \qquad 3\text{-}1$$

Where M is the moisture content (wt.%), m_1 is the mass of the empty tray, m_2 is the mass of the tray and the sample before drying and m_3 is the mass of the tray and the sample after drying.

3.2.1.2 Volatile matter

A sample weighing 1 ± 0.1g is heated to 900 ℃ for 7 minutes in an inert atmosphere. The absence of air is crucial to prevent oxidation of the sample, which could lead to inaccurate results. Subsequently, the sample is removed and allowed to cool to room temperature before being weighed again. The volatile matter content is calculated using Equation 3-2 following the ISO 562 standard of 2010.

$$V = \frac{100 \times (m_2 - m_3)}{m_2 - m_1} - \omega_{H_2O} \quad 3\text{-}2$$

With V the volatile matter content (wt.%), ω_{H_2O} the mass (wt.%) of the moisture content calculated in Equation 3-1, m_1 is the mass of the empty tray, m_2 is the mass of the tray and the sample before drying and m_3 is the mass of the tray and the sample after drying.

3.2.1.3 Ash yield

A sample weighing 1.0 ± 0.1 g is placed into a crucible and placed in an ashing oven at room temperature. It is gradually heated to 500 ℃ over one hour and maintained at this temperature for thirty minutes. The temperature is then raised to 815 ℃ and held until complete combustion of the sample occurs. After complete combustion, the sample is allowed to cool to room temperature, and the ash yield is calculated using Equation 3-3, following the ISO 1171 standard from 2010.

$$A_C = \frac{m_2 - m_3}{m_2 - m_1} \times 100 \quad 3\text{-}3$$

Where A_C is the ash yield (wt.%), m_1 is the mass of the empty tray, m_2 is the mass of the tray and the sample before drying and m_3 is the mass of the tray and the sample after drying

3.2.2 Surface area analysis

The surface areas of the activated carbons were assessed using low-pressure CO_2 and N_2 adsorption at 0 ℃ and -196 ℃, respectively, on a Micromeritics 3-Flex analyzer. Initially, the amount of adsorbate gas corresponding to the monomolecular layer on the material's surface was calculated, followed by the determination of the material's surface area. The isotherm measurements were conducted over a range of partial pressures (P/Po) from 0 to 0.03 for CO2 and from 0 to 1.0 for N2. Subsequently, the Dubinin-Radushkevich (D-R) and Brunauer-Emmet-Teller (BET) isotherm models were employed to compute the surface area.

3.2.2.1 Sample preparation

The sample tube was thoroughly cleaned with acetone to ensure no particles from previous experiments could interfere with the result of the analysis. Next, the sample tube was inserted into a drying oven to ensure that all the acetone evaporated and none remained to affect the experiment. About 0.3 ± 0.01 g sample was weighed and inserted into the tube. A filler rod was used to improve the accuracy of the experiments by reducing dead space for samples with surface areas < 100 m^2/g. The sample was inserted in the degassing port of the Micromeritics 3-Flex and degassed for 12 hours at a vacuum of 3 μmHg and a temperature of 380 ℃ before analysis.

3.2.2.2 Sample analysis

The initial gas mass in the storage vessel is precisely measured before the analysis. The gas expands through an expansion valve into the sample, where it adsorbs partially onto the sorbent material's external and internal pore surfaces. The volume of gas adsorbed onto the sorbent material is calculated once adsorption equilibrium is achieved at a specific partial pressure (P/Po). Equilibrium is confirmed when stable pressure and temperature conditions are observed with no further changes. Following equilibrium, the Horvath-Kawazoe (H-K) pore size analysis method is applied to determine the maximum pore volume and median pore width based on the resulting adsorption isotherms.

3.3 Microreactor for adsorption and desorption kinetics

3.3.1 Reactor design and experimental procedure

The reactor setup is shown in Figure 3-1. The adsorbate gas is a bottle of pure CO_2 mixed with pure N_2 to get a 5 vol.% and 15 vol.% concentration, and the desorption carrier gas is pure N_2. The reactor with a volume of 411.85 mL is loaded with about 6g of the adsorbent material, so a fixed bed height of 60 mm was obtained. The loaded reactor is then placed inside a furnace to maintain isothermal conditions, and the furnace is set to the desired experimentation temperature. Once the desired temperature is reached, the reactor and the system are purged with pure N_2 for 15 min at 500 mL/min to remove any contaminants that may be present in the system or the sample. Both adsorption and desorption occur at the same temperature.

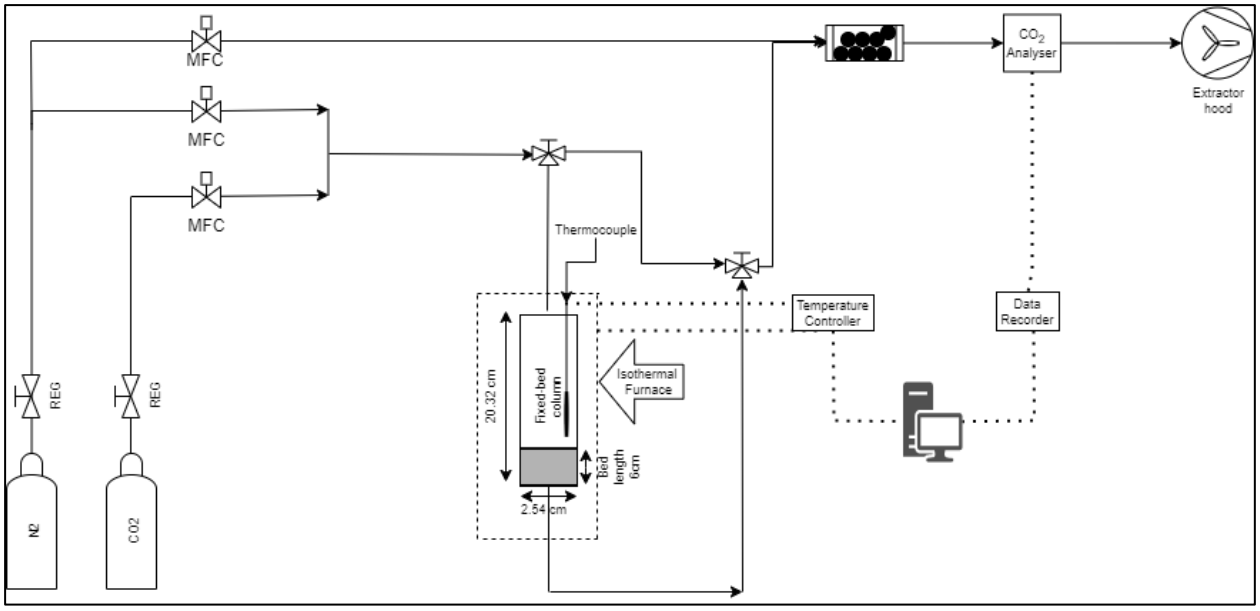

Figure 3-1: Experimental setup of fixed-bed reactor.

Once the purge is complete, the CO_2 mixture is fed through the reactor at a flow rate of 500mL/min (with individual gas flow rates in Table 3-2) and left on until the CO_2 analyser (MGA-3000 Multi Gas Analyser; ADC, UK) indicates saturation of the sample. At this point, the adsorption part of the experiment is complete, and the desorption can commence by closing the CO_2 feed and opening the pure N_2 feed again. This results in a lower concentration of CO_2 outside of the activated carbon, which, together with the temperature, causes the CO_2 gas to desorb from the samples. The analyser records the reduction in the CO_2 concentration until complete desorption is indicated by having a zero per cent reading. This two-phase experimental run is considered to be one cycle. The adsorption and desorption cycles are repeated 10 times, and considered as one experiment.

This procedure is repeated with a 15% CO_2 concentration, but since the analyser can only read a concentration up to 5%, the 15% CO_2 feed gas is diluted back down to 5%. This is done by feeding a separate line of pure N_2 into an empty-volume cylinder filled with stainless steel ball bearings to ensure that the flow through the cylinder is turbulent and mixed thoroughly.

Table 3-2: Gas feed flow rates under experimental conditions.

Gas	**5 vol.% CO_2**	**15 vol.% CO_2**
CO_2 flow rate, *mL/min*	25	75
N_2 flow rate, *mL/min*	475	425
Total flow rate, *mL/min*	500	500

This experimental setup uses 5 and 15 vol.% CO_2 concentrations that are in the range of flue gasses reported by (Strickroth *et al.*, 2020) at 13.3 vol.% CO_2 for a coal-fired power station, while David et al., (2007) report a range of 3 – 15 vol.% for coal-fired power stations. The temperature range is not chosen for the same reason as typical temperatures can reach 150 ℃, and at that temperature, adsorption becomes less viable due to significantly reduced adsorption capacity. The range from 30 – 70 ℃ provides a good overview of how sorbent performance changes at different temperatures.

3.4 Data processing

The fixed bed reactor experimental data obtained directly from the CO_2 analyser must be converted from the analyser sensor signal to CO_2 concentration to be used in the required calculations. The 5 vol.% CO_2 data and the 15 vol.% CO2 data were determined using Equation

3-4 so that the data was strictly between 0 and 5 vol.%. For the 5 vol.% data, the parameter values in Equation 3-4 were adjusted accordingly and then readjusted for the 15 vol.% CO_2 data so that all the analyser concentration data was strictly in the ranges of 0 – 5 vol.% and 0 – 15 vol.%, respectively.

$$C = \left[\frac{C_x - C_{Z_{min}}}{C_{Z_{max}} - C_{Z_{min}}}\right] \times \left(C_{A_{max}} - C_{A_{min}}\right) \quad 3\text{-}4$$

Where C is the corrected CO_2 concentration, C_x (%) is the analyser sensor reading, $C_{Z_{min}}$ (%) is the minimum analyser sensor reading, $C_{Z_{max}}$ (%) is the maximum analyser sensor reading, $C_{A_{min}}$ (%) is the minimum actual concentration of the gas and $C_{A_{max}}$ (%) is the maximum actual concentration of the gas.

To further convert the vol% data to quantity adsorbed, Equation 3-5 is used:

$$q_i = \int_{t=deadtime}^{t=final} \frac{(C_0 - C_i)}{C_0} v_i \Delta t \quad 3\text{-}5$$

Where q_i (mmol) is the quantity of the gas i adsorbed, C_0 (mmol) is the feed concentration and C_i (mmol) is the feed concentration at time t and v_i is the flow rate of the adsorbed gas.

For desorption, Equation 3-6 is used instead:

$$q_i = \int_{t=deadtime}^{t=final} \frac{C_i}{C_0} v_i \Delta t \quad 3\text{-}6$$

3.5 Modelling of adsorption and desorption reaction kinetics

The calculation methods for the model validation, well-mixed and plug-flow models discussed in this section, are used, assuming that all gasses follow ideal gas behaviour. The error analysis of the experimental results is shown in Appendix D. The error analysis is a standard method that uses 3 experimental runs to determine the following: average adsorption and desorption kinetics, standard deviation, and 95% confidence interval. This calculated data is then used to determine the experimental deviation.

3.5.1 Calculation procedure for model validation

Four methods were used to determine the fitted model's accuracy: the mean absolute error (MAE) in, the root mean squared error (RMSE), the quality of fit percentage (QOF%) and the R-squared value presented in Equation 3-7 – 3-10. MAE and RMSE are standard statistical regression indicators. The MAE was chosen to measure the average of the absolute differences and give equal weight to all errors, thus making them less sensitive to outliers. The RMSE, however, measures the average of the square of the differences and gives more weight to the larger differences. RMSE also has the same units as the original data, which can aid in interpretations. Combining the two indicators is a good representation of a model compared to the actual data (Willmott and Matsuura, 2005; Karunasingha, 2022). R^2 is another standard statistical measure that determines the proportion of the dependent variable's variation predicted from the independent variable, while QOF% is a percentage of the variation of the model from the independent variable (Keer et al., 2023).

$$MAE = mean\left(\left|x_{exp} - x\right|\right) \tag{3-7}$$

$$RMSE = \sqrt{mean\left(x_{exp} - x\right)^2} \tag{3-8}$$

Where x_{exp} is the original experimental data, and x is the predicted data value.

$$QOF\% = 100 \times \left[1 - \frac{\sum_1^N \frac{\left|x_{exp} - x\right|}{x_{exp}}}{N}\right] \tag{3-9}$$

$$R^2 = 1 - \left[\frac{\sum_1^N \left(x_{exp} - x\right)^2}{\sum_1^N \left(x_{exp} - \bar{x}\right)^2}\right] \tag{3-10}$$

Where $\bar{x}$ is the mean of the difference between the original experimental data and the predicted model data value, and N is the number of experimental data points.

3.5.2 Kinetic modelling for adsorption and desorption

The six kinetic rate models fitted (three for adsorption and three for desorption) to the resulting experimental data are Pseudo-first order, Pseudo-second order, and Avrami equations, as shown in Equations 3-11 – 3-16.

$$\frac{\mathrm{q}_t^a}{\mathrm{q}_e^a} = [1 - \exp(-k_1 t)] \quad 3\text{-}11$$

$$\frac{\mathrm{q}_t^d}{\mathrm{q}_e^d} = [1 - \exp(-\mathrm{k}_1' t)] \quad 3\text{-}12$$

$$\mathrm{q}_t^a = \frac{q_e^{a\,2} k_2 t}{1 + \mathrm{q}_e^a k_2 t} \quad 3\text{-}13$$

$$\mathrm{q}_t^d = \frac{q_e^{d\,2} \mathrm{k}_2' t}{1 + \mathrm{q}_e^d \mathrm{k}_2' t} \quad 3\text{-}14$$

$$\frac{\mathrm{q}_t^a}{\mathrm{q}_e^a} = 1 - exp[-((k_A t)^n)] \quad 3\text{-}15$$

$$\mathrm{y} = 1 - exp\left[-\left((k_A{}' t)^{n_A{}'}\right)\right] \quad 3\text{-}16$$

These equations are used in Matlab with a simple optimiser consisting of a distance function that is minimised by varying the parameters $k_1, \mathrm{k}_1', k_2, \mathrm{k}_2', k_A, k_A{}', n$, and $n_A{}'$, respectively. The inbuild Matlab function *fminsearch* uses the Nelder-Mead numerical method to find the minimum value of the distance function.

3.5.3 Activation energy

The well-known Arrhenius equation was used to determine the activation energy of the activated carbon sorbents from the Avrami kinetic rate constant obtained from the microreactor experiments. By taking the natural logarithm of the Arrhenius equation, Equation 3-17, changes to the form presented in Equation 3-18, and the plot of ln(kA) against 1/T can be created (Wei, Yu, Xie, *et al.*, 2017).

$$k = Ae^{\left(\frac{-E_a}{RT}\right)} \quad 3\text{-}17$$

$$\ln(k_A) = \ln(A) - \left(\frac{E_a}{RT}\right) \quad 3\text{-}18$$

Then, a straight-line plot can be made by rearranging Equation 3-18 so that it is in the form *y=mx+c*.

$$\ln(k_A) = -\left(\frac{E_a}{R}\right)\left(\frac{1}{T}\right) + \ln(A) \quad 3\text{-}19$$

E_a is then calculated using the slope so that $Ea = \frac{(-R\ x\ slope)}{1000}$. (kJ/mol)

3.6 Thermodynamic calculations

The equations and calculations used to determine the thermodynamic properties are explained in this section.

3.6.1 Enthalpy, entropy and Gibbs free energy

The following three thermodynamic parameters are calculated using the same method to determine the activation energy, but here, we use the Vant Hoff equation at equilibrium (∆G = 0), (Equation 3-23) and the Gibbs free energy equation, Equation 3-20.

$$\Delta G = \Delta H - T\Delta S \quad \text{3-20}$$

$$\Delta G = \Delta G^{\theta} + RTln\left(K^{\theta}\right) \quad \text{3-21}$$

At equilibrium (∆G = 0), thus

$$\Delta G^{\theta} = -RTln\left(K^{\theta}\right) \quad \text{3-22}$$

By combining equation 3-20 and 3-22, it becomes:

$$ln\left(K^{\theta}\right) = -\left(\frac{\Delta H^{\theta}}{R}\right)\left(\frac{1}{T}\right) + \left(\frac{\Delta S}{R}\right) \quad \text{3-23}$$

Where K^{θ} is standard equilibrium constant. Kd distribution coefficient is obtained and converted into a standard equilibrium distribution coefficient to calculate a standard equilibrium constant. The equilibrium constant is calculated as follows:

$$K_d = \frac{\mathrm{q}_e^a}{C_e} \quad \text{3-24}$$

With q_e^a the adsorption capacity at equilibrium and C_e the concentration of the adsorbate at equilibrium. K_d can be directly determined from the experiments and is an experimental equilibrium constant (Chen et al., 2021). However, K_d has dimensions, and the standard equilibrium constant in the Vant Hoff equation is dimensionless, therefore K_d must be converted into a standard equilibrium constant by using Equation 3-25 (Chen et al., 2021).

$$K_d^\theta = \frac{\left(\frac{q_e^a}{q^\theta}\right)}{\left(\frac{C_e}{C^\theta}\right)} = K_d\left(\frac{C^\theta}{q^\theta}\right) \quad \text{3-25}$$

Where C^θ and q^θ are the standard states of solution in gas and solid form, respectively (Chen et al., 2021). The standard states are a reference state as the baseline for calculating thermodynamic parameters. According to IUPAC proposition, C^θ is selected as 1 mol L^{-1} (Chen et al., 2021), while q^θ is recommended as a standard state of adsorption for 2-dimensional gases as 1.39 X 10^{-7} mol m^{-2} (Savara, 2013).

After the transformation into the standard equilibrium constant, a linear plot of $ln\left(K_d^\theta\right)$ against 1/T is used to calculate the following:

$$\Delta H^\theta = \frac{-R \times slope}{100} \quad \text{3-26}$$

$$\Delta S^\theta = \frac{R \times intecept}{100} \quad \text{3-27}$$

ΔH^θ and ΔS^θ can then be substituted into equation 3-20 to calculate ΔG^θ

3.7 Adsorption and desorption breakthrough modelling

As discussed in Section 2.13, the equations that model breakthrough behaviour are complex and challenging to solve. Thus, in this study, the adsorption breakthrough curves are modelled using the Avami kinetic model, and the desorption breakthrough curves are modelled using a modified Avrami equation so that the model can be fitted to the desorption curve. This is done to determine if a simple model such as Avrami can be used to describe the breakthrough behaviour of laboratory-scale fixed-bed reactors. The modified Avrami equation is used as:

$$y = e^{-\left(k_A' t\right)^{n_A'}} \quad \text{3-28}$$

Where y represents the desorption proportion, k_A' (s^{-1}) is the Avrami desorption kinetic constant and n_A' the Avrami desorption exponent.

Chapter 4

CHAPTER 4: CHARACTERIZATION OF ADSORBENTS: RESULTS

The characterisation results discussed in this section are those obtained from the proximate and ultimate analyses, surface area properties and scanning electron microscopy (SEM) analyses on the granular activated carbon.

4.1 Proximate and ultimate analysis

The carbon activation process involves high temperatures that effectively remove volatile components from the sample, resulting in low volatile matter content observed in the activated carbon samples. Proximate and ultimate analysis results for samples CQ650, CQ30P, and CQ006 are presented in Table 4-1. Proximate analysis data are reported on an air-dried basis, while ultimate analysis results are reported on a dry ash-free basis. Both the proximate and ultimate analyses were completed in the North-West University Laboratory.

CQ006 sample has the highest fixed carbon content at 88.0 wt.%, and CQ30P, with 84.0 wt.%, has the lowest fixed carbon content. A positive correlation between the fixed carbon content and the maximum adsorption capacity can be observed, as the organic part of the activated carbon provides the surface area for the molecules to adsorb (Keza *et al.*, 2022). It must be noted that it is not the only parameter that determines the adsorption capacity.

Regarding the inherent moisture, CQ650 has the highest recorded inherent moisture content at 6.42 wt.% compared to the rest of the activated carbon samples. The highest ash yield came from CQ30P at 9.90 wt.%, more than double the ash yield of the second-highest sample, CQ650, at 4.07 wt.%. On a dry-ash-free basis, CQ30P displayed the highest carbon content at 96.3 wt.%, and CQ650 had the lowest carbon content at 94.1 wt.%. All the activated carbons have a high carbon content; the results for the other elements are compared in Table 4-1.

Table 4-1: Proximate and ultimate analysis for CQ650, CQ30P, CQ006 and PCX1

Proximate analysis results (wt.%, air dried basis)			
Sample ID/properties	**CQ650**	**CQ30P**	**CQ006**
Inherent moisture	6.42	3.99	6.10
Ash yield	4.07	9.90	2.31
Volatile matter	5.01	2.11	3.59
Fixed carbon	84.5	84.0	88.0
Calorific value (MJ/kg)	28.72	28.56	29.97
Ultimate analysis results (wt.% dry ash-free basis)			
Sample ID/properties	**CQ650**	**CQ30P**	**CQ006**
Carbon	94.1	96.3	95.2
Hydrogen	0.37	0.48	0.40
Nitrogen	0.48	0.59	0.43
Oxygen	4.87	2.12	3.80
Total sulphur	0.16	0.52	0.13

4.2 Surface area, pore size distribution, pore volume and porosity analysis

The micropore size distribution was evaluated with CO_2 adsorption at 273 K, while the mesopores and macropores were evaluated with N_2 adsorption at 77 K. CQ650 had the largest amount of micropores, followed by CQ006 and CQ30P. CQ650 and CQ006 both have a well-developed microporous structure and architecture.

Regarding mesopores and macropores evaluated with N_2, spikes at pore sizes less than 100Å indicate many mesopores in the samples. However, no macropores were present in the three samples. Due to the significant differences in the pore size distribution analysis, a difference in surface area, adsorption capacity and pore volume is expected.

The sorbent properties, such as micropore surface area, BET surface area, average pore diameter, micropore volume and porosity, are presented in Table 4-2. The micropore surface area indicates the porosity and potential CO_2 sorption capacity. CQ650 has the highest micropore

surface area at 735 m^2/g, followed by CQ006 at 671 m^2/g and CQ30P at 532 m^2/g. Therefore, CQ650 is expected to have the highest adsorption capacity among the three samples. The same trend is seen regarding the BET surface area, as CQ650 has the highest, followed by CQ006 and CQ30P. A higher surface area and pore volume naturally correspond to higher adsorption capacities as there is more space for the individual CO_2 molecules to attach and migrate into the sorbent.

It can be noted from Table 4-2 that the calculated D-R micropore surface area is significantly larger than the calculated BET surface area. This is due to the presence of mesopores in the activated carbon samples. The D-R equation can be successfully applied to a porous material when that material is purely microporous; however, if mesopores are also present like it is here, then the D-R equation tends to overestimate the micropore volume and, in turn, overestimate the micropore surface area (Villarroel-Rocha *et al.*, 2013).

Table 4-2: The surface area, average pore diameter, micropore volume and porosity recorded for CQ650, CQ30P and CQ006 evaluated with CO_2

Properties / Sample ID	**CQ650**	**CQ30P**	**CQ006**
D-R micropore surface area, *m^2/g*	735.0±27.0	518.8±1.90	670.8±31.8
BET surface area, *m^2/g*	517.1±4.50	355.7±1.1	473.2±5.90
D-R limiting micropore volume, *cm^3/g*	0.295±0.011	0.207±0.001	0.269±0.013
H-K average pore diameter, *Å*	4.03±0.02	4.07±0.00	3.92±0.02
Porosity, % $(3\text{Å} \leq d_p \leq 5\text{Å})$	25.9±0.900	16.8±0.05	27.7±0.750

4.3 Scanning electron microscopy analysis

The SEM images were obtained from the North-West University Laboratory for Electron Microscopy (LEM), Potchefstroom. The micrographs of the activated carbons are presented in Figure 4-1. The images reveal an irregular and heterogeneous surface morphology characterized by a well-developed pore structure. The surface of the activated carbons exhibits intricate cracks and crevices, displaying varied pore shapes and sizes across the entire surface. The typical particle sizes of the activated carbons used for the SEM analysis are 1 mm in diameter.

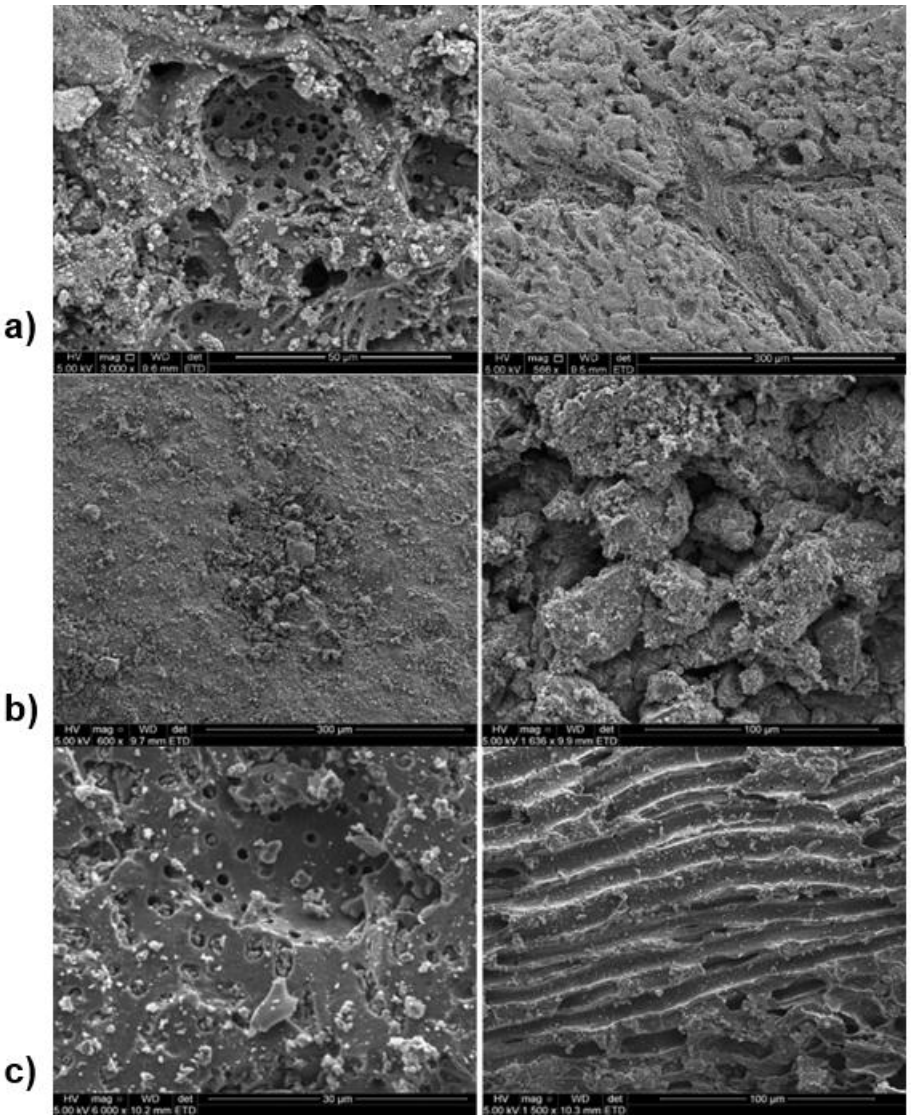

- **Figure 4-1: SEM micrographs of a) CQ650, b) CQ30P and c) CQ006 (Jacobs, 2018).**

4.4 Activated carbon characterisation results compared with literature

The characterisation results of the activated carbons investigated in this study compared well to characterisation results reported for other activated carbons, silica and zeolites in literature. See Table 4-3 for the compared results.

Shafeeyan et al., (2015) investigated the equilibrium adsorption of CO_2 on ammonia-modified activated carbon samples. They reported that the activated carbon sample had a BET surface area of 768 m2/g, which was more significant than what was experimentally obtained for the activated carbon samples investigated in this study. CQ650 had the highest surface area in this study, with a BET surface area of 517 m^2/g, which is less than the reported value of Shafeeyan. Rashidi et al., (2016) reported a BET surface area of 660 m^2/g and a pore volume of 0.67 cm^3/g while using a Norit SX2 activated carbon sample. These surface areas and pore volumes are significantly greater than the values reported by this study.

The CO_2 adsorption on zeolite 13X, 4A and 5A was determined by Hauchhum and Mahanta, (2017). Surface areas of 720, 650 and 434 m^2/g, respectively, were reported. Here, zeolite 13X and 5A outperformed the activated carbons, but CQ650 and CQ006 had a greater BET surface area than the zeolite 4A did.

Table 4-3: Adsorbent characterisation: Results of this study compared with results reported in literature

Sample Type	Sample name	Activation method	Commercially available [Y/N]	Pressure, *bar*	Temperature range, *°C*	BET surface area, m^2/g	Average pore diameter, *nm*	Pore volume, cm^3/g	Ash yield, *%*	C%	N%	H%	S%	O%	References
AC	CQ650	Steam, KOH	Y	1.0	30-70	517.1	0.40	0.30	4.1	94	0.48	0.37	0.16	4.9	This study
AC	CQ30P	Steam, KOH	Y	1.0	30-70	355.7	0.41	0.21	9.9	96	0.59	0.48	0.52	2.1	
AC	CQ006	Steam, Acid washed	Y	1.0	30-70	473.2	0.39	0.27	2.3	95	0.43	0.40	0.13	3.8	
AC	DARCO FDG	-	N	1.0	18-130	1060	-	-	-	-	-	-	-	-	Ammendola et al., 2017
AC	Norit SX2	Steam, Acid	Y	1.0	25-120	660.7	4.05	0.67	-	77	0.33	1.61	0.05	20	Rashidi et al., 2016
AC	C-500	HMMM[1] resin	N	1.0	30-100	-	3.50	-	2.9	64	21	1.90	-	13	Goel et al., 2016
AC	C-600	HMMM resin	N	1.0	30-100	-	3.50	-	3.7	63	16	2.60	-	18	
AC	C-700	HMMM resin	N	1.0	30-100	463.0	3.50	0.48	2.9	62	14	1.40	-	23	
AC	C-800	HMMM resin	N	1.0	30-100	112.0	3.50	0.12	2.7	64	9	1.90	-	25	

Table 4-3: Adsorbent characterisation from this study and comparison with results recorded from literature (continued)

Sample Type	Sample name	Activation method	Commercially available [Y/N]	Pressure, *bar*	Temperature range, *°C*	BET surface area, m^2/g	Average pore diameter, *nm*	Pore volume, cm^3/g	Ash yield, *%*	C%	N%	H%	S%	O%	References
Zeolite	13X	-	Y	4.0	25-60	720.0	10.0	-	-	-	-	-	-	-	Hauchhum and Mahanta, 2014b
Zeolite	5A	-	Y	4.0	25-60	650.0	5.00	-	-	-	-	-	-	-	
Zeolite	4A	-	Y	4.0	25-60	434.0	4.00	-	-	-	-	-	-	-	
AC	Coconut fibre	-	N	4.0	25-60	354.0	1.50	-	-	-	-	-	-	-	
AC	GAC	Ammonia modified	Y	1.0	30	768.0	-	0.39	5.20	92	0.30	1.20	0.20	5.9	Shafeeyan et al., 2015

[1]

[1] [1] Hexamethoxymethylmelamine

Chapter 5

CHAPTER 5: RESULTS AND DISCUSSION: ADSORPTION AND DESORPTION EXPERIMENTS

The experimental results are presented in this chapter. Comparisons are drawn between this study's results and those reported in the open literature to show the effects of the feed concentration and temperatures on the sorbent performance, quantities of CO_2 adsorbed and desorbed, and the differences between the sorbents.

5.1 Cyclic performance of adsorption and desorption of activated carbons

The cyclic operation of the experiment showed that the sorbents performed consistently across the 10 cycles. Figure 5-1 and Figure 5-2 show that each sorbent has a consistent period, with each adsorption and desorption taking approximately the same time to complete as the previous one. This behaviour is consistent regardless of the feed concentration or the temperature.

This cyclic comparison also clearly shows fundamental differences between the sorbents, as the variance in completion time significantly differs from one sorbent to the next. At the higher feed concentration shown in Figure 5-2, the difference in the completion time between CQ650 and CQ30P is significantly less than the time difference with the 5 vol.% feed concentration, whereas CQ006 was the fastest sorbent by a large margin in both 5 vol.% and 15vol.% feed concentrations.

The lack of any degradation across 10 cycles indicates that the experimental temperatures are not enough to change the structure of the activated carbon samples, which would cause a change in their adsorption/desorption behaviour. This fact bodes well for use in industrial applications as the sorbents can be used repeatedly, lowering the consumable cost of constantly changing the sorption material. It also shows that these specific activated carbons can withstand even higher temperatures; how high they can handle without degradation would need to be investigated.

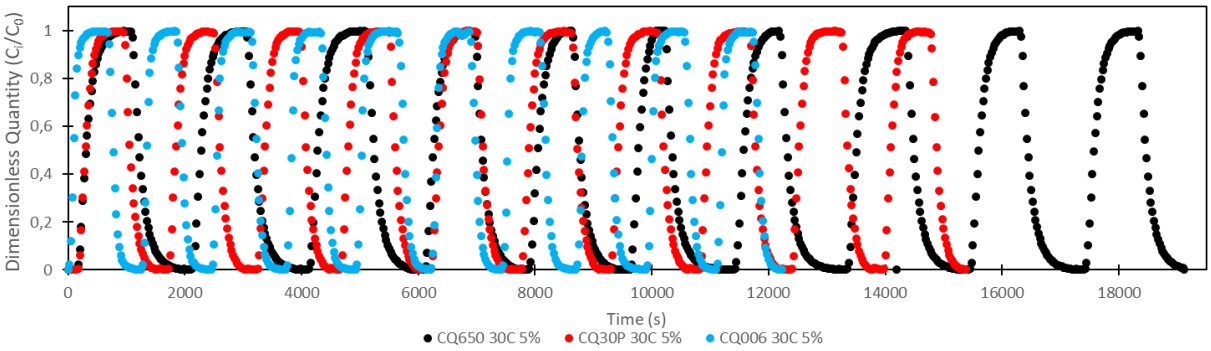

Figure 5-1: Cyclic performance of CQ650, CQ30P and CQ006 with 5 vol.% CO_2 at 30 ℃ for 10 cycles.

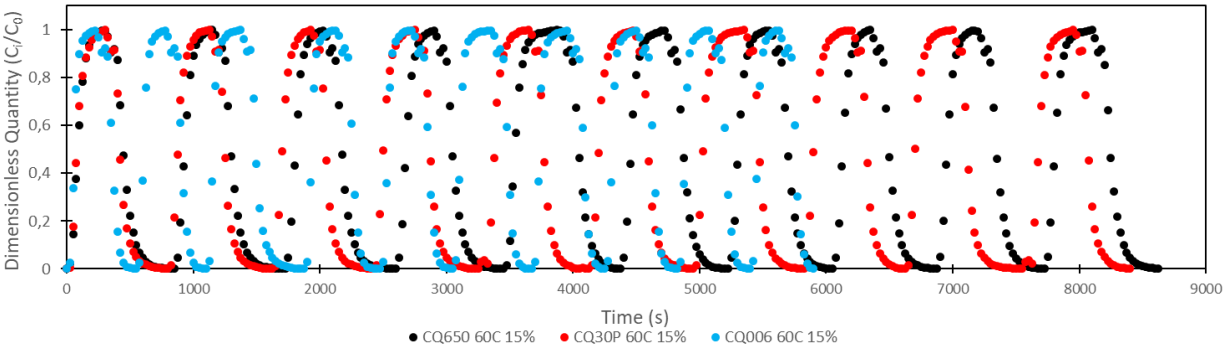

Figure 5-2: Cyclic performance of CQ650, CQ30P and CQ006 with 15 vol.% CO_2 at 60 ℃ for 10 cycles.

5.2 Evaluation of the effect of feed concentration on sorbent performance

The feed concentration of CO_2 significantly affects the sorbent capacity and their overall performance.

The correlation seen in this section is especially beneficial for industrial applications that aim to capture CO_2 from processes. Increasing the concentration of the CO_2 before it is sent to the capture process can increase the efficiency of that process.

The CO_2 feed concentration significantly affects the sorbent's adsorption/desorption performance. There is a clear distinction between the 5 vol.% and 15 vol.% feed concentration regarding adsorption and desorption performance. From Figure 5-3 and Figure 5-4, it is clear that all the sorbents respond similarly to the increase in the feed concentration, with the rate of adsorption and desorption increasing with the increased feed concentration.

The difference can be seen in the time it takes for the sorbent to reach saturation, with the times presented in Table 5-1. From both the adsorption and desorption times, the increase in the concentration of the CO_2 feed significantly affects the sorbent performance. Adsorption and desorption occur at a much higher rate for the 15 vol.% CO_2 than the 5 vol.% CO_2. CQ650 and CQ006 are the most sensitive to the concentration change in adsorption, as the 15 vol.% feed reduced the saturation time by 250 seconds and 300 seconds, respectively.

In desorption, the effect of the increased concentration is reversed as CQ650 is the least affected with only a 50s difference in saturation times, while CQ30P is the most affected with a saturation time difference of 400s. These 'reversals' of sorbent performance from adsorption and desorption also occur at the other temperatures (40, 60 and 70 ℃) tested.

The result obtained in this study matches the results in other literature where the higher CO_2 concentrations were associated with shorter breakthrough times and steeper breakthrough curves due to the increased driving force of CO_2 molecules along the pores (Tsiotsias *et al.*, 2023). The driving force is increased by the increased CO_2 feed partial pressure (increased concentration) of the gas flow along the pores of the sorbent, which thermodynamically favours the CO_2 adsorption process that then results in higher CO_2 uptake values (Tsiotsias *et al.*, 2023).

Table 5-1: Difference between sorbents' time to saturation at 5 vol.% vs 15 vol.% CO_2 feed concentrations

	Adsorption performance at 30 ℃
Sorbent	**Time difference between saturation (s) @ 5 vol.% and 15 vol.% CO_2 feed**
CQ650	250
CQ30P	150
CQ006	300
	Desorption performance at 50 ℃
Sorbent	**Time difference between saturation (s) @ 5 vol.% and 15 vol.% CO_2 feed**
CQ650	50
CQ30P	400
CQ006	275

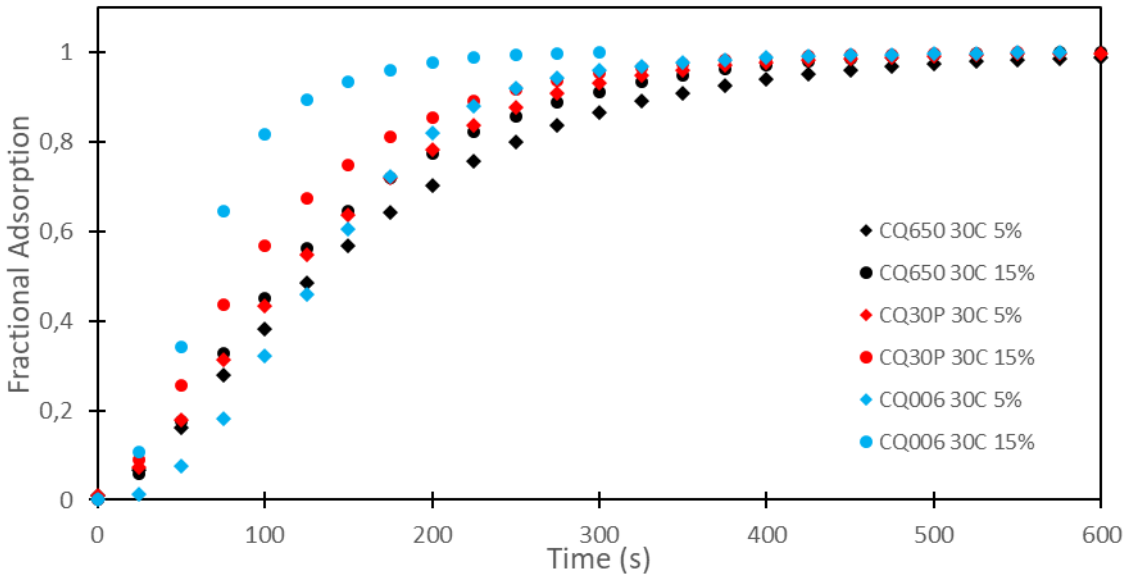

Figure 5-3: Adsorption performance of CQ650, CQ30P and CQ006 at 30 ℃, and 5 and 15 vol.% feed concentrations.

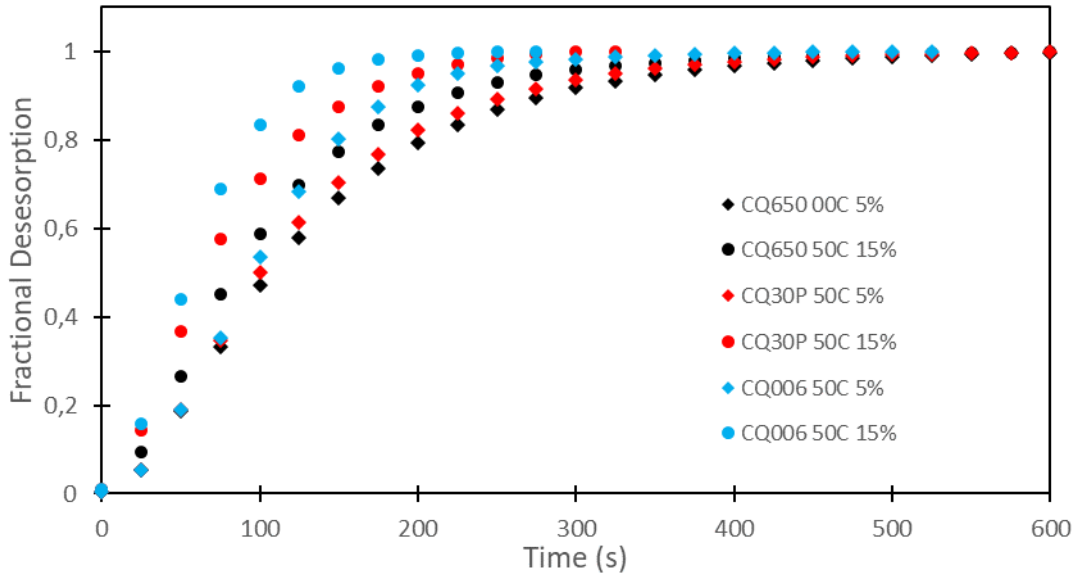

Figure 5-4: Desorption performance of CQ650, CQ30P and CQ006 at 50 ℃, and 5% and 15% feed concentrations.

5.3 Effect of temperature on sorbent adsorption and desorption performance

Temperature is known to affect the adsorption and desorption rate significantly. In this section, the results of the effect of temperature on the adsorption and desorption, as well as the effect of temperature on the quantities adsorbed and desorbed, are discussed.

5.3.1 Effect of temperature on sorbent adsorption performance

It is well known that there is a strong correlation between the quantity adsorbed and the time required to reach adsorption equilibrium. The reason for this relationship is due to the increase in kinetic energy that the CO_2 molecules experience with the increase in temperature, which can be seen in this study (Section 5.3.1) and the studies by (Shafeeyan, 2015; Raganati, Chirone and Ammendola, 2020; Dziejarski and Kisiela-Czajka, 2021) in which they all show decreased adsorption capacities with increased temperature.

In Figure 5-5, the adsorption performance shows an improvement where the lowest temperature is at the bottom of the graph, and each subsequent higher temperature is incrementally above the previous. For CQ650, the difference in performance between the temperatures is well defined in steps, whereas for CQ30P and CQ006, the difference in performance between 40 ℃ and 50 ℃ is insignificant.

The range of saturation times between the individual sorbents is also different from one another. The largest difference is with CQ650, followed by CQ006 and CQ30P. For CQ30P, apart from 30 ℃, the adsorption performance at 40, 50 and 60 ℃ is very similar, which could make this sorbent more suitable for lower-temperature applications. The sorption capacity of the sorbents is discussed in more detail in Section 5.4.

Similar to the 5 vol.% CO_2 concentration adsorption performance, Figure 5-6 shows the 15 vol.% CO_2 concentration effect, and the results remain relatively the same. The variance between the temperature curves for CQ650 and CQ30P are visually the same, but there are clear distinctions between the graphs. However, the CQ006 points are more clustered, indicating that there is not much difference in the adsorption performance in the temperature range of 30 ℃ to 70 ℃.

The difference between the temperatures is their time to reach saturation. The saturation times differ from the lowest to the highest temperature for CQ650, CQ30P, and CQ006 at 5 vol.% CO_2 feed are 125 s, 175 s, and 325 s, respectively. Then, the time differences for the 15 vol.% CO_2 feed are 350s, 325s and 125s, respectively. The time till saturation for all the sorbents is presented in Table 5-2.

From the time differences at 5 vol.% CO_2 fees, it is clear that CQ650 is the least affected, followed by CQ30P and CQ006. But, at 15 vol.% CO_2 feed, the order is reversed, with CQ650 being the most affected and CQ006 being the least affected.

Table 5-2: Effect of temperature on adsorption performance at 5 vol.% and 15 vol.% CO_2 feed concentrations

	Temperature				
	30 ℃	**40 ℃**	**50 ℃**	**60 ℃**	**70 ℃**
Sorbent	**Saturation time (s) @ 5 vol.% CO_2 feed**				
CQ650	750	725	675	650	625
CQ30P	825	775	725	700	650
CQ006	750	600	500	475	425
	Temperature				
	30 ℃	**40 ℃**	**50 ℃**	**60 ℃**	**70 ℃**
Sorbent	**Saturation time (s) @ 15 vol.% CO_2 feed**				
CQ650	700	525	500	400	350
CQ30P	625	525	475	375	300
CQ006	400	400	375	350	275

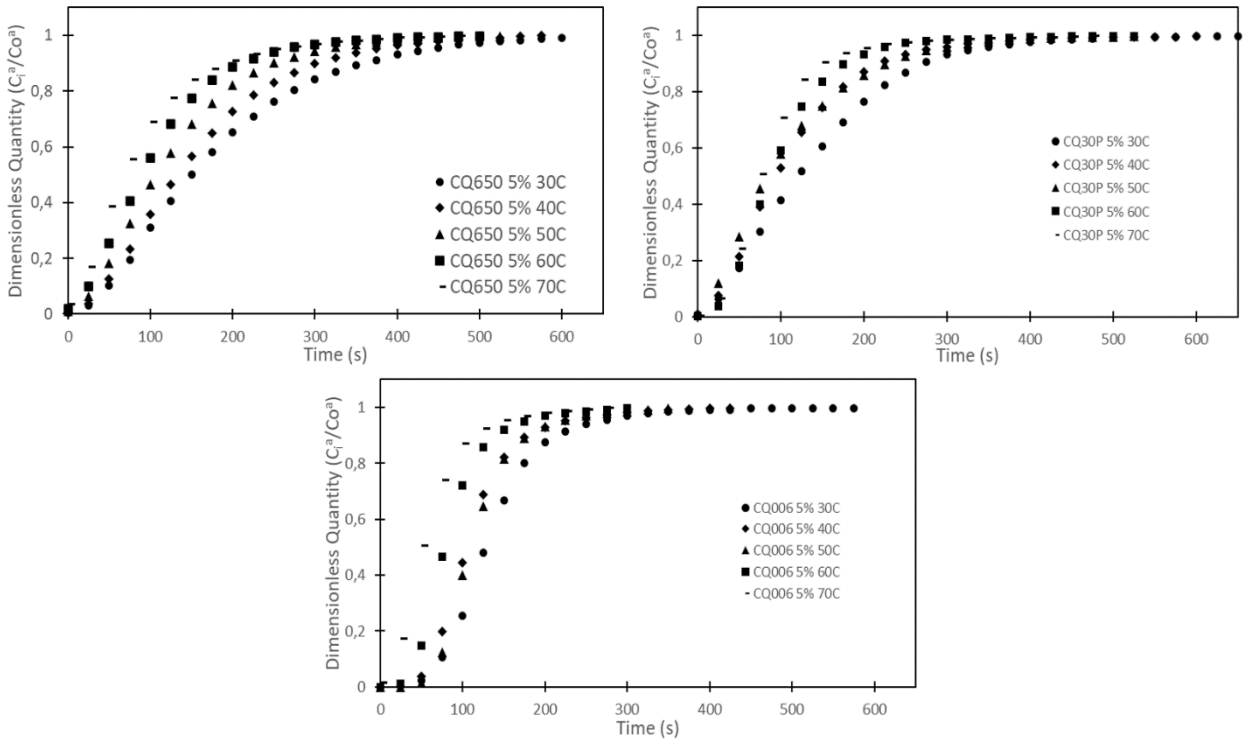

Figure 5-5: Temperature effect on adsorption performance of CQ650, CQ30P and CQ006 at 5 vol.% CO_2 and 30, 40, 50, 60 and 70 ℃.

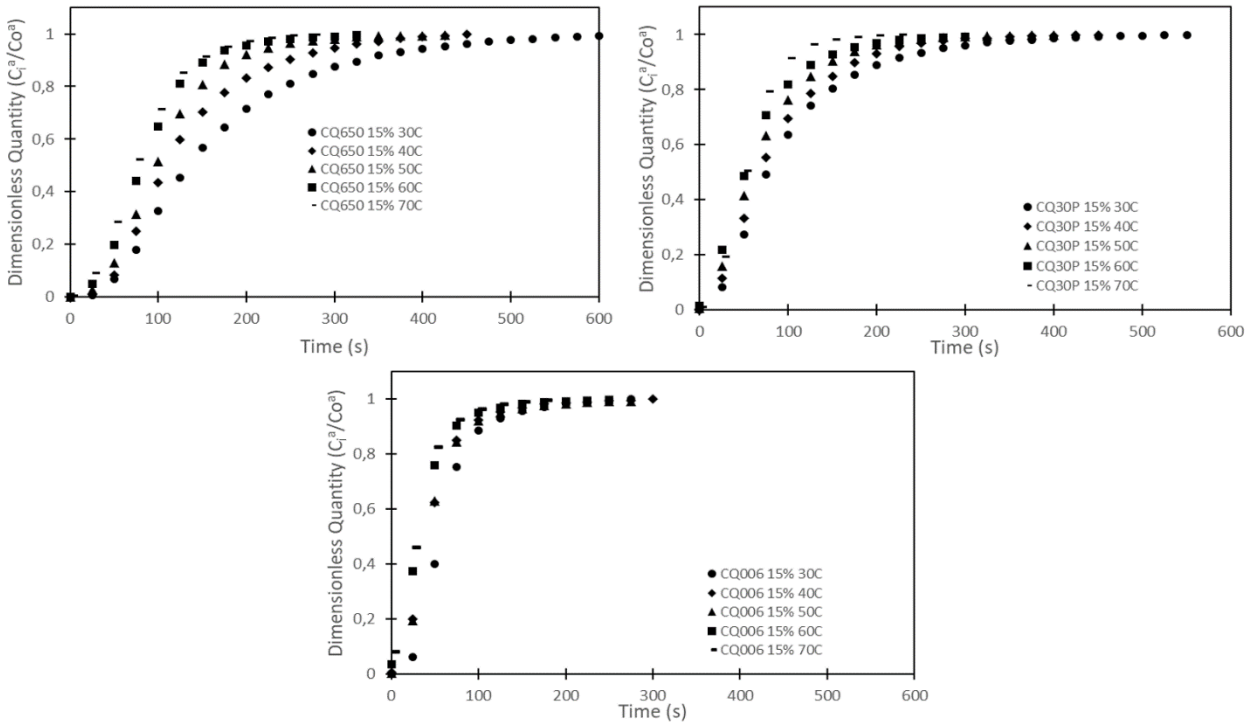

Figure 5-6: Temperature effect on adsorption performance of CQ650, CQ30P and CQ006 at 15 vol.% CO_2 and 30, 40, 50, 60 and 70 ℃.

5.3.2 Effect of temperature on sorbent desorption performance

The effect of temperature on desorption follows the same trend as that of adsorption since it is temperature-dependent. In Figure 5-7, there are clear distinctions between the temperature graphs, with the temperatures of 50 ℃ and 60 ℃ affecting the performance less. With CQ650 and CQ30P, there is a negligible difference between 40 ℃ and 50 ℃ and 50 ℃ and 70 ℃, respectively. Whereas with CQ006, the negligible difference is at 30 ℃ and 40 ℃. The variance also remains relatively similar between the sorbents for desorption at 5 vol.l% CO_2 feed.

At 15 vol.% CO_2 feed concentration, Figure 5-8, the variance and the difference between sorbent performance are reduced, and the slopes are steeper, indicating faster desorption. All the sorbents are affected by the increasing temperature, with CQ650 being the least affected in terms of the time till saturation. When looking at the difference between the time till saturation of the lowest and highest temperatures, one can determine how much each sorbent is affected by the increasing temperature. All the saturation times are presented in Table 5-3.

The difference between the saturation times of CQ650, CQ30P and CQ006 at 5% CO_2 are 200s, 150s and 225s, respectively. While at 15 vol.% CO_2 feed, the differences are 400s, 225s and 225s, respectively. Thus, at 5 vol.%, CQ650 is the least affected by the increasing temperature, followed by CQ30P and CQ006. However, at 15 vol.% CO_2 feed, CQ650 is now the most affected

by the temperature increase, and CQ006 is the least affected. This reversal is the same as the adsorption performance in Section 5.3.1.

Table 5-3: Effect of temperature on desorption performance at 5 vol.% and 15 vol.% CO_2 feed concentrations

	Temperature				
	30 ℃	**40 ℃**	**50 ℃**	**60 ℃**	**70 ℃**
Sorbent	**Saturation time (s) @ 5 vol.% CO_2 feed**				
CQ650	850	825	750	650	650
CQ30P	800	800	775	725	650
CQ006	725	700	650	625	500
	Temperature				
	30 ℃	**40 ℃**	**50 ℃**	**60 ℃**	**70 ℃**
Sorbent	**Saturation time (s) @ 15 vol.% CO_2 feed**				
CQ650	875	850	775	525	475
CQ30P	725	700	650	625	500
CQ006	600	550	475	450	375

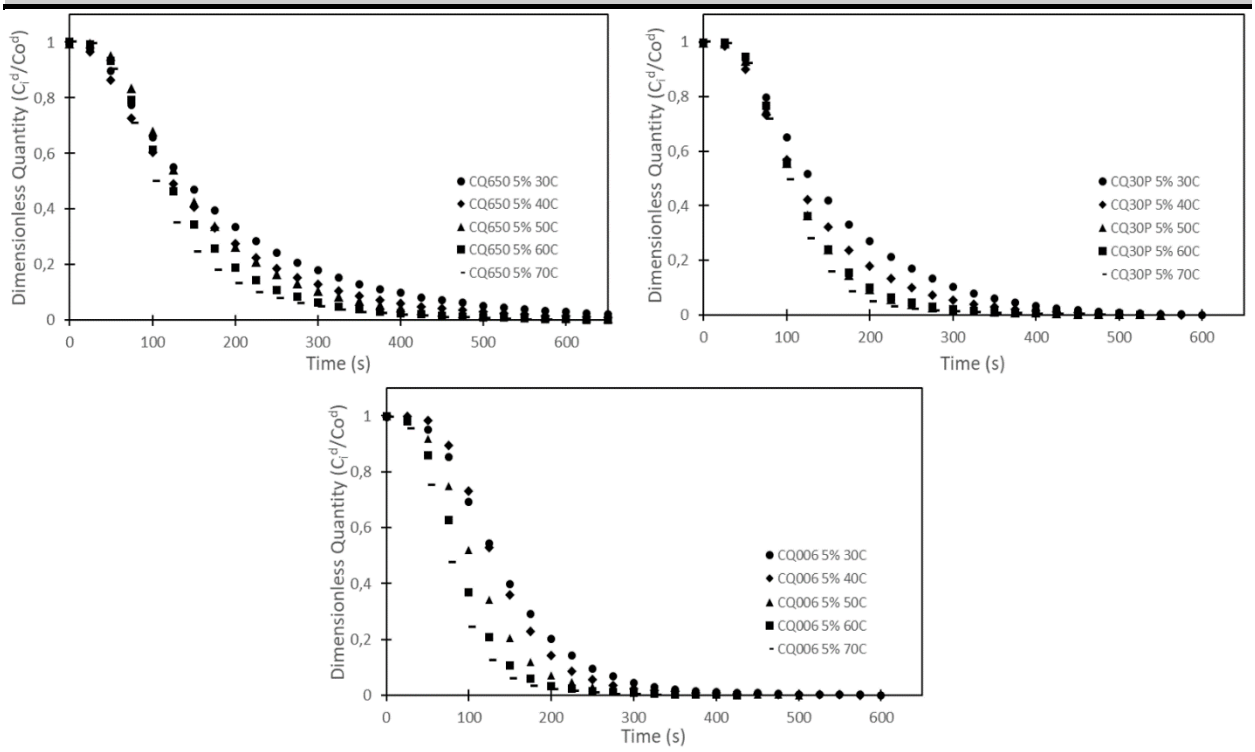

Figure 5-7: Temperature effect on desorption performance of CQ650, CQ30P and CQ006 at 5 vol.% CO_2 and 30, 40, 50, 60 and 70 ℃.

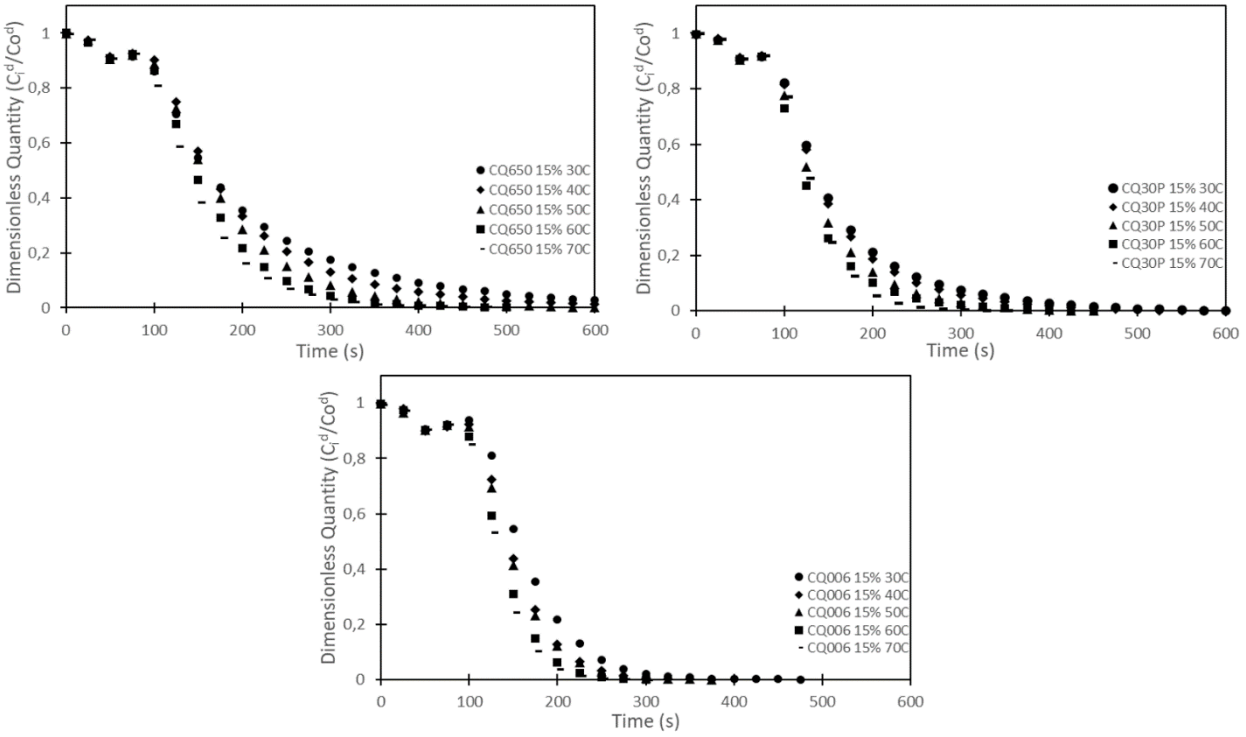

Figure 5-8: Temperature effect on desorption performance of CQ650, CQ30P and CQ006 at 15 vol.% CO_2 and 30, 40, 50, 60 and 70 ℃

5.4 Effect of temperature on the quantity adsorbed and desorbed for 5 and 15 vol.% CO_2

5.4.1 Effect of temperature on the quantity adsorbed

There is not a direct correlation between the adsorption performance and the quantities adsorbed, as the difference between the adsorbed quantity CQ30P between 40, 50 and 60 ℃ is minimal, which is the same as shown in Figure 5-5 above for the adsorption performance of CQ30P. There, the exact temperatures have only a small effect on the adsorption performance. Generally, temperature has a more significant effect on the quantity adsorbed.

In the case of CQ650, the variance between each temperature is evident, as in Figure 5-4, showing again that CQ650 is very much affected by temperature differences. However, when looking at CQ006 in Figure 5-9, it is shown that at 50 ℃ and 60 ℃ have near identical adsorption quantities, but in Figure 5-5 above, the adsorption performance of CQ006 at 40 ℃ and 50 ℃ is near identical. There are similarities between the adsorption performance and the quantity adsorbed for all the sorbents, but they are not exact and should be considered a generalised correlation.

Table 5-4: Total quantity adsorbed for CQ650, CQ30P and CQ006 at 5 vol.% and 15 vol.% CO_2 feed concentrations

	Temperature				
	30 ℃	**40 ℃**	**50 ℃**	**60 ℃**	**70 ℃**
Sorbent	**Total quantity adsorbed (mmol/g) @ 5 vol.% CO_2 feed**				
CQ650	0.96	0.79	0.69	0.57	0.46
CQ30P	0.85	0.70	0.66	0.62	0.55
CQ006	0.83	0.71	0.61	0.58	0.52
	Temperature				
	30 ℃	**40 ℃**	**50 ℃**	**60 ℃**	**70 ℃**
Sorbent	**Total quantity adsorbed (mmol/g) @ 15 vol.% CO_2 feed**				
CQ650	1.67	1.47	1.15	0.88	0.68
CQ30P	1.03	0.80	0.61	0.46	0.40
CQ006	1.03	0.65	0.62	0.47	0.41

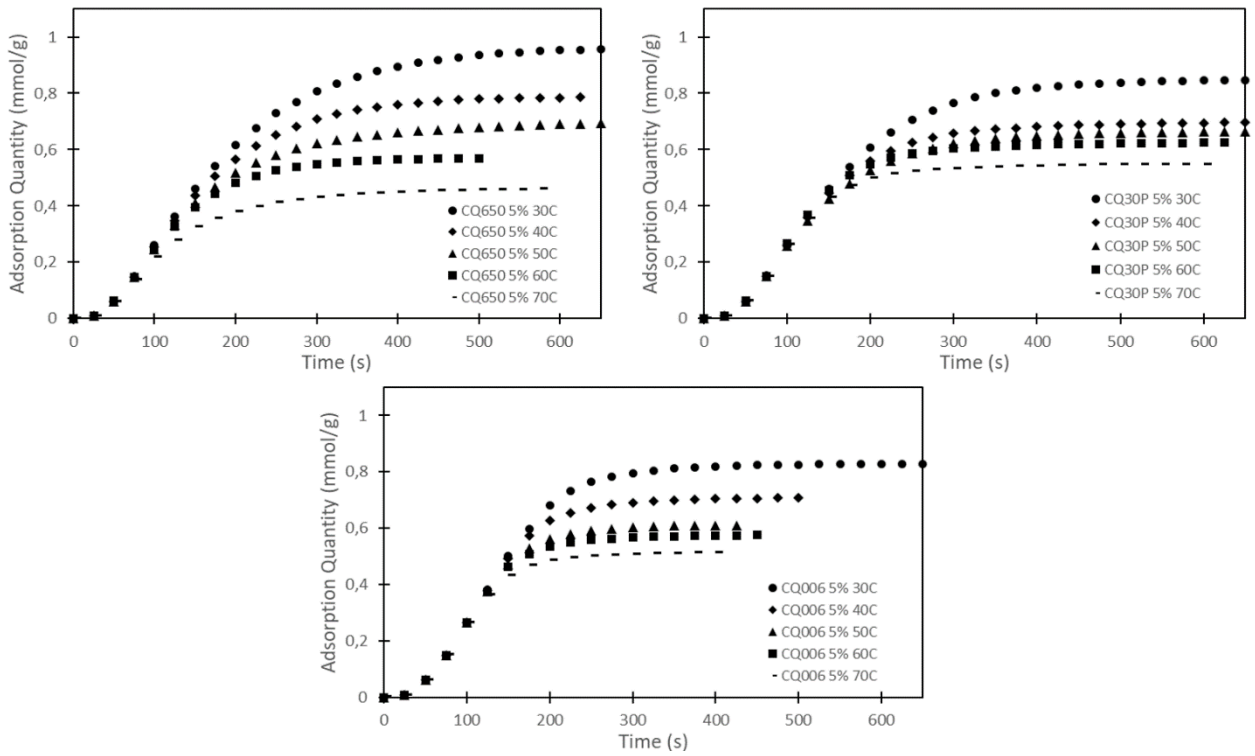

Figure 5-9: Effect of temperature on CO_2 adsorption capacity for CQ650, CQ30P and CQ006 at 5 vol.% CO_2 and 30, 40, 50, 60 and 70 ℃

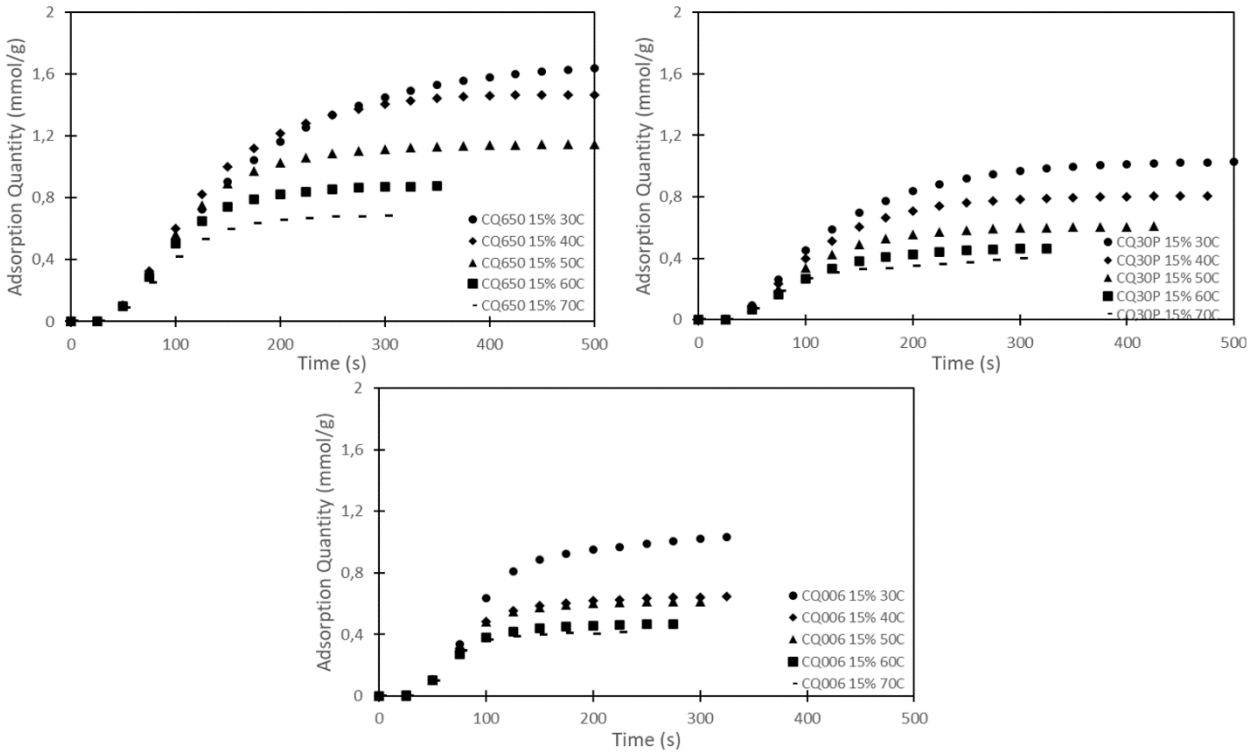

Figure 5-10: Effect of temperature on CO_2 adsorption capacity for CQ650, CQ30P and CQ006 at 15 vol.% CO_2 and 30, 40, 50, 60 and 70 ℃

5.4.2 Effect of temperature on the quantity desorbed

The desorbed quantities reflect the same result as those adsorbed for all sorbents. The highest quantities desorbed are recorded at the lowest temperatures. Again, CQ650 desorbs the most at 5 and 15 vol.% CO_2 feed concentrations, as expected. The most significant difference between the desorbed quantities can be seen in the desorption of the 15 vol.% CO_2 feed, where the higher concentration highlights the differences between the sorbents. The other obvious observation is the amount of CO_2 desorbed at higher temperatures, indicating that these sorbents are not well suited for high-temperature applications. This can be seen in Table 5-5, where the adsorbed and desorbed quantities are presented.

CQ650 has the most clearly defined differences between the quantities adsorbed at the different temperatures, as seen in Figure 5-11. Further, CQ30P is the least affected by the temperature increase from 40 ℃ to 60 ℃, while in Figure 5-12 (the 15 vol.% CO_2 feed), it is least affected by the increase from 60 ℃ to 70 ℃. The effect of the temperature on the desorption quantity is correlated to the effect of temperature on the adsorption quantity, and this is an expected result: as the adsorption quantity increases, the desorption quantity should also increase, and if the adsorption quantity decreases, the desorption quantity also decreases.

Table 5-5: Total quantity desorbed for CQ650, CQ30P and CQ006 at 5 and 15 vol.% CO_2 feed concentrations

	Temperature				
	30 ℃	**40 ℃**	**50 ℃**	**60 ℃**	**70 ℃**
Sorbent	**Total quantity desorbed (mmol/g) @ 5 vol.% CO_2 feed**				
CQ650	0.92	0.78	0.67	0.56	0.46
CQ30P	0.77	0.66	0.65	0.60	0.52
CQ006	0.83	0.69	0.67	0.57	0.51
	Temperature				
	30 ℃	**40 ℃**	**50 ℃**	**60 ℃**	**70 ℃**
Sorbent	**Total quantity desorbed (mmol/g) @ 15 vol.% CO_2 feed**				
CQ650	1.62	1.43	1.14	0.88	0.71
CQ30P	1.00	0.80	0.61	0.47	0.41
CQ006	1.04	0.91	0.65	0.54	0.45

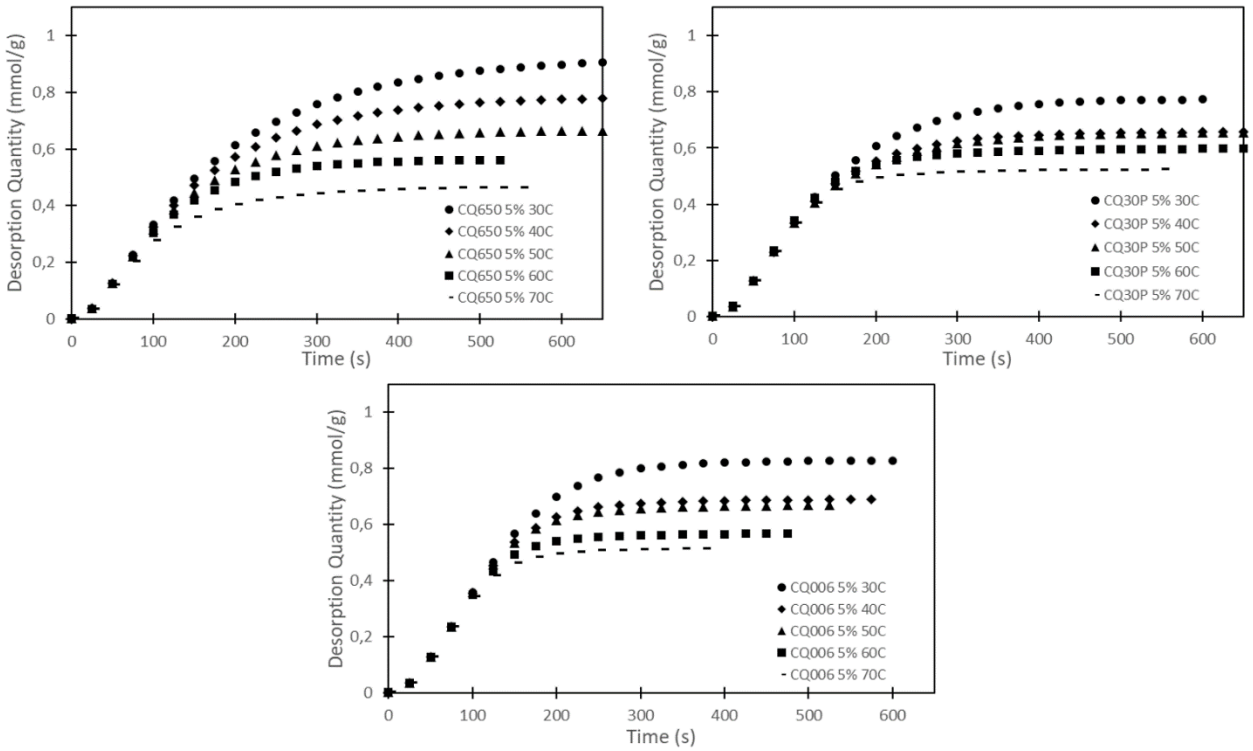

Figure 5-11: Effect of temperature on the quantity desorbed for CQ650, CQ30P and CQ006 at 5 vol.% CO_2 and 30, 40, 50, 60 and 70 ℃

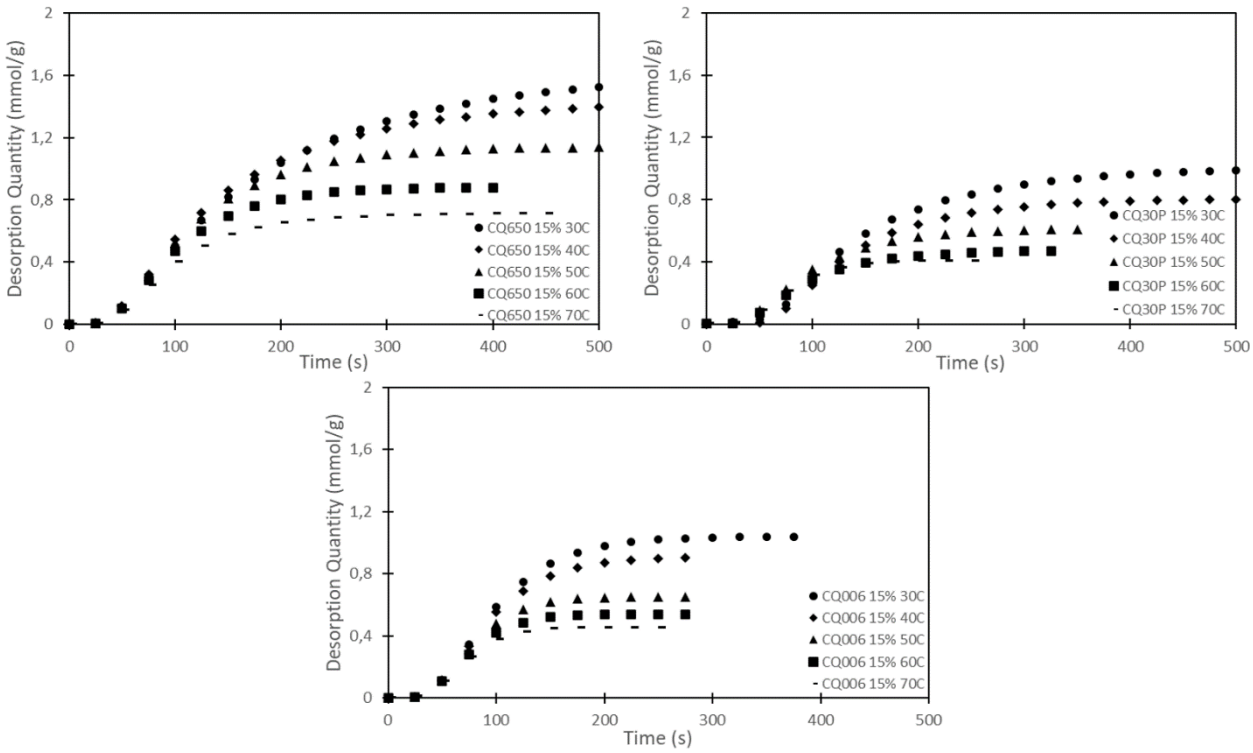

Figure 5-12: Effect of temperature on the quantity desorbed for CQ650, CQ30P and CQ006 at 15 vol.% CO_2 and 30, 40, 50, 60 and 70 ℃

5.5 Desorption efficiency

Looking at the individual cycle's desorption efficiency of the sorbents from the 5 vol.% CO_2 feed in Figure 5-13, CQ006 has the highest desorption efficiency, followed by CQ650 and CQ30P. CQ006 consistently reached 100% desorption efficiency for the temperatures tested, with the lowest desorption efficiency at 93.2%, an average desorption efficiency of 98.2%, and a standard deviation of 1.3% across the temperatures. Secondly, CQ650 has an average desorption efficiency of 96.5%, with the lowest desorption efficiency reaching 88.8%. It also has a few maximum desorption efficiencies of 100% but less than CQ006. Furthermore, CQ650 has an average standard deviation of 2.8% across the temperature range. CQ30P was the worst-performing sorbent, with an average desorption efficiency of 93.4% and did not reach 100% desorption efficiency once while having a low desorption efficiency of 88.2%. CQ30P does have a slightly lower average standard deviation than CQ650 at 2.0%. The average desorption efficiencies are presented in Table 5-6.

The cycle desorption efficiencies of the 15 vol.% CO_2 feed concentration in Figure 5-14 show a similar result as the 5 vol.% CO_2 feed concentration, where CQ006 is the best-performing sorbent, followed by CQ650 and CQ30P, respectively. CQ006 has an average desorption efficiency of 99.1%, a maximum of 100%, a low of 96.6% and an average standard deviation of 0.7%. CQ650

follows with an average desorption efficiency of 95.1%, a lower number of 100% desorption efficiencies than CQ006, a low desorption efficiency of 83.1% and an average standard deviation of 2.9%. Again, CQ30P is the worst-performing sorbent with an average desorption efficiency of 92.0%, a low of 86% and no 100% maximum desorption efficiencies. Generally, there is no real difference between the sorbent's desorption efficiencies when they are compared to each other between the 5 and 15 vol.% CO_2 feed concentrations, and they rank the same for both concentrations. A desorption efficiency of 100% was not achieved in all of the experiments, as every experiment is subject to experimental uncertainty. This less than 100% desorption efficiency also occurred in experiments done by (Raganati et al., 2015; Raganati et al., 2020).

When considering industrial applications concerning the desorption efficiency of the sorbents, it would be wise to avoid the conditions that had a significant effect on desorption. A low desorption efficiency would waste resources in terms of energy as less CO_2 would be adsorbed on the subsequent cycle, impacting the efficiency of the adsorption cycles and the overall efficiency of the process.

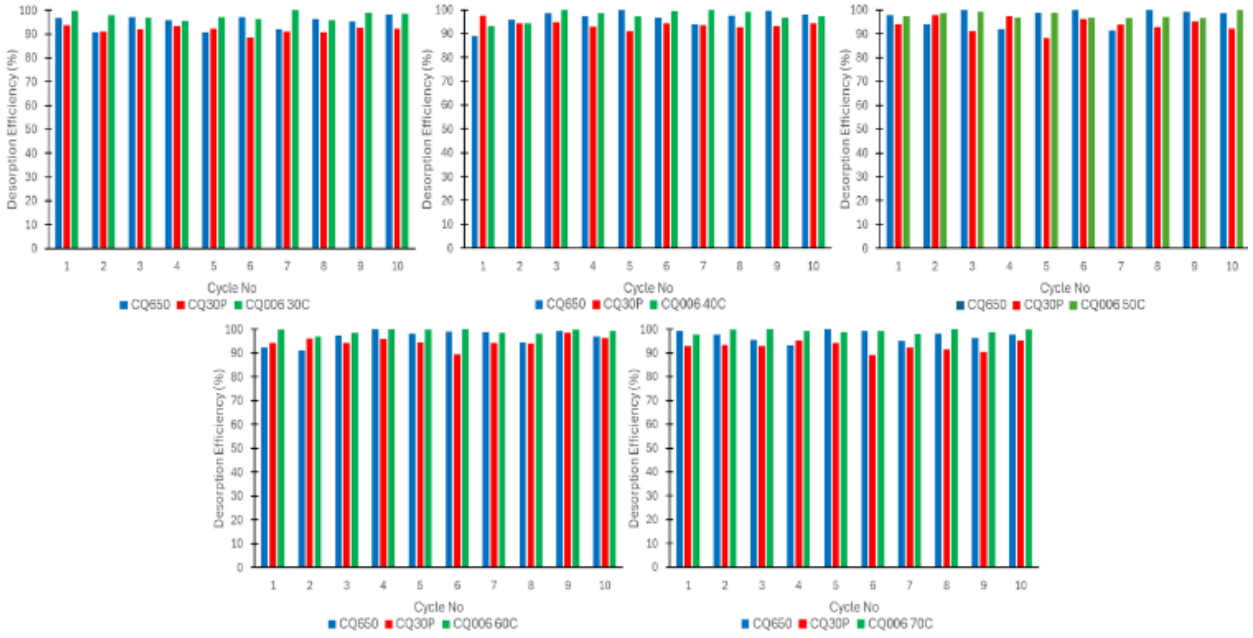

Figure 5-13: Desorption efficiency per cycle of CQ650, CQ30P and CQ006 at 5% CO_2 feed concentration and 30, 40, 50, 60 and 70 ℃

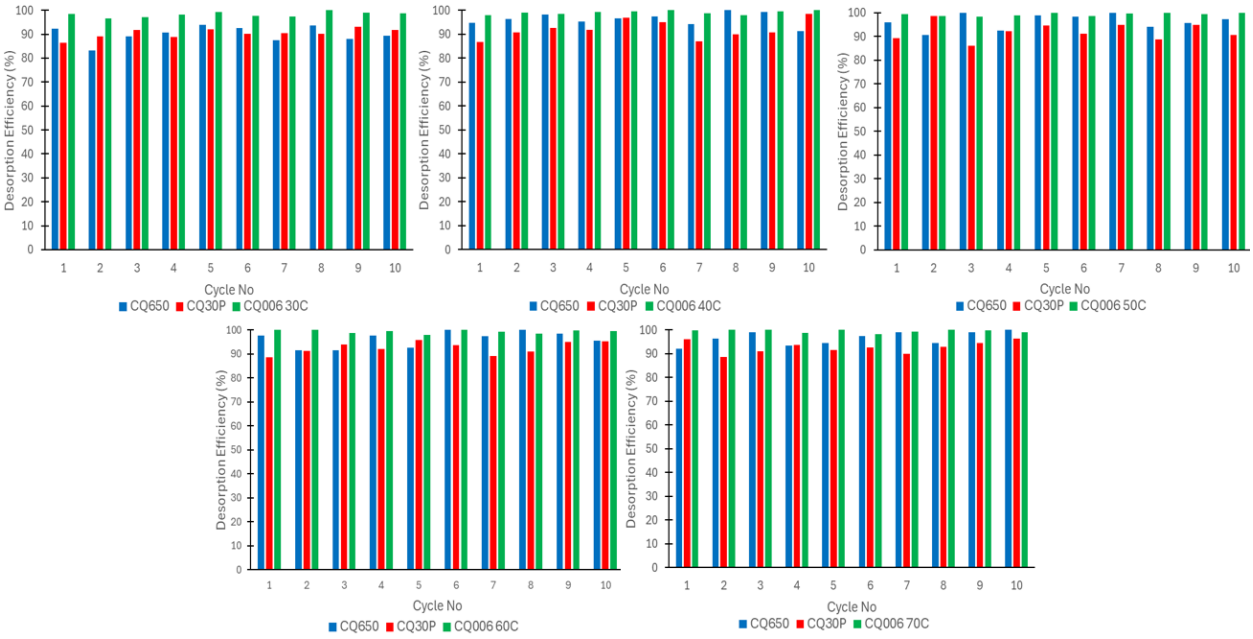

Figure 5-14: Desorption efficiency per cycle of CQ650, CQ30P and CQ006 at 15% CO_2 feed concentration and 30, 40, 50, 60 and 70 ℃

Table 5-6: Overall desorption efficiencies for CQ650, CQ30P and CQ006 at 5 and 15 vol.% CO_2 feed concentrations

	Temperature					
	30 ℃	**40 ℃**	**50 ℃**	**60 ℃**	**70 ℃**	**Average**
Sorbent	**Desorption efficiency (%) @ 5 vol.% CO_2 feed**					
CQ650	95.0±0.05	96.6±0.07	97.1±0.07	96.7±0.06	97.2±0.03	96.5±0.06
CQ30P	91.7±0.02	93.9±0.02	93.8±0.06	94.8±0.04	92.7±0.03	93.4±0.03
CQ006	97.7±0.02	97.6±0.03	97.7±0.01	99.0±0.006	99.1±0.004	98.3±0.01
	Temperature					
	30 ℃	**40 ℃**	**50 ℃**	**60 ℃**	**70 ℃**	**Average**
Sorbent	**Desorption efficiency (%) @ 15 vol.% CO_2 feed**					
CQ650	90.0±0.07	96.3±0.04	96.4±0.06	96.3±0.07	96.6±0.05	95.1±0.06
CQ30P	90.4±0.03	92.0±0.10	92.1±0.09	92.6±0.04	92.7±0.04	92.0±0.06
CQ006	98.2±0.007	99.0±0.003	99.3±0.002	99.4±0.003	99.5±0.003	99.1±0.003

5.6 Comparison with literature

The experimental results determined in this study for the activated carbon samples are compared with similar adsorption and desorption experimental results reported in the literature in Table 5-7. The adsorption quantities for the GAC and OXA-GAC activated carbon samples reported by (Shafeeyan *et al.*, 2015) at 1 bar pressure and a CO_2 feed concentration of 15 vol.% are comparable to the maximum quantities reported in this study; however, the saturation times are significantly longer. At 45 ℃, the saturation quantities reported for GAC and OXA-GAC are 0.19 and 0.51 mmol/g, respectively, while the saturated quantity of CQ650 at 40 ℃ and the same feed conditions, is 0.71 mmol/g, which beats both GAC and OXA-GAC while taking less time. CQ30P and CQ006 are close in comparison and exhibited shorter saturation times.

Plaza et al. (2010) experimented on commercial activated carbon at 30 and 40 ℃ and 14 vol.% CO_2 feed rate, and they found adsorption quantities of 0.56 and 0.46 mmol/g, respectively; this result compares well with the three activated carbons tested in this study with all three activated carbon samples having a higher saturated adsorption capacity. Only CQ006 performed marginally less at 40 ℃ with a saturated quantity of 0.33 mmol/g.

Desorption results reported by Raganati et al. (2015, 2020) for activated carbon samples Norit and DARCOFGD are in the range of 0.18 – 0.43 mmol/g with temperatures at 40 – 70 ℃ and a CO_2 feed of 5 and 10 vol.%. Norit at 40 ℃ and 5 vol.% CO_2 feed has a desorption quantity of 0.43

mmol/g, and it matches CQ650 at the same conditions with a quantity of 0.39 mmol/g. CQ30P and CQ006 are not up to par with quantities of 0.33 and 0.35 mmol/g, respectively. Again, all the samples of this study have significantly less desorption times. For the DARCOFGD sample at 50 ℃ and 10 vol.% CO_2 feed, a desorption quantity is reported as 0.31 mmol/g with a completion time of 480 seconds. This study did not investigate a 10% CO_2 feed, but the DARCOFGD results are lower than CQ650 at 5 vol.% CO_2 feed with a reported result of 0.33 mmol/g. This indicates that CQ650 is an excellent sorbent at the low to medium temperatures studied in this report. Raganati et al. (2015, 2020) also reported desorption efficiency results of 90% for the two activated carbons at 5 and 10 vol.% CO_2 feed concentrations and a temperature range of 40 – 70 ℃, and this is in line with CQ30P from this study at the same temperatures for 5 and 15 vol.% CO_2 feed concentrations which are 92.0% and 93.4%, respectively. However, the Norit and DARCOFGD results are lower than CQ650 and CQ 006, which have a desorption efficiency of 96.5% and 98.1% at the 5 vol.% CO_2 feed concentration, respectively, and 95.1% and 99.1% at the 15 vol.% CO_2 feed concentration, respectively.

Table 5-7: Comparison of adsorption and desorption results with literature

Sample name	Pressure, *bar*	Temperature Range, ℃	Inlet CO_2 concentration, *Vol.%*	Flow rate, *L/min*	Quantity adsorbed, *mmol/g*	Quantity desorbed, *mmol/g*	Adsorption saturation time *(s)*	Desorption saturation time *(s)*	Reference
CQ650	1.0	30–70	5	0.5	0.23–0.48	0.23–0.46	625-750	650-850	This study
CQ30P	1.0	30–70	5	0.5	0.28–0.42	0.23–0.39	650-825	650-800	
CQ006	1.0	30–70	5	0.5	0.26–0.41	0.26–0.41	425-750	500-725	
CQ650	1.0	30–70	15	0.5	0.36–0.83	0.36–0.81	350-700	475-875	
CQ30P	1.0	30–70	15	0.5	0.20–0.52	0.30–0.50	400-625	375-500	
CQ006	1.0	30–70	15	0.5	0.23–0.52	0.23–0.52	275-400	500-725	
GAC	1.0	30–60	15	0.1	0.64–1.12	Complete desorption	750-1200	–	Shafeeyan, 2015
OXA-GAC	1.0	30–60	15	0.1	1.12–1.71	Complete desorption	700-1200	–	
WIRAC	1.0	20–80	14.5	0.175	0.76–0.81	Complete desorption	540-900	–	Wei and Zhao, 2021
AC-3-700	1.0	30–100	12.5	0.08	0.53–1.44	Complete desorption	2100	–	Kaur et al., 2020
AC	1.0	25–90	10	0.25	0.82–2.61	–	–	–	Dziejarski & Kisiela-Czajka, 2021
Norit	1.0	40–70	5	1.13	0.20–0.43	0.18–0.43	1200+	900–1200	Raganati et al., 2020
DARCOFGD	1.0	50	10	1.13	–	0.31	–	480	Raganati et al., 2015
AC	1.0	30–40	14	0.1	0.46–0.56	–	1080	–	Plaza et al., 2010
Coconut shell AC	1.0	35	13	0.1	0.25	–	–	–	Naksusuk & Tangsathitkulchai, 2019

Chapter 6

CHAPTER 6: RESULTS AND DISCUSSION: KINETIC MODELLING

In this section, three kinetic models are tested on CQ650, CQ30P, and CQ006 to find the most accurate model and to fit it to the experimental data. A thermodynamic analysis is done from the kinetic model results to determine the change in enthalpy, entropy and Gibbs free energy and the activation energy for adsorption and desorption.

6.1 Kinetic modelling

The kinetic modelling of the experimental data was done using Matlab's Nelder Mead regression. The results of the Pseudo-first-order, Pseudo-second-order and Avrami kinetic models are presented in this section.

6.1.1 Selecting the most accurate model for adsorption and desorption

To select the most accurate kinetic model for the adsorption and desorption experimental data at 5 and 15 vol.% CO_2 feed concentrations and the temperatures of 30, 40, 50, 60 and 70 ℃, the following parameters are looked at: QOF%, R^2 value, MAE and the RMSE. The results presented in Figure 6-1 exemplify the fitting observed for the sorbents at 40 ℃ and 5 vol.% CO_2 feed concentration. Similar plots at the other temperatures and concentrations are presented in Appendix B.

There are definitive shortcomings in the PFO and PSO's ability to predict CO_2 adsorption onto porous activated carbon, with reports from several investigators indicating that the models overestimate the CO_2 uptake in the early stages of adsorption and underestimate the uptake in the later stages of adsorption (Ammendola et al., 2017; Raganati et al., 2018; Fatima et al., 2023).

The R^2 value for all three kinetic models is high, meaning that the models can predict the adsorption and desorption behaviour, with the PFO having an R^2 average value of 0.991 and a lowest value of 0.981. PSO is the least-fitting model according to the QOF% and $R^{2,}$ with an average value of 0.957 and a lowest value of 0.921. The three models can predict the adsorption and desorption behaviour; the most accurate is thus the Avrami model, not only for the results displayed in Figure 6-1 but also for all the temperatures and feed concentrations used in this study. Visually, it can be seen that Avrami is the most accurate of the three models, and this is supported by data from the performance metrices (MAE, RMSE, R^2, and QOF%) given in Table 6-1.

The Avrami kinetic model consistently exhibited QOF% of ≥ 98.2% (98.2 – 99.8%), while the PFO and PSO varied more substantially. PFO is the second most accurate model with a QOF% in the

91.0 – 99.1% range but significantly less consistent than the Avrami kinetic model. Thus, while the PFO, in some cases, can be as accurate as the Avrami, it is not as consistent and, therefore, can not accurately predict the behaviour of adsorption kinetics across a broad range of temperatures, activated carbon samples and feed concentrations of CO_2. Lastly, the PSO model is the most inconsistent and has the lowest overall QOF%, which is more in the range of 80 – 89% QOF%.

The PFO performs has poorer performance at low temperatures and 5 vol.% CO_2 feed than at higher temperatures, with the MAE and RMSE decreasing from 0.379 and 0.609 to 0.0447 and 0.209, respectively, indicating a significant increase in accuracy. In contrast to the 15 vol.% CO_2 feed, the accuracy remains relatively constant throughout the temperature range. A similar trend can be seen for the PSO model at 5 vol.% and 15 vol.% CO_2 feed, showing better fit for both concentrations at all temperatures.

In the Avrami model, however, the opposite is true at 5 vol.% CO_2 feed the accuracy decreases from lower to higher temperatures. The QOF% is still very high, but the absolute error increased by a factor of 10 from the lowest to the highest temperature. Although this increase may seem significant, the error at the low temperatures is very small and remains very small at the highest temperature even though it increased. Looking at the 15 vol.% CO_2 feed MAE and RMSE, the exact opposite is true, with the absolute error decreasing by a factor of up to 10 from the lowest to the highest temperature.

The desorption results in Figure 6-2 are similar to the adsorption data presented in Figure 6-1, with the Avrami rate model showing the best fit among the three tested models. However, the trend of the increase or decrease in the accuracy of the Avrami model as the temperatures varies across the 5 and 15 vol.% CO_2 feed concentrations, are not present in the desorption results. The Avrami kinetic model has a more stable MAE and RMSE across the experimented conditions, as indicated in Table 6-2.

Similar trends can be seen from all of the samples and experimental conditions tested, and the performance metrices used in this study indicate that Avrami is the most accurate and consistent of the models tested. The rest of the results are presented in Table 6-3 –Table 6-6.

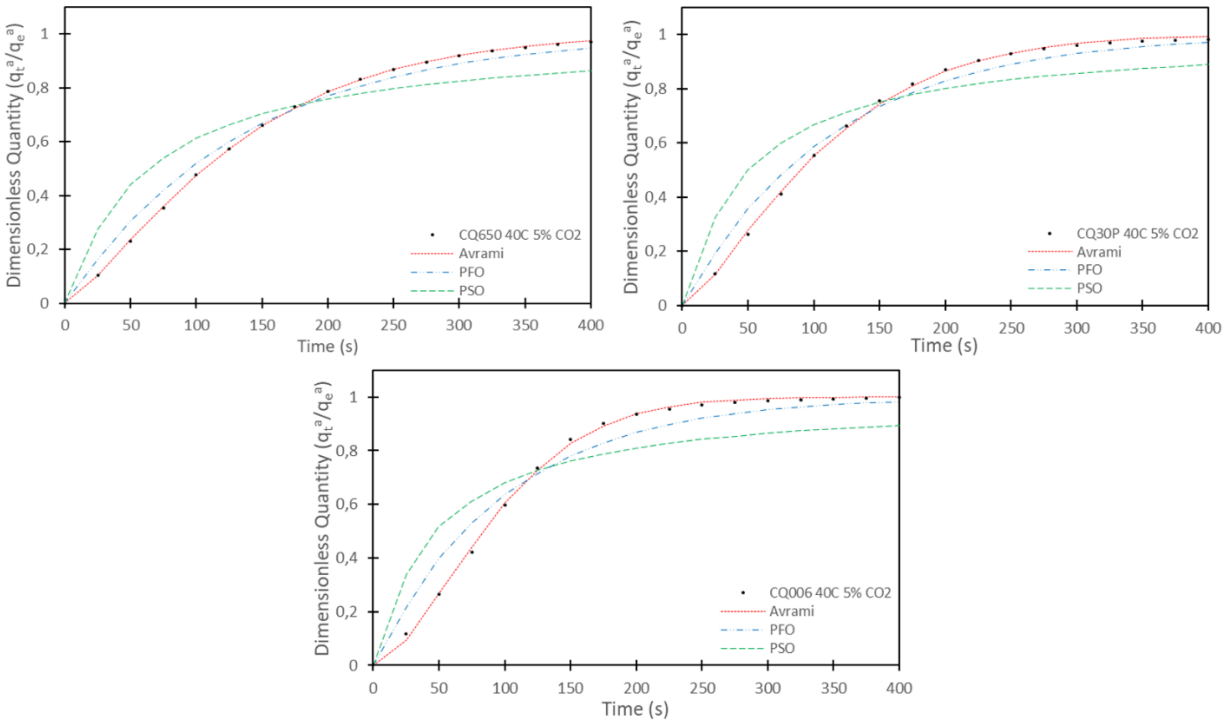

Figure 6-1: CQ650, CQ30P and CQ006 with the PFO, PSO and Avrami rate models fitted to the adsorption experimental rate data at 40℃ and 5 vol.% CO_2 feed concentration

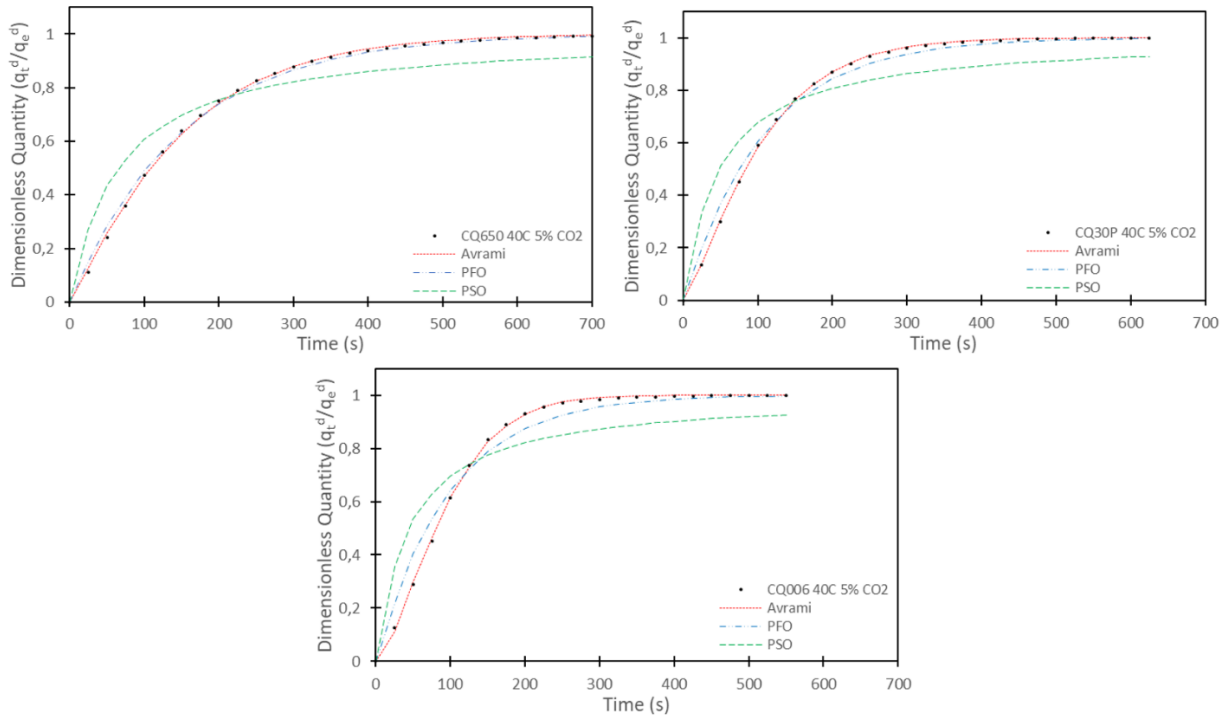

Figure 6-2: CQ650, CQ30P and CQ006 with the PFO, PSO and Avrami rate models fitted to the desorption experimental rate data at 40 ℃ and 5 vol.% CO_2 feed concentration

Table 6-1: PFO, PSO and Avrami rate model parameters fitted to the experimental adsorption results with accuracy indicators for CQ650

		5 vol.% CO_2					15 vol.% CO_2				
Model	**Parameter**	**30 ℃**	**40 ℃**	**50 ℃**	**60 ℃**	**70 ℃**	**30 ℃**	**40 ℃**	**50 ℃**	**60 ℃**	**70 ℃**
PFO	k_1, *1/s (x10^{-2})*	0.638	0.759	0.858	1.01	1.02	0.728	0.96	1.17	1.42	1.56
	MAE	0.384	0.386	0.293	0.280	0.0613	0.357	0.407	0.452	0.424	0.344
	RMSE	0.613	0.613	0.537	0.524	0.246	0.597	0.637	0.672	0.650	0.586
	R^2	0.996	0.995	0.995	0.994	0.998	0.996	0.993	0.991	0.991	0.990
	QOF%	96.3	96.1	97.1	97.2	99.1	92.6	91.0	92.1	91.9	93.8
PSO	k_2, *mmol/g.s (x10^{-2})*	1.36	1.60	1.87	2.18	2.32	1.52	1.98	2.53	2.96	3.22
	MAE	4.23	3.67	3.33	2.89	2.26	3.61	3.04	3.05	2.45	2.10
	RMSE	2.06	1.91	1.83	1.70	1.50	1.90	1.74	1.75	1.56	1.45
	R^2	0.957	0.953	0.955	0.952	0.966	0.950	0.949	0.946	0.953	0.940
	QOF%	89.7	89.5	91.7	91.9	96.3	83.0	80.7	83.8	83.1	86.1
Avrami	k_A, *1/s (x10^{-2})*	0.613	0.727	0.824	0.965	1.00	0.700	0.918	1.12	1.35	1.48
	n	1.26	1.29	1.26	1.28	1.11	1.26	1.34	1.42	1.46	1.427
	MAE *(x10^{-2})*	0.577	0.635	0.914	0.887	1.80	1.46	1.52	2.53	1.20	0.787
	RMSE	0.0713	0.0769	0.0923	0.0937	0.133	0.120	0.122	1.42	0.106	0.0885
	R^2	0.999	0.999	0.999	0.999	0.999	0.999	0.999	0.999	0.999	0.999
	QOF%	99.01	98.6	99.0	98.8	99.8	99.1	99.5	99.7	98.9	98.2

Table 6-2: PFO, PSO and Avrami rate model parameters fitted to the experimental desorption results with accuracy indicators for CQ650

		5 vol.% CO_2					15 vol.% CO_2				
Model	**Parameter**	**30 ℃**	**40 ℃**	**50 ℃**	**60 ℃**	**70 ℃**	**30 ℃**	**40 ℃**	**50 ℃**	**60 ℃**	**70 ℃**
PFO	k_1, *1/s (x10^{-2})*	0.604	0.677	0.800	0.976	1.05	0.621	0.776	1.02	1.21	1.28
	MAE	0.103	0.0828	0.103	0.125	0.0431	0.182	0.136	0.295	0.257	0.218
	RMSE	0.319	0.287	0.319	0.352	0.207	0.367	0.368	0.538	0.507	0.466
	R^2	0.999	0.999	0.998	0.997	0.998	0.998	0.998	0.996	0.994	0.996
	QOF%	98.4	98.7	98.6	98.4	99.3	95.5	96.2	94.1	95.0	95.8
PSO	k_2, *mmol/g.s (x10^{-2})*	1.35	1.55	1.81	2.18	2.40	1.37	1.74	2.21	2.62	2.79
	MAE	3.73	3.50	2.97	2.61	2.08	3.66	3.15	2.98	2.51	2.35
	RMSE	1.93	1.87	1.72	1.62	1.44	1.90	1.77	1.72	1.58	1.53
	R^2	0.969	0.969	0.967	0.962	0.969	0.965	0.961	0.963	0.949	0.960
	QOF%	93.9	95.5	95.2	94.5	96.8	88.7	90.3	86.6	88.2	90.0
Avrami	k_A, *1/s (x10^{-2})*	0.591	0.665	0.783	0.948	1.03	0.609	0.759	0.976	1.16	1.23
	n	1.11	1.10	1.12	1.169	1.07	1.14	1.14	1.28	1.30	1.28
	MAE *(x10^{-2})*	9.91	1.67	2.35	0.995	2.20	4.31	3.73	1.66	0.729	1.15
	RMSE	0.0984	0.128	0.138	0.0979	0.147	0.177	0.192	0.120	0.0840	0.106
	R^2	0.999	0.999	0.999	0.999	0.999	0.999	0.999	0.999	0.999	0.999
	QOF%	99.8	99.8	99.6	99.5	99.8	98.7	98.3	99.3	99.7	99.8

Table 6-3: PFO, PSO and Avrami rate model parameters fitted to the experimental adsorption results with accuracy indicators for CQ30P

		5 vol.% CO_2					15 vol.% CO_2				
Model	**Parameter**	**30 ℃**	**40 ℃**	**50 ℃**	**60 ℃**	**70 ℃**	**30 ℃**	**40 ℃**	**50 ℃**	**60 ℃**	**70 ℃**
PFO	k_1, *1/s (x10^{-2})*	5.67	0.888	0.974	1.03	1.14	0.981	1.24	1.36	1.32	2.25
	MAE	0.494	0.372	0.424	0.519	0.425	0.193	0.260	0.210	0.584	0.254
	RMSE	0.672	0.609	0.632	0.717	0.650	0.435	0.508	0.457	0.634	0.438
	R^2	0.992	0.993	0.994	0.991	0.993	0.997	0.995	0.995	0.988	0.994
	QOF%	95.3	96.9	95.9	96.2	96.6	95.3	95.5	96.6	94.8	97.5
PSO	k_2, *mmol/g.s (x10^{-2})*	6.45	2.00	2.11	2.30	2.57	2.09	2.59	2.90	2.71	4.91
	MAE	1.94	2.07	1.68	1.82	1.73	1.48	1.07	1.06	0.931	0.724
	RMSE	1.37	1.44	1.29	1.35	1.32	1.21	1.03	1.03	0.964	0.844
	R^2	0.944	0.950	0.957	0.950	0.960	0.957	0.956	0.958	0.941	0.971
	QOF%	88.6	92.8	90.3	91.9	93.1	88.1	88.5	90.8	88.2	93.4
Avrami	k_A, *1/s (x10^{-2})*	0.704	0.852	0.928	0.978	1.09	0.947	1.18	1.30	1.35	2.16
	n	1.35	1.31	1.36	1.42	1.39	1.23	1.31	1.29	1.31	1.30
	MAE *(x10^{-2})*	0.525	2.05	1.25	5.41	5.64	1.22	0.373	0.587	1.58	2.07
	RMSE	0.0715	0.142	0.110	0.215	0.0235	0.109	0.0607	0.0755	0.108	0.138
	R^2	0.999	0.999	0.999	0.999	0.999	0.999	0.999	0.999	0.999	0.999
	QOF%	99.0	99.5	98.6	99.2	99.5	99.4	98.7	98.8	98.6	98.4

Table 6-4: PFO, PSO and Avrami rate model parameters fitted to the experimental desorption results with accuracy indicators for CQ30P

		5 vol.% CO_2					15 vol.% CO_2				
Model	**Parameter**	**30 ℃**	**40 ℃**	**50 ℃**	**60 ℃**	**70 ℃**	**30 ℃**	**40 ℃**	**50 ℃**	**60 ℃**	**70 ℃**
PFO	k_1, *1/s (x10^{-2})*	0.800	0.930	0.984	1.08	1.27	0.949	1.08	1.35	1.38	1.96
	MAE	0.277	0.212	0.275	0.290	0.367	0.0677	0.120	0.148	0.0788	0.205
	RMSE	0.526	0.460	0.504	0.523	0.605	0.254	0.345	0.384	0.279	0.451
	R^2	0.996	0.997	0.996	0.994	0.994	0.999	0.997	0.996	0.998	0.991
	QOF%	96.8	97.8	97.2	97.4	97.1	97.5	96.9	97.0	98.3	97.3
PSO	k_2, *mmol/g.s (x10^{-2})*	1.71	2.11	2.20	2.48	2.88	2.07	2.36	2.85	3.02	4.29
	MAE	1.74	1.96	1.80	1.87	1.54	1.61	1.40	1.00	1.12	0.815
	RMSE	1.32	1.40	1.34	1.37	1.24	1.27	1.18	1.00	1.06	0.902
	R^2	0.951	0.963	0.958	0.960	0.961	0.963	0.956	0.951	0.964	0.939
	QOF%	90.4	93.8	92.7	94.4	93.6	91.9	91.1	90.8	88.2	92.5
Avrami	k_A, *1/s (x10^{-2})*	0.770	0.897	0.944	1.04	1.21	0.928	1.05	1.30	1.34	1.86
	n	1.25	1.23	1.27	1.30	1.38	1.12	1.18	1.23	1.16	1.35
	MAE *(x10^{-2})*	0.462	1.02	1.41	5.18	2.73	1.36	0.983	0.405	0.732	1.29
	RMSE	0.0680	0.142	0.118	0.204	0.164	0.116	0.0986	0.0636	0.0846	0.102
	R^2	0.999	0.999	0.999	0.999	0.999	0.999	0.999	0.999	0.999	0.999
	QOF%	99.0	99.6	99.4	99.5	99.1	99.5	99.8	99.1	99.5	98.3

Table 6-5: PFO, PSO and Avrami rate model parameters fitted to the experimental adsorption results with accuracy indicators for CQ006

		5 vol.% CO_2					15 vol.% CO_2				
Model	**Parameter**	**30 ℃**	**40 ℃**	**50 ℃**	**60 ℃**	**70 ℃**	**30 ℃**	**40 ℃**	**50 ℃**	**60 ℃**	**70 ℃**
PFO	k_1, *1/s (x10^{-2})*	0.872	1.03	1.13	1.20	1.36	1.62	1.68	1.90	2.27	2.66
	MAE	0.981	0.857	0.773	0.710	0.522	0.458	0.512	0.169	0.170	0.151
	RMSE	0.990	0.926	0.879	0.842	0.708	0.670	0.712	0.388	0.410	0.384
	R^2	0.984	0.981	0.982	0.984	0.986	0.987	0.985	0.994	0.993	0.991
	QOF%	92.7	93.2	92.8	93.8	95.2	90.4	89.5	95.0	95.7	96.8
PSO	k_2, *mmol/g.s (x10^{-2})*	1.86	2.18	2.33	2.53	2.93	3.44	3.53	4.14	4.92	5.79
	MAE	1.73	1.42	1.16	1.21	1.13	0.945	0.873	0.844	0.719	0.604
	RMSE	1.32	1.19	1.08	1.10	1.06	0.0971	0.933	0.907	0.847	0.775
	R^2	0.932	0.921	0.932	0.934	0.933	0.944	0.939	0.967	0.955	0.962
	QOF%	84.8	85.7	85.0	86.8	89.3	81.6	80.1	89.6	90.6	92.1
Avrami	k_A, *1/s (x10^{-2})*	0.825	0.967	1.06	1.13	1.30	1.55	1.60	1.84	2.18	2.54
	n	1.57	1.58	1.58	1.57	1.49	1.52	1.58	1.32	1.34	1.35
	MAE *(x10^{-2})*	2.60	2.70	2.44	2.93	2.64	4.12	3.66	4.82	2.24	1.19
	RMSE	0.161	0.164	0.156	0.171	0.162	0.202	0.188	0.212	0.147	0.108
	R^2	0.999	0.999	0.999	0.999	0.999	0.999	0.999	0.999	0.999	0.999
	QOF%	97.7	97.4	96.9	97.3	97.9	99.5	99.2	99.3	99.5	98.8

Table 6-6: PFO, PSO and Avrami rate model parameters fitted to the experimental desorption results with accuracy indicators for CQ006

		5 vol.% CO_2					15 vol.% CO_2				
Model	**Parameter**	**30 ℃**	**40 ℃**	**50 ℃**	**60 ℃**	**70 ℃**	**30 ℃**	**40 ℃**	**50 ℃**	**60 ℃**	**70 ℃**
PFO	k_1, *1/s (x10^{-2})*	0.857	1.04	1.05	1.21	1.33	6.29	1.43	1.77	1.97	2.15
	MAE	0.749	0.613	0.684	0.675	0.615	0.343	0.391	0.333	0.273	0.280
	RMSE	0.864	0.783	0.827	0.807	0.767	0.561	0.624	0.575	0.516	0.529
	R^2	0.990	0.988	0.986	0.989	0.988	0.993	0.991	0.989	0.994	0.991
	QOF%	94.3	95.4	94.7	93.1	92.8	93.6	92.5	93.8	94.6	95.3
PSO	k_2, *mmol/g.s (x10^{-2})*	1.85	2.29	2.30	2.64	2.88	7.85	3.06	3.78	4.12	4.69
	MAE	1.83	1.65	1.61	1.40	1.23	1.10	1.06	0.837	0.692	0.769
	RMSE	1.35	1.28	1.27	1.18	1.11	1.04	1.03	0.914	0.827	0.874
	R^2	0.946	0.935	0.932	0.948	0.944	0.957	0.948	0.937	0.964	0.962
	QOF%	87.4	89.8	88.5	86.2	89.3	86.5	84.2	86.5	87.5	89.7
Avrami	k_A, *1/s (x10^{-2})*	0.809	0.979	0.990	1.14	1.25	1.36	1.36	1.67	1.86	2.03
	n	1.47	1.47	1.51	1.54	1.54	1.42	1.43	1.44	1.42	1.45
	MAE *(x10^{-2})*	1.02	1.49	1.76	2.22	2.11	0.713	0.482	0.358	0.505	0.108
	RMSE	0.0995	0.122	0.132	0.148	0.145	0.0822	0.0685	0.0589	0.0707	0.179
	R^2	0.999	0.999	0.999	0.999	0.999	0.999	0.999	0.999	0.999	0.999
	QOF%	98.2	98.3	98.3	98.2	98.1	99.6	99.4	98.6	97.9	98.4

6.1.2 Kinetic rate modelling

The experimental adsorption and desorption rate data from the fixed bed reactor on CQ650, CQ30P and CQ006 at 5 vol.% and 15 vol.% with temperatures at 30, 40, 50, 60 and 70 ℃ are modelled with the Avrami kinetic rate model and discussed in this section. The reported data is a normalised dimensionless quantity (qt/qe) as a function of time (s) in Figure 6-3 and Figure 6-4 with the Avrami parameters and the MAE RMSE and QOF% presented in Table 6-7.

The Avrami rate constant (k_A) results indicate that the rate of adsorption increases with increasing temperatures, which is attributed to the higher kinetic energy that the CO_2 possesses at higher temperatures and that lets the CO_2 molecules migrate faster into the pores of the sorbents (Raganati et al., 2020). In terms of the model fitting, an average QOF% at 5 vol.% CO_2 feed and all temperatures for CQ650, CQ30P, and CQ006 are 99.0, 99.2 and 97.3, respectively, while the QOF% for the 15 vol.% CO_2 feed are 99.1, 98.8 and 99.3, respectively. Looking at the MAE, RMSE and R^2 metrics, Avrami is a better-fitting model having an MAE value that is 2 orders of magnitude smaller than PFO and PSO. Further, the RMSE of Avrami is 10 times less than that of the other 2 models. The Avrami kinetic model is, according to all the metrics, an adequate predictor for adsorption rate behaviour for the studied sorbents at the various reaction temperatures used in this investigation.

With the increase in kinetic energy, a significant decrease in the adsorption quantity was observed, as expected, as discussed in Section 5.4. The decreased desorption quantity can also be attributed to the exothermic nature of the adsorption process, and as a result, the maximum and minimum quantities are achieved at 30 and 70 ℃, respectively (Raganati et al., 2020).

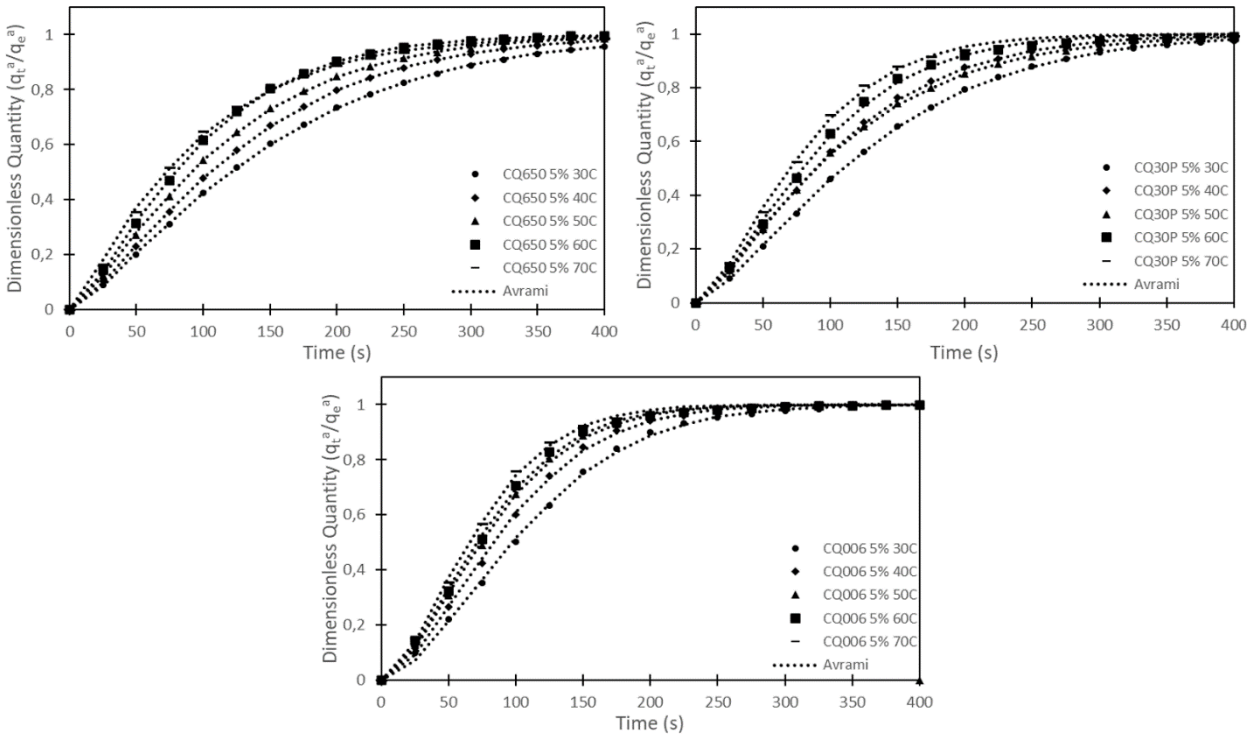

Figure 6-3: CQ650, CQ30P and CQ006 at fixed inlet concentration of 5 vol.% CO_2 at 30, 40, 50, 60 and 70 ℃ adsorption Avrami model fit

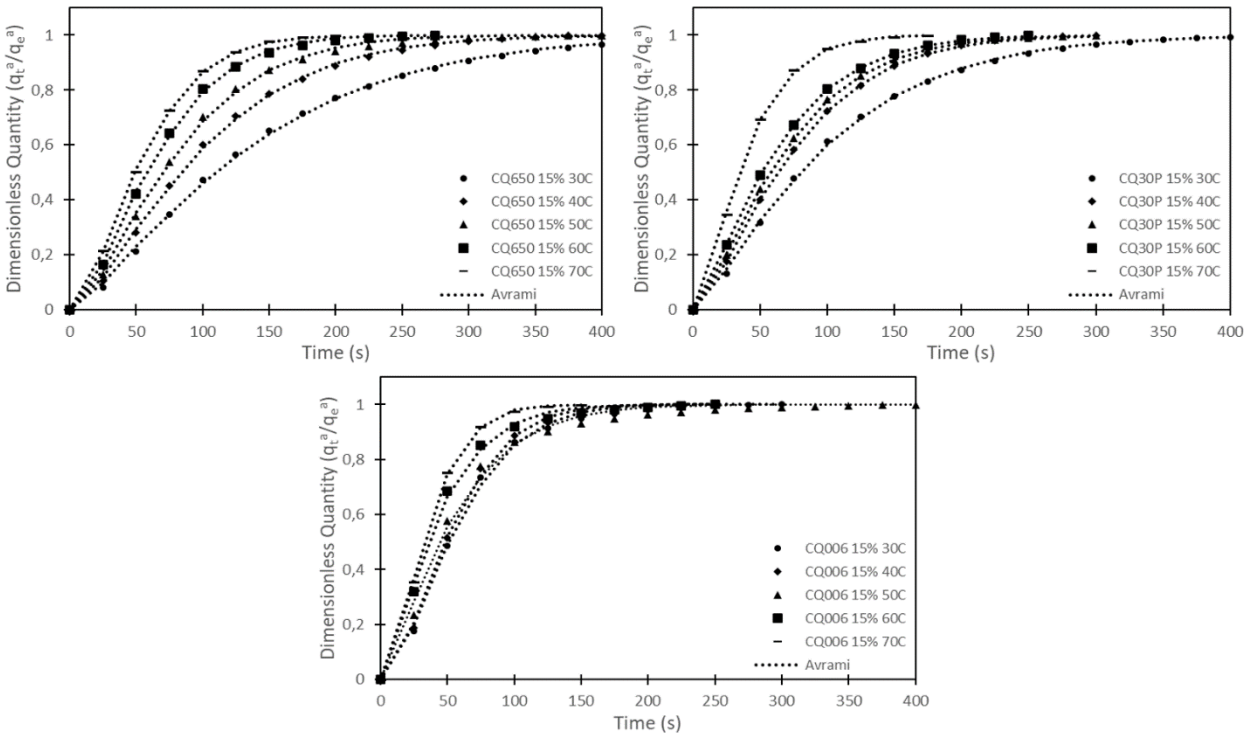

Figure 6-4: CQ650, CQ30P and CQ006 at fixed inlet concentration of 15 vol.% CO_2 at 30, 40, 50, 60 and 70 ℃ adsorption Avrami model fit

Figure 6-5 and Figure 6-6 show the desorption results for CQ650, CQ30P, and CQ006, which are very similar to the adsorption results. Also, Table 6-8 contains the Avrami rate model parameters with their respective performance indicators. In general, the desorption of CO_2 takes slightly longer than the adsorption, indicated by the smaller value of k_A when compared to similar conditions with adsorption. Then, a similar trend to adsorption appears where the slowest desorption rate occurs at 30 ℃ and the highest at 70 ℃. There is also the same decrease in the quantities desorbed with increased temperatures. Furthermore, Avrami model adequately predicts desorption rate behaviour as well, with the average for the 5 vol.% CO_2 feed QOF% being 99.5% for CQ650, 99.3% for CQ30P and 98.2% for CQ006, while the 15 vol.% CO_2 feed results are 99.2%, 99.2% and 98.8%, respectively.

One of the metrices that shows how well the Avrami kinetic model can predict adsorption behaviour is the R^2 value. For all sorbents, reaction temperatures and CO_2 feed concentrations, the R^2 value is ≈ 1.0. Every calculated R^2 value came to a value of ≥ 0.999, indicating that the model is well suited to these experimental adsorption and desorption kinetic data.

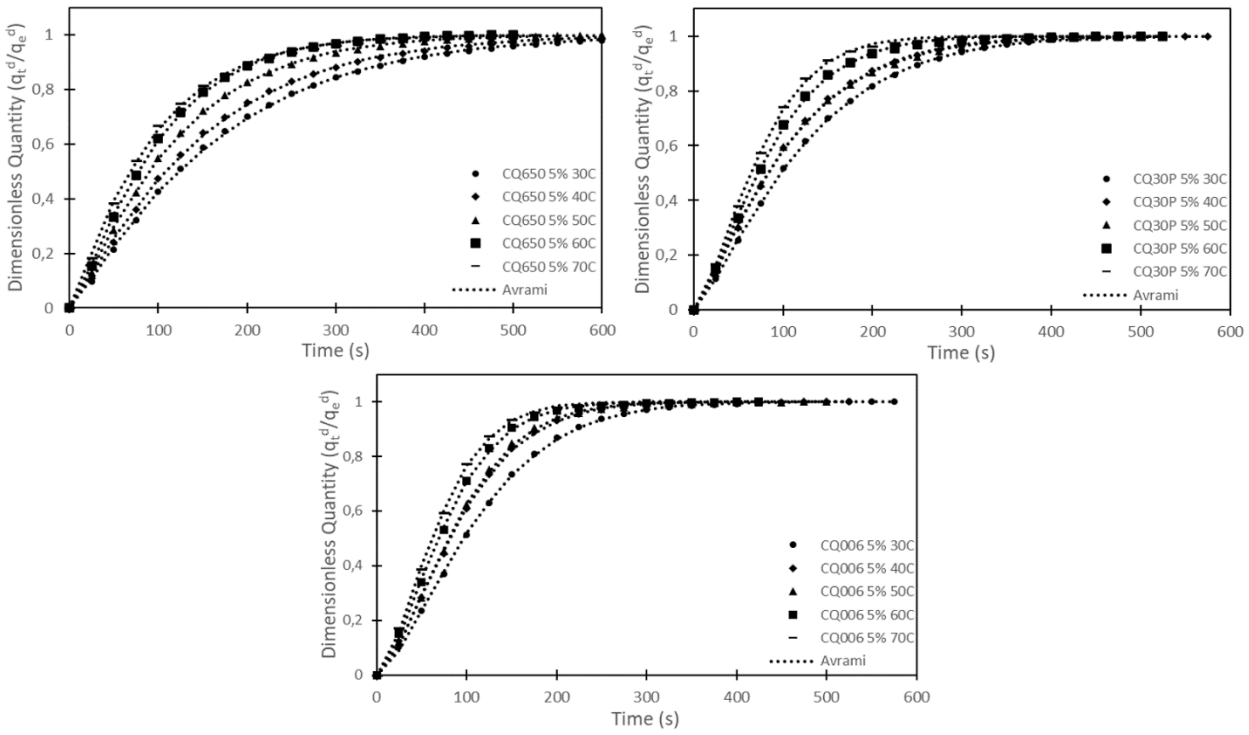

Figure 6-5: CQ650, CQ30P and CQ006 at fixed inlet concentration of 5 vol.% CO_2 at 30, 40, 50, 60 and 70 ℃ desorption Avrami model fit

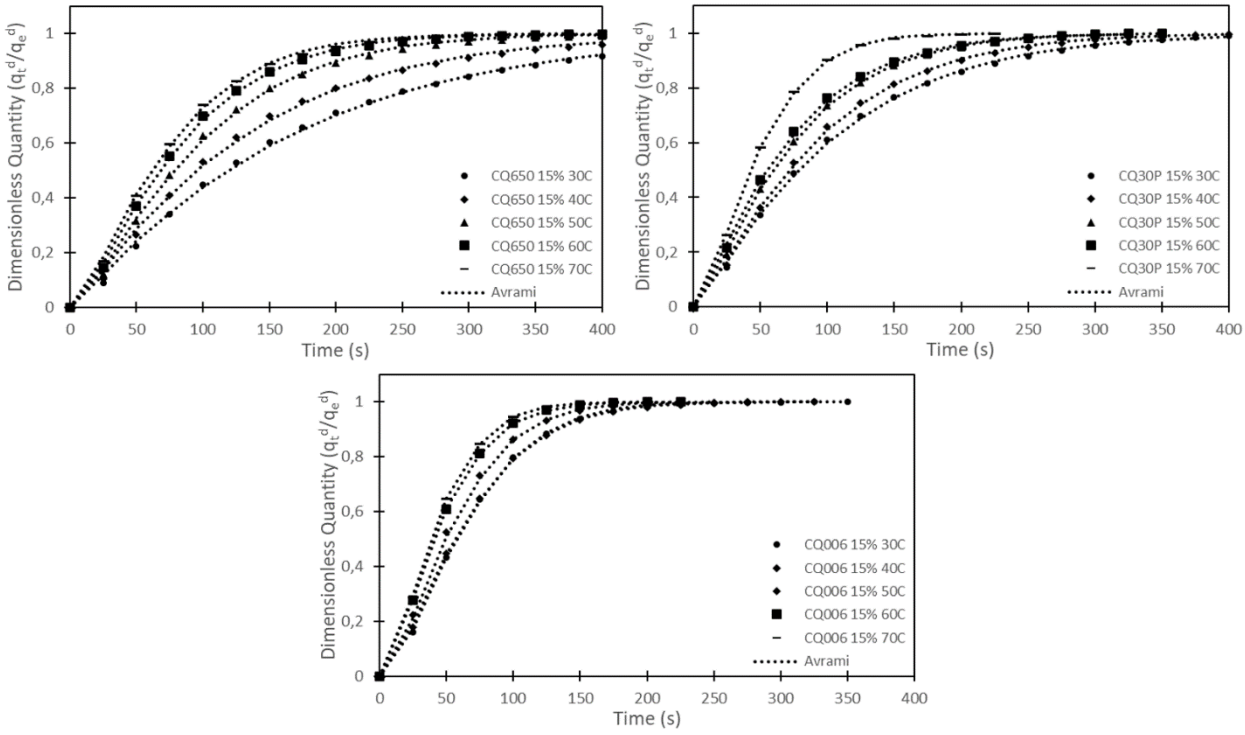

Figure 6-6: CQ650, CQ30P and CQ006 at fixed inlet concentration of 15 vol.% CO_2 at 30, 40, 50, 60 and 70 ℃ desorption Avrami model fit

Table 6-7: Avrami rate model adsorption parameters of CQ650, CQ30P and CQ006 for 30, 40, 50, 60 and 70 ℃ at 5 and 15 vol.% CO_2 feed concentrations

		5 vol.% Inlet CO_2 Concentration					15 vol.% Inlet CO_2 Concentration				
Sample	**Parameter**	**30 ℃**	**40 ℃**	**50 ℃**	**60 ℃**	**70 ℃**	**30 ℃**	**40 ℃**	**50 ℃**	**60 ℃**	**70 ℃**
CQ650	**k_A,** *1/s ($x10^{-2}$)*	0.613	0.727	0.824	0.965	1.00	0.700	0.918	1.12	1.35	1.48
	n	1.26	1.29	1.26	1.28	1.11	1.26	1.34	1.42	1.46	1.47
	MAE *($x10^{-2}$)*	0.577	0.635	0.914	0.887	1.80	1.46	1.52	2.53	1.20	0.787
	RSME	0.0713	0.0769	0.0923	0.0937	0.133	0.120	0.122	1.42	0.106	0.0885
	R^2	0.999	0.999	0.999	0.999	0.999	0.999	0.999	0.999	0.999	0.999
	QOF%	99.0	98.6	99.0	98.8	99.8	99.1	99.5	99.7	98.9	98.2
CQ30P	**k_A,** *1/s ($x10^{-2}$)*	0.704	0.852	0.928	0.978	1.09	0.947	1.18	1.30	1.35	2.16
	n	1.35	1.31	1.36	1.41	1.39	1.23	1.31	1.29	1.31	1.30
	MAE *($x10^{-2}$)*	0.525	2.05	1.25	5.41	5.64	1.22	0.373	0.587	1.58	2.07
	RSME	0.0715	0.142	0.110	0.215	0.235	0.109	0.0607	0.0755	0.108	0.138
	R^2	0.999	0.999	0.999	0.999	0.999	0.999	0.999	0.999	0.999	0.999
	QOF%	99.0	99.5	98.6	99.2	99.5	99.4	98.7	98.8	98.6	98.4
CQ006	**k_A,** *1/s ($x10^{-2}$)*	0.819	0.967	1.06	1.13	1.30	1.55	1.60	1.84	2.18	2.54
	n	1.57	1.58	1.58	1.57	1.49	1.52	1.58	1.32	1.34	1.35
	MAE *($x10^{-2}$)*	2.60	2.70	2.44	2.93	2.64	4.12	3.67	4.82	2.24	1.19
	RSME	0.161	0.164	0.156	0.171	0.162	0.202	0.188	0.212	0.147	0.108
	R^2	0.999	0.999	0.999	0.999	0.999	0.999	0.999	0.999	0.999	0.997
	QOF%	97.7	97.4	96.3	97.3	97.9	99.5	99.2	99.3	99.5	98.8

Table 6-8: Avrami rate model desorption parameters of CQ650, CQ30P and CQ006 for 30, 40, 50, 60 and 70 ℃ at 5 and 15 vol.% CO_2 feed concentrations

		5 vol.% Inlet CO_2 Concentration					15 vol.% Inlet CO_2 Concentration				
Sample	**Parameter**	**30 ℃**	**40 ℃**	**50 ℃**	**60 ℃**	**70 ℃**	**30 ℃**	**40 ℃**	**50 ℃**	**60 ℃**	**70 ℃**
CQ650	**k_A,** *1/s ($x10^{-2}$)*	0.591	0.665	0.783	0.948	1.03	0.609	0.759	0.976	1.16	1.23
	n	1.11	1.10	1.12	1.169	1.07	1.14	1.14	1.28	1.30	1.28
	MAE *($x10^{-2}$)*	9.91	1.67	2.35	0.995	2.20	4.31	3.73	1.66	0.729	1.15
	RSME	0.0984	0.128	0.138	0.0979	0.147	0.177	0.192	0.120	0.0840	0.106
	R^2	0.999	0.999	0.999	0.999	0.999	0.999	0.999	0.999	0.999	0.999
	QOF%	99.8	99.8	99.6	99.5	99.8	98.7	98.3	99.3	99.7	99.8
CQ30P	**k_A,** *1/s ($x10^{-2}$)*	0.770	0.897	0.944	1.04	1.21	0.928	1.05	1.30	1.34	1.86
	n	1.25	1.23	1.27	1.30	1.38	1.12	1.18	1.23	1.16	1.35
	MAE *($x10^{-2}$)*	0.462	1.02	1.41	5.18	2.73	1.36	0.983	0.405	0.732	1.29
	RSME	0.0680	0.101	0.118	0.204	0.164	0.116	0.0986	0.0636	0.0846	0.102
	R^2	0.999	0.999	0.999	0.996	0.999	0.999	0.999	0.999	0.999	0.999
	QOF%	99.0	99.6	99.4	99.5	99.1	99.5	99.8	99.1	99.5	98.3
CQ006	**k_A,** *1/s ($x10^{-2}$)*	0.909	0.979	0.990	1.14	1.25	1.36	1.36	1.67	1.86	2.03
	n	1.47	1.47	1.51	1.54	1.54	1.42	1.43	1.44	1.42	1.45
	MAE *($x10^{-2}$)*	1.02	1.49	1.76	2.22	2.11	0.713	0.482	0.358	0.505	1.08
	RSME	0.0995	0.122	0.132	0.148	0.145	0.0822	0.0685	0.0589	0.0707	0.179
	R^2	0.999	0.999	0.999	0.999	0.999	0.999	0.999	0.999	0.999	0.997
	QOF%	98.2	98.3	98.3	98.2	98.1	99.6	99.4	98.6	97.9	98.4

6.1.3 Comparison with literature

The adsorption and desorption rate results obtained from this study were compared to results reported in the open literature from similar experimental setups and conditions and presented in Table 6-9. The adsorption rate of CO_2 on GAC and OXA-GAC activated carbon samples was investigated by Shafeeyan (2015), and it found that the Avrami kinetic rate model, compared to the PFO and PSO, fitted their experimental results the best. The study found a k_A and n parameter in the range of 0.008 – 0.013 and 0.91 – 1.03, respectively. The Avrami rate constant (k_A) is in the same range as found in this study; however, the stretching parameter (n) is notably smaller. As seen in this study result, the stretching parameter can vary dramatically between different types of sorbents.

Conversely, Ammendola et al. (2017) found that the PFO adequately predicted adsorption behaviour with a reported kinetic rate of 0.006 – 0.012. The rate constant is also in line with the result found in this study, with a rate of 0.006 – 0.013 as reported. The similarity between the two PFO results suggests that the Avrami rate model might be a better fit. Lui et al., (2019) showed that Avrami could be used to describe decomposition kinetics that involves growing voids that are randomly distributed and reported a decomposition R^2 0.984 to 0.997 for temperatures ranging from 95℃ to 125℃. This high R^2 value was found in this study for all of the temperatures tested, indicating the randomly distributed voids in these activated carbon samples.

Table 6-9: Comparison of kinetic parameters and conditions: this study and open literature

Sample type	Sample name	Pressure (bar)	Temperature range (℃)	Inlet CO_2 concentration (vol %)	Flow rate (L/min)	Reactor setup	Model fitted	Parameter(s)	Parameter value(s)	Reference(s)
Activated carbon	CQ650	1	30-70	5 & 15	0.5	Fixed-bed	Avrami	k_A n	0.006-0.0015 1.11-1.47	This study
Activated carbon	CQ30P	1	30-70	5 & 15	0.5	Fixed-bed	Avrami	k_A n	0.007-0.019 1.31-1.39	
Activated carbon	CQ006	1	30-70	5 & 15	0.5	Fixed-bed	Avrami	k_A n	0.008-0.013 1.42-1.58	
Activated carbon	DARCO	1	18-130	1-15	1.0	Fluidised bed	PFO	k_1	0.006-0.012	Ammendola et al., 2017
Activated carbon	-	1	30-90	10	12	Fixed-bed	PFO	k_1	0.097-0.24	G. Ibrahim & A. Al-Meshragi, 2020
Activated carbon	GAC	1	30-60	15	0.05-0.1	Fixed-bed	Avrami	k_A n	0.008-0.013 0.91-1.03	Shafeeyan, 2015

Activated carbon	C-500 C-600 C-700	1	30	10	0.05	Fixed-bed	PFO	k_1	0.017 0.016 0.029	Goel et al., 2016
Amine-functionalized sorbent	PEHA loaded SBA-16	1	70	15	0.1	Fixed-bed	Avrami	k_A n	-	(Lui *et al.*, 2019)

6.1.4 Adsorption activation energy

The kinetic rate constant used for the estimation of the adsorption activation energy is taken from the fitting of the Avrami adsorption kinetic model to the experimental data, as it is the model that fits the experimental results the best. The activation energy can be determined from the Arrhenius plots of Ln k_A against 1/T and then using the slope of the straight line. The activation energies are presented in Table 6-10 for the 5 vol.% and 15 vol.% CO_2 concentrations.

The activation energy for all the activated carbons is positive, which means an increase in the temperature leads to an increase in the reaction rate. The relatively low values for the activation energy align with other reported values in the literature and indicate physical adsorption with weak attraction forces. The activation energies for the 5 vol.% CO_2 feed of CQ650, CQ30P and CQ006 are 8.74, 7.12 and 7.00 kJ/mol, respectively. The 15 vol.% CO_2 feed activation energies are 13.38, 11.56 and 10.27 kJ/mol, respectively. The values of the adsorption activation energy agree well with reported data for activated carbons by (Ammendola et al., 2017) of 7.13 kJ/mol and 23.74 kJ/mol reported by (Sing and Kumar, 2017).

It can also be observed from Figure 6-7 and Figure 6-8 that the steepness of the slope correlates with the activation energies of each sorbent. A steeper slope indicates a higher activation energy and a shallower slope indicates a lower activation energy. CQ650 has the highest activation energy at 5 and 15 vol.% CO_2 concentrations and slopes of -1050.93 and -1609.27, respectively. At the same time, CQ006 has the lowest activation energies at 5 and 15 vol.% CO_2 concentrations with corresponding slopes of -842.13 and -1235.27, respectively.

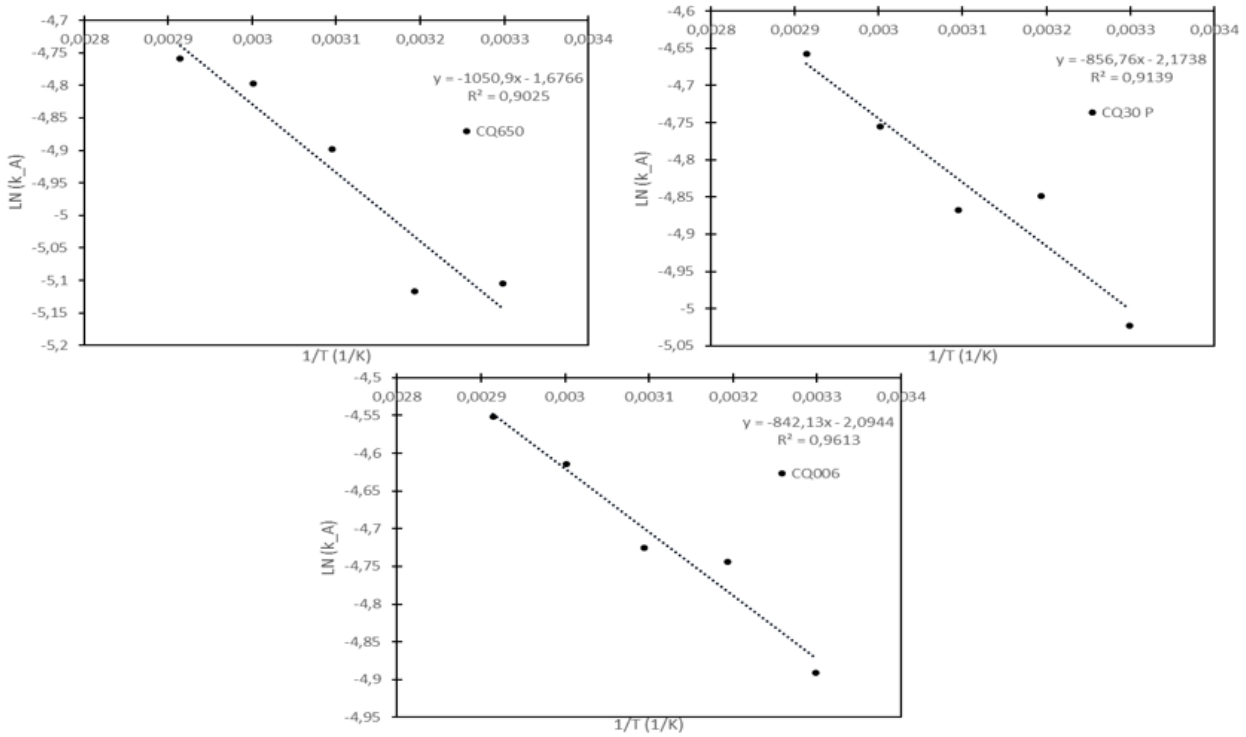

Figure 6-7: Arrhenius plots of (Ln(k_A) vs 1/T) for CQ650, CQ30P and CQ006 at 5 vol.% CO_2 feed concentration

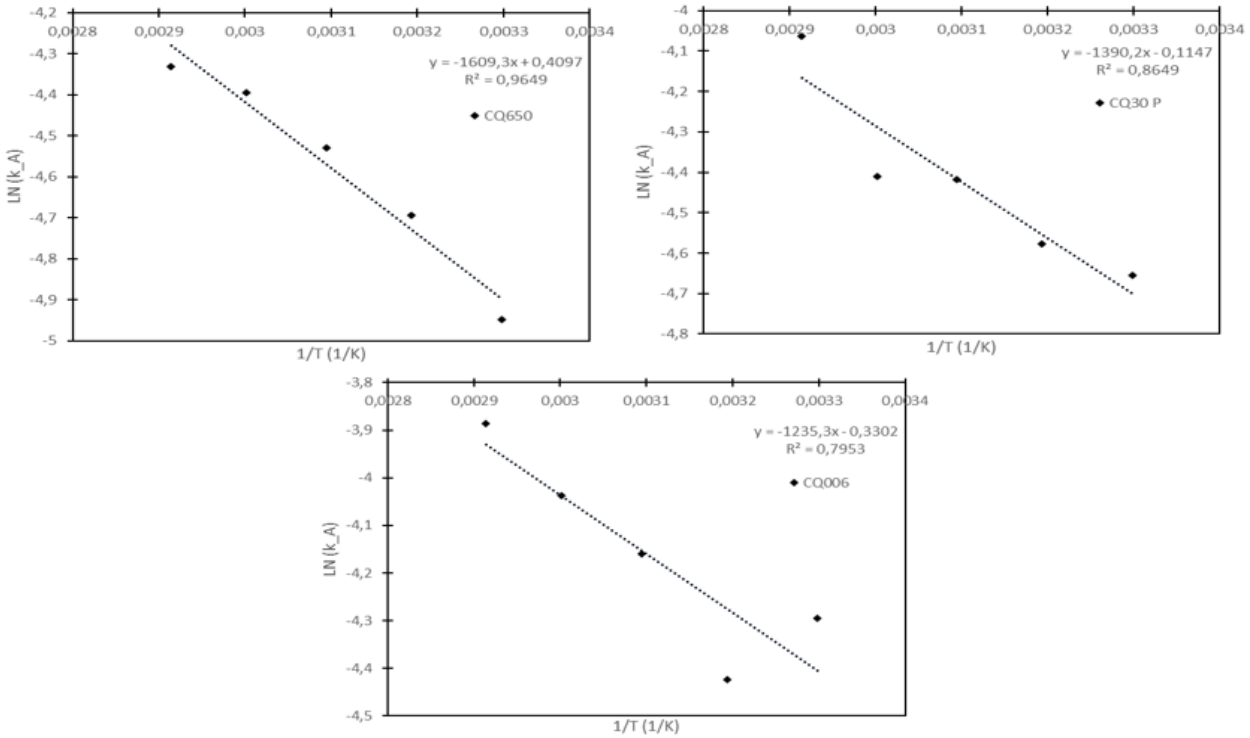

Figure 6-8: Arrhenius plots of (Ln(k_A) vs 1/T) for CQ650, CQ30P and CQ006 at 15 vol% CO_2 feed concentration

Generally, an increase in the activation energy results in a decrease in the reaction rate (Rashidi et al., 2021); however, the modelling results show that the reaction rate increases when the CO_2 feed rate increases. The increase in the activation energy from the 5 vol.% to the 15 vol.% CO_2 feed is, on average, a 54% increase, but the concentration increase is 3-fold. Thus, the overall reaction rate still increases despite the higher activation energy.

Table 6-10: Adsorption activation energies of CQ650, CQ30P and CQ006 at 5 and 15 vol.% CO_2 feed concentrations

5 vol.% CO_2 feed concentration			
Sample	**CQ650**	**CQ30P**	**CQ006**
R^2	0.903	0.914	0.961
Activation energy (E_a, kJ/mol)	8.74	7.12	7.00
15 vol.% CO_2 feed concentration			
Sample	**CQ650**	**CQ30P**	**CQ006**
R^2	0.965	0.865	0.795
Activation energy (E_a, kJ/mol)	13.38	11.56	10.27

6.1.5 Desorption activation energy

In the evaluation of the desorption activation energy, the same method was used to estimate the adsorption activation energy. All desorption activation energies are also positive, indicating that the rate consistently increasesith increasing temperature, implying an increased desorption rate (Teng *et al.*, 2017). The desorption activation energy data are reported in Table 6-11.

The activation energy of CQ650 is the highest of the three samples at 12.73 kJ/mol and 15.83 kJ/mol for the 5 and 15 vol.% CO_2 feed, respectively. CQ30P is next with 9.08 kJ/mol and 14.07 kJ/mol, while the lowest reported desorption activation energy is for CQ006 at 8.80 kJ/mol and 9.60 kJ/mol for the 5 and 15 vol.% feed concentrations, respectively. These results support the data in Section 5.3.2, where the sorbent with the lowest activation energy has the lowest saturation time, and the longest saturation time corresponds with the highest activation energy.

The low activation energies found in this study are in range with expected desorption activation energies for physical desorption, being around 15.86 kJ/mol Teng et al. (2017), while values of 9.47 kJ/mol and 12.66 kJ/mol have been reported by Wei et al. (2017) for two different activated carbon samples. Furthermore, the desorption activation energies are higher than the adsorption

activation energies for all the samples and concentrations; this aligns with the general principle for exothermic reactions, where the activation energy for the endothermic reverse reaction is greater than that of the forward reaction. Figure 6-9 and Figure 6-10 show the Arrhenius plots for CQ650, CQ30P and CQ006 at 5 and 15 vol.%, respectively.

Since it is shown that a higher desorption activation energy results in a longer saturation time, this would have a negative impact on energy consumption in an industrial application. A sorbent with a high adsorption capacity and a competitive saturation time might become less suitable when a regeneration cycle is involved, as there might be another sorbent with lesser adsorption qualities but is overall more economically viable. When designing a large-scale adsorption/desorption application, the energy requirement factor must be studied.

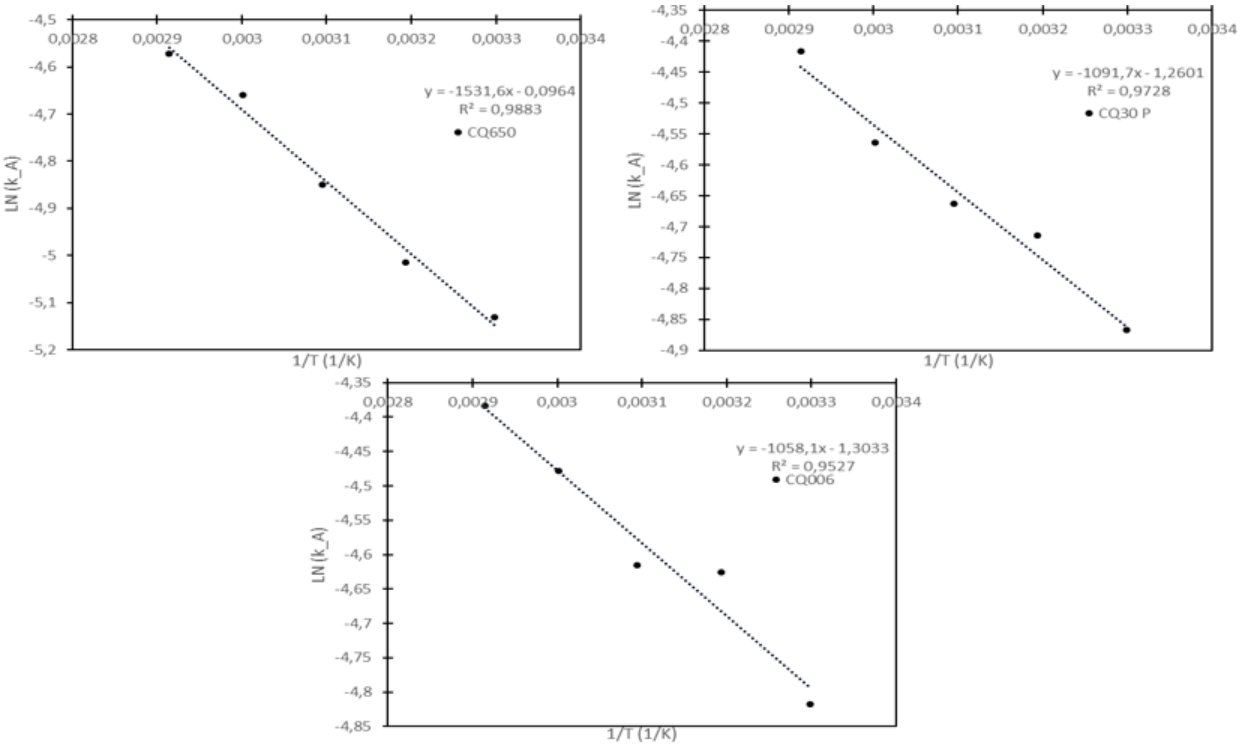

Figure 6-9: Desorption Arrhenius plots of ($Ln(k_A)$ vs 1/T) for CQ650, CQ30P and CQ006 at 5 vol.% CO_2 feed concentration

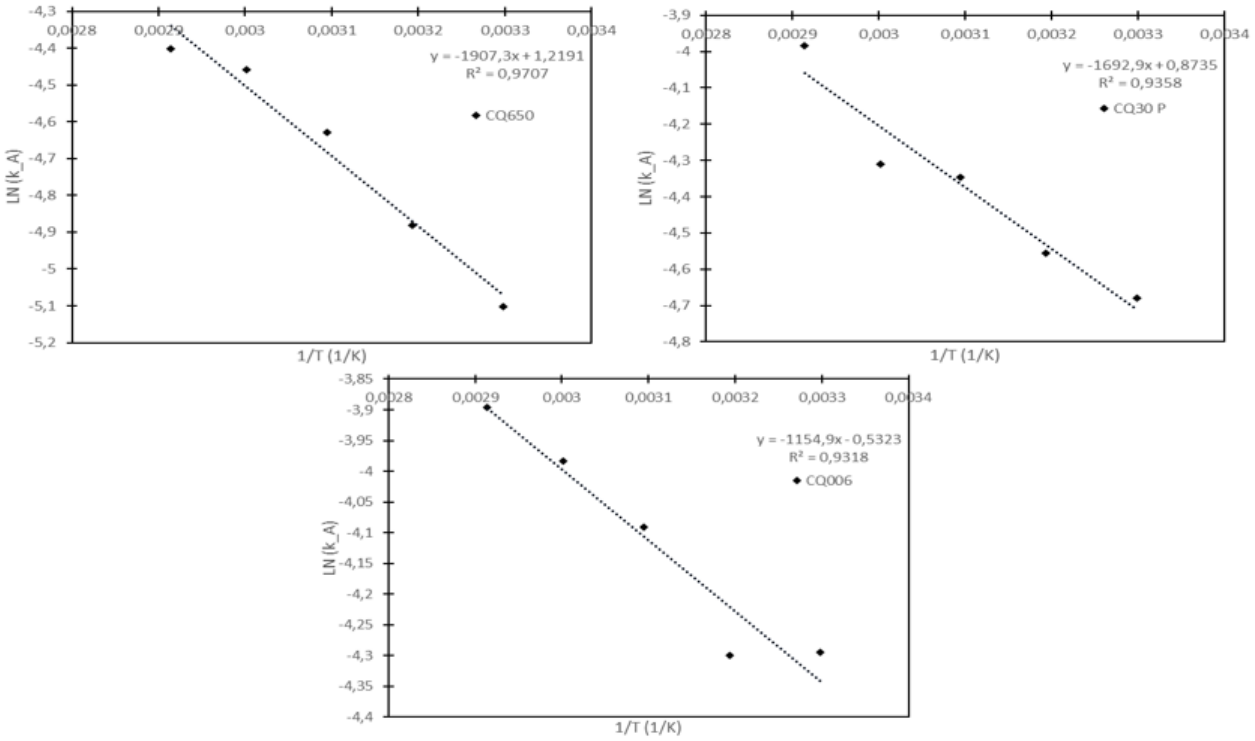

Figure 6-10: Desorption Arrhenius plots of (Ln(k_A) vs 1/T) for CQ650, CQ30P and CQ006 at 15 vol.% CO_2 feed concentration

Table 6-11: Desorption activation energies of CQ650, CQ30P and CQ006 at 5 and 15 vol.% CO_2 feed concentrations

5 vol.% CO_2 feed concentration			
Sample	**CQ650**	**CQ30P**	**CQ006**
R^2	0.9883	0.9728	0.9527
Activation energy (E_d, kJ/mol)	12.73	9.08	8.80
15 vol.% CO_2 feed concentration			
Sample	**CQ650**	**CQ30P**	**CQ006**
R^2	0.9707	0.9358	0.9318
Activation Energy (E_d, kJ/mol)	15.86	14.07	9.60

6.1.6 Comparison with literature

A comparison with relevant literature is made in Table 6-12, where Ammendola et al., (2017) reported activation energy for DARGO FDG-activated carbon at 10 vol.% CO_2 feed concentration

of 7.13 kJ/mol and is between the values at 5 vol.% (7.00 kJ/mol) and 15 vol.% (10.27 kJ/mol) reported in this investigation. Furthermore, Goel et al. (2016) reported similar results for C-700 activated carbon at 10 and 20 vol.% CO2 feed concentrations as 7.70 kJ/mol and 9.05 kJ/mol, respectively. These results are on the low end of that found in this study; however, they do match the result of CQ006 at 5 and 15 vol.% CO_2 feed concentrations. Rashidi et al., 2016 reported adsorption activation energies of between 3 and 4 kJ/mol, but it was for a 99.8 vol.% CO_2 feed concentration. The low adsorption activation energy is due to the specialised activated carbon used by the study.

The desorption activation energy results reported in this study (9.60 – 15.86 kJ/mol) are in line with the results reported by Wei, Yu et al., (2017) (9.47 – 12.66 kJ/mol) for 15 vol.% CO_2 feed concentration. Teng et al., 2017 have reported a desorption activation energy of 15.86 kJ/mol, which is identical to the desorption activation energy of CQ650 at 15 vol.% CO_2 feed concentration. All desorption activation energies are similar to results reported in the literature.

Table 6-12: Adsorption and desorption activation energies compared with results in open literature

Sample type	Sample name	Pressure (bar)	Temperature range (°C)	Inlet CO_2 concentration (vol.%)	Flow rate (L/min)	Adsorption activation energy E_a (kJ/mol)	Desorption activation energy E_d (kJ/mol)	Reference(s)
Activated carbon	CQ650	1	30 – 70	5	0.5	8.74	12.73	This study
Activated carbon	CQ30P	1	30 – 70	5	0.5	7.12	9.08	
Activated carbon	CQ006	1	30 – 70	5	0.5	7.00	8.80	
Activated carbon	CQ650	1	30 – 70	15	0.5	13.38	15.86	
Activated carbon	CQ30P	1	30 – 70	15	0.5	11.56	14.07	
Activated carbon	CQ006	1	30 – 70	15	0.5	10.27	9.60	
Activated carbon	DARCO FGD	1	30 – 100	10	1.0	7.13	–	Ammendola et al., 2017
Activated carbon	C-700	1	30 – 100	10 – 20	0.05	7.70 – 9.05	–	Goel et al., 2016
Activated carbon	Norit SX2	1	25 – 120	99.8	–	3 – 4	–	Rashidi, et al., 2016
Mesoporous silica	MCM-41-TEPA	4	35 – 70	10	0.002	–	15.86	Teng et al., 2017
Activated carbon	WIRAC	1	100 – 150	15	–		9.47 – 12.66	Wei et al., 2017

6.2 Thermodynamic analysis

The thermodynamic evaluation carried out on the three activated carbon samples, CQ650, CQ30P and CQ006, is presented in this section. The enthalpy, entropy and Gibbs free energy changes are determined from the kinetic rate constant for the activation energy and an equilibrium constant from the fixed-bed reactor experiments.

6.2.1 Enthalpy, entropy and Gibbs free energy

The change in enthalpy, entropy and Gibbs free energy were determined from the data collected from the kinetics reactor experiments. Since the Vant Hoff equation is used to determine the thermodynamic properties, and the equation makes use of a standard equilibrium constant which is not directly determined by the reactor experiments, a standard equilibrium constant needs to be calculated from the available data of the experiment. This procedure is explained in Section 3.6.1. All the thermodynamic data are presented in Table 6-13.

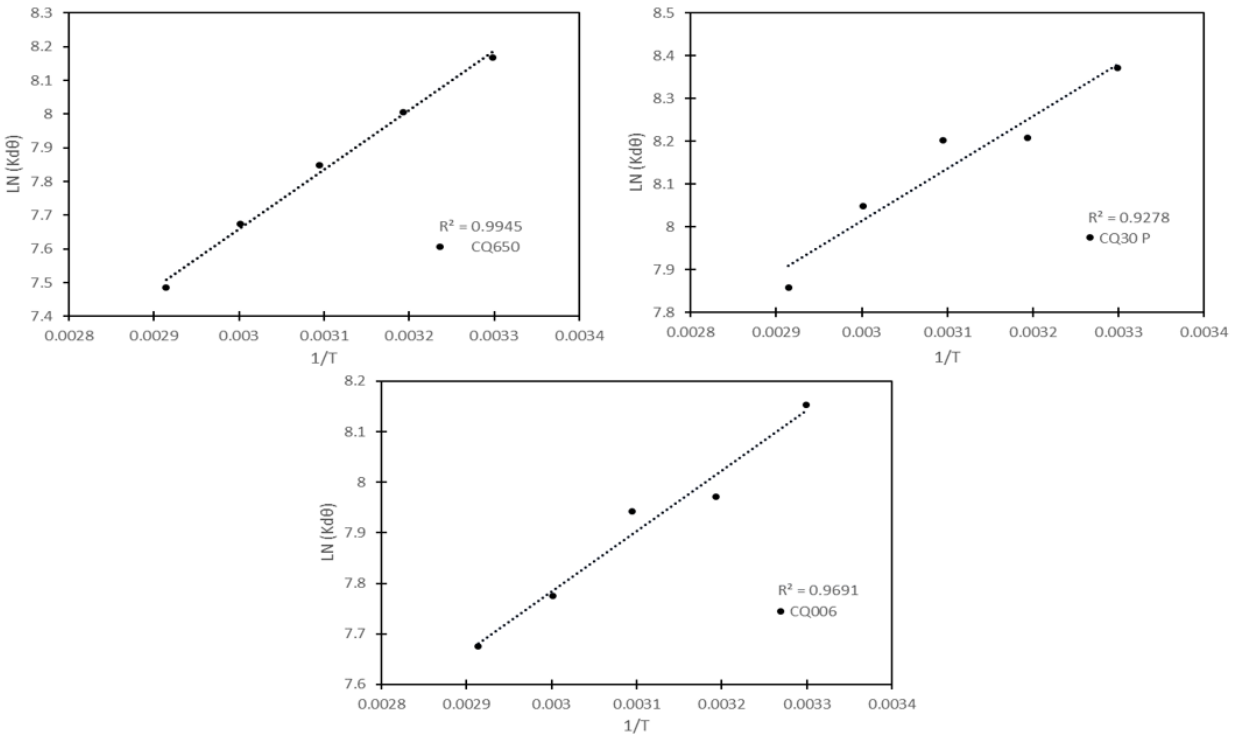

Figure 6-11: Plot of (Ln(K_d^{θ}) vs 1/T) for CQ650, CQ30P and CQ006 at 5 vol.% CO_2 feed concentration

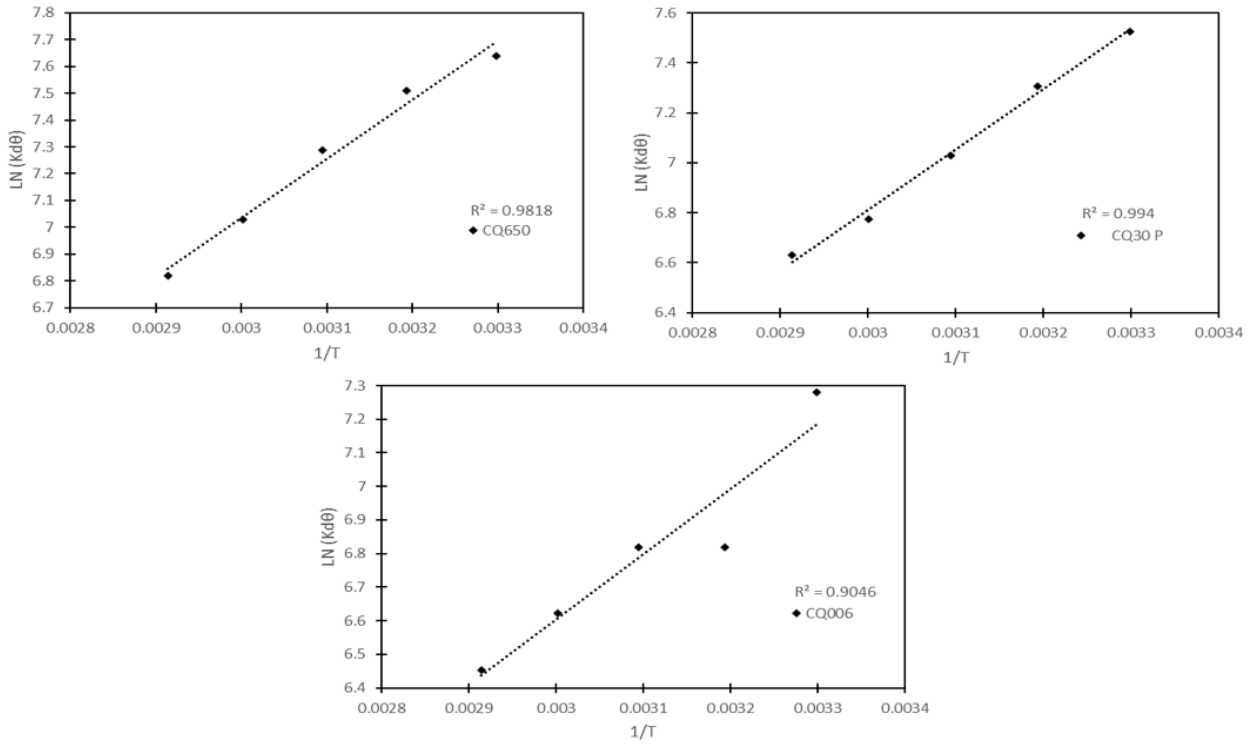

Figure 6-12: Plot of ($Ln(K_d^{\theta})$ vs 1/T) for CQ650, CQ30P and CQ006 at 15 vol.% CO_2 feed concentration

The enthalpy change (ΔH^{θ}) of all the sorbents for the 5 and 15 vol.% CO_2 feed concentrations are negative, indicating that the adsorption process is exothermic, and the relatively low value of ΔH^{θ} indicates a physical adsorption process. For typical chemical adsorption, the ΔH^{θ} values are 80 – 200 kJ/mol, while the range for physical adsorption is 20 - 40 kJ/mol (Ammendola et al., 2017). The ΔH^{θ} for CQ650, CQ30P and CQ006 for the 5 vol.% CO_2 feed are –14.64, –10.18 and –9.95 kJ/mol, respectively, while the 15 vol.% feed are –18.30, –20.13 and –16.10, respectively. The difference in the values from CQ650 to CQ006 indicates that the attractive force between adsorbent and adsorbate gets slightly weaker or stronger as the value of ΔH^{θ} varies between the different sorbents.

The negative values of entropy change (ΔS^{θ}) for all of the sorbents suggest that the CO_2 molecules entered a more orderly state after adsorption occurred, implying that the molecules were more disorderly in their gaseous phase, and this result is what is expected during adsorption. However, the minimal value of ΔS^{θ} is an insignificant change in entropy due to the minimum free space available on the activated carbon surface.

The change in the Gibbs free energy is negative for all samples and temperatures, indicating that the adsorption of the CO_2 on the sorbent pore surfaces is spontaneous. ΔG^{θ} increases with an increase in temperature, resulting in less adsorption at higher temperatures. This reduction in

adsorption was also seen in Section 5.4, where the quantity adsorbed decreased with increasing temperature. ΔG^{θ} with the 5 vol.% CO_2 feed is higher than the 15 vol.% feed, indicating that adsorption is more favourable at higher concentrations and lower temperatures.

Table 6-13: The change in enthalpy, entropy and Gibbs free energy for CQ650, CQ30P and CQ006

5 vol.% CO_2 feed			
Thermodynamic property	**CQ650**	**CQ30P**	**CQ006**
R^2	0.9945	0.9278	0.9691
ΔH^{θ}, kJ/mol	–14.64	–10.18	–9.95
ΔS^{θ}, kJ/mol	–0.00198	–0.004	–0.004
$\Delta G^{\theta}_{30\ ^{o}C}$ kJ/mol	–20.63	–21.12	–20.52
$\Delta G^{\theta}_{40\ ^{o}C}$ kJ/mol	–20.82	–21.48	–20.87
$\Delta G^{\theta}_{50\ ^{o}C}$ kJ/mol	–21.03	–21.84	–21.22
$\Delta G^{\theta}_{60\ ^{o}C}$ kJ/mol	–21.22	–22.21	–21.56
$\Delta G^{\theta}_{70\ ^{o}C}$ kJ/mol	–21.42	–22.57	–21.91
15 vol.% CO_2 feed			
Thermodynamic property	**CQ650**	**CQ30P**	**CQ006**
R^2	0.9818	0.9940	0.9046
ΔH^{θ}, kJ/mol	–18.30	–20.13	–16.10
ΔS^{θ}, kJ/mol	–0.0033	–0.0038	–0.0066
$\Delta G^{\theta}_{30\ ^{o}C}$ kJ/mol	–19.39	–18.99	–18.10
$\Delta G^{\theta}_{40\ ^{o}C}$ kJ/mol	–19.42	–18.95	–18.17
$\Delta G^{\theta}_{50\ ^{o}C}$ kJ/mol	–19.46	–18.91	–18.23
$\Delta G^{\theta}_{60\ ^{o}C}$ kJ/mol	–19.45	–18.87	–18.30
$\Delta G^{\theta}_{70\ ^{o}C}$ kJ/mol	–19.53	–18.84	–18.37

This exothermic nature of adsorption could potentially reduce the energy requirements as the heat of adsorption could be used to keep the temperature stable at the desired adsorption temperature (depending on the process). In upscaled industrial applications, a considerable amount of heat would be produced by all the endothermic reactions such that some heat may be

used in the endothermic desorption reactions, reducing the amount of additional heat required. Furthermore, for a practical use case, the sorbent type would influence the overall design, and that may be that the best-performing sorbent in the singular process may not be the best in terms of overall efficiency.

6.2.2 Comparison with literature

The thermodynamic properties determined in this study for the activated carbon samples CQ650, CQ30P, and CQ006 are compared with thermodynamic results on activated carbons reported in the literature and presented in Table 6-14. Rashidi et al. (2016) investigated the thermodynamics of CO_2 adsorption on Norit SX2, reporting changes in enthalpy and entropy of –19.66 kJ/mol and –0.059 kJ/mol, respectively, while Goel et al. (2016) reported changes in enthalpy and entropy of C-700 as –39.56 kJ/mol and 0.075 kJ/mol, respectively. These findings are well aligned with the findings in the change in enthalpy and entropy in this study, with the results ranging from –9.95 to –20.13 kJ/mol and from –0.004 to –0.0066 kJ/mol, respectively.

Goel et al. (2016) also reported changes in the Gibbs free energy from –11.7 to –17.5 kJ/mol for a temperature range of 30 to 100 ℃ and a feed concentration of 10 vol.%. This result compares well with the values from this study reported as –18.10 to –19.53 kJ/mol in the temperature range of 30 to 70 ℃ with a feed concentration of 15 vol.%.

Table 6-14: Adsorption thermodynamic results from this study compared with results in open literature

Sample type	Sample name	Pressure (bar)	Temperature range (°C)	Inlet CO_2 concentration (vol%)	Flow rate (L/min)	ΔG° (kJ/mol)	ΔH° (kJ/mol)	ΔS° (kJ/mol)	Reference(s)
Activated carbon	CQ650	1	30–70	5	0.5	–20.63 to –21.42	–14.64	–0.0020	This study
Activated carbon	CQ30P	1	30–70	5	0.5	–21.12 to –22.57	–10.18	–0.004	
Activated carbon	CQ006	1	30–70	5	0.5	–20.52 to –21.91	–9.95	–0.004	
Activated carbon	CQ650	1	30–70	15	0.5	–19.39 to –19.53	–18.30	–0.0033	
Activated carbon	CQ30P	1	30–70	15	0.5	–18.99 to –18.84	–20.13	–0.0038	
Activated carbon	CQ006	1	30–70	15	0.5	–18.10 to –18.37	–16.10	–0.0066	
Activated carbon	DARCO FGD	1	30-100	1-15	1.0	–1.93 to –3.58	–7.98	–0.016	Ammendola et al., 2017
Activated carbon	C-700	1	30-100	10	0.05	–11.7 to –17.5	–39.56	0.075	Goel et al., 2016
Activated carbon	Coconut fibre	4	25-60	14	15	–6.82 to –7.65)	–14.98	26	Hauchhum and Mahanta, 2017
Activated carbon	Norit SX2	1	25-120	–	–	–1.79 to 4.17	–19.66	–0.059	Rashidi et al., 2016

6.3 Breakthrough modelling

The breakthrough curve indicates the ratio of the outlet concentration from the column to the feed concentration against contact time; thus, the breakthrough occurs when the feed leaving the adsorption column spikes as unadsorbed solute rises (Al Mesfer and Danish, 2018). The adsorption capacity of the adsorbent reduces suddenly after the breakthrough time as a significant part of the adsorption process occurs in narrow adsorption of mass transfer zone (Shen *et al.*, 2010; Al Mesfer and Danish, 2018). A longer breakthrough time corresponds to a lower feed flow rate and leads to higher adsorption capacity for the adsorbents. Further, the increased adsorption capacity at slower feed rates can affect the volume of flue gas per unit of time to be treated from the combustion process at an industrial scale (Al Mesfer and Danish, 2018).

6.3.1 Breakthrough modelling with Avrami

Considering that the Avrami model can accurately simulate the CO_2 adsorption process and the breakthrough curve is similar, it seems reasonable to use the Avrami equation to model the adsorption breakthrough curves. The arbitrary constant k_A is always positive, and n is > 1 always irrespective of any other factor (Singh *et al.*, 2023). The parameter values (k_A and n) that depict the curve's steepness and spread, respectively, depend on the operation and reactor parameters, such as bed height, flow rate and initial concentration (Singh *et al.*, 2023).

From Figure 6-13 and Figure 6-14, it is apparent that the Avrami equation fits the breakthrough data well, and the accuracy indicators in Table 6-15 support the model fitting. The most apparent indication is that the R^2 value for all sorbents, temperatures and concentrations is > 0.996, and it indicates that the Avrami equation can predict the behaviour of the adsorption breakthrough data. Furthermore, the QOF% is around 98%, while the lowest QOF% is 96.4%. The parameter value of k_A is slightly less than that of the adsorption model fit but is in the same range, while the parameter n is slightly more. The other noticeable difference is in the MAE and RMSE values, which are all higher than their adsorption counterparts.

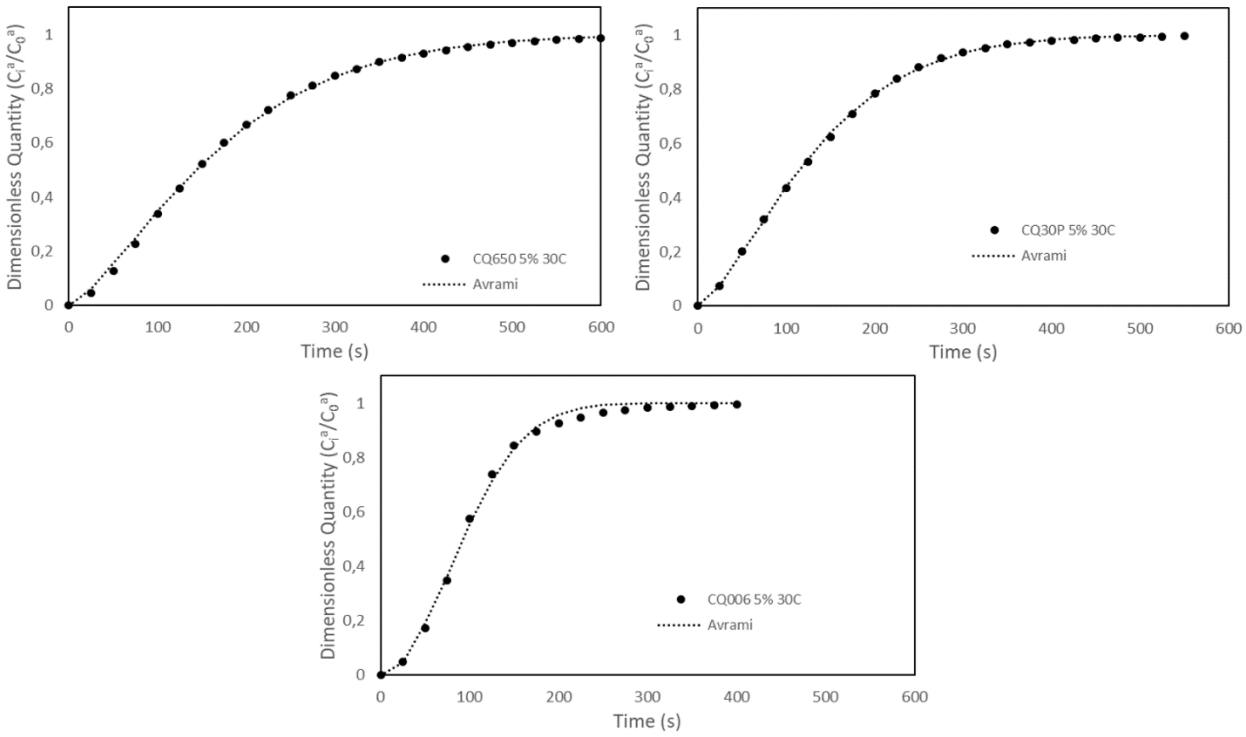

Figure 6-13: Avrami adsorption breakthrough modelling for CQ650, CQ30P and CQ006 at 30 ℃ and 5 vol.% CO_2 feed concentration

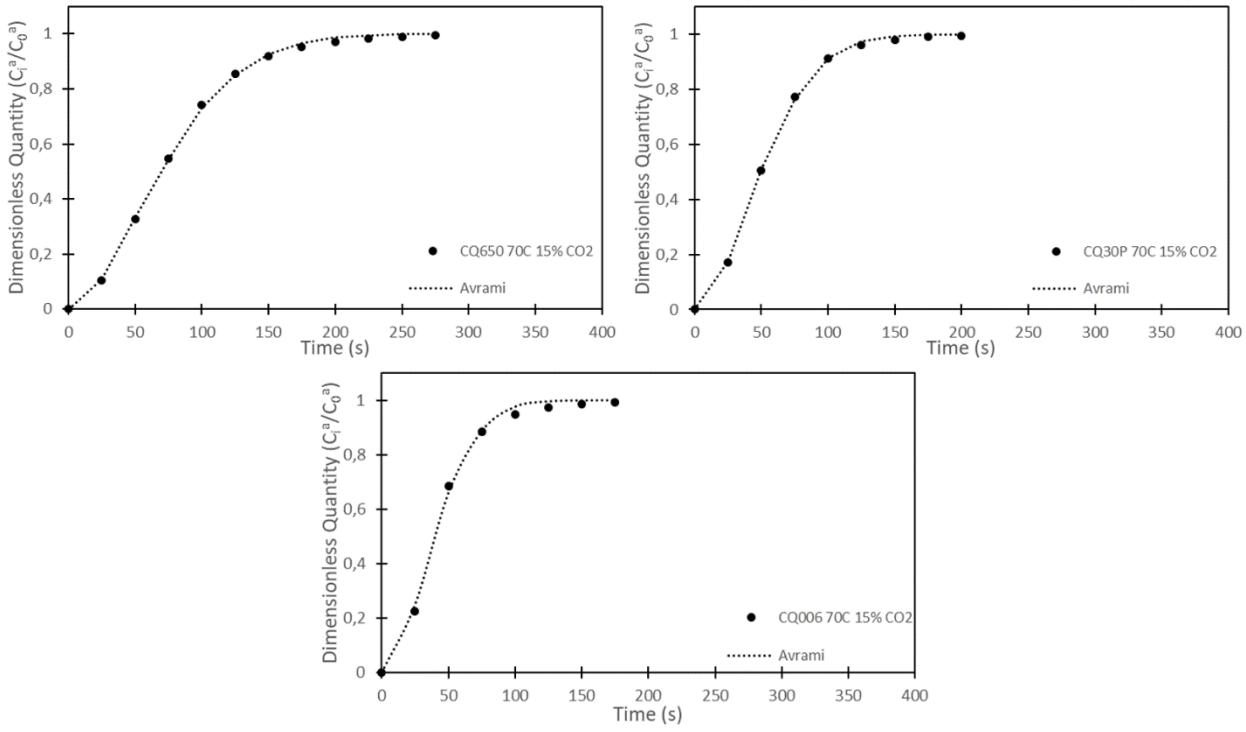

Figure 6-14: Avrami adsorption breakthrough modelling for CQ650, CQ30P and CQ006 at 70 ℃ and 15 vol.% CO_2 feed concentration

However, the modified Avrami equation used for the desorption breakthrough does not fit as well as the adsorption. While the R^2 value indicates that the model can predict the desorption behaviour, the QOF% is significantly lower. The QOF% is consistently in the 70 % and is as low as 64.4%. The k'_A values are similar to their adsorption counterparts, while the n'_A parameter is noticeably higher. Also, the fit from Figure 6-15 and Figure 6-16 is visually not as good, and from Table 6-16, the MAE and RMSE values are also higher than the desorption equivalent.

On a laboratory scale, it seems possible to use the standard Avrami equation to predict the breakthrough behaviour of sorbents in a fixed-bed reactor, but the adsorption breakthrough fit is better than the fit for the desorption breakthrough curve.

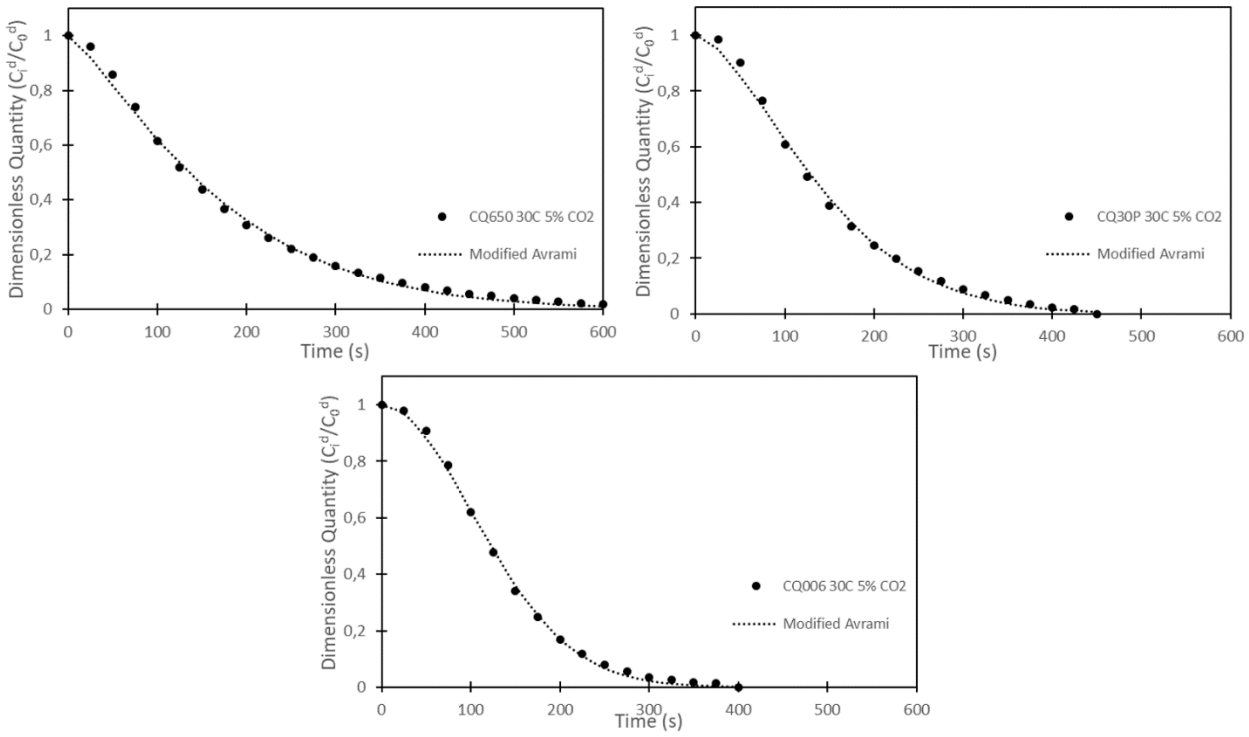

Figure 6-15: Avrami desorption breakthrough modelling for CQ650, CQ30P and CQ006 at 30 ℃ and 5 vol.% CO_2 feed concentration

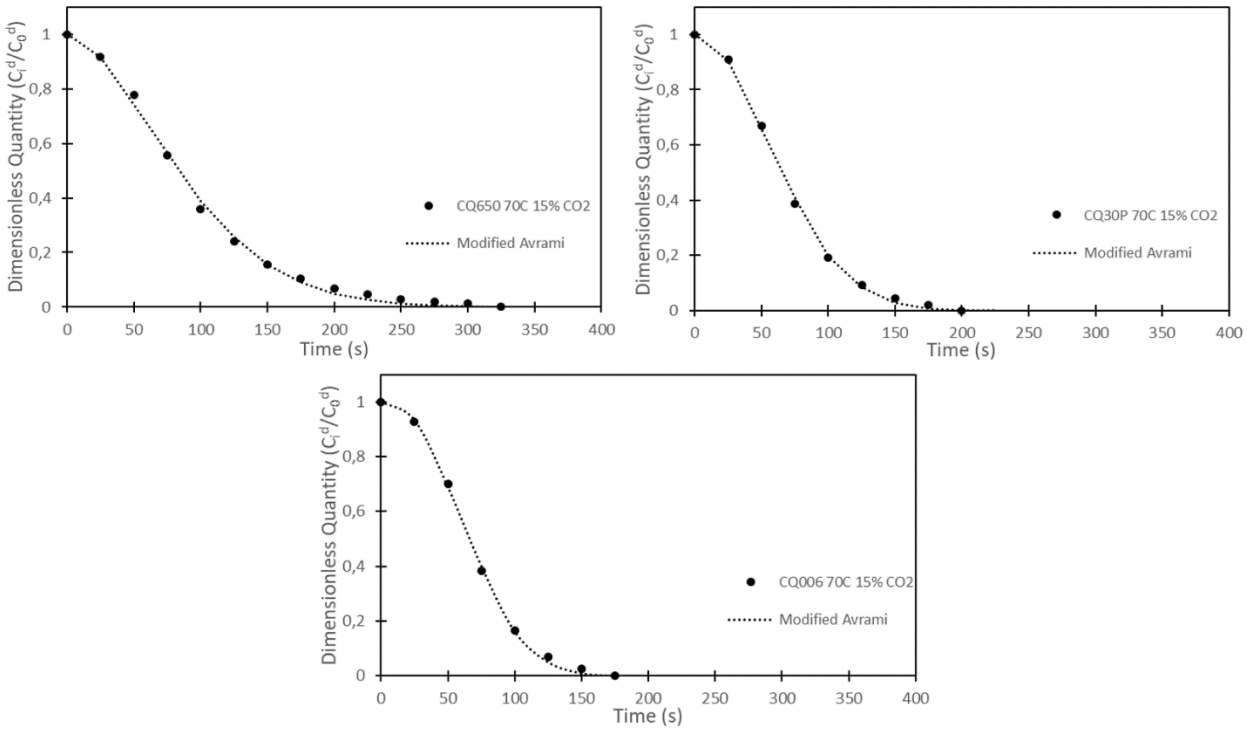

Figure 6-16: Avrami desorption breakthrough modelling for CQ650, CQ30P and CQ006 at 70 ℃ and 15 vol.% CO_2 feed concentration

Table 6-15: Avrami model breakthrough parameters for adsorption of CQ650, CQ30P and CQ006 at 30, 40, 50, 60 and 70 °C at 5 vol.% and 15 vol.% CO_2 feed concentration

		5 vol.% Inlet CO_2 Concentration					15 vol.% Inlet CO_2 Concentration				
Sample	**Parameter**	**30 °C**	**40 °C**	**50 °C**	**60 °C**	**70 °C**	**30 °C**	**40 °C**	**50 °C**	**60 °C**	**70 °C**
CQ650	**k_A,** *1/s ($x10^{-2}$)*	0.527	0.600	0.699	0.809	0.972	0.671	0.868	0.970	1.14	1.17
	n	1.38	1.42	1.47	1.55	1.30	1.24	1.40	1.70	1.73	1.71
	MAE *($x10^{-2}$)*	2.02	2.05	2.29	2.02	7.71	5.33	6.40	3.73	2.77	1.05
	RMSE	0.142	0.143	0.151	0.142	0.278	0.231	0.253	0.193	0.166	0.106
	R^2	0.999	0.999	0.999	0.999	0.997	0.998	0.997	0.999	0.999	0.999
	QOF%	98.9	99.2	99.3	99.5	97.3	97.5	96.8	99.7	99.1	98.8
CQ30P	**k_A,** *1/s ($x10^{-2}$)*	0.673	0.849	0.824	1.05	1.14	1.00	1.12	1.40	2.72	1.66
	n	1.41	1.43	1.32	1.60	1.79	1.27	1.35	1.42	1.44	1.78
	MAE *($x10^{-2}$)*	0.759	1.64	2.74	5.48	6.14	8.61	3.45	1.98	2.72	0.934
	RMSE	0.0871	0.128	0.166	0.234	0.248	0.293	0.186	0.141	0.165	0.0966
	R^2	0.999	0.999	0.999	0.998	0.998	0.996	0.998	0.999	0.998	0.999
	QOF%	98.8	99.5	97.8	98.4	99.1	96.4	97.5	97.6	97.5	98.7
CQ006	**k_A,** *1/s ($x10^{-2}$)*	0.901	1.15	1.28	1.45	1.48	1.73	1.95	1.93	2.11	2.09
	n	1.93	1.79	1.65	.65	1.63	1.71	1.67	1.74	1.69	1.80
	MAE *($x10^{-2}$)*	7.65	7.45	6.30	5.36	5.30	8.02	6.32	4.87	3.60	2.63
	RSME	0.277	0.273	0.251	0.232	0.230	0.283	0.251	0.221	0.0190	0.162
	R^2	0.998	0.997	0.997	0.997	0.997	0.996	0.996	0.998	0.998	0.998
	QOF%	99.8	98.7	98.7	98.3	98.0	97.6	97.8	97.6	98.2	99.6

Table 6-16: Avrami model breakthrough parameters for desorption of CQ650, CQ30P and CQ006 at 30, 40, 50, 60 and 70 ℃ at 5 vol.% and 15 vol.% CO_2 feed concentrations

		5 vol.% Inlet CO_2 Concentration					15 vol.% Inlet CO_2 Concentration				
Sample	**Parameter**	**30 ℃**	**40 ℃**	**50 ℃**	**60 ℃**	**70 ℃**	**30 ℃**	**40 ℃**	**50 ℃**	**60 ℃**	**70 ℃**
CQ650	**k'_A,** *1/s (x10^{-2})*	0.545	0.588	0.755	0.774	0.910	0.669	0.794	0.811	1.00	0.967
	n'_A	1.26	1.30	1.26	1.46	1.46	1.17	1.22	1.52	1.50	1.68
	MAE *(x10^{-2})*	8.56	10.2	4.26	8.55	13.5	16.4	10.1	5.00	2.19	53.3
	RMSE	0.293	0.319	0.206	0.292	0.368	0.405	0.318	0.224	0.148	0.231
	R^2	0.997	0.997	0.998	0.997	0.995	0.994	0.996	0.998	0.999	0.997
	QOF%	86.9	77.0	84.7	71.5	64.9	79.9	70.3	80.6	87.9	78.4
CQ30P	**k'_A,** *1/s (x10^{-2})*	0.390	0.735	0.777	0.998	1.06	0.942	15.8	8.13	1.10	1.28
	n'_A	2.66	1.58	1.42	1.63	1.89	1.37	1.60	1.58	1.78	1.95
	MAE *(x10^{-2})*	41.8	9.03	13.6	4.70	3.34	15.3	15.8	8.13	11.3	2.12
	RMSE	0.646	0.301	0.369	0.217	0.183	0.391	0.397	0.285	0.337	0.146
	R^2	0.991	0.997	0.995	0.998	0.999	0.993	0.993	0.995	0.995	0.999
	QOF%	78.3	77.5	76.7	70.6	64.4	69.6	68.3	74.8	63.2	83.1
CQ006	**k'_A,** *1/s (x10^{-2})*	0.675	0.925	0.992	0.985	1.11	1.11	1.10	1.21	1.32	13.0
	n'_A	1.91	1.82	1.84	2.29	2.22	1.78	1.72	1.88	2.02	2.29
	MAE *(x10^{-2})*	3.70	2.14	3.07	5.61	4.24	2.07	2.58	2.05	2.08	2.61
	RMSE	0.192	0.146	0.175	0.237	0.206	0.144	0.161	0.143	0.144	0.162
	R^2	0.999	0.999	0.999	0.998	0.998	0.999	0.998	0.999	0.998	0.998
	QOF%	81.1	78.9	72.5	64.8	67.5	86.9	86.1	86.6	86.4	84.4

Chapter 7

CHAPTER 7: CONCLUSIONS AND RECOMMENDATIONS

7.1 Conclusions

The main findings of this study are:

Three commercially available activated carbon samples (CQ650, CQ30P and CQ006) obtained from ChemQuest (Germiston, South Africa) were investigated for their suitability for use in a dry sorbent carbon capture process. The activated carbon samples underwent characterisation through various techniques, including ultimate and proximate analysis, surface area analysis, pore size distribution and pore volume analysis. Additionally, SEM was used to compare the intrinsic characteristics and morphology of the activated carbon samples among themselves and against findings documented in the open literature.

The findings on the characterisation of the activated carbon samples show that CQ006 has the highest fixed carbon content at 88.0%, while the highest elemental carbon content experimentally recorded was for CQ30P at 96.3%. All three samples displayed high BET surface areas and inherent micropore structures. CQ650 stood out with the highest surface and micropore surface areas at 735 m^2/g and 517 m^2/g, respectively. The average pore diameter, determined using the Horvath-Kawazoe method, was 3.92 – 4.07 Å across all three samples. CQ006 had the highest porosity within the pore diameter range of 3 – 5 Å, at 27.7%. Additionally, the SEM analysis revealed intricate cracks and crevasses on the surface of the activated carbons, contributing to highly uneven topography. The characterisation results in this study compared well with other results found in the open literature.

A micro fixed-bed reactor at the Noth-West University (Potchefstroom) was used to assess the kinetic rate of CO_2 adsorption and desorption on the activated carbon samples. The experimentation involved the evaluation of CO_2 adsorption and desorption kinetics at temperatures of 30, 40, 50, 60 and 70 ℃ using feed concentrations of 5 and 15 vol.% CO_2 at ambient pressure (≈1 bar). CQ650 has been identified as the best adsorbent for CO_2 adsorption and desorption, demonstrating superior performance in adsorption capacity across all temperatures and CO_2 concentrations. For the 5 vol.% CO_2 feed, CQ650 had a capacity of 0.48 mmol/g at 30℃, followed by CQ30P and CQ006 with capacities of 0.42 mmol/g and 0.41 mmol/g, respectively. Similarly, at 15 vol.% CO_2 feed and 30 ℃, CQ650 had a capacity of 0.83 mmol/g, followed by CQ30P at 0.52 mmol/g and CQ006 at 0.50 mmol/g.

Three kinetic rate models were used to characterise the individual adsorption and desorption rates: Pseudo-first order (PFO), Pseudo-second order (PSO), and Avrami kinetic model, to

identify the most predictive adsorption and desorption kinetic rate model for modelling the CO_2 adsorption and desorption rates of the activated carbon samples. The goodness of fit for each model was assessed based on the MAE, RMSE, QOF% and R^2 values. Avrami was the most suitable model across all temperatures and CO_2 feed concentrations, with an average QOF% and R^2 value for all adsorption conditions of CQ650 as 99.1% and 0.999, respectively, followed by PFO with 94.7% and 0.994, respectively and PSO with 87.6% and 0.952, respectively. Further, all of the kinetic rate constants followed the expected trends; that is, an increase in temperature leads to an increase in the kinetic rate constant and a decrease in the adsorption capacity for all sorbents under both CO_2 feed concentrations. The same results were found for the desorption kinetic constants, which increased with increasing temperatures.

All adsorption and desorption activation energies were positive, indicating that adsorption and desorption rates increase with increasing temperatures. The desorption activation energy is also slightly higher than the adsorption activation energies for all sorbents because desorption is more exothermic than adsorption.

The thermodynamic analysis determined that all the values for the change in enthalpy were negative, indicating that the reaction is exothermic for the adsorption of CO_2 onto the activated carbons. The maximum change in enthalpy recorded was 20.13 kJ/mol, meaning that it is within the accepted range (20 – 40 kJ/mol) for the adsorption mechanism to be physical adsorption. The entropy was also negative, implying that the CO_2 progresses from a more chaotic state to a slightly more orderly state during the adsorption process, but the small values of the entropy change make the transition negligible. On the other hand, all the values for the Gibbs free energy were negative as well, indicating that the adsorption of CO_2 is spontaneous onto the activated carbons. The value of the Gibbs free energy increased with increasing temperature, resulting in lower spontaneity and less favourable adsorption at high temperatures.

The breakthrough modelling using the Avrami equation yielded satisfactory results in predicting the adsorption breakthrough curves. The obtained QOF% is in the range of 96% – 98%, and an R^2 value of > 0.996 indicates that the Avrami equation is an adequate predictor of the breakthrough behaviour with the experimental conditions tested. The prediction of the desorption breakthrough behaviour is not as good as the adsorption breakthrough prediction; with a QOF% range of 64% – 89%, it varies considerably more than the adsorption breakthrough QOF%. However, the R^2 value is still > 0.99, which indicates that the desorption breakthrough prediction is not as accurate at specific times, but it can predict the overall behaviour well.

When looking at all of the results of this investigation regarding the dry-activated carbon adsorbents, CQ650 is the best overall when considering the experimental conditions. The CQ650

sample does not always perform the best, as in the case of the saturation times, but with a very high adsorption capacity, especially at 15% CO_2 feed concentration and for all the temperatures tested, it is better suited to a wide range of conditions.

7.2 Recommendations

Following the findings reported in this study, the following are recommended as value-added future research directions.

- Investigate the effect of desorption temperature on the quantity desorbed by keeping the adsorption temperature constant and varying the desorption temperature.
- Use a mass balance differential equation with axial dispersion to model the desorption mechanism.
- Design and develop a laboratory-scale fluidised bed to perform adsorption and desorption experiments to better evaluate the kinetics suitable for circulating fluidised bed design.
- Investigate multi-component flue gas mixtures containing SO_2, CO_2, NO_x, O_2 and H_2O to evaluate a sorbent's affinity for different flue gas molecules using a fluidised bed microreactor.
- Use more complex breakthrough curve modelling techniques, such as the transient gas-phase mass balance for a differential control volume of an adsorption column, to understand, describe and predict the breakthrough mechanism more accurately.

7.3 Contribution to knowledge

The following contributions were made to the existing knowledge and field of science:

- Adsorption and desorption kinetic rate data collected from a micro fixed-bed reactor setup
- The adsorption and desorption (regeneration) properties of the activated carbon samples were determined from a 10 cycle regeneration process.
- Determination of the thermodynamic data for dry activated carbon sorbents from the CO_2 adsorption kinetic using only the data micro fixed bed reactor.
- Confirming the validity of the Avrami kinetic rate model to the kinetic rate of CO_2 desorption onto dry activated carbon samples. The results recorded in this investigation compared well with results published in open literature.

BIBLIOGRAPHY

Abd, A.A., Othman, M.R. and Kim, J. (2021) 'A review on application of activated carbons for carbon dioxide capture: present performance, preparation, and surface modification for further improvement', *Environmental Science and Pollution Research*, 28(32), pp. 43329–43364. Available at: https://doi.org/10.1007/s11356-021-15121-9.

Abu-Zahra, M.R.M., Sodiq, A. and Feron, P.H.M. (2016) 'Commercial liquid absorbent-based PCC processes', in *Absorption-Based Post-combustion Capture of Carbon Dioxide*. Elsevier, pp. 757–778. Available at: https://doi.org/10.1016/B978-0-08-100514-9.00029-9.

Adelodun, A.A., Ngila, J.C., Kim, D.-G. and Jo, Y.-M. (2017) 'Isotherm, Thermodynamic and Kinetic Studies of Selective CO2 Adsorption on Chemically Modified Carbon Surfaces', *Aerosol and Air Quality Research*, 16(12), pp. 3312–3329. Available at: https://doi.org/10.4209/aaqr.2016.01.0014.

Al-Ghouti, M.A. and Da'ana, D.A. (2020) 'Guidelines for the use and interpretation of adsorption isotherm models: A review', *Journal of Hazardous Materials*, 393, p. 122383. Available at: https://doi.org/10.1016/j.jhazmat.2020.122383.

Allen, D.T., Barteau, M.A., Burkart, M., Dunn, J., Gaffney, A.M., Gupta, R., Hazari, N., Kanan, M., Kenis, P., Klee, H., Sant, G.N. and Tway, C.L. (2019) *Gaseous Carbon Waste Streams Utilization*. Edited by T. Fryberger, M. Shelton-Davenport, C. Tran, A. Sberegaeva, J.I. Nguyen, J. Wolfman, and S. Banskota. Washington, D.C.: National Academies Press. Available at: https://doi.org/10.17226/25232.

Al-Marri, M.J., Kuti, Y.O., Khraisheh, M., Kumar, A. and Khader, M.M. (2017) 'Kinetics of CO_2 Adsorption/Desorption of Polyethyleneimine-Mesoporous Silica', *Chemical Engineering & Technology*, 40(10), pp. 1802–1809. Available at: https://doi.org/10.1002/ceat.201600452.

Álvarez-Gutiérrez, N., García, S., Gil, M.V., Rubiera, F. and Pevida, C. (2016) 'Dynamic Performance of Biomass-Based Carbons for CO_2 /CH_4 Separation. Approximation to a Pressure Swing Adsorption Process for Biogas Upgrading', *Energy & Fuels*, 30(6), pp. 5005–5015. Available at: https://doi.org/10.1021/acs.energyfuels.6b00664.

Ammendola, P., Raganati, F. and Chirone, R. (2017) 'CO2 adsorption on a fine activated carbon in a sound assisted fluidized bed: Thermodynamics and kinetics', *Chemical Engineering Journal*, 322, pp. 302–313. Available at: https://doi.org/10.1016/J.CEJ.2017.04.037.

Anderson, T.R., Hawkins, E. and Jones, P.D. (2016) 'CO2, the greenhouse effect and global warming: from the pioneering work of Arrhenius and Callendar to today's Earth System Models', *Endeavour*, 40(3), pp. 178–187. Available at: https://doi.org/10.1016/j.endeavour.2016.07.002.

Azizian, S. and Bashiri, H. (2008) 'Description of Desorption Kinetics at the Solid/Solution Interface Based on the Statistical Rate Theory', *Langmuir*, 24(22), pp. 13013–13018. Available at: https://doi.org/10.1021/la8029769.

Bamdad, H., Hawboldt, K. and MacQuarrie, S. (2018) 'Nitrogen Functionalized Biochar as a Renewable Adsorbent for Efficient CO_2 Removal', *Energy & Fuels*, 32(11), pp. 11742–11748. Available at: https://doi.org/10.1021/acs.energyfuels.8b03056.

Beck, B., Surridge, T. and Hietkamp, S. (2013) 'The South African Centre for Carbon Capture and Storage Delivering CCS in the Developing World', *Energy Procedia*, 37, pp. 6502–6507. Available at: https://doi.org/10.1016/j.egypro.2013.06.580.

Bhatta, L.K.G., Subramanyam, S., Chengala, M.D., Olivera, S. and Venkatesh, K. (2015a) 'Progress in hydrotalcite like compounds and metal-based oxides for CO2 capture: a review', *Journal of Cleaner Production*, 103, pp. 171–196. Available at: https://doi.org/10.1016/j.jclepro.2014.12.059.

Bhatta, L.K.G., Subramanyam, S., Chengala, M.D., Olivera, S. and Venkatesh, K. (2015b) 'Progress in hydrotalcite like compounds and metal-based oxides for CO2 capture: a review', *Journal of Cleaner Production*, 103, pp. 171–196. Available at: https://doi.org/10.1016/j.jclepro.2014.12.059.

Bolan, S., Padhye, L.P., Jasemizad, T., Govarthanan, M., Karmegam, N., Wijesekara, H., Amarasiri, D., Hou, D., Zhou, P., Biswal, B.K., Balasubramanian, R., Wang, H., Siddique, K.H.M., Rinklebe, J., Kirkham, M.B. and Bolan, N. (2024) 'Impacts of climate change on the fate of contaminants through extreme weather events', *Science of The Total Environment*, 909, p. 168388. Available at: https://doi.org/10.1016/j.scitotenv.2023.168388.

Brunauer, S., Emmett, P.H. and Teller, E. (1938a) 'Adsorption of Gases in Multimolecular Layers', *Journal of the American Chemical Society*, 60(2), pp. 309–319. Available at: https://doi.org/10.1021/ja01269a023.

Brunauer, S., Emmett, P.H. and Teller, E. (1938b) 'Adsorption of Gases in Multimolecular Layers', *Journal of the American Chemical Society*, 60(2), pp. 309–319. Available at: https://doi.org/10.1021/ja01269a023.

Cazorla-Amorós, D., Alcañiz-Monge, J. and Linares-Solano, A. (1996) 'Characterization of Activated Carbon Fibers by CO $_2$ Adsorption', *Langmuir*, 12(11), pp. 2820–2824. Available at: https://doi.org/10.1021/la960022s.

Chegeni, A., Babaeipour, V., Fathollahi, M. and Hosseini, S.G. (2022) 'Modeling of CO2 Adsorption Isotherms, Kinetics and Thermodynamics Equilibrium, and the Brunauer−Emmett−Teller Analysis onto KO2 Pellets', *Journal of Cluster Science*, 33(5), pp. 2167–2178. Available at: https://doi.org/10.1007/s10876-021-02142-0.

Chen, T., Da, T. and Ma, Y. (2021) 'Reasonable calculation of the thermodynamic parameters from adsorption equilibrium constant', *Journal of Molecular Liquids*, 322, p. 114980. Available at: https://doi.org/10.1016/j.molliq.2020.114980.

Choi, S., Moon, H., Bang, M., Kim, K., Park, Y.-K. and Cho, H.H. (2021) 'Efficient design of heat exchange for CFB reactors in CO2 capture system regarding geometry-induced secondary flow', *Energy Conversion and Management*, 235, p. 113995. Available at: https://doi.org/10.1016/j.enconman.2021.113995.

Chulliyil, H.M., Hamdani, I.R., Ahmad, A., Al Shoaibi, A. and Chandrasekar, S. (2024) 'Enhanced moisture adsorption of activated carbon through surface modification', *Results in Surfaces and Interfaces*, 14, p. 100170. Available at: https://doi.org/10.1016/j.rsurfi.2023.100170.

de Coninck, H. and Benson, S.M. (2014) 'Carbon Dioxide Capture and Storage: Issues and Prospects', *Annual Review of Environment and Resources*, 39(1), pp. 243–270. Available at: https://doi.org/10.1146/annurev-environ-032112-095222.

Czerw, K., Baran, P. and Zarębska, K. (2017) 'Application of the stretched exponential equation to sorption of mine gases and sorption induced swelling of bituminous coal', *International Journal of Coal Geology*, 173, pp. 76–83. Available at: https://doi.org/10.1016/j.coal.2017.02.010.

David, E., Stanciu, V., Sandru, C., Armeanu, A. and Niculescu, V. (2007) 'Exhaust gas treatment technologies for pollutant emission abatement from fossil fuel power plants', in *Sustainable Development and Planning III*. Southampton, UK: WIT Press, pp. 923–932. Available at: https://doi.org/10.2495/SDP070882.

Du, X., Cheng, Y., Liu, Z., Yin, H., Wu, T., Huo, L. and Shu, C. (2021) 'CO2 and CH4 adsorption on different rank coals: A thermodynamics study of surface potential, Gibbs free energy change and entropy loss', *Fuel*, 283, p. 118886. Available at: https://doi.org/10.1016/j.fuel.2020.118886.

Dziejarski, B. and Kisiela-Czajka, A. (2021) ‘Kinetic and equilibrium study of the CO2 adsorption on activated carbon’, *INTERNATIONAL SCIENTIFIC JOURNAL ‘MACHINES. TECHNOLOGIES. MATERIALS’*, 15(8), pp. 299–302.

Fatima, S.S., Borhan, A., Ayoub, M. and Ghani, N.A. (2023) ‘Modeling of CO2 Adsorption on Surface-Functionalized Rubber-Seed Shell Activated Carbon: Isotherm and Kinetic Analysis’, *Processes*, 11(10), p. 2833. Available at: https://doi.org/10.3390/pr11102833.

Figueroa, J.D., Fout, T., Plasynski, S., McIlvried, H. and Srivastava, R.D. (2008) ‘Advances in CO2 capture technology—The U.S. Department of Energy’s Carbon Sequestration Program’, *International Journal of Greenhouse Gas Control*, 2(1), pp. 9–20. Available at: https://doi.org/10.1016/S1750-5836(07)00094-1.

G. Ibrahim, H. and A. Al-Meshragi, M. (2020) ‘Experimental Study of Adsorption on Activated Carbon for CO $_2$ Capture’, in *CO2 Sequestration*. IntechOpen. Available at: https://doi.org/10.5772/intechopen.85834.

Gao, X., Yang, S., Hu, L., Cai, S., Wu, L. and Kawi, S. (2022) ‘Carbonaceous materials as adsorbents for CO2 capture: synthesis and modification’, *Carbon Capture Science & Technology*, 3, p. 100039. Available at: https://doi.org/10.1016/j.ccst.2022.100039.

Glenna, D.M., Jana, A., Xu, Q., Wang, Y., Meng, Y., Yang, Y., Neupane, M., Wang, L., Zhao, H., Qian, J. and Snyder, S.W. (2023) ‘Carbon Capture: Theoretical Guidelines for Activated Carbon-Based CO $_2$ Adsorption Material Evaluation’, *The Journal of Physical Chemistry Letters*, 14(47), pp. 10693–10699. Available at: https://doi.org/10.1021/acs.jpclett.3c02711.

Goel, C., Kaur, H., Bhunia, H. and Bajpai, P.K. (2016) ‘Carbon dioxide adsorption on nitrogen enriched carbon adsorbents: Experimental, kinetics, isothermal and thermodynamic studies’, *Journal of CO2 Utilization*, 16, pp. 50–63. Available at: https://doi.org/10.1016/j.jcou.2016.06.002.

Gong, J., Liu, J., Chen, X., Jiang, Z., Wen, X., Mijowska, E. and Tang, T. (2015) ‘Converting real-world mixed waste plastics into porous carbon nanosheets with excellent performance in the adsorption of an organic dye from wastewater’, *Journal of Materials Chemistry A*, 3(1), pp. 341–351. Available at: https://doi.org/10.1039/C4TA05118A.

Grace, J.R. and Lim, C.J. (2013) ‘Properties of circulating fluidized beds (CFB) relevant to combustion and gasification systems’, *Fluidized Bed Technologies for Near-Zero Emission Combustion and Gasification*, pp. 147–176. Available at: https://doi.org/10.1533/9780857098801.1.147.

Gunawan, T., Wijiyanti, R. and Widiastuti, N. (2018) 'Adsorption–desorption of CO_2 on zeolite-Y-templated carbon at various temperatures', *RSC Advances*, 8(72), pp. 41594–41602. Available at: https://doi.org/10.1039/C8RA09200A.

Günther, S., Menteş, T.O., Niño, M.A., Locatelli, A., Böcklein, S. and Wintterlin, J. (2014) 'Desorption kinetics from a surface derived from direct imaging of the adsorbate layer', *Nature Communications*, 5(1), p. 3853. Available at: https://doi.org/10.1038/ncomms4853.

Halder, G., Khan, A.A. and Dhawane, S. (2016) 'Fluoride Sorption Onto a Steam-Activated Biochar Derived From *Cocos nucifera* Shell', *CLEAN - Soil, Air, Water*, 44(2), pp. 124–133. Available at: https://doi.org/10.1002/clen.201400649.

Hao, W., Björkman, E., Lilliestråle, M. and Hedin, N. (2013) 'Activated carbons prepared from hydrothermally carbonized waste biomass used as adsorbents for CO2', *Applied Energy*, 112, pp. 526–532. Available at: https://doi.org/10.1016/j.apenergy.2013.02.028.

Hauchhum, L. and Mahanta, P. (2014a) 'Carbon dioxide adsorption on zeolites and activated carbon by pressure swing adsorption in a fixed bed', *International Journal of Energy and Environmental Engineering*, 5(4), pp. 349–356. Available at: https://doi.org/10.1007/s40095-014-0131-3.

Hauchhum, L. and Mahanta, P. (2014b) 'Carbon dioxide adsorption on zeolites and activated carbon by pressure swing adsorption in a fixed bed', *International Journal of Energy and Environmental Engineering*, 5(4), pp. 349–356. Available at: https://doi.org/10.1007/s40095-014-0131-3.

Hauchhum, L. and Mahanta, P. (2017) 'Performance enhancement of CO 2 capture from flue gas in a bubbling fluidized bed', *Journal of the Energy Institute*, 90(5), pp. 764–775. Available at: https://doi.org/10.1016/j.joei.2016.06.007.

He, L., Fan, Y., Bellettre, J., Yue, J. and Luo, L. (2020) 'A review on catalytic methane combustion at low temperatures: Catalysts, mechanisms, reaction conditions and reactor designs', *Renewable and Sustainable Energy Reviews*, 119, p. 109589. Available at: https://doi.org/10.1016/j.rser.2019.109589.

Heydari-Gorji, A. and Sayari, A. (2011) 'CO2 capture on polyethylenimine-impregnated hydrophobic mesoporous silica: Experimental and kinetic modeling', *Chemical Engineering Journal*, 173(1), pp. 72–79. Available at: https://doi.org/10.1016/j.cej.2011.07.038.

Hou, D., Al-Tabbaa, A., O'Connor, D., Hu, Q., Zhu, Y.-G., Wang, L., Kirkwood, N., Ok, Y.S., Tsang, D.C.W., Bolan, N.S. and Rinklebe, J. (2023) 'Sustainable remediation and redevelopment of brownfield sites', *Nature Reviews Earth & Environment*, 4(4), pp. 271–286. Available at: https://doi.org/10.1038/s43017-023-00404-1.

Hulicova-Jurcakova, D., Puziy, A.M., Poddubnaya, O.I., Suárez-García, F., Tascón, J.M.D. and Lu, G.Q. (2009) 'Highly Stable Performance of Supercapacitors from Phosphorus-Enriched Carbons', *Journal of the American Chemical Society*, 131(14), pp. 5026–5027. Available at: https://doi.org/10.1021/ja809265m.

Jacobs, A. (2018) *Adsorption studies for carbon dioxide capture from multicomponent flue gases using activated carbon sorbents.* Potchefstroom.

Jagtoyen, M. and Derbyshire, F. (1998) 'Activated carbons from yellow poplar and white oak by H3PO4 activation', *Carbon*, 36(7–8), pp. 1085–1097. Available at: https://doi.org/10.1016/S0008-6223(98)00082-7.

Jansen, D., Gazzani, M., Manzolini, G., Dijk, E. van and Carbo, M. (2015) 'Pre-combustion CO2 capture', *International Journal of Greenhouse Gas Control*, 40, pp. 167–187. Available at: https://doi.org/10.1016/j.ijggc.2015.05.028.

Kabir, M., Habiba, U.E., Khan, W., Shah, A., Rahim, S., Rios-Escalante, P.R.D. los, Farooqi, Z.-U.-R., Ali, L. and Shafiq, M. (2023) 'Climate change due to increasing concentration of carbon dioxide and its impacts on environment in 21st century; a mini review', *Journal of King Saud University - Science*, 35(5), p. 102693. Available at: https://doi.org/10.1016/j.jksus.2023.102693.

Kakaras, E., Koumanakos, A.K. and Doukelis, A. (2012) 'Pressurized fluidized bed combustion (PFBC) combined cycle systems', in *Combined cycle systems for near-zero emission power generation*. Athens: Woodhead Publishing Limited, pp. 220–233.

Kamran, U. and Park, S.-J. (2021) 'Chemically modified carbonaceous adsorbents for enhanced CO2 capture: A review', *Journal of Cleaner Production*, 290, p. 125776. Available at: https://doi.org/10.1016/j.jclepro.2020.125776.

Kanniche, M., Gros-Bonnivard, R., Jaud, P., Valle-Marcos, J., Amann, J.-M. and Bouallou, C. (2010) 'Pre-combustion, post-combustion and oxy-combustion in thermal power plant for CO2 capture', *Applied Thermal Engineering*, 30(1), pp. 53–62. Available at: https://doi.org/10.1016/j.applthermaleng.2009.05.005.

Karunasingha, D.S.K. (2022) ‘Root mean square error or mean absolute error? Use their ratio as well’, *Information Sciences*, 585, pp. 609–629. Available at: https://doi.org/10.1016/j.ins.2021.11.036.

Kaur, B., Gupta, R.K. and Bhunia, H. (2020) ‘CO_2 capture on activated carbon from PET (polyethylene terephthalate) waste: Kinetics and modeling studies’, *Chemical Engineering Communications*, 207(8), pp. 1031–1047. Available at: https://doi.org/10.1080/00986445.2019.1635466.

Keer, M., Lohiya, H. and Chouhan, S. (2023) ‘Goodness of Fit for Linear Regression using R squared and Adjusted R-Squared’, *International Journal of Research Publication and Reviews*, 4(3), pp. 2431–2439.

Keller, J. u and Staudt, R. (2005) *Gas Adsorption Equilibria*. Boston: Kluwer Academic Publishers. Available at: https://doi.org/10.1007/b102056.

Keza, B.C.B., Argönül, A. and Alp, D. (2022) ‘Measurement of carbon dioxide adsorption capacity on selected Turkish lignites’, *International Journal of Greenhouse Gas Control*, 115, p. 103608. Available at: https://doi.org/10.1016/j.ijggc.2022.103608.

Khan, U., Ogbaga, C.C., Abiodun, O.-A.O., Adeleke, A.A., Ikubanni, P.P., Okoye, P.U. and Okolie, J.A. (2023) ‘Assessing absorption-based CO2 capture: Research progress and techno-economic assessment overview’, *Carbon Capture Science & Technology*, 8, p. 100125. Available at: https://doi.org/10.1016/j.ccst.2023.100125.

Kim, K.H. and Kim, Y. (2008) ‘Theoretical Studies for Lewis Acid−Base Interactions and C−H···O Weak Hydrogen Bonding in Various CO_2 Complexes’, *The Journal of Physical Chemistry A*, 112(7), pp. 1596–1603. Available at: https://doi.org/10.1021/jp709648q.

Knowlton, T.M. (2013) ‘Fluidized bed reactor design and scale-up’, *Fluidized Bed Technologies for Near-Zero Emission Combustion and Gasification*, pp. 481–523. Available at: https://doi.org/10.1533/9780857098801.2.481.

Knowlton, T.M., Karri, S.B.R. and Issangya, A. (2005) ‘Scale-up of fluidized-bed hydrodynamics’, *Powder Technology*, 150(2), pp. 72–77. Available at: https://doi.org/10.1016/j.powtec.2004.11.036.

Król-Morkisz, K. and Pielichowska, K. (2019) ‘Thermal Decomposition of Polymer Nanocomposites With Functionalized Nanoparticles’, *Polymer Composites with Functionalized*

Nanoparticles: Synthesis, Properties, and Applications, pp. 405–435. Available at: https://doi.org/10.1016/B978-0-12-814064-2.00013-5.

Kruk, M. and Jaroniec, M. (2001) 'Gas Adsorption Characterization of Ordered Organic−Inorganic Nanocomposite Materials', *Chemistry of Materials*, 13(10), pp. 3169–3183. Available at: https://doi.org/10.1021/cm0101069.

Leung, D.Y.C., Caramanna, G. and Maroto-Valer, M.M. (2014a) 'An overview of current status of carbon dioxide capture and storage technologies', *Renewable and Sustainable Energy Reviews*, 39, pp. 426–443. Available at: https://doi.org/10.1016/j.rser.2014.07.093.

Leung, D.Y.C., Caramanna, G. and Maroto-Valer, M.M. (2014b) 'An overview of current status of carbon dioxide capture and storage technologies', *Renewable and Sustainable Energy Reviews*, 39, pp. 426–443. Available at: https://doi.org/10.1016/j.rser.2014.07.093.

Li, J.-R., Sculley, J. and Zhou, H.-C. (2012) 'Metal–Organic Frameworks for Separations', *Chemical Reviews*, 112(2), pp. 869–932. Available at: https://doi.org/10.1021/cr200190s.

Liu, J., Wang, Y., Benin, A.I., Jakubczak, P., Willis, R.R. and LeVan, M.D. (2010) 'CO_2/H_2O Adsorption Equilibrium and Rates on Metal−Organic Frameworks: HKUST-1 and Ni/DOBDC', *Langmuir*, 26(17), pp. 14301–14307. Available at: https://doi.org/10.1021/la102359q.

Liu, Y. and Yu, X. (2018) 'Carbon dioxide adsorption properties and adsorption/desorption kinetics of amine-functionalized KIT-6', *Applied Energy*, 211, pp. 1080–1088. Available at: https://doi.org/10.1016/j.apenergy.2017.12.016.

Lu, G., Wei, C., Wang, J., Yan, G., Zhang, J. and Song, Y. (2018) 'Methane Adsorption Characteristics and Adsorption Model Applicability of Tectonically Deformed Coals in the Huaibei Coalfield', *Energy & Fuels*, 32(7), pp. 7485–7496. Available at: https://doi.org/10.1021/acs.energyfuels.8b01397.

Lui, Y., Wu, J., Zhang, C., Chen, Y., Xiong, M., Shi, R., Lin, X. and Yu, X. (2019) 'Thermodynamic and kinetic study of CO2 adsorption/desorption amine-functionalized sorbents', *Indian Journal of Chemical Technology*, 26, pp. 473–482. Available at: https://nopr.niscpr.res.in/bitstream/123456789/52675/1/IJCT%2026%286%29%20473-482.pdf (Accessed: 7 December 2024).

Lussier, M.G., Zhang, Z. and Miller, D.J. (1998) 'Characterizing rate inhibition in steam/hydrogen gasification via analysis of adsorbed hydrogen', *Carbon*, 36(9), pp. 1361–1369. Available at: https://doi.org/10.1016/S0008-6223(98)00123-7.

Ma, X., Yang, Y., Wu, Q., Liu, B., Li, D., Chen, R., Wang, C., Li, H., Zeng, Z. and Li, L. (2020) 'Underlying mechanism of CO2 uptake onto biomass-based porous carbons: Do adsorbents capture CO2 chiefly through narrow micropores?', *Fuel*, 282, p. 118727. Available at: https://doi.org/10.1016/j.fuel.2020.118727.

Mallesh, D., Anbarasan, J., Mahesh Kumar, P., Upendar, K., Chandrashekar, P., Rao, B.V.S.K. and Lingaiah, N. (2020) 'Synthesis, characterization of carbon adsorbents derived from waste biomass and its application to CO2 capture', *Applied Surface Science*, 530, p. 147226. Available at: https://doi.org/10.1016/j.apsusc.2020.147226.

Marsh, H. and Rodríguez-Reinoso, F. (2006a) 'Activation Processes (Thermal or Physical)', *Activated Carbon*, pp. 243–321. Available at: https://doi.org/10.1016/B978-008044463-5/50019-4.

Marsh, H. and Rodríguez-Reinoso, F. (2006b) 'Characterization of Activated Carbon', in *Activated Carbon*. Elsevier, pp. 143–242. Available at: https://doi.org/10.1016/B978-008044463-5/50018-2.

Martínez de Yuso, A., Rubio, B. and Izquierdo, M.T. (2014) 'Influence of activation atmosphere used in the chemical activation of almond shell on the characteristics and adsorption performance of activated carbons', *Fuel Processing Technology*, 119, pp. 74–80. Available at: https://doi.org/10.1016/j.fuproc.2013.10.024.

Mathangi, J.B., Sadeesh Sharma, M., Mercy Jacquline, B. and Helen Kalavathy, M. (2018) 'Development of carbon-based material from biomass for the removal of Ni2+ and CO2 from fluid phase', *Vacuum*, 158, pp. 236–248. Available at: https://doi.org/10.1016/j.vacuum.2018.09.056.

Mayoral, M.C., Izquierdo, M.T., Andrés, J.M. and Rubio, B. (2001) 'Different approaches to proximate analysis by thermogravimetry analysis', *Thermochimica Acta*, 370(1–2), pp. 91–97. Available at: https://doi.org/10.1016/S0040-6031(00)00789-9.

Mazlan, M.A.F., Uemura, Y., Yusup, S., Elhassan, F., Uddin, A., Hiwada, A. and Demiya, M. (2016) 'Activated Carbon from Rubber Wood Sawdust by Carbon Dioxide Activation', *Procedia Engineering*, 148, pp. 530–537. Available at: https://doi.org/10.1016/j.proeng.2016.06.549.

Mcsweeney, R. and Timperley, J. (2018) *The Carbon Brief Profile: South Africa*. Available at: https://www.carbonbrief.org/the-carbon-brief-profile-south-africa (Accessed: 27 September 2022).

Medina-Rodriguez, B.X. and Alvarado, V. (2021) 'Use of Gas Adsorption and Inversion Methods for Shale Pore Structure Characterization', *Energies*, 14(10), p. 2880. Available at: https://doi.org/10.3390/en14102880.

Al Mesfer, M.K. and Danish, M. (2018) 'Breakthrough adsorption study of activated carbons for CO2 separation from flue gas', *Journal of Environmental Chemical Engineering*, 6(4), pp. 4514–4524. Available at: https://doi.org/10.1016/j.jece.2018.06.042.

Mesfer, M.K. Al, Danish, M., Khan, M.I., Ali, I.H., Hasan, M. and Jery, A. El (2020) 'Continuous Fixed Bed CO2 Adsorption: Breakthrough, Column Efficiency, Mass Transfer Zone', *Processes*, 8(10), p. 1233. Available at: https://doi.org/10.3390/pr8101233.

Nakao, S., Yogo, K., Goto, K., Kai, T. and Yamada, H. (2019) *Advanced CO2 Capture Technologies*. Cham: Springer International Publishing. Available at: https://doi.org/10.1007/978-3-030-18858-0.

Naksusuk, S. and Tangsathitkulchai, C. (2019) 'Carbon Dioxide Capture in a Fixed Bed of Coconut Shell Activated Carbon Impregnated With Sodium Hydroxide: Effects of Carbon Pore Texture and Alkali Loading', *Engineering Journal*, 23(4), pp. 29–48. Available at: https://doi.org/10.4186/ej.2019.23.4.29.

NASA (2022) *The Effects of Climate Change*. Available at: https://climate.nasa.gov/effects/ (Accessed: 12 July 2022).

Okolo, G.N. (2017) *Adsorption properties of South African bituminous coals relevant to carbon dioxide storage*. North-West University.

Olivares-Marín, M., Fernández-González, C., Macías-García, A. and Gómez-Serrano, V. (2006) 'Thermal behaviour of lignocellulosic material in the presence of phosphoric acid. Influence of the acid content in the initial solution', *Carbon*, 44(11), pp. 2347–2350. Available at: https://doi.org/10.1016/j.carbon.2006.04.004.

Omidi, M., Fatehinya, A., Farahani, M., Akbari, Z., Shahmoradi, S., Yazdian, F., Tahriri, M., Moharamzadeh, K., Tayebi, L. and Vashaee, D. (2017) 'Characterization of biomaterials', in *Biomaterials for Oral and Dental Tissue Engineering*. Elsevier, pp. 97–115. Available at: https://doi.org/10.1016/B978-0-08-100961-1.00007-4.

Osman, A.I., Hefny, M., Abdel Maksoud, M.I.A., Elgarahy, A.M. and Rooney, D.W. (2021) 'Recent advances in carbon capture storage and utilisation technologies: a review', *Environmental*

Chemistry Letters, 19(2), pp. 797–849. Available at: https://doi.org/10.1007/s10311-020-01133-3.

Panczyk, T. and Rudzinski, W. (2004) 'A Statistical Rate Theory Approach to Kinetics of Dissociative Gas Adsorption on Solids', *Journal of Physical Chemistry*, 108, pp. 2898–2909.

Patil, P., Jeppu, G., Girish, C.R. and Mohan, B. (2024) 'Development of a comprehensive analytical solution for modeling adsorption kinetics and equilibrium', *Separation Science and Technology*, 59(3), pp. 373–394. Available at: https://doi.org/10.1080/01496395.2024.2319146.

Pezoti, O., Cazetta, A.L., Bedin, K.C., Souza, L.S., Martins, A.C., Silva, T.L., Santos Júnior, O.O., Visentainer, J. V. and Almeida, V.C. (2016) 'NaOH-activated carbon of high surface area produced from guava seeds as a high-efficiency adsorbent for amoxicillin removal: Kinetic, isotherm and thermodynamic studies', *Chemical Engineering Journal*, 288, pp. 778–788. Available at: https://doi.org/10.1016/j.cej.2015.12.042.

Plaza, M.G., García, S., Rubiera, F., Pis, J.J. and Pevida, C. (2010) 'Post-combustion CO2 capture with a commercial activated carbon: Comparison of different regeneration strategies', *Chemical Engineering Journal*, 163(1–2), pp. 41–47. Available at: https://doi.org/10.1016/j.cej.2010.07.030.

Prauchner, M.J., Sapag, K. and Rodríguez-Reinoso, F. (2016) 'Tailoring biomass-based activated carbon for CH4 storage by combining chemical activation with H3PO4 or ZnCl2 and physical activation with CO2', *Carbon*, 110, pp. 138–147. Available at: https://doi.org/10.1016/j.carbon.2016.08.092.

Qi, S., Adham, S.S., Snoeyink, V.L. and Lykins, B.W. (1994) 'Prediction and Verification of Atrazine Adsorption by PAC', *Journal of Environmental Engineering*, 120(1), pp. 202–218. Available at: https://doi.org/10.1061/(ASCE)0733-9372(1994)120:1(202).

Raganati, F., Alfe, M., Gargiulo, V., Chirone, R. and Ammendola, P. (2018) 'Isotherms and thermodynamics of CO2 adsorption on a novel carbon-magnetite composite sorbent', *Chemical Engineering Research and Design*, 134, pp. 540–552. Available at: https://doi.org/10.1016/j.cherd.2018.04.037.

Raganati, F., Alfe, M., Gargiulo, V., Chirone, R. and Ammendola, P. (2019) 'Kinetic study and breakthrough analysis of the hybrid physical/chemical CO2 adsorption/desorption behavior of a magnetite-based sorbent', *Chemical Engineering Journal*, 372, pp. 526–535. Available at: https://doi.org/10.1016/j.cej.2019.04.165.

Raganati, F., Ammendola, P. and Chirone, R. (2015) 'Effect of acoustic field on CO2 desorption in a fluidized bed of fine activated carbon', *Particuology*, 23, pp. 8–15. Available at: https://doi.org/10.1016/j.partic.2015.02.001.

Raganati, F., Chirone, R. and Ammendola, P. (2020) 'CO $_2$ Capture by Temperature Swing Adsorption: Working Capacity As Affected by Temperature and CO $_2$ Partial Pressure', *Industrial & Engineering Chemistry Research*, 59(8), pp. 3593–3605. Available at: https://doi.org/10.1021/acs.iecr.9b04901.

Rashidi, N.A., Bokhari, A. and Yusup, S. (2021) 'Evaluation of kinetics and mechanism properties of CO2 adsorption onto the palm kernel shell activated carbon', *Environmental Science and Pollution Research*, 28(26), pp. 33967–33979. Available at: https://doi.org/10.1007/s11356-020-08823-z.

Rashidi, N.A., Yusup, S. and Borhan, A. (2016) 'Isotherm and Thermodynamic Analysis of Carbon Dioxide on Activated Carbon', *Procedia Engineering*, 148, pp. 630–637. Available at: https://doi.org/10.1016/j.proeng.2016.06.527.

Román, S., González, J.F., González-García, C.M. and Zamora, F. (2008) 'Control of pore development during CO2 and steam activation of olive stones', *Fuel Processing Technology*, 89(8), pp. 715–720. Available at: https://doi.org/10.1016/j.fuproc.2007.12.015.

Rouzitalab, Z., Mohammady Maklavany, D., Rashidi, A. and Jafarinejad, S. (2018) 'Synthesis of N-doped nanoporous carbon from walnut shell for enhancing CO2 adsorption capacity and separation', *Journal of Environmental Chemical Engineering*, 6(5), pp. 6653–6663. Available at: https://doi.org/10.1016/j.jece.2018.10.035.

Samanta, A., Zhao, A., Shimizu, G.K.H., Sarkar, P. and Gupta, R. (2012) 'Post-Combustion CO $_2$ Capture Using Solid Sorbents: A Review', *Industrial & Engineering Chemistry Research*, 51(4), pp. 1438–1463. Available at: https://doi.org/10.1021/ie200686q.

Savara, A. (2013) 'Standard States for Adsorption on Solid Surfaces: 2D Gases, Surface Liquids, and Langmuir Adsorbates', *The Journal of Physical Chemistry C*, 117(30), pp. 15710–15715. Available at: https://doi.org/10.1021/jp404398z.

Seki, H. and Suzuki, A. (1999) 'Kinetic Study of Lead Adsorption to Composite Biopolymer Adsorbent', *Journal of Colloid and Interface Science*, 211(2), pp. 375–379. Available at: https://doi.org/10.1006/jcis.1998.6000.

Seredych, M., Jagiello, J. and Bandosz, T.J. (2014) 'Complexity of CO2 adsorption on nanoporous sulfur-doped carbons – Is surface chemistry an important factor?', *Carbon*, 74, pp. 207–217. Available at: https://doi.org/10.1016/j.carbon.2014.03.024.

Sevilla, M., Falco, C., Titirici, M.-M. and Fuertes, A.B. (2012) 'High-performance CO2 sorbents from algae', *RSC Advances*, 2(33), p. 12792. Available at: https://doi.org/10.1039/c2ra22552b.

Sevilla, M. and Mokaya, R. (2014) 'Energy storage applications of activated carbons: supercapacitors and hydrogen storage', *Energy Environ. Sci.*, 7(4), pp. 1250–1280. Available at: https://doi.org/10.1039/C3EE43525C.

Shafeeyan, M. saleh (2015) *Fixed-bed adsorption of carbon dioxide onto ammonia-modified activated carbon: Experimental and modelling study*. University of Malaya. Available at: http://studentsrepo.um.edu.my/5754/1/Shafeeyan-PhD_Thesis-KHA110017.pdf (Accessed: 28 November 2023).

Shafeeyan, M.S., Daud, W.M.A.W., Shamiri, A. and Aghamohammadi, N. (2015) 'Modeling of Carbon Dioxide Adsorption onto Ammonia-Modified Activated Carbon: Kinetic Analysis and Breakthrough Behavior', *Energy & Fuels*, 29(10), pp. 6565–6577. Available at: https://doi.org/10.1021/acs.energyfuels.5b00653.

Shafeeyan, M.S., Wan Daud, W.M.A. and Shamiri, A. (2014) 'A review of mathematical modeling of fixed-bed columns for carbon dioxide adsorption', *Chemical Engineering Research and Design*, 92(5), pp. 961–988. Available at: https://doi.org/10.1016/j.cherd.2013.08.018.

Shen, C., Grande, C.A., Li, P., Yu, J. and Rodrigues, A.E. (2010) 'Adsorption equilibria and kinetics of CO2 and N2 on activated carbon beads', *Chemical Engineering Journal*, 160(2), pp. 398–407. Available at: https://doi.org/10.1016/j.cej.2009.12.005.

Sinazo Mkoko (2024) *South Africa launches its first CCUS research site*, *ESI Africa*.

Sing, Vinod. and Kumar, E. (2017) *Estimation of Thermodynamic Properties of CO2 Adsorption on Activated Carbon*.

Singh, G., Bahadur, R., Mee Lee, J., Young Kim, I., Ruban, A.M., Davidraj, J.M., Semit, D., Karakoti, A., Al Muhtaseb, A.H. and Vinu, A. (2021) 'Nanoporous activated biocarbons with high surface areas from alligator weed and their excellent performance for CO2 capture at both low and high pressures', *Chemical Engineering Journal*, 406, p. 126787. Available at: https://doi.org/10.1016/j.cej.2020.126787.

Singh, G., Lakhi, K.S., Sil, S., Bhosale, S. V., Kim, I., Albahily, K. and Vinu, A. (2019) 'Biomass derived porous carbon for CO2 capture', *Carbon*, 148, pp. 164–186. Available at: https://doi.org/10.1016/j.carbon.2019.03.050.

Singh, J., Kumaresan, S.K., Swaroop, S. and Mishra, V. (2023) 'Development of predictive model for the fixed-bed column reactor', *Applied Water Science*, 13(5), p. 114. Available at: https://doi.org/10.1007/s13201-023-01920-7.

Sloss, L. (2017) *Emissions from coal-fired utilities in South Africa and neighbouring countries and potential for reduction*. London.

Smith, N., Miller, G., Aandi, I., Gadsden, R. and Davison, J. (2013) 'Performance and Costs of CO2 Capture at Gas Fired Power Plants', *Energy Procedia*, 37, pp. 2443–2452. Available at: https://doi.org/10.1016/j.egypro.2013.06.125.

Song, T., Liao, J., Xiao, J. and Shen, L. (2015) 'Effect of micropore and mesopore structure on CO2 adsorption by activated carbons from biomass', *New Carbon Materials*, 30(2), pp. 156–166. Available at: https://doi.org/10.1016/S1872-5805(15)60181-0.

Stanger, R., Wall, T., Spörl, R., Paneru, M., Grathwohl, S., Weidmann, M., Scheffknecht, G., McDonald, D., Myöhänen, K., Ritvanen, J., Rahiala, S., Hyppänen, T., Mletzko, J., Kather, A. and Santos, S. (2015) 'Oxyfuel combustion for CO2 capture in power plants', *International Journal of Greenhouse Gas Control*, 40, pp. 55–125. Available at: https://doi.org/10.1016/j.ijggc.2015.06.010.

Stannard, W. (2018) 'The Greenhouse Effect: An Evaluation of Arrhenius' Thesis and a New Energy Equilibrium Model', *Natural Science*, 10(01), pp. 1–10. Available at: https://doi.org/10.4236/ns.2018.101001.

Strickroth, A., Schumacher, M., Hasse, G.W. and Kgomo, I. (2020) 'Next-generation, affordable SO2 abatement for coal-fired power generation - A comparison of limestone-based wet flue gas desulphurization and Sulfacid® technologies for Medupi power station', *Journal of the Southern African Institute of Mining and Metallurgy*, 120(10). Available at: https://doi.org/10.17159/2411-9717/1252/2020.

Sun, W., Lipka, S.M., Swartz, C., Williams, D. and Yang, F. (2016) 'Hemp-derived activated carbons for supercapacitors', *Carbon*, 103, pp. 181–192. Available at: https://doi.org/10.1016/j.carbon.2016.02.090.

Teng, Y., Liu, Z., Xu, G. and Zhang, K. (2017) 'Desorption Kinetics and Mechanisms of CO2 on Amine-Based Mesoporous Silica Materials', *Energies*, 10(1), p. 115. Available at: https://doi.org/10.3390/en10010115.

Thommes, M. and Cychosz, K.A. (2014) 'Physical adsorption characterization of nanoporous materials: progress and challenges', *Adsorption*, 20(2–3), pp. 233–250. Available at: https://doi.org/10.1007/s10450-014-9606-z.

Tsiotsias, A.I., Georgiadis, A.G., Charisiou, N.D. and Goula, M.A. (2023) 'CO2 Physisorption over an Industrial Molecular Sieve Zeolite: An Experimental and Theoretical Approach', *Materials*, 16(20), p. 6656. Available at: https://doi.org/10.3390/ma16206656.

Villarroel-Rocha, J., Barrera, D., Blanco, A.A.G., Jalil, Ma.E.R. and Sapag, K. (2013) 'Importance of the α_s -plot Method in the Characterization of Nanoporous Materials', *Adsorption Science & Technology*, 31(2–3), pp. 165–183. Available at: https://doi.org/10.1260/0263-6174.31.2-3.165.

Wall, T.F. (2007) 'Combustion processes for carbon capture', *Proceedings of the Combustion Institute*, 31(1), pp. 31–47. Available at: https://doi.org/10.1016/j.proci.2006.08.123.

Wang, P., Guo, Y., Zhao, C., Yan, J. and Lu, P. (2017) 'Biomass derived wood ash with amine modification for post-combustion CO 2 capture', *Applied Energy*, 201, pp. 34–44. Available at: https://doi.org/10.1016/j.apenergy.2017.05.096.

Wang, Z. (2018) '1.23 Energy and Air Pollution', in *Comprehensive Energy Systems*. Elsevier, pp. 909–949. Available at: https://doi.org/10.1016/B978-0-12-809597-3.00127-9.

Wei, M., Yu, Q., Duan, W., Yang, F., Wu, T., Zuo, Z., Qin, Q. and Dai, J. (2017) 'CO2 desorption kinetics for waste ion-exchange resin-based activated carbon by model-fitting and model-free', *Thermochimica Acta*, 655, pp. 52–62. Available at: https://doi.org/10.1016/j.tca.2017.06.008.

Wei, M., Yu, Q., Xie, H., Zuo, Z., Hou, L. and Yang, F. (2017) 'Kinetics studies of CO2 adsorption and desorption on waste ion-exchange resin-based activated carbon', *International Journal of Hydrogen Energy*, 42(44), pp. 27122–27129. Available at: https://doi.org/10.1016/j.ijhydene.2017.09.102.

Wei, M. and Zhao, Q. (2021) 'CO2 Adsorption and Desorption by Waste Ion-Exchange Resin–Based Activated Carbon on Fixed Bed', *Frontiers in Energy Research*, 9. Available at: https://doi.org/10.3389/fenrg.2021.772710.

Willmott, C. and Matsuura, K. (2005) 'Advantages of the mean absolute error (MAE) over the root mean square error (RMSE) in assessing average model performance', *Climate Research*, 30, pp. 79–82. Available at: https://doi.org/10.3354/cr030079.

Wjihi, S., Aouaini, F., Erto, A., Balsamo, M. and Lamine, A. Ben (2021) 'Advanced interpretation of CO2 adsorption thermodynamics onto porous solids by statistical physics formalism', *Chemical Engineering Journal*, 406, p. 126669. Available at: https://doi.org/10.1016/j.cej.2020.126669.

Xin-hui, D., Srinivasakannan, C., Jin-hui, P., Li-bo, Z. and Zheng-yong, Z. (2011) 'Comparison of activated carbon prepared from Jatropha hull by conventional heating and microwave heating', *Biomass and Bioenergy*, 35(9), pp. 3920–3926. Available at: https://doi.org/10.1016/j.biombioe.2011.06.010.

Yang, K., Peng, J., Srinivasakannan, C., Zhang, L., Xia, H. and Duan, X. (2010) 'Preparation of high surface area activated carbon from coconut shells using microwave heating', *Bioresource Technology*, 101(15), pp. 6163–6169. Available at: https://doi.org/10.1016/j.biortech.2010.03.001.

Yoro, K. and Sekoai, P. (2016) 'The Potential of CO2 Capture and Storage Technology in South Africa's Coal-Fired Thermal Power Plants', *Environments*, 3(4), p. 24. Available at: https://doi.org/10.3390/environments3030024.

Yu, Q. and Brilman, D.W.F. (2017) 'Design Strategy for CO2 Adsorption from Ambient Air Using a Supported Amine Based Sorbent in a Fixed Bed Reactor', *Energy Procedia*, 114, pp. 6102–6114. Available at: https://doi.org/10.1016/j.egypro.2017.03.1747.

Zdravkov, B., Čermák, J., Šefara, M. and Janků, J. (2007) 'Pore classification in the characterization of porous materials: A perspective', *Open Chemistry*, 5(2), pp. 385–395. Available at: https://doi.org/10.2478/s11532-007-0017-9.

Zhang, T., Walawender, W., Fan, L., Fan, M., Daugaard, D. and Brown, R. (2004) 'Preparation of activated carbon from forest and agricultural residues through CO activation', *Chemical Engineering Journal*, 105(1–2), pp. 53–59. Available at: https://doi.org/10.1016/j.cej.2004.06.011.

APPENDIX A SUPPLEMENTARY EXPERIMENTAL DATA

Analysis of the effect of feed concentration on sorbent adsorption and desorption performance

This section provides supplementary graphs of the effect of feed concentration on sorbent performance for CQ650, CQ30P, and CQ006 in Figure A-1 and Figure A-2. The sorbents are compared with each other at fixed temperatures. This comparison clearly shows the differences between the sorbents and the difference the feed concentration makes, moving from 5% to 15% CO_2 feed. The higher CO_2 feed concentration significantly impacts the sorbent performance, resulting in higher adsorption capacities and increased kinetic rates for adsorption and desorption.

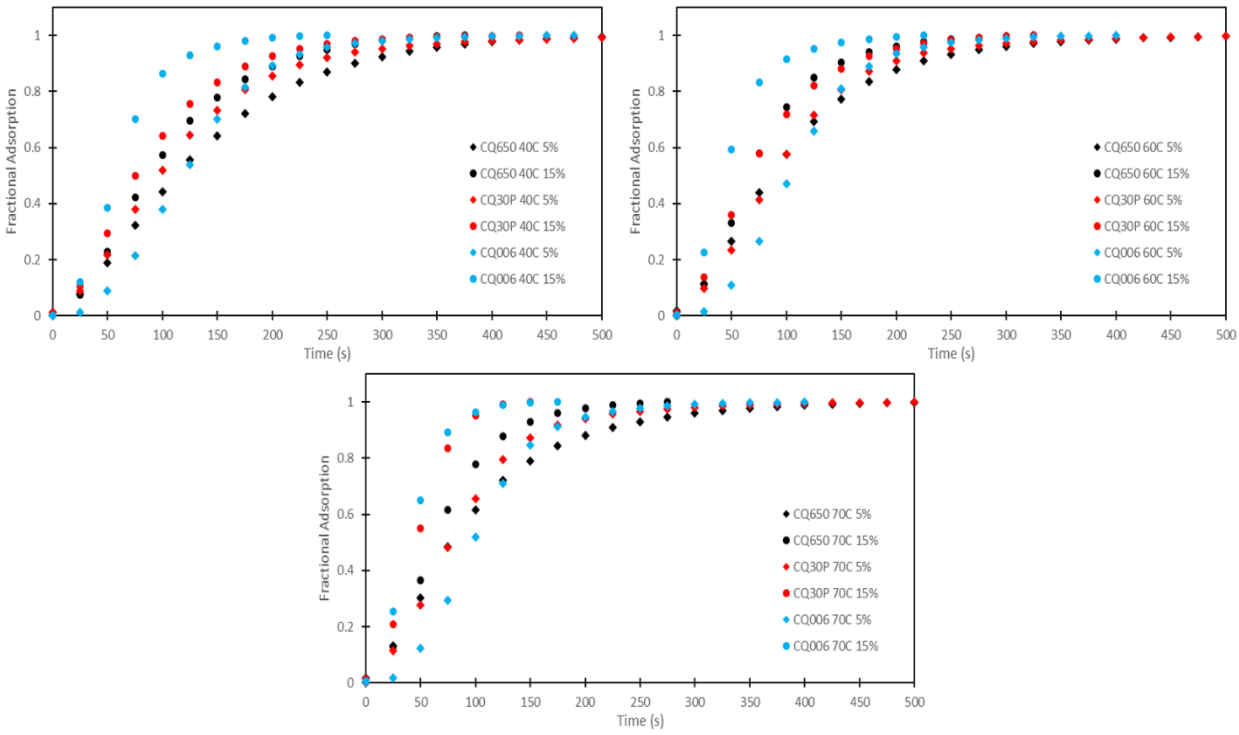

Figure A-1: Sorbent adsorption performance at a fixed temperature and both 5% and 15% CO_2 feed conditions

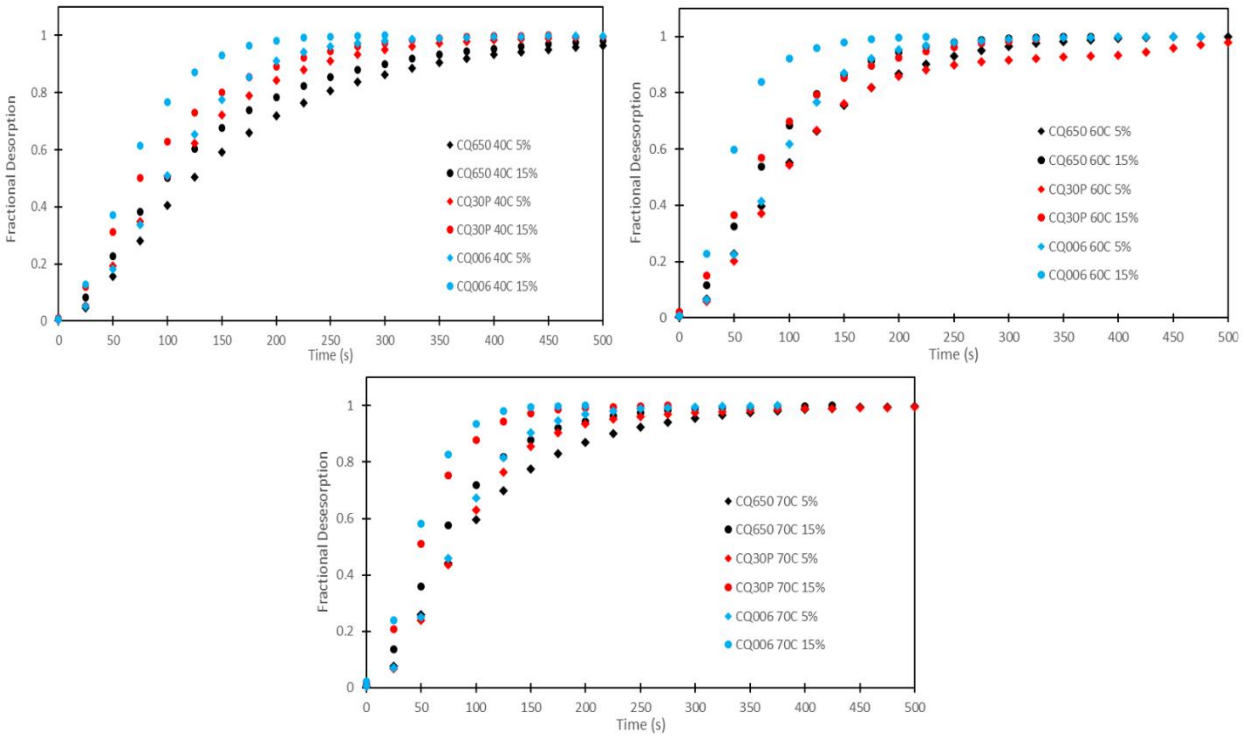

Figure A-2: Sorbent desorption performance at a fixed temperature and both 5% and 15% CO_2 feed conditions

APPENDIX B KINETIC MODELLING

Most accurate model

The rest of the kinetic models are shown in Figure B-1 to Figure B-12, and in all conditions tested, the Avrami kinetic model is the best overall model for adsorption and desorption, describing the process well, and the results, regarding the MAE, RMSE and QOF%, all support the claim that Avrami is the most accurate.

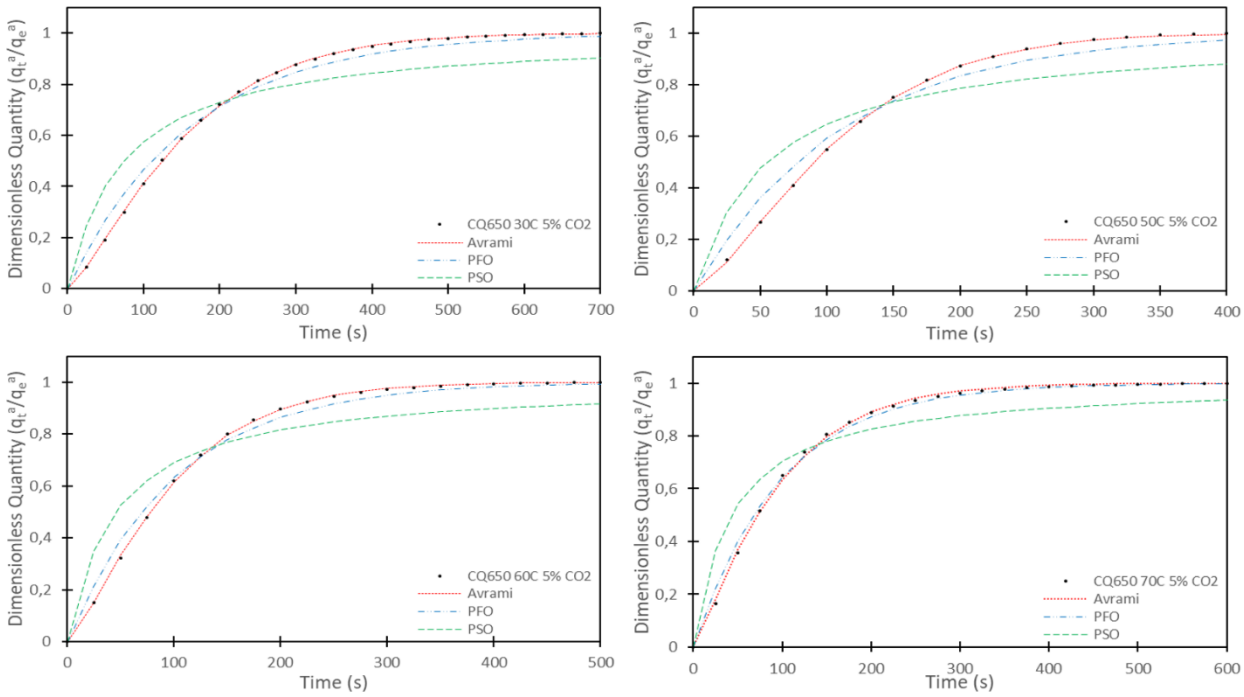

Figure B-1: Most accurate adsorption model for CQ650 at 30, 50, 60, 70 ºC and 5% CO_2 feed

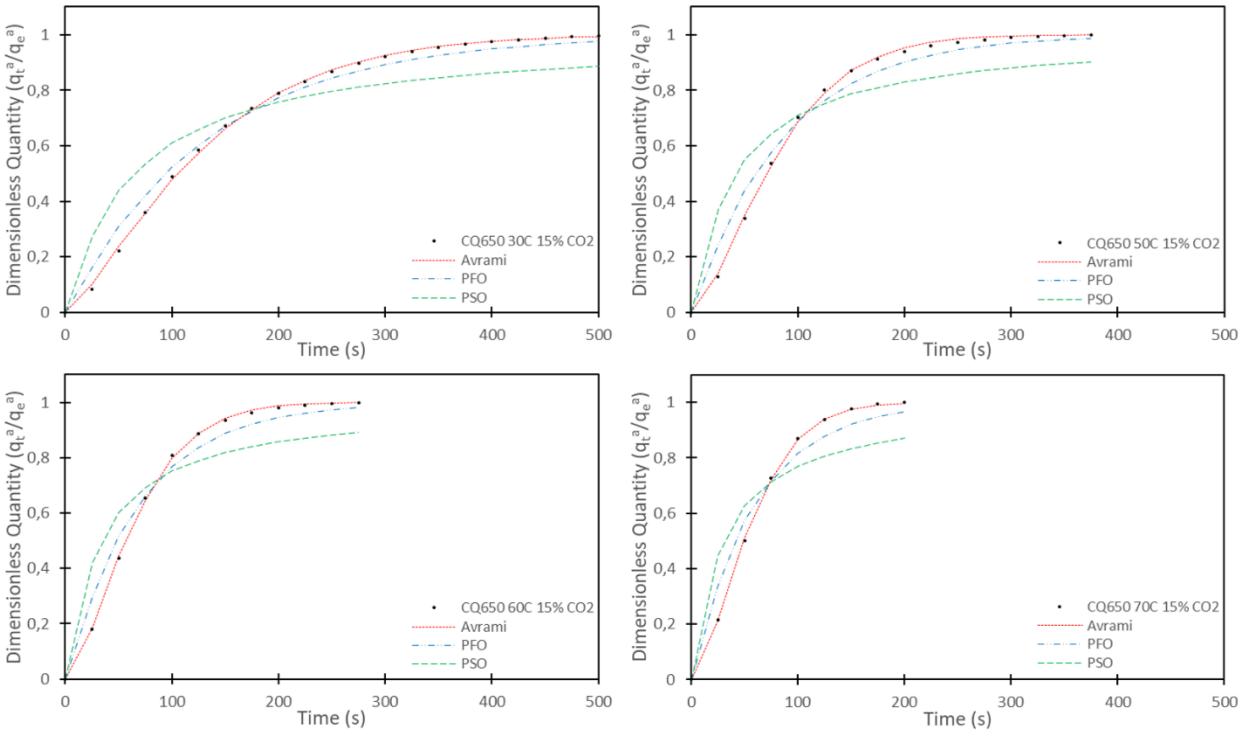

Figure B-2: Most accurate adsorption model for CQ650 at 30, 50, 60, 70 °C and 15% CO_2 feed

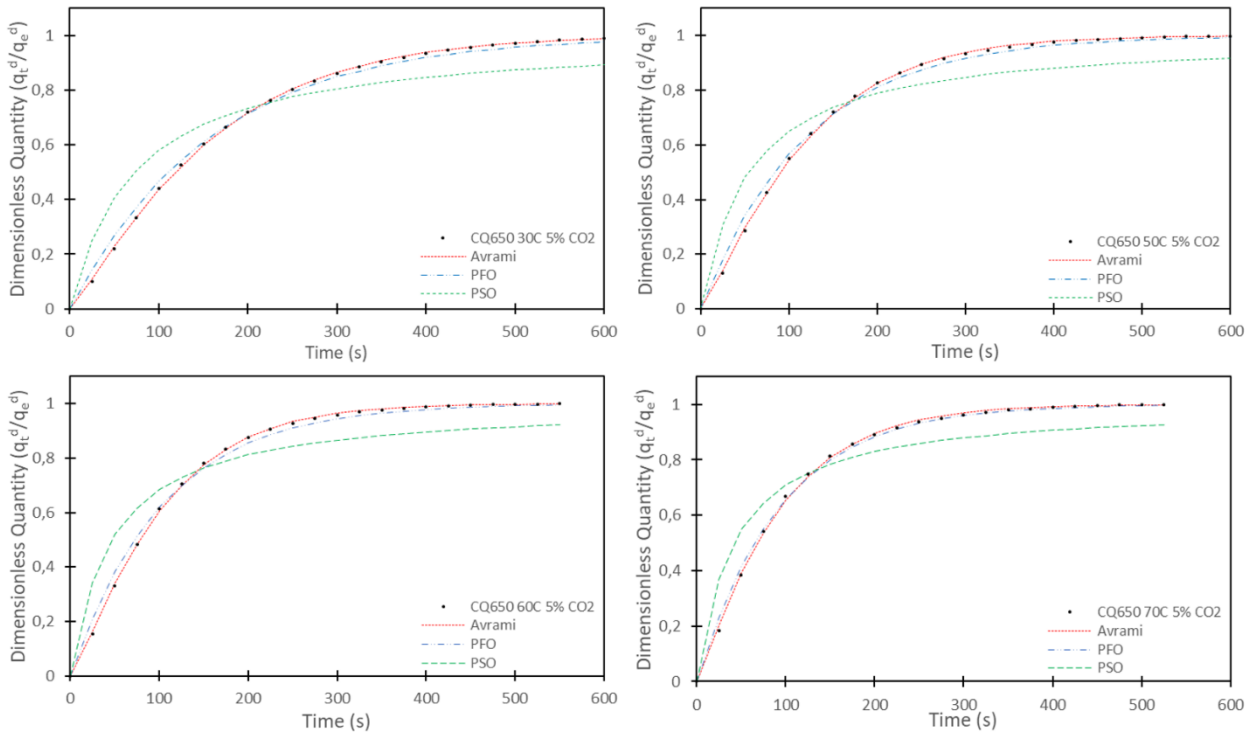

Figure B-3: Most accurate desorption model for CQ650 at 30, 50, 60, 70 °C and 5% CO_2 feed

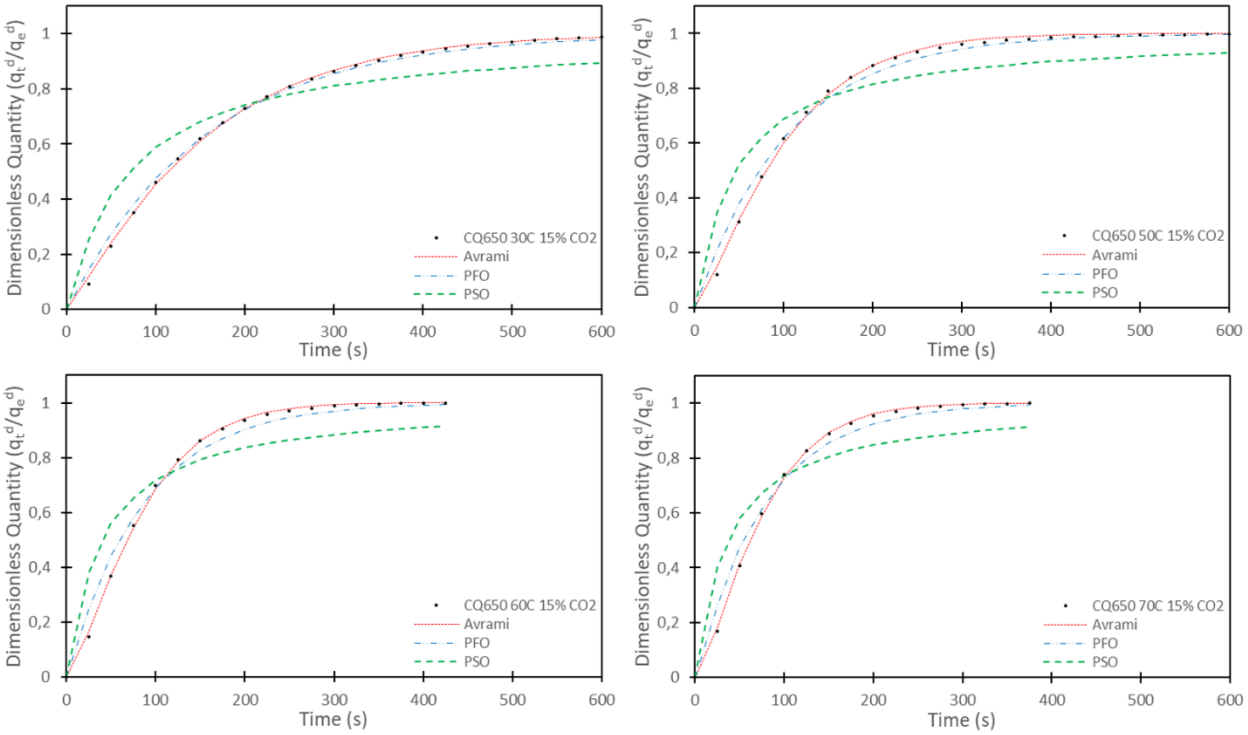

Figure B-4: Most accurate desorption model for CQ650 at 30, 50, 60, 70 °C and 15% CO_2 feed

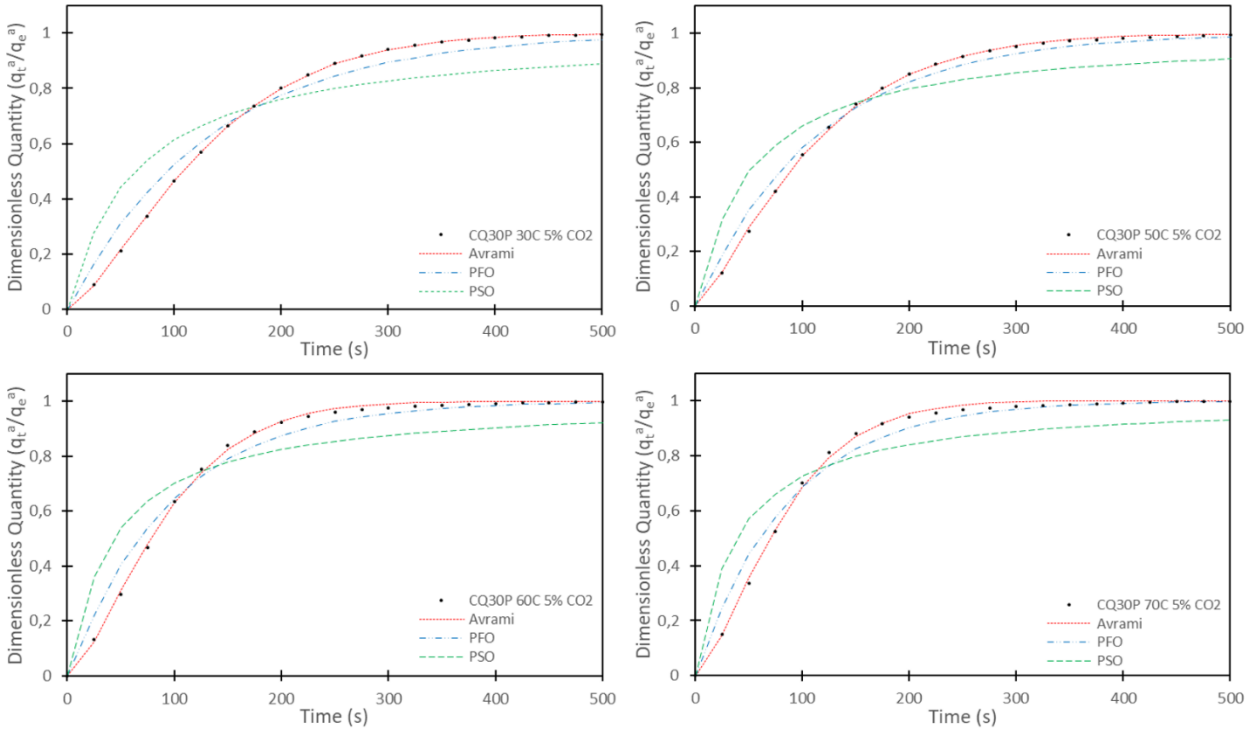

Figure B-5: Most accurate adsorption model for CQ30P at 30, 50, 60, 70 °C and 5% CO_2 feed

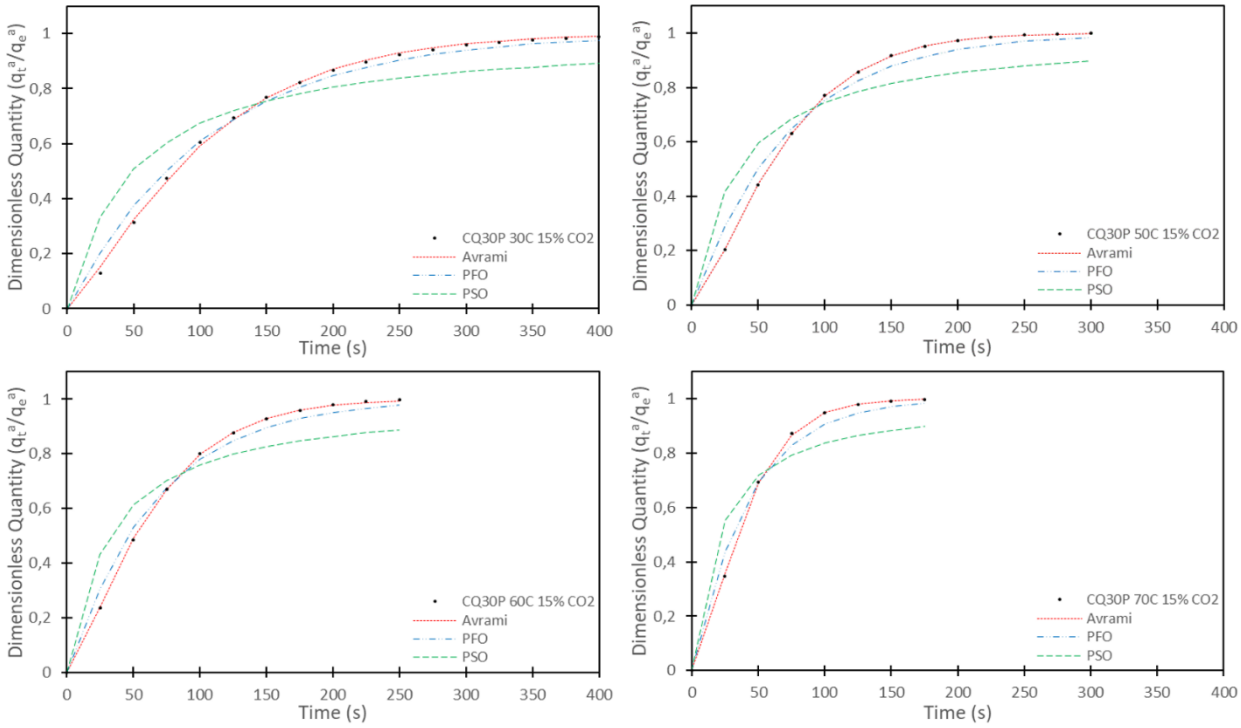

Figure B-6: Most accurate adsorption model for CQ30P at 30, 50, 60, 70 °C and 15% CO_2 feed

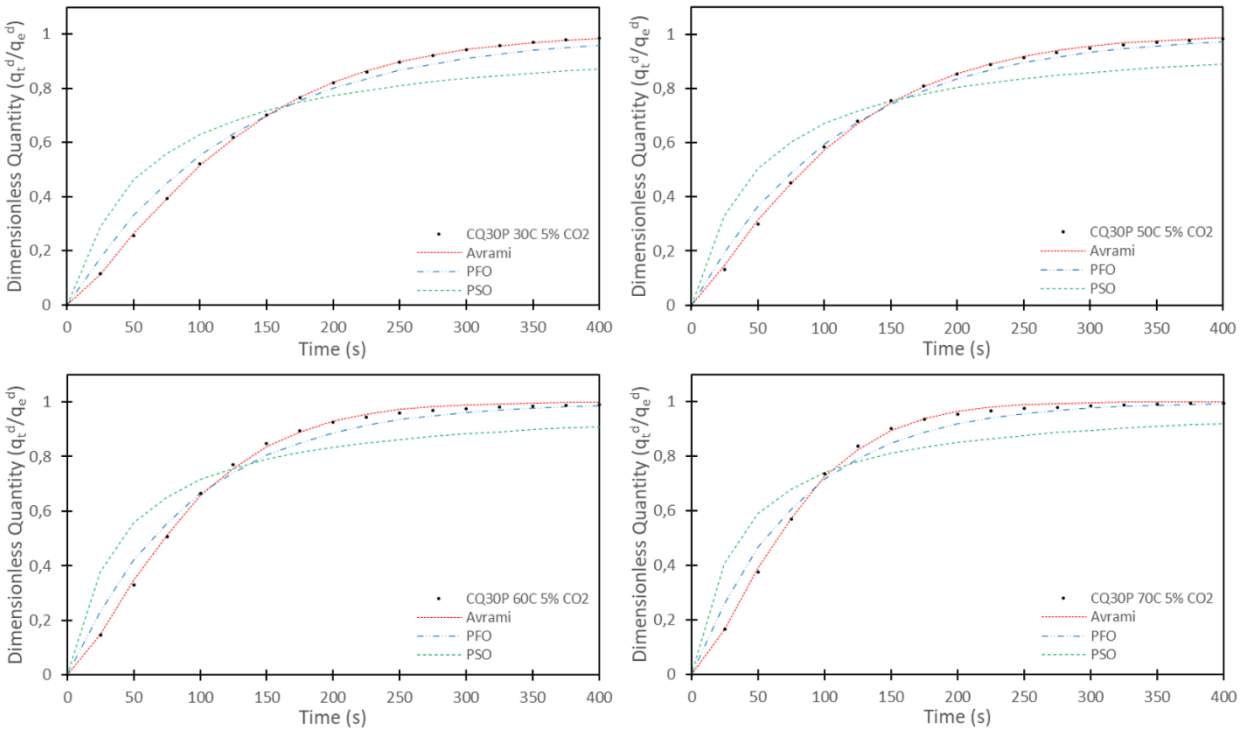

Figure B-7: Most accurate desorption model for CQ30P at 30, 50, 60, 70 °C and 5% CO_2 feed

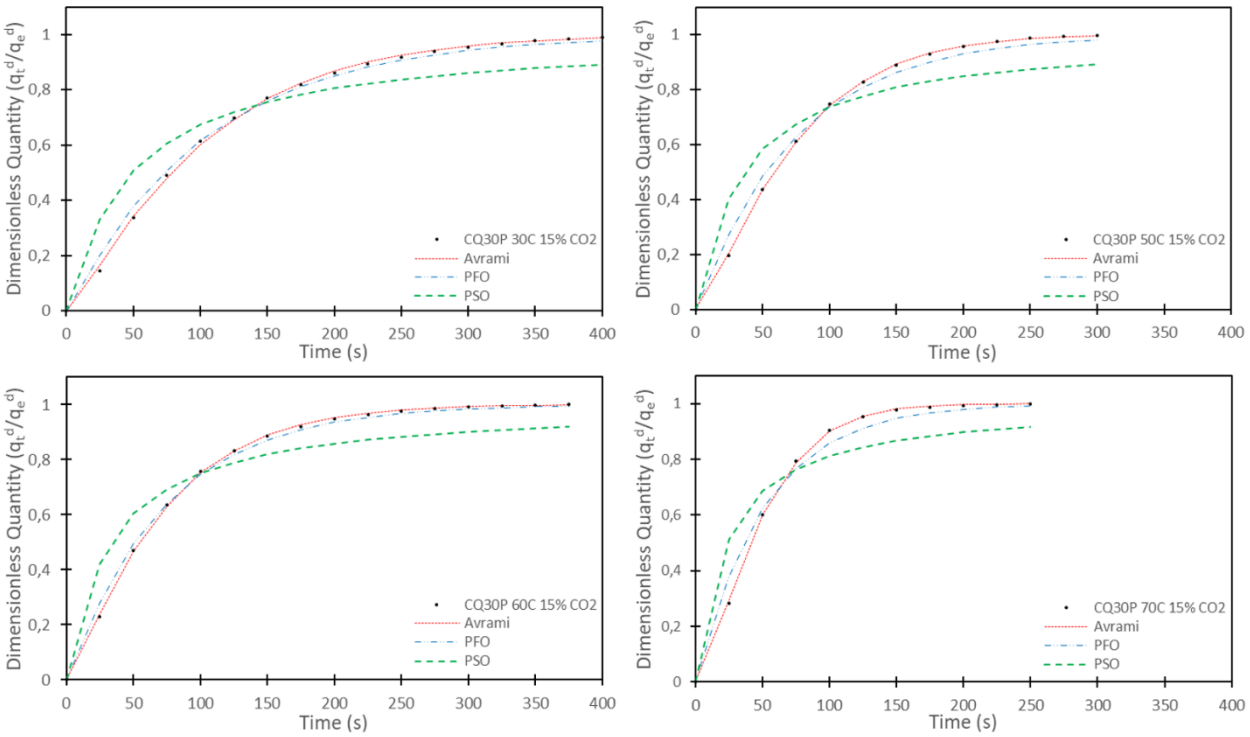

Figure B-8: Most accurate desorption model for CQ30P at 30, 50, 60, 70 °C and 15% CO_2 feed

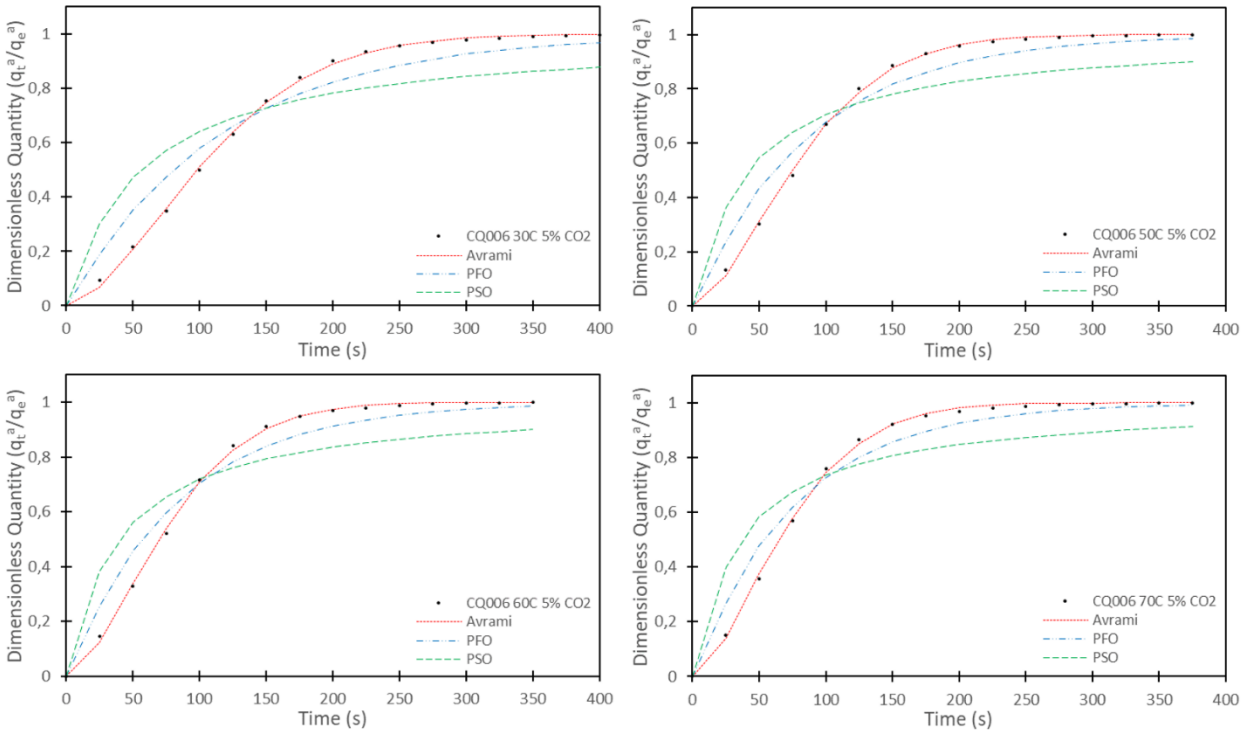

Figure B-9: Most accurate adsorption model for CQ006 at 30, 50, 60, 70 °C and 5% CO_2 feed

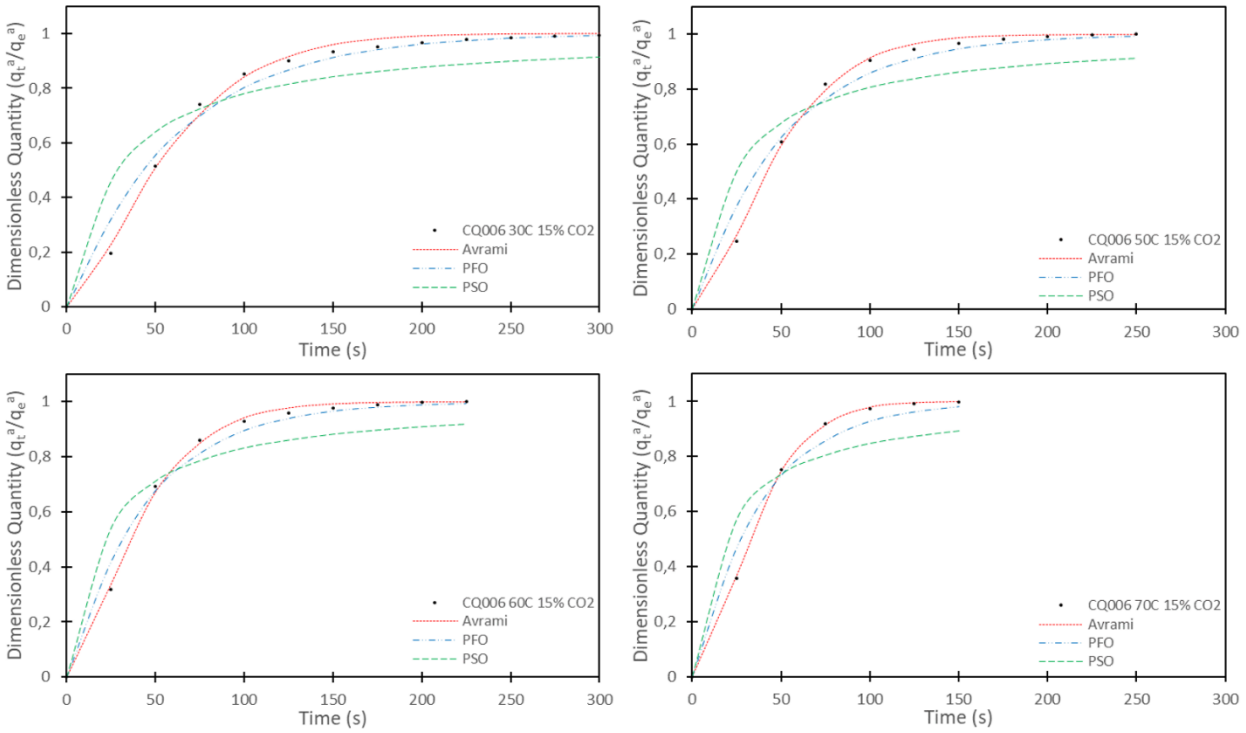

Figure B-10: Most accurate adsorption model for CQ006 at 30, 50, 60, 70 °C and 15% CO_2 feed

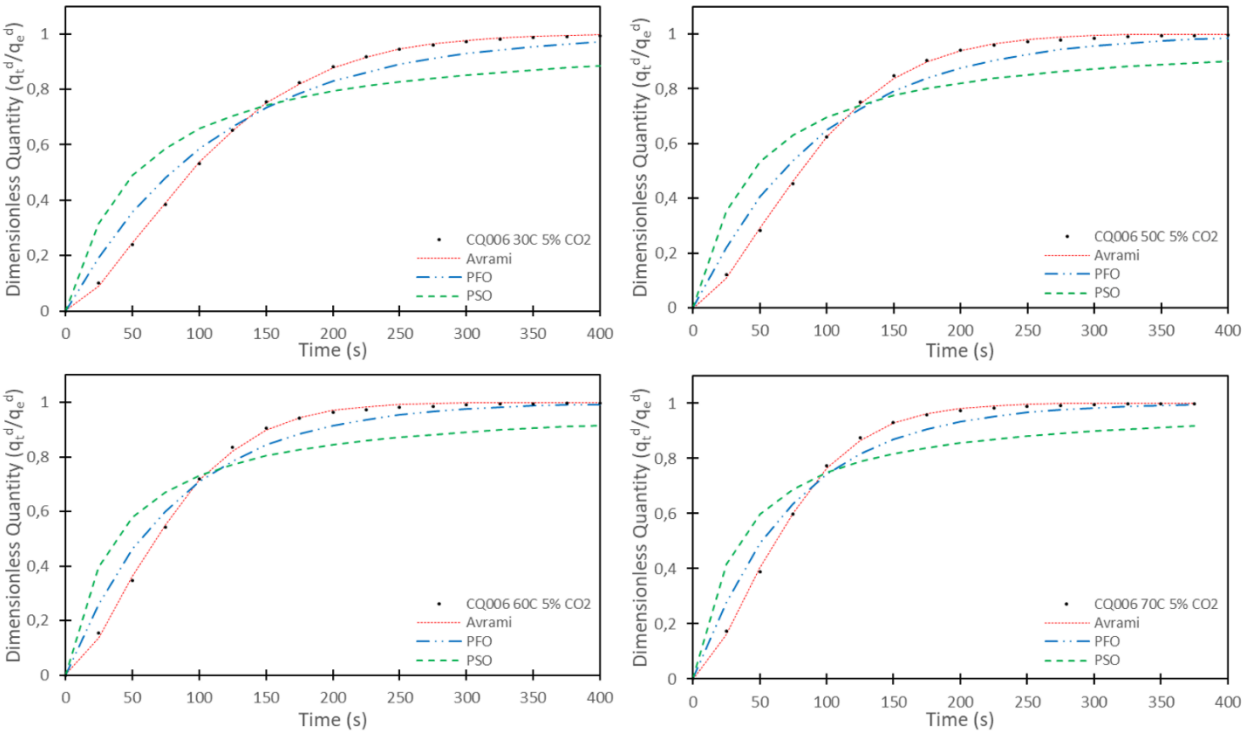

Figure B-11: Most accurate desorption model for CQ006 at 30, 50, 60, 70 °C and 5% CO_2 feed

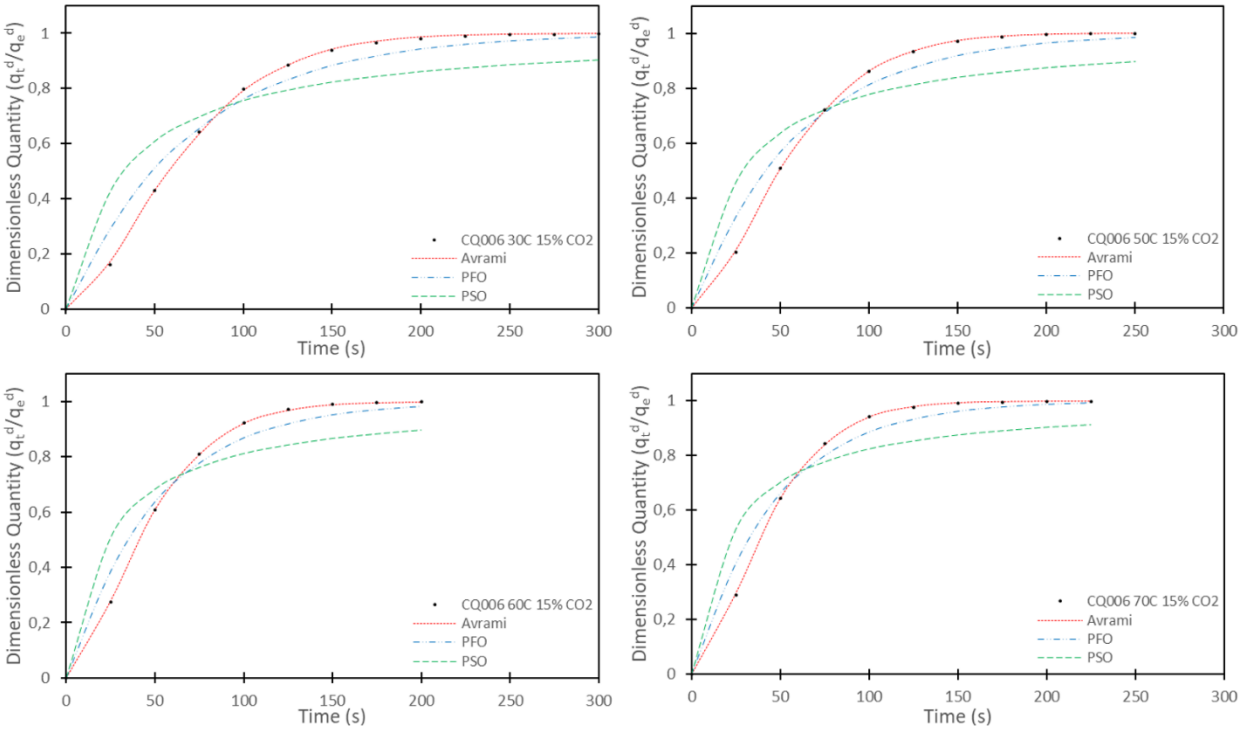

Figure B-12: Most accurate desorption model for CQ006 at 30, 50, 60, 70 ºC and 15% CO_2 feed

APPENDIX C BREAKTHROUGH MODELLING

Breakthrough adsorption modelling with Avrami and desorption modelling with a modified Avrami equation

Adsorption 5% CO_2 feed concentration

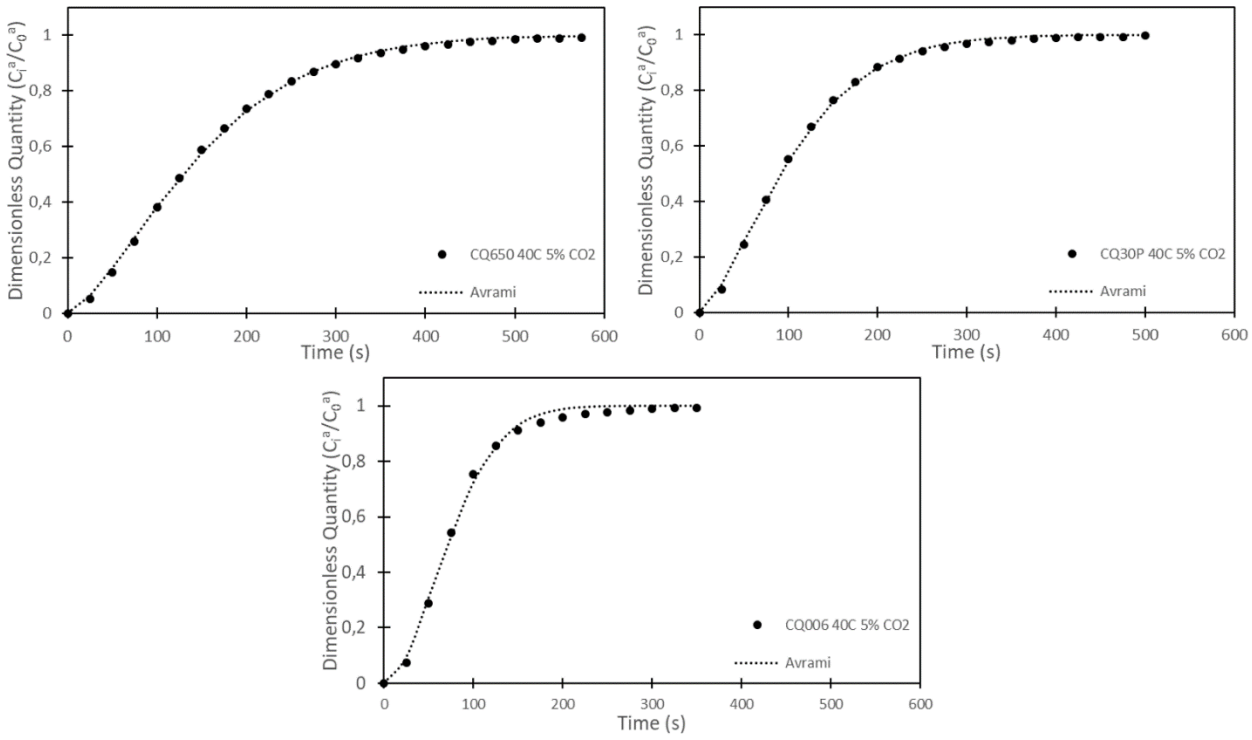

Figure C-1: Avrami adsorption breakthrough modelling for CQ650, CQ30P and CQ006 at 40 °C and 5% CO_2 feed

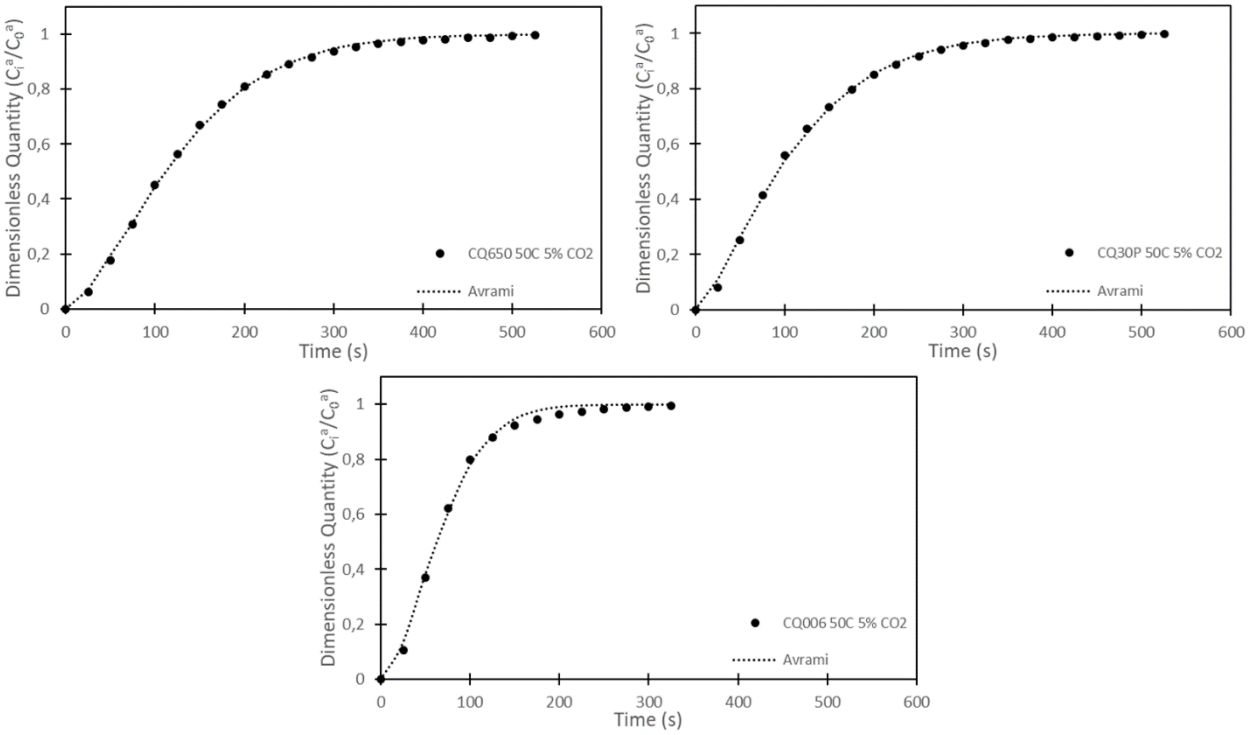

Figure C-2: Avrami adsorption breakthrough modelling for CQ650, CQ30P and CQ006 at 50 °C and 5% CO_2 feed

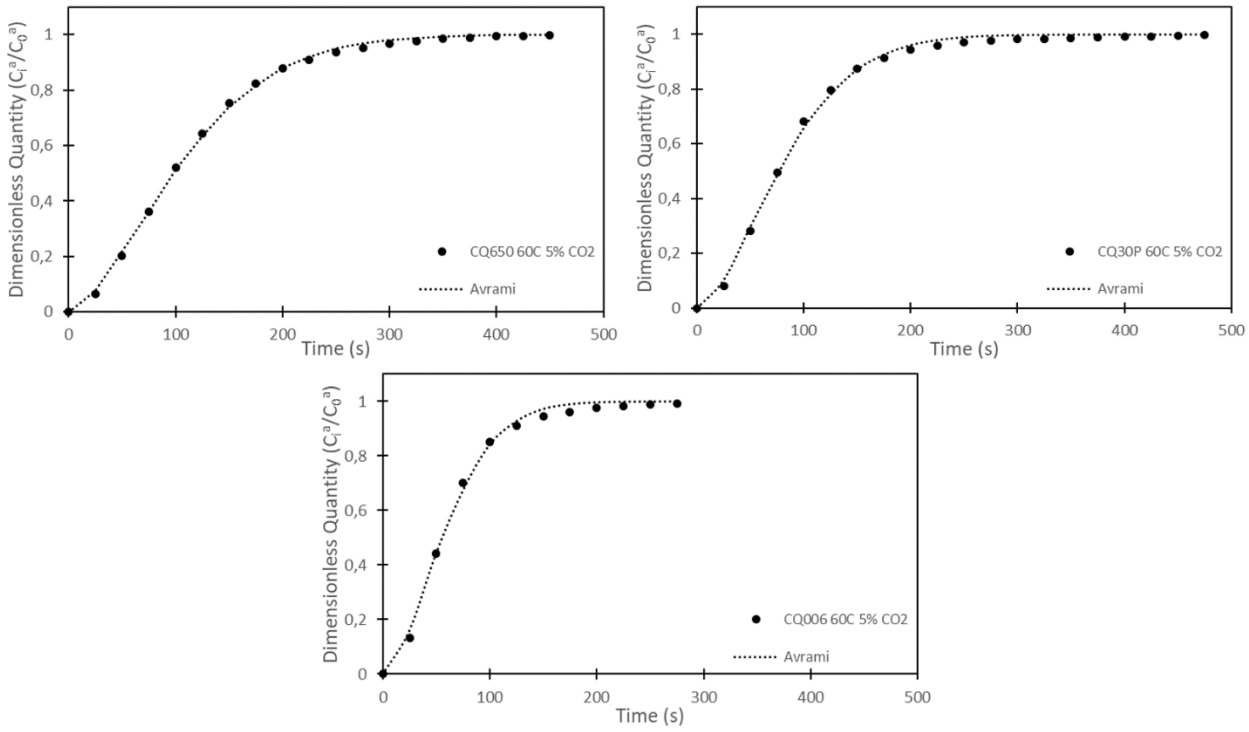

Figure C-3: Avrami adsorption breakthrough modelling for CQ650, CQ30P and CQ006 at 60 °C and 5% CO_2 feed

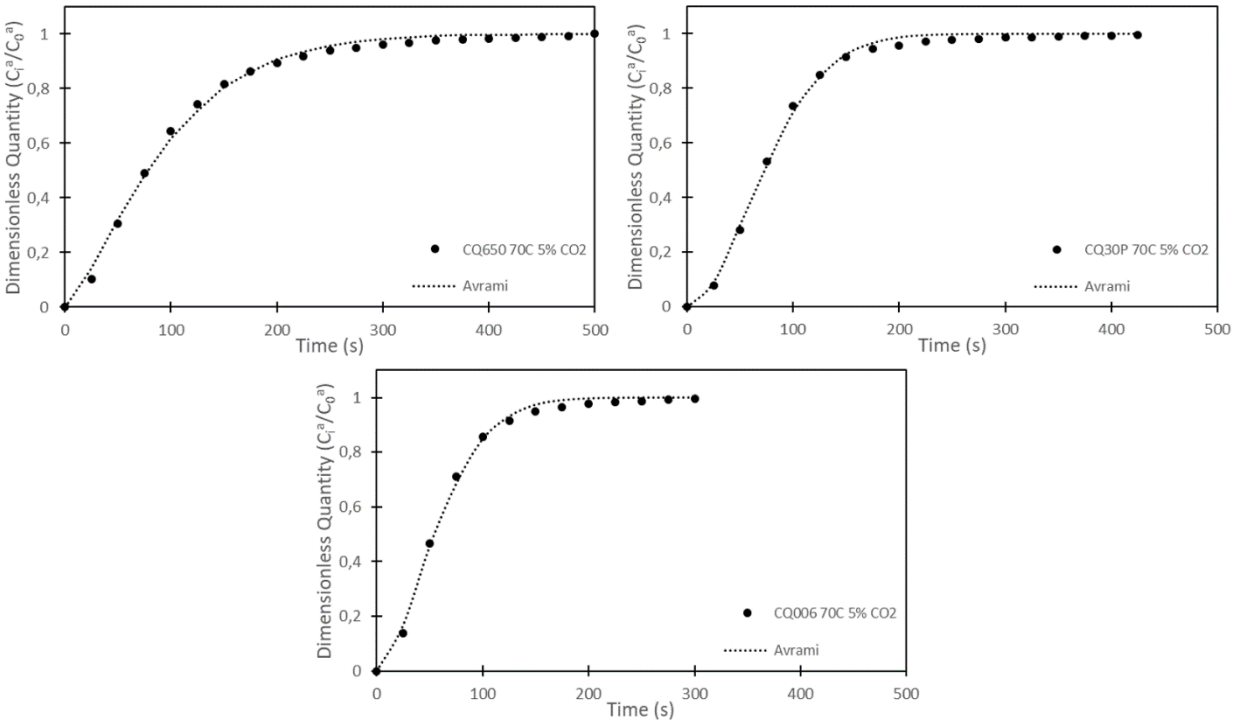

Figure C-4: Avrami adsorption breakthrough modelling for CQ650, CQ30P and CQ006 at 70 °C and 5% CO_2 feed

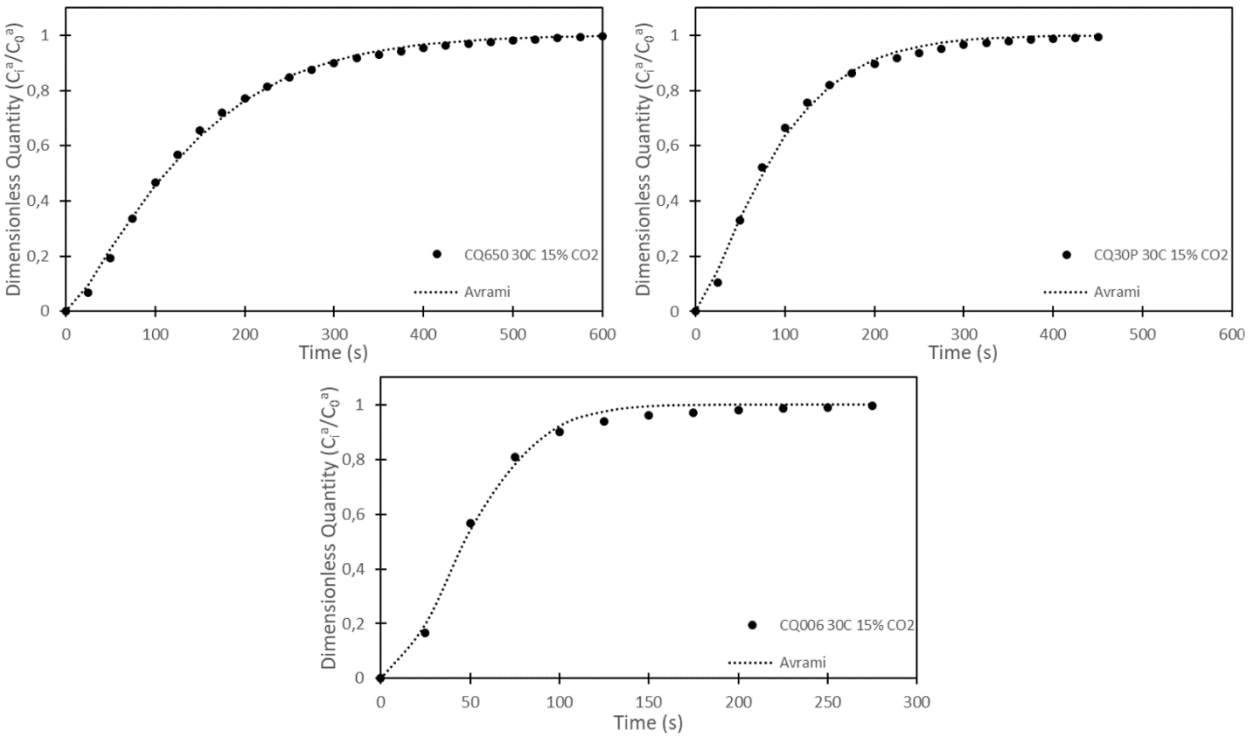

Figure C-5: Avrami adsorption breakthrough modelling for CQ650, CQ30P and CQ006 at 30 °C and 15% CO_2 feed

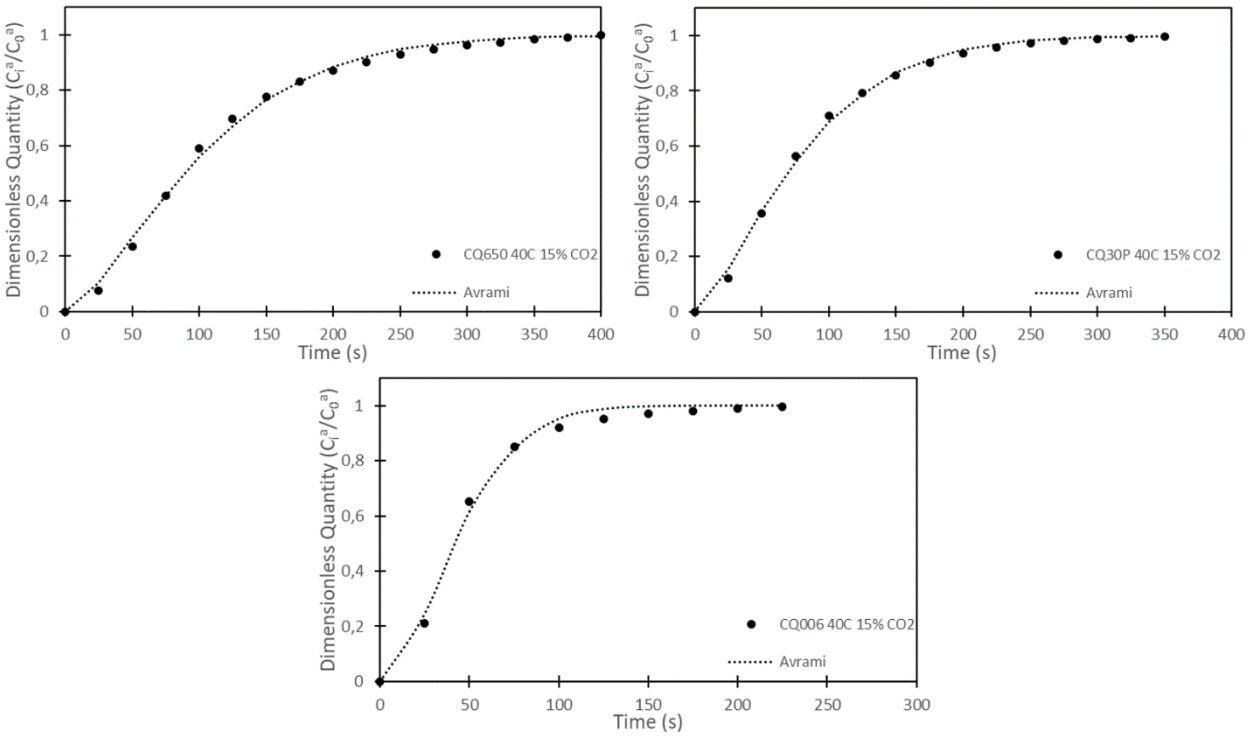

Figure C-6: Avrami adsorption breakthrough modelling for CQ650, CQ30P and CQ006 at 40 ºC and 15% CO_2 feed

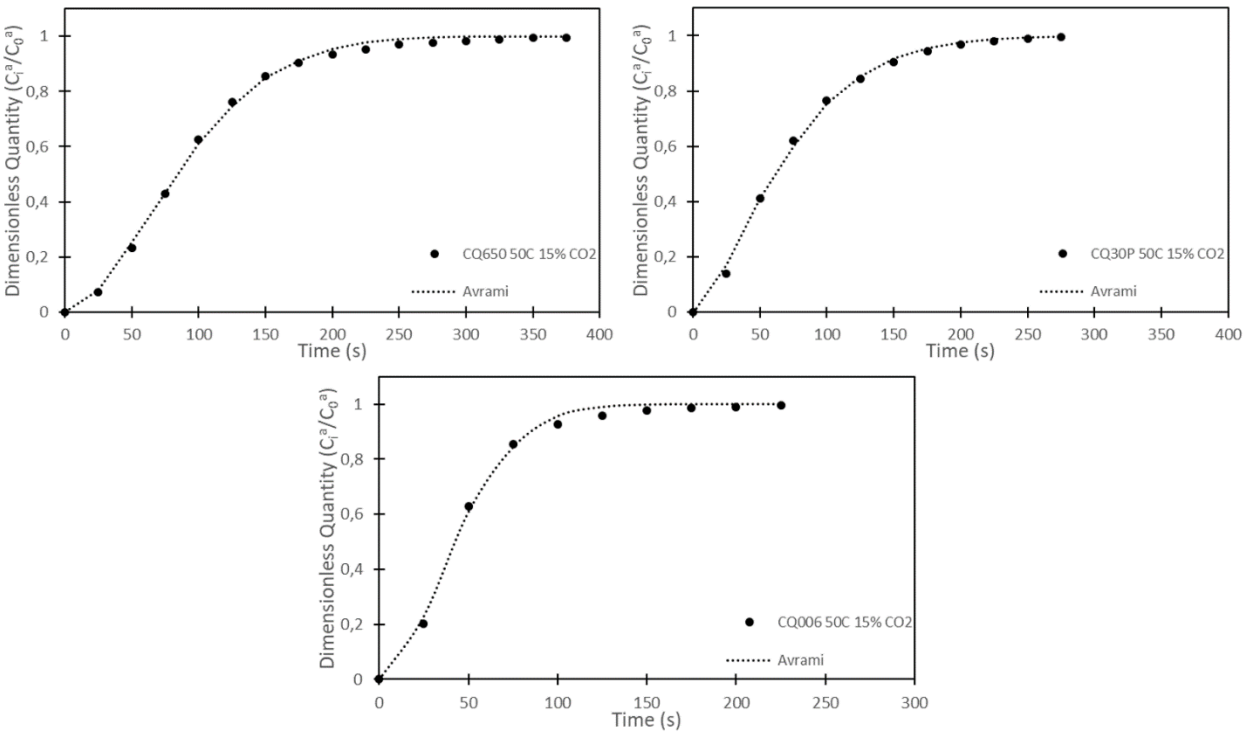

Figure C-7: Avrami adsorption breakthrough modelling for CQ650, CQ30P and CQ006 at 50 ºC and 15% CO_2 feed

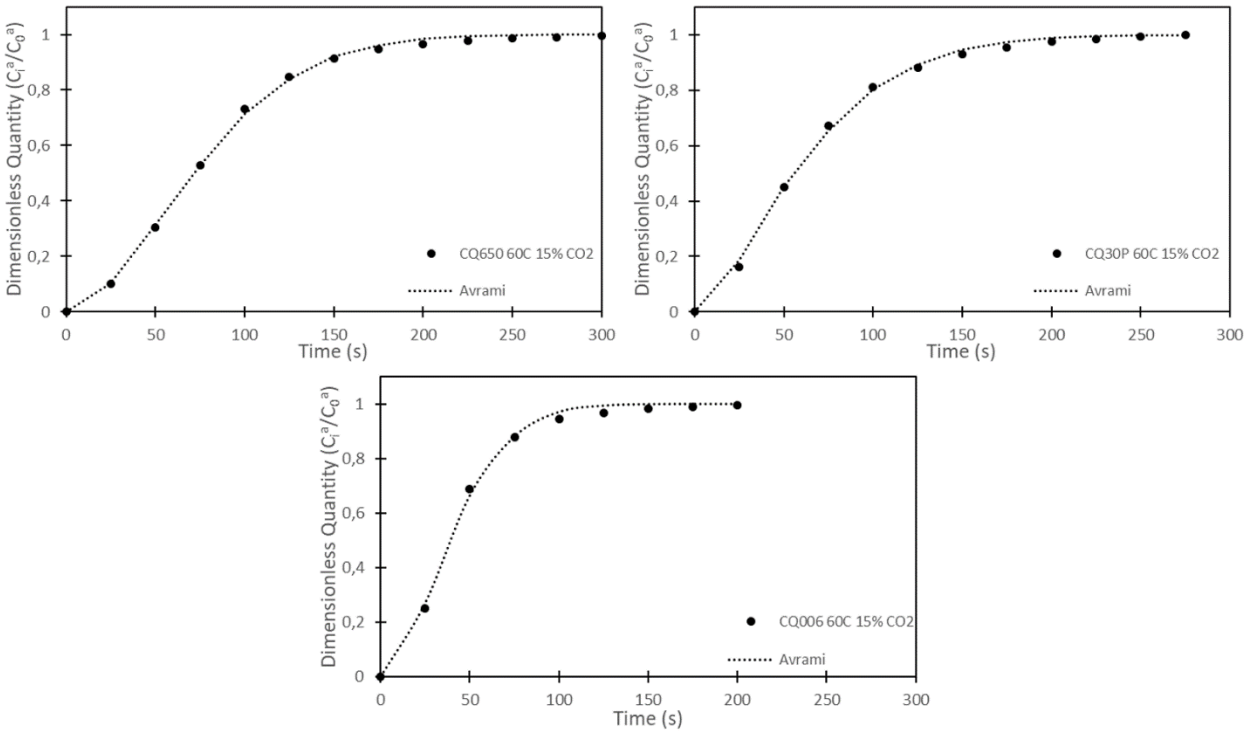

Figure C-8: Avrami adsorption breakthrough modelling for CQ650, CQ30P and CQ006 at 60 °C and 15% CO_2 feed

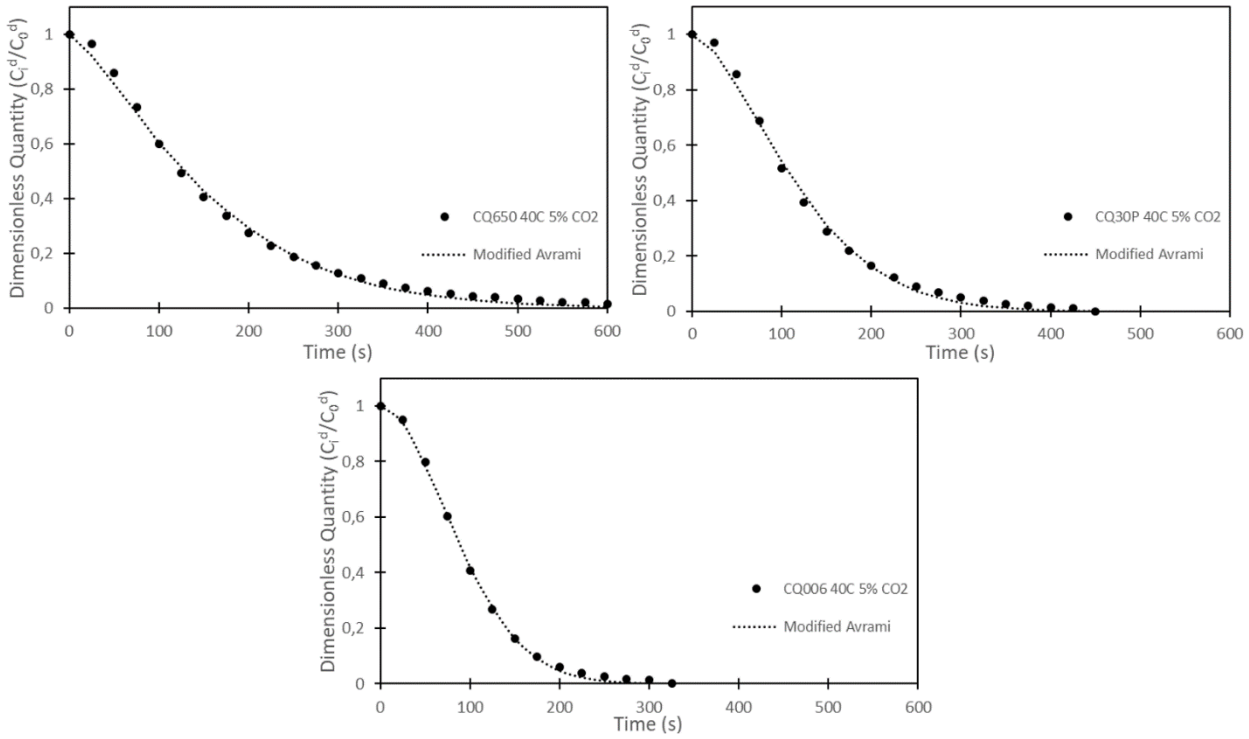

Figure C-9: Avrami desorption breakthrough modelling for CQ650, CQ30P and CQ006 at 40 °C and 5% CO_2 feed

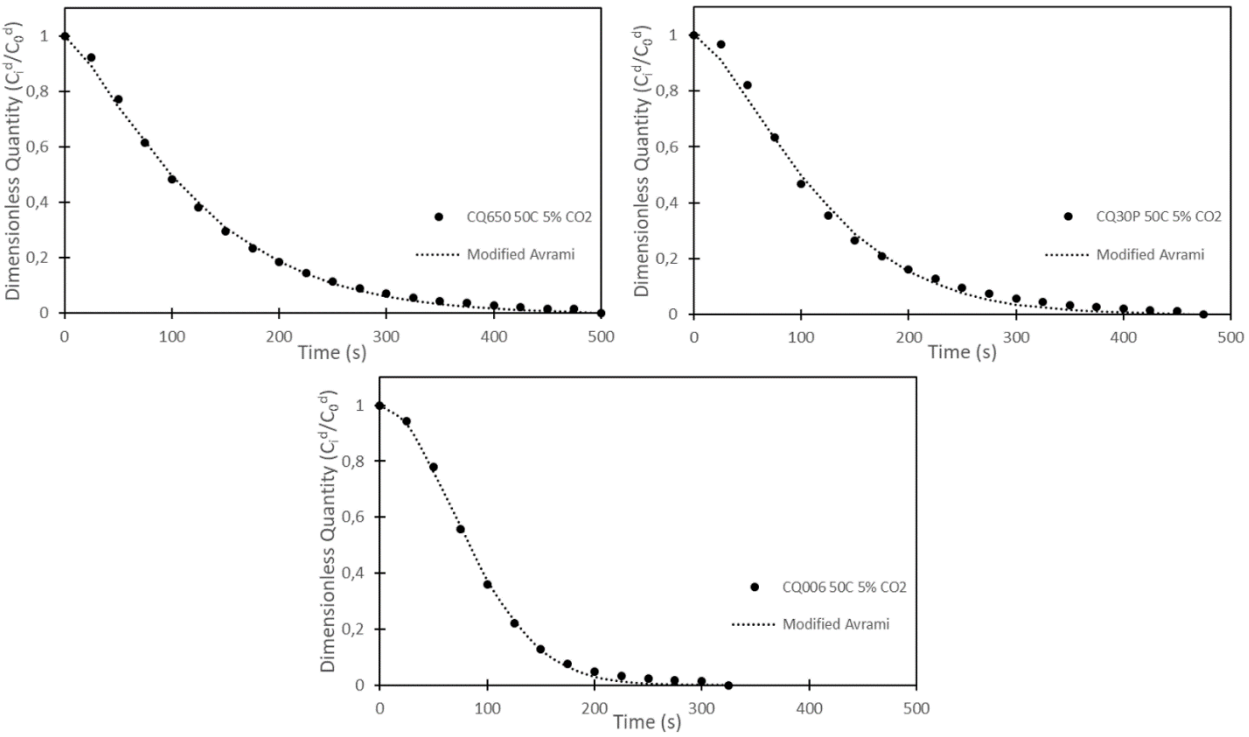

Figure C-10: Avrami desorption breakthrough modelling for CQ650, CQ30P and CQ006 at 50 °C and 5% CO_2 feed

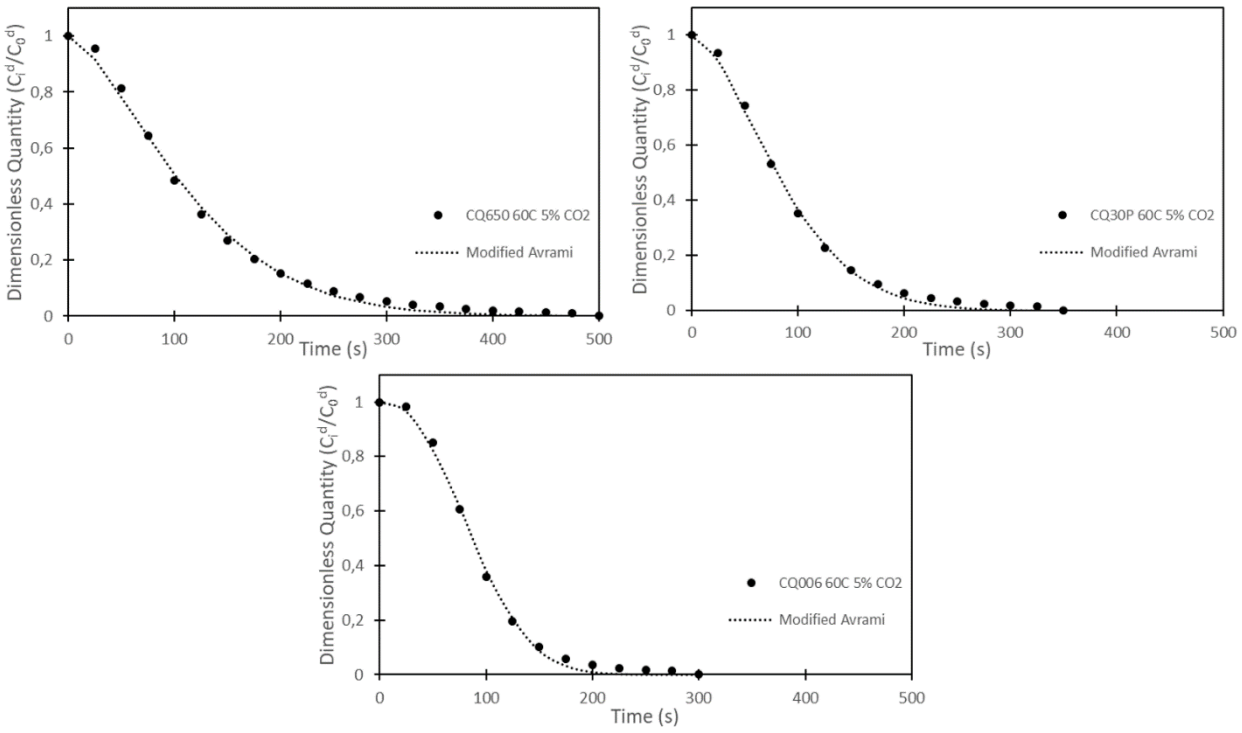

Figure C-11: Avrami desorption breakthrough modelling for CQ650, CQ30P and CQ006 at 60 °C and 5% CO_2 feed

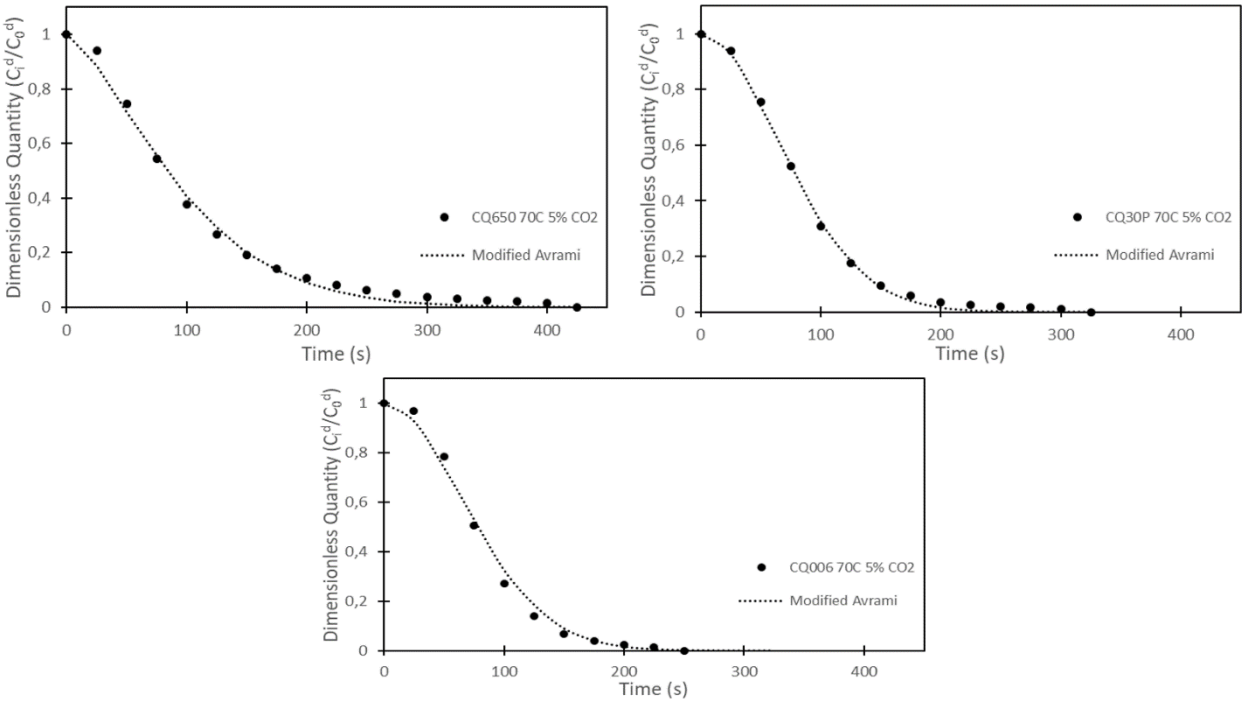

Figure C-12: Avrami desorption breakthrough modelling for CQ650, CQ30P and CQ006 at 70 °C and 5% CO_2 feed

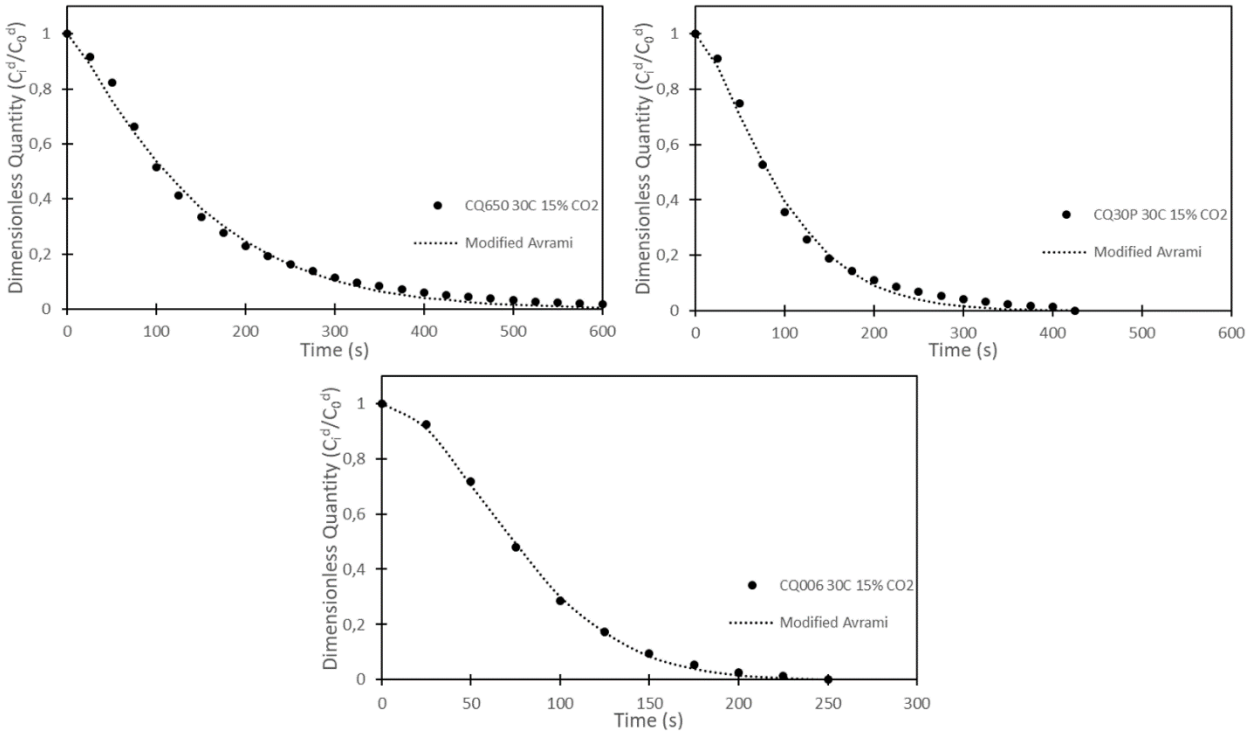

Figure C-13: Avrami desorption breakthrough modelling for CQ650, CQ30P and CQ006 at 30 °C and 15% CO_2 feed

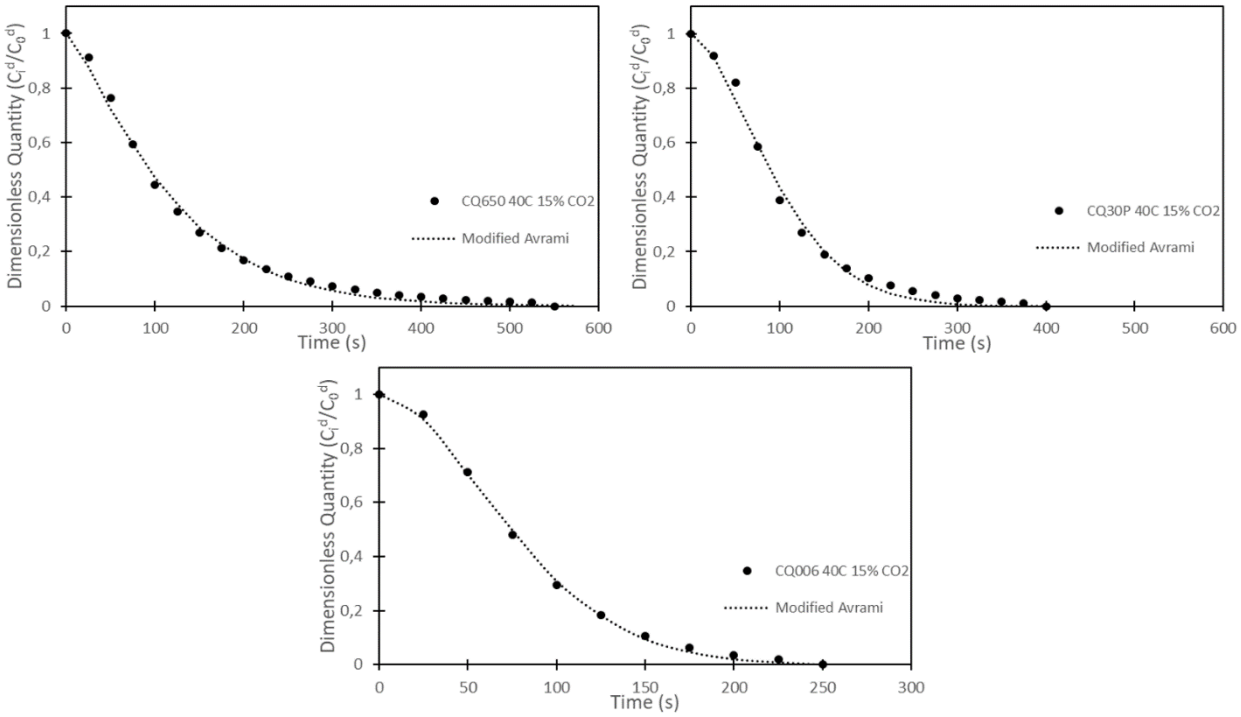

Figure C-14: Avrami desorption breakthrough modelling for CQ650, CQ30P and CQ006 at 40 °C and 15% CO_2 feed

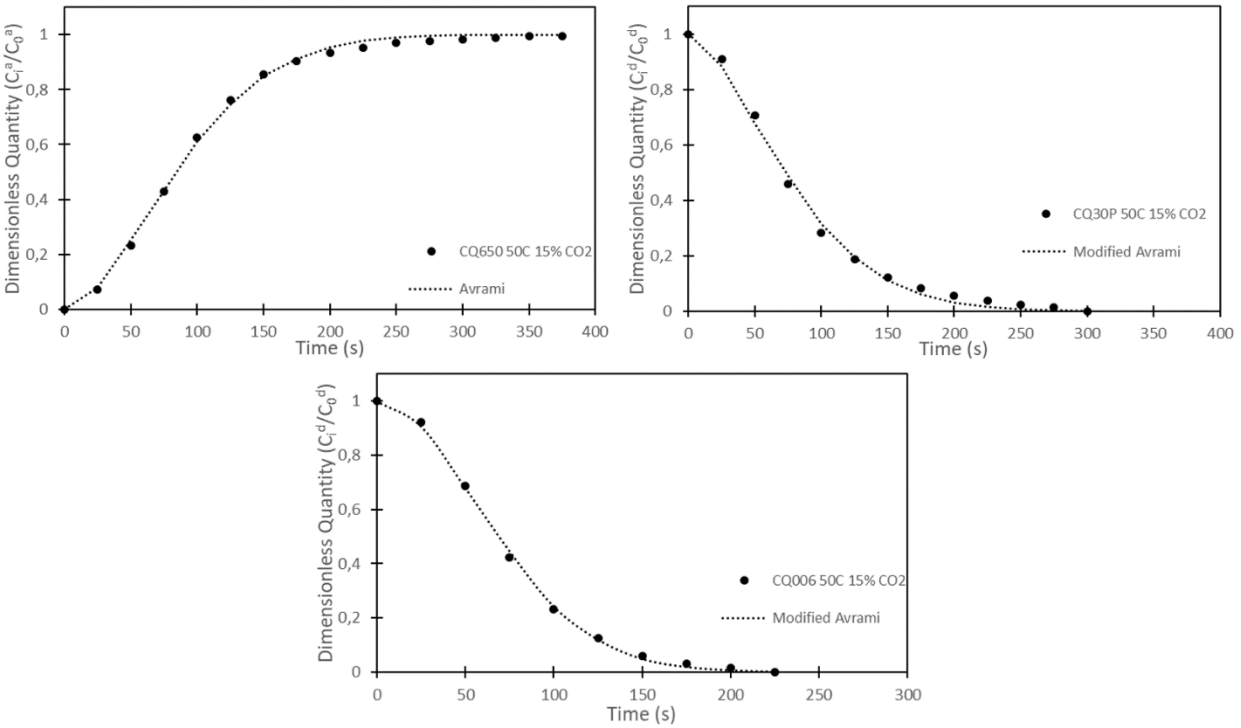

Figure C-15: Avrami desorption breakthrough modelling for CQ650, CQ30P and CQ006 at 50 °C and 15% CO_2 feed

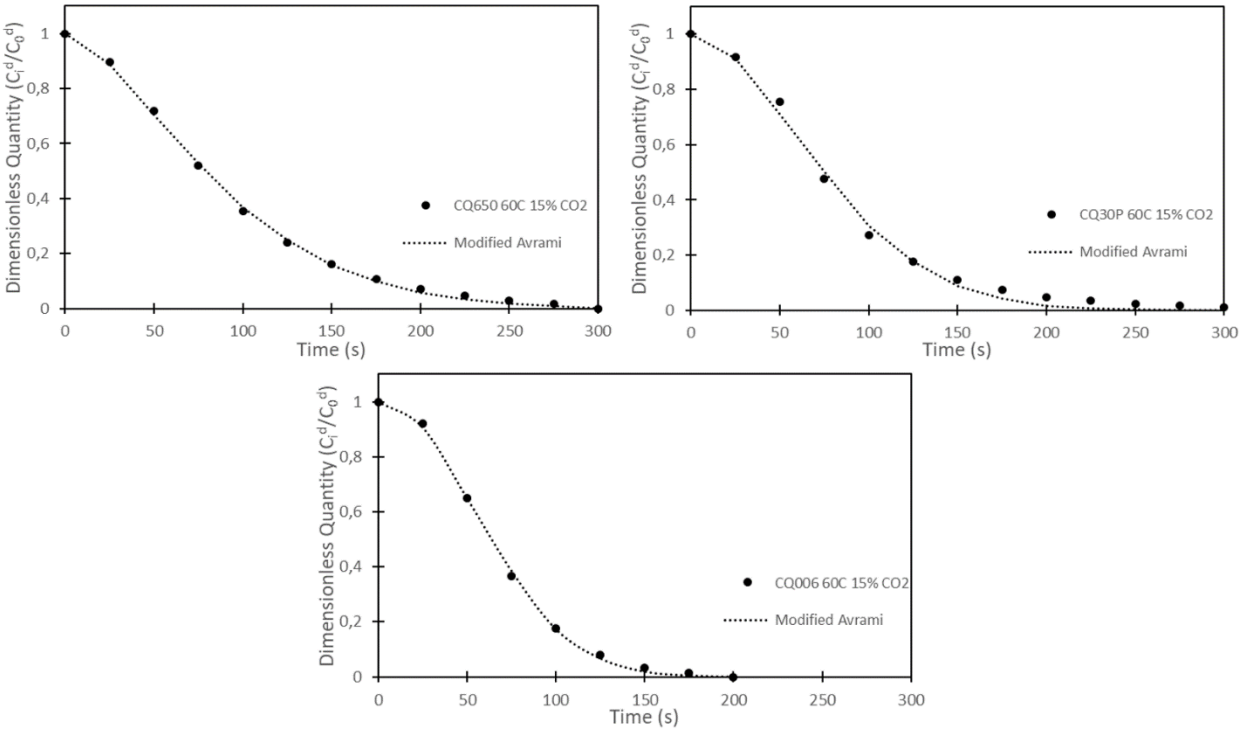

Figure C-16: Avrami desorption breakthrough modelling for CQ650, CQ30P and CQ006 at 60 ºC and 15% CO_2 feed

APPENDIX D REPEATABILITY STUDY

An adsorption and desorption rate experimental analysis was performed on CQ650, CQ30P and CQ006 sorbent samples at 30, 50 and 70 °C and 5 and 15 vol% CO_2, with a 95% confidence interval. The adsorption and desorption rate error analysis shown in Figure D-1 to Figure D-6 and the resulting data in Table D-1 to Table D-12 show excellent reproducibility for all sorbents tested.

CQ650 Adsorption and desorption

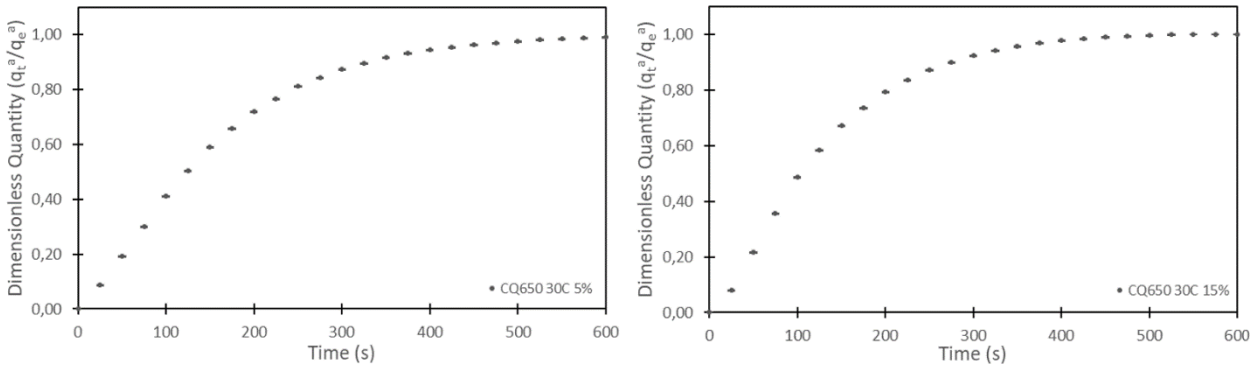

Figure D-1: Experimental adsorption rate error analysis done on CQ650 at 30 °C and 5 and 15% CO_2 feed

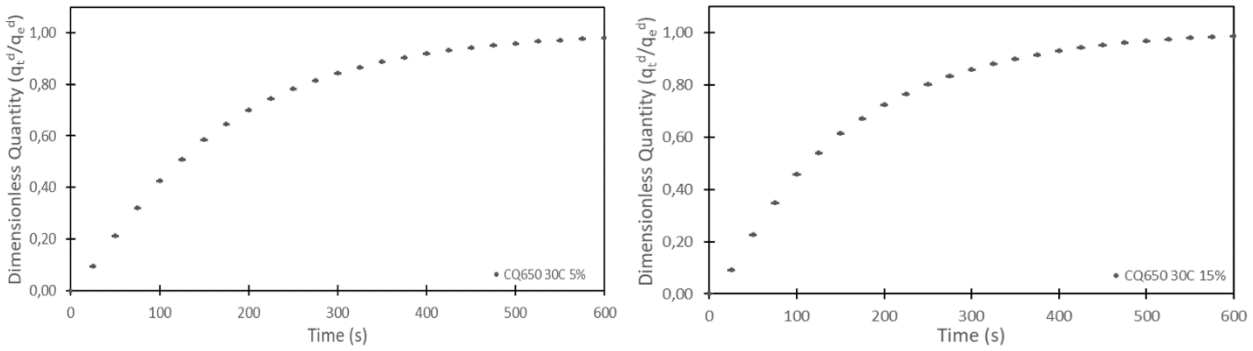

Figure D-2: Experimental desorption rate error analysis done on CQ650 at 30 °C and 5 and 15% CO_2 feed

Table D-1: Experimental adsorption rate error analysis done on CQ650 at 30 °C and 5% CO_2 feed

CQ650 30 °C 5% CO_2 feed adsorption reproducibility											
Time (s)	**Run 1 (qt/qe)**	**Run 2 (qt/qe)**	**Run 3 (qt/qe)**	**Avg ads**	**Std dev**	**95% Conf int**	**Exp deviation %**	**Expt deviation**	**Final data**		
0	0.00	0.00	0.00	0.00	0.0E+00	0.0E+00	0.0E+00	0.0E+00	0.0E+00	±	0.0E+00
25	0.09	0.09	0.09	0.09	1.2E-03	1.9E-03	2.7E-03	2.7E-05	8.7E-02	±	2.7E-05
50	0.19	0.20	0.19	0.19	2.4E-03	3.7E-03	4.5E-03	4.5E-05	1.9E-01	±	4.5E-05
75	0.30	0.31	0.30	0.30	2.8E-03	4.5E-03	4.1E-03	4.1E-05	3.0E-01	±	4.1E-05
100	0.41	0.42	0.41	0.41	2.8E-03	4.4E-03	3.0E-03	3.0E-05	4.1E-01	±	3.0E-05
125	0.50	0.51	0.50	0.50	2.6E-03	4.2E-03	2.2E-03	2.2E-05	5.0E-01	±	2.2E-05
150	0.59	0.59	0.59	0.59	2.3E-03	3.7E-03	1.5E-03	1.5E-05	5.9E-01	±	1.5E-05
175	0.65	0.66	0.66	0.66	2.2E-03	3.5E-03	1.2E-03	1.2E-05	6.6E-01	±	1.2E-05
200	0.72	0.72	0.72	0.72	2.1E-03	3.4E-03	9.8E-04	9.8E-06	7.2E-01	±	9.8E-06
225	0.76	0.77	0.77	0.77	2.1E-03	3.3E-03	8.9E-04	8.9E-06	7.7E-01	±	8.9E-06
250	0.81	0.81	0.81	0.81	2.1E-03	3.4E-03	8.7E-04	8.7E-06	8.1E-01	±	8.7E-06
275	0.84	0.84	0.85	0.84	2.1E-03	3.4E-03	8.6E-04	8.6E-06	8.4E-01	±	8.6E-06
300	0.87	0.87	0.88	0.87	2.2E-03	3.5E-03	8.7E-04	8.7E-06	8.7E-01	±	8.7E-06
325	0.89	0.90	0.90	0.90	2.2E-03	3.5E-03	8.7E-04	8.7E-06	9.0E-01	±	8.7E-06
350	0.91	0.92	0.92	0.92	2.2E-03	3.6E-03	8.8E-04	8.8E-06	9.2E-01	±	8.8E-06
375	0.93	0.93	0.93	0.93	2.2E-03	3.6E-03	8.6E-04	8.6E-06	9.3E-01	±	8.6E-06
400	0.94	0.94	0.95	0.95	2.2E-03	3.5E-03	8.2E-04	8.2E-06	9.5E-01	±	8.2E-06
425	0.95	0.95	0.96	0.96	2.2E-03	3.5E-03	8.0E-04	8.0E-06	9.6E-01	±	8.0E-06
450	0.96	0.96	0.97	0.96	2.1E-03	3.4E-03	7.6E-04	7.6E-06	9.6E-01	±	7.6E-06
475	0.97	0.97	0.97	0.97	2.1E-03	3.3E-03	7.0E-04	7.0E-06	9.7E-01	±	7.0E-06
500	0.98	0.98	0.98	0.98	2.0E-03	3.1E-03	6.4E-04	6.4E-06	9.8E-01	±	6.4E-06
525	0.98	0.98	0.98	0.98	1.9E-03	3.0E-03	5.9E-04	5.9E-06	9.8E-01	±	5.9E-06
550	0.98	0.99	0.99	0.99	1.8E-03	2.9E-03	5.4E-04	5.4E-06	9.9E-01	±	5.4E-06
575	0.99	0.99	0.99	0.99	1.7E-03	2.6E-03	4.4E-04	4.4E-06	9.9E-01	±	4.4E-06

600	0.99	0.99	0.99	0.99	1.5E-03	2.4E-03	3.6E-04	3.6E-06	9.9E-01	±	3.6E-06
625	0.99	0.99	1.00	0.99	1.3E-03	2.1E-03	2.8E-04	2.8E-06	9.9E-01	±	2.8E-06
650	0.99	1.00	1.00	1.00	1.2E-03	1.9E-03	2.3E-04	2.3E-06	1.0E+00	±	2.3E-06
675	1.00	1.00	1.00	1.00	1.0E-03	1.6E-03	1.6E-04	1.6E-06	1.0E+00	±	1.6E-06
							0.42				

Table D-2: Experimental adsorption rate error analysis done on CQ650 at 30 °C and 15% CO_2 feed

CQ650 30 °C 15% CO_2 feed adsorption reproducibility											
Time (s)	**Run 1 (qt/qe)**	**Run 2 (qt/qe)**	**Run 3 (qt/qe)**	**Avg ads**	**Std dev**	**95% Conf int**	**Exp deviation %**	**Expt deviation**	**Final data**		
0	0.00	0.00	0.00	0.00	0.0E+00	0.0E+00	0.0E+00	0.0E+00	0.0E+00	±	0.0E+00
25	0.08	0.08	0.08	0.08	3.0E-03	4.8E-03	1.8E-02	1.8E-04	8.1E-02	±	1.8E-04
50	0.22	0.21	0.22	0.22	5.5E-03	8.7E-03	2.2E-02	2.2E-04	2.2E-01	±	2.2E-04
75	0.36	0.35	0.36	0.36	6.6E-03	1.0E-02	1.9E-02	1.9E-04	3.6E-01	±	1.9E-04
100	0.50	0.48	0.49	0.49	7.0E-03	1.1E-02	1.6E-02	1.6E-04	4.9E-01	±	1.6E-04
125	0.60	0.58	0.58	0.59	7.2E-03	1.1E-02	1.4E-02	1.4E-04	5.9E-01	±	1.4E-04
150	0.68	0.67	0.67	0.67	7.5E-03	1.2E-02	1.3E-02	1.3E-04	6.7E-01	±	1.3E-04
175	0.75	0.73	0.73	0.74	7.6E-03	1.2E-02	1.3E-02	1.3E-04	7.4E-01	±	1.3E-04
200	0.80	0.79	0.79	0.79	7.5E-03	1.2E-02	1.1E-02	1.1E-04	7.9E-01	±	1.1E-04
225	0.85	0.83	0.83	0.84	7.4E-03	1.2E-02	1.0E-02	1.0E-04	8.4E-01	±	1.0E-04
250	0.88	0.87	0.87	0.87	7.0E-03	1.1E-02	9.1E-03	9.1E-05	8.7E-01	±	9.1E-05
275	0.91	0.89	0.90	0.90	6.6E-03	1.1E-02	7.7E-03	7.7E-05	9.0E-01	±	7.7E-05
300	0.93	0.92	0.92	0.92	6.2E-03	9.9E-03	6.6E-03	6.6E-05	9.2E-01	±	6.6E-05
325	0.95	0.94	0.94	0.94	5.7E-03	9.0E-03	5.4E-03	5.4E-05	9.4E-01	±	5.4E-05
350	0.96	0.95	0.96	0.96	5.1E-03	8.1E-03	4.3E-03	4.3E-05	9.6E-01	±	4.3E-05
375	0.98	0.96	0.97	0.97	4.5E-03	7.2E-03	3.4E-03	3.4E-05	9.7E-01	±	3.4E-05
400	0.98	0.98	0.98	0.98	3.8E-03	6.0E-03	2.3E-03	2.3E-05	9.8E-01	±	2.3E-05

425	0.99	0.98	0.98	0.99	3.0E-03	4.8E-03	1.5E-03	1.5E-05	9.9E-01	±	1.5E-05
450	0.99	0.99	0.99	0.99	2.2E-03	3.6E-03	8.0E-04	8.0E-06	9.9E-01	±	8.0E-06
475	1.00	0.99	0.99	1.00	1.5E-03	2.4E-03	3.7E-04	3.7E-06	1.0E+00	±	3.7E-06
500	1.00	1.00	1.00	1.00	7.6E-04	1.2E-03	9.3E-05	9.3E-07	1.0E+00	±	9.3E-07
							2.3				

Table D-3: Experimental desorption rate error analysis done on CQ650 at 30 °C and 5% CO_2 feed

CQ650 30 °C 5% CO_2 feed desorption reproducibility											
Time (s)	**Run 1 (qt/qe)**	**Run 2 (qt/qe)**	**Run 3 (qt/qe)**	**Avg des**	**Std dev**	**95% Conf int**	**Exp deviation %**	**Expt deviation**	**Final data**		
0	0.00	0.00	0.00	0.00	0.0E+00	0.0E+00	0.0E+00	0.0E+00	0.0E+00	±	0.0E+00
25	0.10	0.10	0.10	0.10	3.1E-04	5.0E-04	1.6E-04	1.6E-06	9.5E-02	±	1.6E-06
50	0.21	0.21	0.21	0.21	6.1E-04	9.7E-04	2.8E-04	2.8E-06	2.1E-01	±	2.8E-06
75	0.32	0.32	0.32	0.32	7.2E-04	1.2E-03	2.6E-04	2.6E-06	3.2E-01	±	2.6E-06
100	0.43	0.43	0.43	0.43	7.4E-04	1.2E-03	2.0E-04	2.0E-06	4.3E-01	±	2.0E-06
125	0.51	0.51	0.51	0.51	6.3E-04	1.0E-03	1.2E-04	1.2E-06	5.1E-01	±	1.2E-06
150	0.59	0.59	0.59	0.59	6.2E-04	9.8E-04	1.0E-04	1.0E-06	5.9E-01	±	1.0E-06
175	0.65	0.65	0.65	0.65	6.5E-04	1.0E-03	1.0E-04	1.0E-06	6.5E-01	±	1.0E-06
200	0.70	0.70	0.70	0.70	6.8E-04	1.1E-03	1.0E-04	1.0E-06	7.0E-01	±	1.0E-06
225	0.75	0.74	0.74	0.74	7.6E-04	1.2E-03	1.2E-04	1.2E-06	7.4E-01	±	1.2E-06
250	0.79	0.78	0.78	0.78	8.0E-04	1.3E-03	1.3E-04	1.3E-06	7.8E-01	±	1.3E-06
275	0.82	0.81	0.81	0.82	8.4E-04	1.3E-03	1.4E-04	1.4E-06	8.2E-01	±	1.4E-06
300	0.85	0.84	0.84	0.84	8.4E-04	1.3E-03	1.3E-04	1.3E-06	8.4E-01	±	1.3E-06
325	0.87	0.87	0.87	0.87	8.8E-04	1.4E-03	1.4E-04	1.4E-06	8.7E-01	±	1.4E-06
350	0.89	0.89	0.89	0.89	9.3E-04	1.5E-03	1.5E-04	1.5E-06	8.9E-01	±	1.5E-06
375	0.91	0.90	0.90	0.90	9.2E-04	1.5E-03	1.5E-04	1.5E-06	9.0E-01	±	1.5E-06
400	0.92	0.92	0.92	0.92	9.2E-04	1.5E-03	1.5E-04	1.5E-06	9.2E-01	±	1.5E-06

425	0.93	0.93	0.93	0.93	9.3E-04	1.5E-03	1.5E-04	1.5E-06	9.3E-01	±	1.5E-06
450	0.94	0.94	0.94	0.94	9.3E-04	1.5E-03	1.5E-04	1.5E-06	9.4E-01	±	1.5E-06
475	0.95	0.95	0.95	0.95	9.1E-04	1.5E-03	1.4E-04	1.4E-06	9.5E-01	±	1.4E-06
500	0.96	0.96	0.96	0.96	9.0E-04	1.4E-03	1.3E-04	1.3E-06	9.6E-01	±	1.3E-06
525	0.97	0.97	0.97	0.97	8.6E-04	1.4E-03	1.2E-04	1.2E-06	9.7E-01	±	1.2E-06
550	0.97	0.97	0.97	0.97	8.3E-04	1.3E-03	1.1E-04	1.1E-06	9.7E-01	±	1.1E-06
575	0.98	0.98	0.98	0.98	8.1E-04	1.3E-03	1.1E-04	1.1E-06	9.8E-01	±	1.1E-06
600	0.98	0.98	0.98	0.98	7.9E-04	1.3E-03	1.0E-04	1.0E-06	9.8E-01	±	1.0E-06
625	0.99	0.99	0.98	0.98	7.6E-04	1.2E-03	9.3E-05	9.3E-07	9.8E-01	±	9.3E-07
650	0.99	0.99	0.99	0.99	7.1E-04	1.1E-03	8.1E-05	8.1E-07	9.9E-01	±	8.1E-07
675	0.99	0.99	0.99	0.99	6.7E-04	1.1E-03	7.2E-05	7.2E-07	9.9E-01	±	7.2E-07
700	0.99	0.99	0.99	0.99	6.3E-04	1.0E-03	6.3E-05	6.3E-07	9.9E-01	±	6.3E-07
725	0.99	0.99	0.99	0.99	5.8E-04	9.2E-04	5.3E-05	5.3E-07	9.9E-01	±	5.3E-07
750	1.00	1.00	1.00	1.00	5.3E-04	8.5E-04	4.5E-05	4.5E-07	1.0E+00	±	4.5E-07
750	1.00	1.00	1.00	1.00	5.3E-04	8.5E-04	4.5E-05	4.5E-07	1.0E+00	±	4.5E-07
							0.049				

Table D-4: Experimental desorption rate error analysis done on CQ650 at 30 °C and 15% CO_2 feed

CQ650 30 °C 15% CO_2 feed desorption reproducibility											
Time (s)	**Run 1 (qt/qe)**	**Run 2 (qt/qe)**	**Run 3 (qt/qe)**	**Avg des**	**Std dev**	**95% Conf int**	**Exp deviation %**	**Expt deviation**	**Final data**		
0	0.00	0.00	0.00	0.00	0.0E+00	0.0E+00	0.0E+00	0.0E+00	0.0E+00	±	0.0E+00
25	0.09	0.09	0.09	0.09	1.0E-03	1.6E-03	1.9E-03	1.9E-05	9.1E-02	±	1.9E-05
50	0.23	0.23	0.23	0.23	1.8E-03	2.8E-03	2.2E-03	2.2E-05	2.3E-01	±	2.2E-05
75	0.35	0.35	0.35	0.35	2.4E-03	3.8E-03	2.6E-03	2.6E-05	3.5E-01	±	2.6E-05
100	0.46	0.46	0.46	0.46	2.8E-03	4.4E-03	2.7E-03	2.7E-05	4.6E-01	±	2.7E-05
125	0.55	0.54	0.54	0.54	3.1E-03	4.9E-03	2.8E-03	2.8E-05	5.4E-01	±	2.8E-05
150	0.62	0.61	0.61	0.62	3.1E-03	5.0E-03	2.5E-03	2.5E-05	6.2E-01	±	2.5E-05
175	0.68	0.67	0.67	0.67	3.2E-03	5.0E-03	2.4E-03	2.4E-05	6.7E-01	±	2.4E-05
200	0.73	0.72	0.72	0.73	3.0E-03	4.8E-03	2.0E-03	2.0E-05	7.3E-01	±	2.0E-05
225	0.77	0.76	0.76	0.77	2.9E-03	4.6E-03	1.7E-03	1.7E-05	7.7E-01	±	1.7E-05
250	0.81	0.80	0.80	0.80	2.6E-03	4.2E-03	1.4E-03	1.4E-05	8.0E-01	±	1.4E-05
275	0.84	0.83	0.83	0.83	2.4E-03	3.8E-03	1.1E-03	1.1E-05	8.3E-01	±	1.1E-05
300	0.86	0.86	0.86	0.86	2.2E-03	3.5E-03	8.8E-04	8.8E-06	8.6E-01	±	8.8E-06
325	0.89	0.88	0.88	0.88	2.0E-03	3.2E-03	7.1E-04	7.1E-06	8.8E-01	±	7.1E-06
350	0.90	0.90	0.90	0.90	1.8E-03	2.8E-03	5.4E-04	5.4E-06	9.0E-01	±	5.4E-06
375	0.92	0.92	0.92	0.92	1.6E-03	2.5E-03	4.2E-04	4.2E-06	9.2E-01	±	4.2E-06
400	0.93	0.93	0.93	0.93	1.4E-03	2.2E-03	3.2E-04	3.2E-06	9.3E-01	±	3.2E-06
425	0.95	0.94	0.94	0.94	1.2E-03	1.9E-03	2.5E-04	2.5E-06	9.4E-01	±	2.5E-06
450	0.96	0.95	0.95	0.95	1.0E-03	1.7E-03	1.8E-04	1.8E-06	9.5E-01	±	1.8E-06
475	0.96	0.96	0.96	0.96	8.8E-04	1.4E-03	1.3E-04	1.3E-06	9.6E-01	±	1.3E-06
500	0.97	0.97	0.97	0.97	7.4E-04	1.2E-03	8.9E-05	8.9E-07	9.7E-01	±	8.9E-07
525	0.98	0.97	0.98	0.98	6.6E-04	1.1E-03	7.2E-05	7.2E-07	9.8E-01	±	7.2E-07
550	0.98	0.98	0.98	0.98	5.8E-04	9.3E-04	5.5E-05	5.5E-07	9.8E-01	±	5.5E-07
575	0.99	0.98	0.99	0.99	5.3E-04	8.4E-04	4.5E-05	4.5E-07	9.9E-01	±	4.5E-07

600	0.99	0.99	0.99	0.99	4.9E-04	7.9E-04	3.9E-05	3.9E-07	9.9E-01	±	3.9E-07
625	0.99	0.99	0.99	0.99	4.4E-04	7.1E-04	3.2E-05	3.2E-07	9.9E-01	±	3.2E-07
650	0.99	0.99	0.99	0.99	3.8E-04	6.0E-04	2.3E-05	2.3E-07	9.9E-01	±	2.3E-07
675	1.00	1.00	1.00	1.00	3.4E-04	5.4E-04	1.9E-05	1.9E-07	1.0E+00	±	1.9E-07
							0.35				

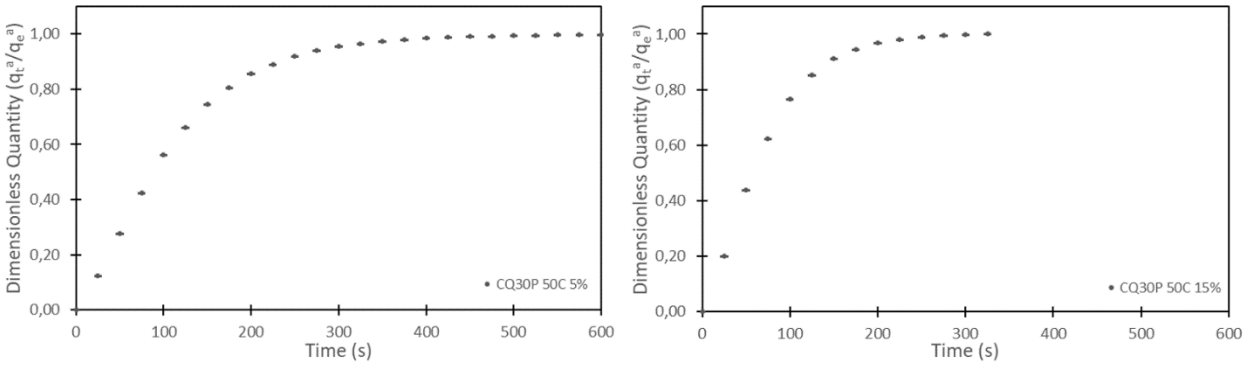

Figure D-3: Experimental adsorption rate error analysis done on CQ30P at 50 ºC and 5 and 15% CO_2 feed

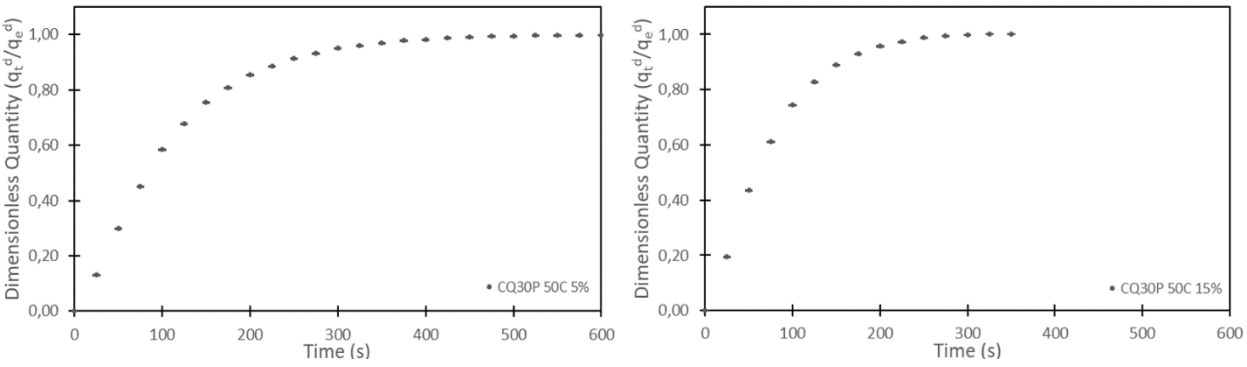

Figure D-4: Experimental desorption rate error analysis done on CQ30P at 50 ºC and 5 and 15% CO_2 feed

Table D-5: Experimental adsorption rate error analysis done on CQ30P at 50 °C and 5% CO_2 feed

CQ30P 50 °C 5% CO_2 feed adsorption reproducibility											
Time (s)	**Run 1 (qt/qe)**	**Run 2 (qt/qe)**	**Run 3 (qt/qe)**	**Avg ads**	**Std dev**	**95% Conf int**	**Exp deviation %**	**Expt deviation**	**Final data**		
0	0.00	0.00	0.00	0.00	0.0E+00	0.0E+00	0.0E+00	0.0E+00	0.0E+00	±	0.0E+00
25	0.13	0.12	0.12	0.12	2.6E-03	4.1E-03	8.5E-03	8.5E-05	1.2E-01	±	8.5E-05
50	0.28	0.28	0.27	0.28	4.2E-03	6.7E-03	1.0E-02	1.0E-04	2.8E-01	±	1.0E-04
75	0.43	0.42	0.42	0.43	4.5E-03	7.2E-03	7.6E-03	7.6E-05	4.3E-01	±	7.6E-05
100	0.57	0.56	0.56	0.56	4.1E-03	6.6E-03	4.9E-03	4.9E-05	5.6E-01	±	4.9E-05
125	0.67	0.66	0.66	0.66	3.8E-03	6.0E-03	3.5E-03	3.5E-05	6.6E-01	±	3.5E-05
150	0.75	0.74	0.74	0.75	3.6E-03	5.7E-03	2.7E-03	2.7E-05	7.5E-01	±	2.7E-05
175	0.81	0.80	0.80	0.81	3.3E-03	5.2E-03	2.1E-03	2.1E-05	8.1E-01	±	2.1E-05
200	0.86	0.86	0.85	0.86	3.0E-03	4.8E-03	1.7E-03	1.7E-05	8.6E-01	±	1.7E-05
225	0.89	0.89	0.89	0.89	2.7E-03	4.3E-03	1.3E-03	1.3E-05	8.9E-01	±	1.3E-05
250	0.92	0.92	0.92	0.92	2.4E-03	3.8E-03	1.0E-03	1.0E-05	9.2E-01	±	1.0E-05
275	0.94	0.94	0.94	0.94	2.1E-03	3.4E-03	7.8E-04	7.8E-06	9.4E-01	±	7.8E-06
300	0.96	0.96	0.95	0.96	2.0E-03	3.1E-03	6.4E-04	6.4E-06	9.6E-01	±	6.4E-06
325	0.97	0.97	0.96	0.97	1.7E-03	2.8E-03	5.0E-04	5.0E-06	9.7E-01	±	5.0E-06
350	0.98	0.97	0.97	0.97	1.6E-03	2.5E-03	4.2E-04	4.2E-06	9.7E-01	±	4.2E-06
375	0.98	0.98	0.98	0.98	1.5E-03	2.4E-03	3.6E-04	3.6E-06	9.8E-01	±	3.6E-06
400	0.99	0.98	0.98	0.98	1.4E-03	2.2E-03	3.2E-04	3.2E-06	9.8E-01	±	3.2E-06
425	0.99	0.99	0.99	0.99	1.3E-03	2.1E-03	2.9E-04	2.9E-06	9.9E-01	±	2.9E-06
450	0.99	0.99	0.99	0.99	1.2E-03	1.9E-03	2.4E-04	2.4E-06	9.9E-01	±	2.4E-06
475	0.99	0.99	0.99	0.99	1.0E-03	1.6E-03	1.7E-04	1.7E-06	9.9E-01	±	1.7E-06
500	1.00	0.99	0.99	0.99	8.9E-04	1.4E-03	1.3E-04	1.3E-06	9.9E-01	±	1.3E-06
525	1.00	1.00	1.00	1.00	6.4E-04	1.0E-03	6.5E-05	6.5E-07	1.0E+00	±	6.5E-07
							0.62				

Table D-6: Experimental adsorption rate error analysis done on CQ30P at 50 °C and 15% CO_2 feed

CQ30P 50 °C 15% CO_2 feed adsorption reproducibility											
Time (s)	**Run 1 (qt/qe)**	**Run 2 (qt/qe)**	**Run 3 (qt/qe)**	**Avg ads**	**Std dev**	**95% Conf int**	**Exp deviation %**	**Expt deviation**	**Final data**		
0	0.00	0.00	0.00	0.00	0.0E+00	0.0E+00	0.0E+00	0.0E+00	0.0E+00	±	0.0E+00
25	0.20	0.20	0.20	0.20	2.2E-03	3.5E-03	3.9E-03	3.9E-05	2.0E-01	±	3.9E-05
50	0.43	0.44	0.44	0.44	3.9E-03	6.1E-03	5.4E-03	5.4E-05	4.4E-01	±	5.4E-05
75	0.62	0.63	0.63	0.62	5.0E-03	8.0E-03	6.4E-03	6.4E-05	6.2E-01	±	6.4E-05
100	0.76	0.77	0.77	0.77	5.6E-03	8.8E-03	6.4E-03	6.4E-05	7.7E-01	±	6.4E-05
125	0.84	0.86	0.85	0.85	5.5E-03	8.7E-03	5.6E-03	5.6E-05	8.5E-01	±	5.6E-05
150	0.91	0.92	0.91	0.91	5.2E-03	8.2E-03	4.7E-03	4.7E-05	9.1E-01	±	4.7E-05
175	0.94	0.95	0.95	0.95	4.6E-03	7.4E-03	3.6E-03	3.6E-05	9.5E-01	±	3.6E-05
200	0.96	0.97	0.97	0.97	3.9E-03	6.3E-03	2.5E-03	2.5E-05	9.7E-01	±	2.5E-05
225	0.98	0.99	0.98	0.98	3.2E-03	5.1E-03	1.7E-03	1.7E-05	9.8E-01	±	1.7E-05
250	0.99	0.99	0.99	0.99	2.4E-03	3.8E-03	9.1E-04	9.1E-06	9.9E-01	±	9.1E-06
275	0.99	1.00	1.00	1.00	1.7E-03	2.7E-03	4.5E-04	4.5E-06	1.0E+00	±	4.5E-06
300	1.00	1.00	1.00	1.00	1.1E-03	1.7E-03	1.8E-04	1.8E-06	1.0E+00	±	1.8E-06
							0.54				

Table D-7: Experimental desorption rate error analysis done on CQ30P at 50 °C and 5% CO_2 feed

CQ30P 50 °C 5% CO_2 feed desorption reproducibility											
Time (s)	**Run 1 (qt/qe)**	**Run 2 (qt/qe)**	**Run 3 (qt/qe)**	**Avg des**	**Std dev**	**95% Conf int**	**Exp deviation %**	**Expt deviation**	**Final data**		
0	0.00	0.00	0.00	0.00	0.0E+00	0.0E+00	0.0E+00	0.0E+00	0.0E+00	±	0.0E+00
25	0.13	0.13	0.13	0.13	4.0E-04	6.4E-04	1.9E-04	1.9E-06	1.3E-01	±	1.9E-06
50	0.30	0.30	0.30	0.30	8.8E-04	1.4E-03	4.2E-04	4.2E-06	3.0E-01	±	4.2E-06
75	0.45	0.45	0.45	0.45	1.3E-03	2.0E-03	5.7E-04	5.7E-06	4.5E-01	±	5.7E-06
100	0.58	0.58	0.59	0.58	1.4E-03	2.2E-03	5.2E-04	5.2E-06	5.8E-01	±	5.2E-06
125	0.68	0.68	0.68	0.68	1.5E-03	2.3E-03	5.0E-04	5.0E-06	6.8E-01	±	5.0E-06
150	0.75	0.76	0.76	0.75	1.4E-03	2.2E-03	4.2E-04	4.2E-06	7.5E-01	±	4.2E-06
175	0.81	0.81	0.81	0.81	1.4E-03	2.3E-03	3.9E-04	3.9E-06	8.1E-01	±	3.9E-06
200	0.85	0.85	0.85	0.85	1.4E-03	2.2E-03	3.6E-04	3.6E-06	8.5E-01	±	3.6E-06
225	0.88	0.89	0.89	0.89	1.3E-03	2.1E-03	3.0E-04	3.0E-06	8.9E-01	±	3.0E-06
250	0.91	0.91	0.91	0.91	1.2E-03	1.9E-03	2.5E-04	2.5E-06	9.1E-01	±	2.5E-06
275	0.93	0.93	0.93	0.93	1.1E-03	1.7E-03	1.9E-04	1.9E-06	9.3E-01	±	1.9E-06
300	0.95	0.95	0.95	0.95	9.9E-04	1.6E-03	1.6E-04	1.6E-06	9.5E-01	±	1.6E-06
325	0.96	0.96	0.96	0.96	9.3E-04	1.5E-03	1.4E-04	1.4E-06	9.6E-01	±	1.4E-06
350	0.97	0.97	0.97	0.97	8.7E-04	1.4E-03	1.2E-04	1.2E-06	9.7E-01	±	1.2E-06
375	0.98	0.98	0.98	0.98	7.9E-04	1.3E-03	1.0E-04	1.0E-06	9.8E-01	±	1.0E-06
400	0.98	0.98	0.98	0.98	7.2E-04	1.1E-03	8.3E-05	8.3E-07	9.8E-01	±	8.3E-07
425	0.99	0.99	0.99	0.99	6.3E-04	1.0E-03	6.4E-05	6.4E-07	9.9E-01	±	6.4E-07
450	0.99	0.99	0.99	0.99	5.5E-04	8.8E-04	4.9E-05	4.9E-07	9.9E-01	±	4.9E-07
475	0.99	0.99	0.99	0.99	5.3E-04	8.4E-04	4.5E-05	4.5E-07	9.9E-01	±	4.5E-07
500	0.99	1.00	1.00	1.00	4.2E-04	6.7E-04	2.8E-05	2.8E-07	1.0E+00	±	2.8E-07
525	1.00	1.00	1.00	1.00	3.6E-04	5.7E-04	2.0E-05	2.0E-07	1.0E+00	±	2.0E-07
							0.064				

Table D-8: Experimental desorption rate error analysis done on CQ30P at 50 °C and 15% CO_2 feed

CQ30P 50 °C 15% CO_2 feed desorption reproducibility											
Time (s)	**Run 1 (qt/qe)**	**Run 2 (qt/qe)**	**Run 3 (qt/qe)**	**Avg des**	**Std dev**	**95% Conf int**	**Exp deviation %**	**Expt deviation**	**Final data**		
0	0.00	0.00	0.00	0.00	0.0E+00	0.0E+00	0.0E+00	0.0E+00	0.0E+00	±	0.0E+00
25	0.20	0.20	0.19	0.20	8.9E-04	1.4E-03	6.5E-04	6.5E-06	2.0E-01	±	6.5E-06
50	0.44	0.44	0.44	0.44	9.4E-04	1.5E-03	3.2E-04	3.2E-06	4.4E-01	±	3.2E-06
75	0.61	0.61	0.61	0.61	5.2E-04	8.3E-04	7.1E-05	7.1E-07	6.1E-01	±	7.1E-07
100	0.74	0.75	0.75	0.75	5.6E-04	9.0E-04	6.8E-05	6.8E-07	7.5E-01	±	6.8E-07
125	0.83	0.83	0.83	0.83	8.1E-04	1.3E-03	1.2E-04	1.2E-06	8.3E-01	±	1.2E-06
150	0.89	0.89	0.89	0.89	1.0E-03	1.6E-03	1.8E-04	1.8E-06	8.9E-01	±	1.8E-06
175	0.93	0.93	0.93	0.93	1.1E-03	1.7E-03	1.9E-04	1.9E-06	9.3E-01	±	1.9E-06
200	0.96	0.96	0.96	0.96	1.0E-03	1.6E-03	1.7E-04	1.7E-06	9.6E-01	±	1.7E-06
225	0.97	0.98	0.98	0.97	9.1E-04	1.5E-03	1.4E-04	1.4E-06	9.7E-01	±	1.4E-06
250	0.99	0.99	0.99	0.99	8.1E-04	1.3E-03	1.1E-04	1.1E-06	9.9E-01	±	1.1E-06
275	0.99	0.99	0.99	0.99	5.8E-04	9.3E-04	5.4E-05	5.4E-07	9.9E-01	±	5.4E-07
300	1.00	1.00	1.00	1.00	2.9E-04	4.6E-04	1.3E-05	1.3E-07	1.0E+00	±	1.3E-07
							0.031				

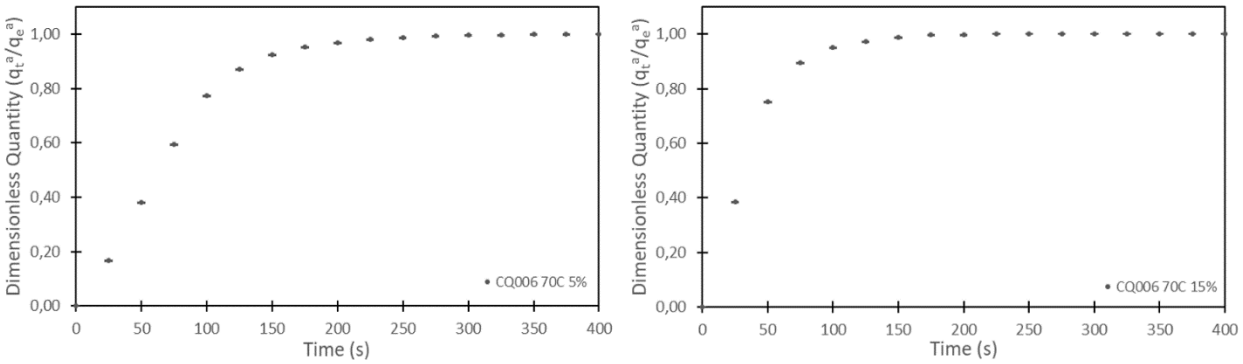

Figure D-5: Experimental adsorption rate error analysis done on CQ006 at 70 ºC and 5 and 15% CO_2 feed

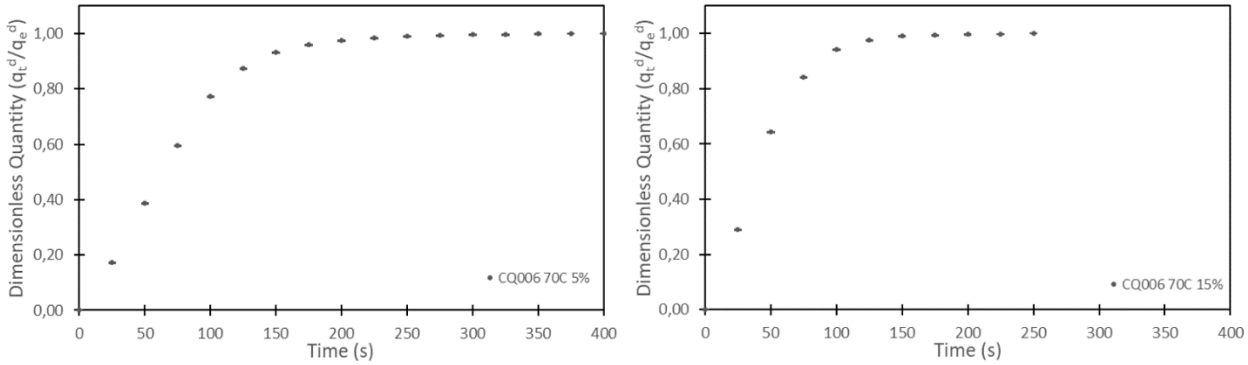

Figure D-6: Experimental desorption rate error analysis done on CQ006 at 70 ºC and 5 and 15% CO_2 feed

Table D-9: Experimental adsorption rate error analysis done on CQ006 at 70 °C and 5% CO_2 feed

CQ006 70 °C 5% CO_2 feed adsorption reproducibility											
Time (s)	**Run 1 (qt/qe)**	**Run 2 (qt/qe)**	**Run 3 (qt/qe)**	**Avg ads**	**Std dev**	**95% Conf int**	**Exp deviation %**	**Expt deviation**	**Final data**		
0	0.00	0.00	0.00	0.00	0.0E+00	0.0E+00	0.0E+00	0.0E+00	0.0E+00	±	0.0E+00
25	0.17	0.17	0.17	0.17	3.3E-03	5.3E-03	1.0E-02	1.0E-04	1.7E-01	±	1.0E-04
50	0.38	0.37	0.39	0.38	7.2E-03	1.1E-02	2.2E-02	2.2E-04	3.8E-01	±	2.2E-04
75	0.59	0.59	0.61	0.59	8.6E-03	1.4E-02	2.0E-02	2.0E-04	5.9E-01	±	2.0E-04
100	0.77	0.77	0.78	0.77	5.7E-03	9.0E-03	6.6E-03	6.6E-05	7.7E-01	±	6.6E-05
125	0.87	0.87	0.88	0.87	3.2E-03	5.1E-03	1.8E-03	1.8E-05	8.7E-01	±	1.8E-05
150	0.92	0.93	0.93	0.92	2.2E-03	3.5E-03	8.3E-04	8.3E-06	9.2E-01	±	8.3E-06
175	0.95	0.95	0.95	0.95	1.9E-03	3.1E-03	6.2E-04	6.2E-06	9.5E-01	±	6.2E-06
200	0.97	0.97	0.97	0.97	1.6E-03	2.6E-03	4.4E-04	4.4E-06	9.7E-01	±	4.4E-06
225	0.98	0.98	0.98	0.98	1.4E-03	2.3E-03	3.3E-04	3.3E-06	9.8E-01	±	3.3E-06
250	0.99	0.99	0.99	0.99	1.2E-03	1.9E-03	2.3E-04	2.3E-06	9.9E-01	±	2.3E-06
275	0.99	0.99	0.99	0.99	1.1E-03	1.7E-03	1.8E-04	1.8E-06	9.9E-01	±	1.8E-06
300	1.00	1.00	1.00	1.00	7.9E-04	1.3E-03	9.9E-05	9.9E-07	1.0E+00	±	9.9E-07
							0.82				

Table D-10: Experimental adsorption rate error analysis done on CQ006 at 70 °C and 15% CO_2 feed

CQ006 70 °C 15% CO_2 feed adsorption reproducibility											
Time (s)	**Run 1 (qt/qe)**	**Run 2 (qt/qe)**	**Run 3 (qt/qe)**	**Avg ads**	**Std dev**	**95% Conf int**	**Exp deviation %**	**Expt deviation**	**Final data**		
0	0.00	0.00	0.00	0.00	0.0E+00	0.0E+00	0.0E+00	0.0E+00	0.0E+00	±	0.0E+00
25	0.39	0.38	0.38	0.38	3.9E-03	6.3E-03	6.4E-03	6.4E-05	3.8E-01	±	6.4E-05
50	0.76	0.75	0.75	0.75	5.3E-03	8.4E-03	5.9E-03	5.9E-05	7.5E-01	±	5.9E-05
75	0.90	0.89	0.89	0.90	5.1E-03	8.0E-03	4.5E-03	4.5E-05	9.0E-01	±	4.5E-05
100	0.95	0.94	0.95	0.95	4.1E-03	6.5E-03	2.8E-03	2.8E-05	9.5E-01	±	2.8E-05
125	0.98	0.97	0.98	0.97	3.4E-03	5.3E-03	1.8E-03	1.8E-05	9.7E-01	±	1.8E-05
150	0.99	0.98	0.99	0.99	2.9E-03	4.5E-03	1.3E-03	1.3E-05	9.9E-01	±	1.3E-05
175	1.00	0.99	1.00	1.00	2.2E-03	3.5E-03	7.8E-04	7.8E-06	1.0E+00	±	7.8E-06
200	1.00	1.00	1.00	1.00	1.3E-03	2.0E-03	2.6E-04	2.6E-06	1.0E+00	±	2.6E-06
							0.33				

Table D-11: Experimental desorption rate error analysis done on CQ006 at 70 °C and 5% CO_2 feed

CQ006 70 °C 5% CO_2 feed desorption reproducibility											
Time (s)	**Run 1 (qt/qe)**	**Run 2 (qt/qe)**	**Run 3 (qt/qe)**	**Avg des**	**Std dev**	**95% Conf int**	**Exp deviation %**	**Expt deviation**	**Final data**		
0	0.00	0.00	0.00	0.00	0.0E+00	0.0E+00	0.0E+00	0.0E+00	0.0E+00	±	0.0E+00
25	0.17	0.17	0.17	0.17	1.2E-03	1.9E-03	1.4E-03	1.4E-05	1.7E-01	±	1.4E-05
50	0.39	0.39	0.39	0.39	1.8E-03	2.9E-03	1.4E-03	1.4E-05	3.9E-01	±	1.4E-05
75	0.59	0.60	0.60	0.60	2.2E-03	3.5E-03	1.3E-03	1.3E-05	6.0E-01	±	1.3E-05
100	0.77	0.77	0.78	0.77	1.7E-03	2.7E-03	6.1E-04	6.1E-06	7.7E-01	±	6.1E-06
125	0.87	0.87	0.88	0.87	1.1E-03	1.8E-03	2.4E-04	2.4E-06	8.7E-01	±	2.4E-06
150	0.93	0.93	0.93	0.93	7.8E-04	1.2E-03	1.0E-04	1.0E-06	9.3E-01	±	1.0E-06
175	0.96	0.96	0.96	0.96	7.3E-04	1.2E-03	8.8E-05	8.8E-07	9.6E-01	±	8.8E-07
200	0.98	0.97	0.98	0.98	7.4E-04	1.2E-03	9.0E-05	9.0E-07	9.8E-01	±	9.0E-07
225	0.98	0.98	0.98	0.98	7.5E-04	1.2E-03	9.1E-05	9.1E-07	9.8E-01	±	9.1E-07
250	0.99	0.99	0.99	0.99	6.9E-04	1.1E-03	7.7E-05	7.7E-07	9.9E-01	±	7.7E-07
275	0.99	0.99	0.99	0.99	6.1E-04	9.7E-04	5.9E-05	5.9E-07	9.9E-01	±	5.9E-07
300	1.00	1.00	1.00	1.00	4.9E-04	7.7E-04	3.8E-05	3.8E-07	1.0E+00	±	3.8E-07
325	1.00	1.00	1.00	1.00	3.5E-04	5.6E-04	2.0E-05	2.0E-07	1.0E+00	±	2.0E-07
350	1.00	1.00	1.00	1.00	2.6E-04	4.1E-04	1.1E-05	1.1E-07	1.0E+00	±	1.1E-07
375	1.00	1.00	1.00	1.00	1.1E-04	1.8E-04	2.1E-06	2.1E-08	1.0E+00	±	2.1E-08
							0.082				

Table D-12: Experimental adsorption rate error analysis done on CQ006 at 70 °C and 15% CO_2 feed

CQ006 70 °C 15% CO_2 feed desorption reproducibility											
Time (s)	**Run 1 (qt/qe)**	**Run 2 (qt/qe)**	**Run 3 (qt/qe)**	**Avg des**	**Std dev**	**95% Conf int**	**Exp deviation %**	**Expt deviation**	**Final data**		
0	0.00	0.00	0.00	0.00	0.0E+00	0.0E+00	0.0E+00	0.0E+00	0.0E+00	±	0.0E+00
25	0.29	0.29	0.29	0.29	1.2E-03	2.0E-03	8.4E-04	8.4E-06	2.9E-01	±	8.4E-06
50	0.64	0.64	0.64	0.64	3.3E-04	5.3E-04	2.8E-05	2.8E-07	6.4E-01	±	2.8E-07
75	0.84	0.84	0.84	0.84	8.0E-04	1.3E-03	1.2E-04	1.2E-06	8.4E-01	±	1.2E-06
100	0.94	0.94	0.94	0.94	1.1E-03	1.8E-03	2.1E-04	2.1E-06	9.4E-01	±	2.1E-06
125	0.98	0.98	0.98	0.98	9.1E-04	1.4E-03	1.3E-04	1.3E-06	9.8E-01	±	1.3E-06
150	0.99	0.99	0.99	0.99	7.2E-04	1.2E-03	8.4E-05	8.4E-07	9.9E-01	±	8.4E-07
175	0.99	1.00	1.00	1.00	5.4E-04	8.6E-04	4.7E-05	4.7E-07	1.0E+00	±	4.7E-07
							0.061				